

DYNAMIC SUSPENSION MODELING OF AN EDDY-CURRENT DEVICE: AN
APPLICATION TO MAGLEV

by

Nirmal Paudel

A dissertation submitted to the faculty of
The University of North Carolina at Charlotte
in partial fulfillment of the requirements
for the degree of Doctor of Philosophy in
Electrical Engineering

Charlotte

2012

Approved by:

Dr. Jonathan Z. Bird

Dr. Yogendra P. Kakad

Dr. Robert W. Cox

Dr. Scott D. Kelly

© 2012
Nirmal Paudel
ALL RIGHTS RESERVED

ABSTRACT

NIRMAL PAUDEL. Dynamic suspension modeling of an eddy-current device: an application to Maglev.
(Under the direction of DR. JONATHAN Z. BIRD)

When a magnetic source is simultaneously oscillated and translationally moved above a linear conductive passive guideway such as aluminum, eddy-currents are induced that give rise to a time-varying opposing field in the air-gap. This time-varying opposing field interacts with the source field, creating simultaneously suspension, propulsion or braking and lateral forces that are required for a Maglev system.

In this thesis, a two-dimensional (2-D) analytic based steady-state eddy-current model has been derived for the case when an arbitrary magnetic source is oscillated and moved in two directions above a conductive guideway using a spatial Fourier transform technique. The problem is formulated using both the magnetic vector potential, \mathbf{A} , and scalar potential, ϕ . Using this novel \mathbf{A} - ϕ approach the magnetic source needs to be incorporated only into the boundary conditions of the guideway and only the magnitude of the source field along the guideway surface is required in order to compute the forces and power loss. The performance of this analytic based steady-state eddy-current model has been validated by comparing it with a 2-D finite-element model. The magnetic source used for the validation is a radially magnetized Halbach rotor, called an electrodynamic wheel (EDW).

The 2-D analytic based transient eddy-current force and power loss equations are derived for the case when an arbitrary magnetic source is moving and oscillating above a conductive guideway. These general equations for force and power loss are derived using a spatial Fourier transform and temporal Laplace transform technique. The derived equations are capable of accounting for step changes in the input parameters, in addition to arbitrary continuous changes in the input conditions. The equations have been validated for both step changes as well as continuous changes in the input

conditions using a 2-D transient finite-element model.

The dynamics of an EDW Maglev is investigated by using both steady-state and transient eddy-current models. The analytic equations for the self as well as mutual damping and stiffness coefficients of an EDW Maglev are derived using the 2-D analytic steady-state eddy-current force equations. It is shown that the steady-state eddy-current model in which the heave velocity is included in the formulation can accurately predict the dynamic behavior of a 2-degree of freedom EDW Maglev vehicle. The 2-D EDW Maglev vehicle has been built using Matlab/SimMechanicsTM.

A 1-degree of freedom pendulum setup of an EDW Maglev has been built in order to investigate the dynamics of an EDW Maglev. The dynamic model of an EDW Maglev has been validated using this pendulum setup. A multi-degree of freedom Maglev vehicle prototype has been constructed using four EDWs. The dynamics of the prototype Maglev has been investigated using the Matlab simulations. This prototype setup will be used to investigate the dynamic behavior of EDW Maglev in the future.

DEDICATION

I dedicate this dissertation to my beloved family. Particularly to my wonderful parents, Punya Prasad Paudel and Shanti Paudel, who have given full support and their unconditional love and to my understanding and patient wife, Anju Luitel Paudel, who has put up with these many years of research, and to our precious daughter Niva, who is the joy of our lives. I must also thank my brothers, Santosh and Ramesh, my sister, Krishna and my brother-in-law, Narendra, who encouraged me in many ways to pursue my dream. Finally, I dedicate this work to my grandfather, Tikaram and my late grandmother, Tulki, both of whom are source of my inspirations.

ACKNOWLEDGMENTS

First and foremost I would like to express my sincere gratitude to my Ph.D. advisor Dr. Jonathan Z. Bird for providing me the wonderful opportunity for the successful completion of my Ph.D. I always respect him for providing me the confidence and support from the beginning to the completion of this dissertation. This would not have been possible without his encouragement and dedication.

I would like to extend my appreciation to the committee members Dr. Yogendra P. Kakad, Dr. Robert W. Cox and Dr. Scott D. Kelly for being in my committee and for their efforts to assess my work.

I would also like express my thanks to Walter Bomela for his invaluable support to construct the experimental setups and Dheeraj Bobba and Subhra Paul for their assistance and the rest of my lab peers for their friendships during the course of my research. I would also like to thank Yawo Amengonu for the interesting discussions on system dynamics and control.

I would like to gratefully acknowledge the University of North Carolina at Charlotte for the tuition grants and the department of electrical and computer engineering for the teaching assistantship.

I would gratefully like to thank National Science Foundation for providing the funding for this research. This material is based upon work supported by the National Science Foundation under Grant No. 0925941.

TABLE OF CONTENTS

LIST OF TABLES	xiii
LIST OF FIGURES	xiv
LIST OF ABBREVIATIONS	xxix
LIST OF SYMBOLS	xxx
CHAPTER 1: INTRODUCTION AND LITERATURE REVIEW	1
1.1 Introduction	1
1.2 Types of Suspension Technologies	2
1.2.1 Electromagnetic Suspension	2
1.2.2 Electrodynamic Suspension	4
1.3 Types of Propulsion Technologies	7
1.3.1 Linear Induction Motor	7
1.3.2 Linear Synchronous Motor	10
1.4 Integrated Propulsion and Suspension Techniques	11
1.4.1 LIM Using Magnetic Attraction	11
1.4.2 Linear Reluctance Motor	12
1.4.3 Iron Cored LSM	12
1.4.4 Electromagnetic River	12
1.4.5 Electrodynamic Wheels	13
1.5 Research Goals	16

1.6	Organization of the Thesis	17
CHAPTER 2: A 2D STEADY-STATE ANALYTIC EDDY-CURRENT MODEL		19
2.1	Introduction	19
2.2	A Review of 2-D Eddy-Current Modeling Techniques	19
2.2.1	Equivalent-Circuit Model	20
2.2.2	Thick and Thin Conductive Sheet Approximation	20
2.2.3	Numerical Methods	21
2.2.4	The Spatial Fourier Transform Method	22
2.3	Fourier Transform 2-D Analytical Steady-State Solution	22
2.3.1	Governing Subdomain Equations	23
2.3.2	Non-Conducting Regions	25
2.3.3	Conducting Guideway Region	26
2.3.4	Boundary Conditions	29
2.3.5	Fourier Transformed Governing Subdomain Equations	31
2.3.6	Fourier Transformed Boundary Conditions	33
2.3.7	The Vector Potential Solution	34
2.3.8	Reflected Field in the Non-Conducting Region	36
2.3.9	Force and Power Equations	37
2.3.9.1	Tensor Force Calculation	37
2.3.9.2	Lorentz Force Calculation	42
2.3.9.3	Force Calculation Using Magnetic Charge	43

	ix
2.3.10 Power Loss Calculation	45
2.3.11 Halbach Rotor Source Field	48
2.3.11.1 The Fourier Transform for the Rotor Source Field	51
2.3.12 Analytic Based Simulation Results and FEA Validations	52
2.3.13 Electrodynamic Wheels in Series	57
2.3.13.1 The Fourier Transform of the EDWs in Series	59
2.3.13.2 EDWs in Series: FEA and Analytic Comparison	60
2.4 Summary	63
CHAPTER 3: A 2-D TRANSIENT ANALYTIC EDDY-CURRENT MODEL	64
3.1 Introduction	64
3.2 A Review of 2-D Transient Eddy-Current Modeling	64
3.3 A 2-D Transient Analytical Modeling	65
3.3.1 Governing Subdomain Equations	66
3.3.1.1 Conducting Guideway Region	67
3.3.1.2 Non-Conducting Regions	67
3.3.1.3 Boundary Conditions	67
3.3.2 Fourier-Laplace Solution for Governing Subdomain Equations	69
3.3.2.1 Fourier and Laplace Transformed Conducting Region	69
3.3.2.2 Fourier Transformed Non-Conducting Region	71
3.3.2.3 Fourier and Laplace Transformed Boundary Conditions	72
3.3.3 Solution to Governing Equation	74

	x
3.3.4	Transient Reflected Flux Density 75
3.3.5	Time Domain Solution 76
3.3.6	Electric Field Intensity and Magnetic Flux Densities 81
3.3.7	Force and Power Loss Calculations 83
3.3.7.1	Tensor Force Calculation 83
3.3.7.2	Lorentz Force Calculation 84
3.3.7.3	Power Loss Calculation 85
3.3.8	Magnetic Source Field-A Halbach Rotor 86
3.3.8.1	Fourier and Laplace Transform for Rotor Source Field 86
3.4	Simulation Results and FEA Validations 87
3.4.1	FEA Model in Magsoft/Flux 2D 93
3.5	Summary 97
CHAPTER 4: ELECTROMECHANICAL DYNAMIC SUSPENSION MODEL 99	
4.1	Introduction 99
4.2	Review on Dynamic Maglev Modeling 99
4.3	Magnetic Damping and Stiffness 105
4.4	Dynamic Modeling Using Steady-State Force Equations 109
4.5	Dynamic Modeling Using Transient Force Equations 111
4.5.1	Vector Potential Step and Impulse Response 112
4.5.2	Validation of Transient Analytic Model Using FEA 115
4.5.3	Dynamic Simulation for Step Change in Weight of the Vehicle 116

4.5.4	Dynamic Simulation for Step Change in ω_m of EDWs	121
4.6	Magnetic Stiffness and Damping of an EDW	125
4.7	Summary	140
CHAPTER 5: EXPERIMENTAL VERIFICATION AND RESULTS		142
5.1	Introduction	142
5.2	Experimental Setup	142
5.2.1	Measurement of guideway irregularities	149
5.3	Calculation of Air and Friction Damping Coefficients	149
5.4	Dynamics of the Forced Pendulum	152
5.4.1	Test-A	154
5.4.2	Test-B	157
5.4.3	Test-C	160
5.4.4	Test-D	162
5.4.5	Test-E	164
5.5	Summary	166
CHAPTER 6: DYNAMICS OF MULTI-DOF EDW MAGLEV		167
6.1	Introduction	167
6.2	Multi-DOF Maglev Experimental Setup	167
6.3	A 6-DOF Simulink Maglev Model	175
6.4	6-DOF Simulation of the EDW Maglev	181
6.5	An EDW Maglev Experiment with z -offset	189

	xii
6.6 Summary	193
CHAPTER 7: CONCLUSION AND FUTURE WORKS	194
7.1 Introduction	194
7.2 Conclusion	194
7.3 Research Contributions	196
7.4 Future Research Works	197
BIBLIOGRAPHY	198
APPENDIX A: A 2-D TRANSIENT FINITE-ELEMENT MODEL	213
A.1 Non-Conducting Regions	213
A.2 Conducting Guideway Region	213
A.3 Boundary Conditions	214
A.4 Rotor Magnetic Field	215
APPENDIX B: ADDITIONAL EXPERIMENTAL RESULTS	217
APPENDIX C: SIMULINK MAGLEV VEHICLE	231

LIST OF TABLES

TABLE 1.1:	Current status of Maglev projects around the world.	9
TABLE 2.1:	Simulation parameters for 2-D steady-state model.	53
TABLE 2.2:	Simulation parameters for EDWs in series.	61
TABLE 3.1:	Mathematica code for tan and cot root calculations.	78
TABLE 3.2:	Simulation parameters for 2-D transient model.	88
TABLE 3.3:	Simulation Parameters for Magsoft Model.	95
TABLE 4.1:	Parameters for 2-DOF Maglev vehicle dynamic simulation.	111
TABLE 4.2:	Simulation parameters for stiffness and damping.	129
TABLE 5.1:	Guideway and EDW parameters of the experimental setup.	144
TABLE 5.2:	Axi-5330/24 brushless PM DC motor parameters.	146
TABLE 5.3:	ABB separately excited DC motor parameters.	146
TABLE 5.4:	Damping and stiffness coefficients from free oscillations.	151
TABLE 5.5:	Pendulum setup parameters.	153
TABLE 5.6:	Initial conditions for Test-B at $t = 0$ s.	158
TABLE 5.7:	Initial conditions for Test-C at $t = 0$ s.	160
TABLE 5.8:	Initial conditions for Test-D at $t = 0$ s.	163
TABLE 5.9:	Initial conditions for Test-E at $t = 0$ s.	165
TABLE 6.1:	Guideway and EDW parameters for the 4-wheel Maglev setup.	169
TABLE 6.2:	Scorpion S-4035-250KV BLDC motor parameters.	171
TABLE 6.3:	Phoenix ICE HV 120 parameters.	171
TABLE 6.4:	The parameters of the experimental Maglev vehicle.	176

LIST OF FIGURES

FIGURE 1.1:	Transrapid EMS with levitation and guidance electromagnets separated.	3
FIGURE 1.2:	Japanese HSST with levitation and guidance electromagnets integrated.	3
FIGURE 1.3:	MagneMotion M ³ Maglev system.	4
FIGURE 1.4:	Normalized force of EDS Maglev for different translational velocity.	5
FIGURE 1.5:	The Japanese MLX01 Maglev using null-flux structure.	6
FIGURE 1.6:	The Inductrack Maglev model using dual-Halbach array and linear synchronous motor.	7
FIGURE 1.7:	Single sided linear induction motor (a) short-stator SLIM (b) long-stator SLIM.	8
FIGURE 1.8:	Double sided linear induction motor.	8
FIGURE 1.9:	The LSM propulsion used for German Transrapid.	10
FIGURE 1.10:	The electromagnetic launch assistance system located at the NASA Marshall Space Flight Center.	14
FIGURE 1.11:	Radial and helical superconducting rotor configurations.	14
FIGURE 1.12:	Magnet wheels rotating above a conductor.	15
FIGURE 1.13:	The translationally moving and rotating EDW above a passive guideway.	16
FIGURE 2.1:	A four pole-pair Halbach rotor.	23
FIGURE 2.2:	A FEA COMSOL model of a four pole-pair Halbach rotor rotating and translationally moving above a long conducting guideway.	24
FIGURE 2.3:	Illustration of the conductive and non-conductive regions and boundaries used by the analytic based 2-D steady-state model.	26
FIGURE 2.4:	Halbach rotor source fields with y -axis offset.	50

FIGURE 2.5:	Lift (normal) force as a function of slip and translational velocity at $v_y = 0\text{ms}^{-1}$.	53
FIGURE 2.6:	Thrust (tangential) force as a function of slip and translational velocity at $v_y = 0\text{ms}^{-1}$.	54
FIGURE 2.7:	Power loss in the conducting guideway as a function of slip and translational velocity at $v_y = 0\text{ms}^{-1}$.	54
FIGURE 2.8:	The lift and thrust force percentage error between the FEA and analytical model as a function of slip for translational velocity, $v_x = 0\text{ms}^{-1}$ and 30ms^{-1} at $v_y = 0\text{ms}^{-1}$.	55
FIGURE 2.9:	Lift (normal) force in the conducting guideway as a function of slip and rotor heave velocity, v_y at translational velocity, $v_x = 0\text{ms}^{-1}$.	56
FIGURE 2.10:	Thrust (tangential) force in the conducting guideway as a function of slip and rotor heave velocity, v_y at translational speed, $v_x = 0\text{ms}^{-1}$.	56
FIGURE 2.11:	A COMSOL FEA result showing the surface plot of A_z in guideway and the contour plot of B_x in non-conducting region for $v_x = 20\text{ms}^{-1}$, $slip = 30\text{ms}^{-1}$ and $v_y = 0\text{ms}^{-1}$.	57
FIGURE 2.12:	A mesh plot of a 2-D steady-state FEA model developed in COMSOL.	57
FIGURE 2.13:	Multiple EDWs in series above a conductive guideway.	58
FIGURE 2.14:	The vector potential contour plot for five EDWs in series using the steady-state FEA model developed in COMSOL.	58
FIGURE 2.15:	The thrust force comparison between analytic and FEA for 5-EDWs in series above a conductive guideway.	61
FIGURE 2.16:	The lift force comparison between analytic and FEA for 5-EDWs in series above a conductive guideway.	62
FIGURE 2.17:	The power loss comparison between analytic and FEA for 5-EDWs in series above a conductive guideway.	62
FIGURE 2.18:	The thrust efficiency comparison between analytic and FEA for 5-EDWs in series above a conductive guideway.	63

FIGURE 3.1:	Illustration of the conductive and non-conductive regions and boundaries used by the analytic based transient model.	66
FIGURE 3.2:	The sample <i>tan</i> and <i>cot</i> roots calculation for $\xi = 250$ and $b = 6.3\text{mm}$.	79
FIGURE 3.3:	Vector potential fields for the transient JMAG model.	89
FIGURE 3.4:	A comparison for the transient lift and thrust forces for a step change in angular velocity from 0 RPM to 3000 RPM.	89
FIGURE 3.5:	A comparison for the transient lift and thrust forces for a step change in angular speed from 0 RPM to 1000 RPM.	90
FIGURE 3.6:	A comparison for the transient power loss for a step change in angular speed from 0 RPM to 3000 RPM.	90
FIGURE 3.7:	A comparison for the transient lift and thrust forces for a step change in air-gap from 10 mm to 15mm at $t = 15$ ms with $\omega_m = 1000\text{RPM}$, $v_x = 0\text{ms}^{-1}$.	91
FIGURE 3.8:	A comparison for the transient lift and thrust forces for a step change in air-gap from 10 mm to 15mm at $t = 15\text{ms}$ with $\omega_m = 0\text{RPM}$, $v_x = 10\text{ms}^{-1}$.	91
FIGURE 3.9:	COMSOL FEA surface plot of A_z in the guideway and contour plot of B_x in the air-region for a step change in v_x from 0ms^{-1} to 10ms^{-1} after 1ms.	92
FIGURE 3.10:	COMSOL FEA plot showing the surface plot of A_z in the guideway and contour plot of B_x in the air-region for a step change in v_x from 0ms^{-1} to 10ms^{-1} after 5ms.	92
FIGURE 3.11:	2D FEA Magsoft model for a 16-segments 4 pole-pairs Halbach rotor rotating above an aluminum sheet guideway.	93
FIGURE 3.12:	FEA Magsoft model for a 32-segments 4 pole-pairs Halbach rotor rotating above an aluminum sheet guideway.	94
FIGURE 3.13:	FEA Magsoft model for a 64-segments 4 pole-pairs Halbach rotor rotating above an aluminum sheet guideway.	94
FIGURE 3.14:	The problem regions of the 2D transient Magsoft model with the mesh.	95

FIGURE 3.15: The thrust force comparison between the Magsoft models, analytic model and COMSOL model.	96
FIGURE 3.16: The lift force comparison between the Magsoft models, analytic model and COMSOL model.	96
FIGURE 3.17: The power loss in the guideway comparison between the Magsoft models, analytic model and COMSOL model.	97
FIGURE 4.1: The EDS Maglev using SCMs used by Coffey et al.	101
FIGURE 4.2: Test vehicle using SCMs over a inverted-T test guideway.	101
FIGURE 4.3: Cross-section of ML-500 test vehicle with inverted-T-shaped guideway configuration.	102
FIGURE 4.4: Cross-section of MLU001 test vehicle with a U-shaped guideway configuration, levitation coils on the ground, and combined propulsion and guidance coils on the side wall.	102
FIGURE 4.5: Cross-section of MLU002 test vehicle with side wall null-flux levitation system.	102
FIGURE 4.6: MLU002N test vehicle photo.	103
FIGURE 4.7: Photo of MLX01 test vehicle at Yamanashi test track.	103
FIGURE 4.8: Sketch and a picture of a PM levitated Maglev in a V-shaped guideway.	104
FIGURE 4.9: Sketch of Maglev model used by Chu and Moon.	104
FIGURE 4.10: A 3-DOF Maglev system on a double L-shaped aluminum guideway.	105
FIGURE 4.11: Maglev vehicle on double L-shaped aluminum sheet guideway: (a) Front view; (b) Side view.	105
FIGURE 4.12: Pendulum experimental setup to determine a magnetic damping.	106
FIGURE 4.13: Magnetic damping measurement (a) Experimental setup (b) Magnetic damping vs velocity.	107
FIGURE 4.14: Magnetic damping and stiffness calculation setup at ANL (a) Schematic diagram (b) Force transducer and magnet support.	108

FIGURE 4.15: (a) The maglev vehicle used for simulation, where B_v , H_v and L_v are the breadth, height and length of the vehicle. (b) Simulink SimMechanics TM EDW Maglev vehicle.	110
FIGURE 4.16: The block diagram showing EDW steady-state model coupled with the mechanical vehicle model.	110
FIGURE 4.17: The block diagram showing EDW transient model coupled with the mechanical vehicle model.	116
FIGURE 4.18: The lift force plot comparison between the FEA transient model and analytical transient model when integrated with the Simulink SimMechanics TM vehicle model.	117
FIGURE 4.19: The thrust force plot comparison between the FEA transient model and analytical transient model when integrated with the Simulink SimMechanics TM vehicle model.	117
FIGURE 4.20: The airgap plot comparison between the FEA transient model and analytical transient model when integrated with the Simulink SimMechanics TM vehicle model.	117
FIGURE 4.21: The weight as a step input. The step change of 50N weight is applied at $t = 5$ s.	119
FIGURE 4.22: Airgap comparison between the steady-state and transient dynamic model for a step change in weight of the vehicle.	119
FIGURE 4.23: Aerodynamic drag force comparison between the steady-state and transient dynamic model for a step change in weight of the vehicle.	119
FIGURE 4.24: Lift force comparison between the steady-state and transient dynamic model for a step change in weight of the vehicle.	120
FIGURE 4.25: Thrust force comparison between the steady-state and transient dynamic model for a step change in weight of the vehicle.	120
FIGURE 4.26: Heave velocity comparison between the steady-state and transient dynamic model for a step change in weight of the vehicle.	120
FIGURE 4.27: Translational velocity comparison between the steady-state and transient dynamic model for a step change in weight of the vehicle.	121

FIGURE 4.28: The percentage error of lift force between the steady-state and transient dynamic model for a step change in weight of the vehicle.	121
FIGURE 4.29: Step change in the angular speed from 400rads^{-1} to 600rads^{-1} at $t = 1\text{s}$	122
FIGURE 4.30: Air-gap comparison between the steady-state and transient dynamic model for a step change in ω_m of the EDWs.	122
FIGURE 4.31: Aerodynamic drag force comparison between the steady-state and transient dynamic model for a step change in ω_m of the EDWs.	123
FIGURE 4.32: Lift force comparison between the steady-state and transient dynamic model for a step change in ω_m of the EDWs.	123
FIGURE 4.33: Air-gap comparison between the steady-state and transient dynamic model for a step change in ω_m of the EDWs.	123
FIGURE 4.34: Translational velocity comparison between the steady-state and transient dynamic model for a step change in ω_m of the EDWs.	124
FIGURE 4.35: Heave velocity comparison between the steady-state and transient dynamic model for a step change in ω_m of the EDWs.	124
FIGURE 4.36: The percentage error of lift force between the steady-state and transient dynamic model for a step change in ω_m of the EDWs.	124
FIGURE 4.37: The thrust, lift and stiffness coefficients as a function of airgap for different rotational velocities at $v_y = 0\text{ms}^{-1}$, ω_m varied.	129
FIGURE 4.38: The thrust, lift and stiffness coefficients as a function of airgap for different translational velocities at $v_y = 0\text{ms}^{-1}$, $\omega_m = 0\text{RPM}$, v_x varied.	130
FIGURE 4.39: The thrust, lift and stiffness coefficients as a function of airgap for different heave velocities at $v_x = 0\text{ms}^{-1}$, $\omega_m = 1000\text{RPM}$, v_y varied.	130
FIGURE 4.40: The thrust, lift and stiffness coefficients as a function of airgap for different heave velocities at $v_x = 0\text{ms}^{-1}$, $\omega_m = 6000\text{RPM}$, v_y varied.	131

FIGURE 4.41: The thrust, lift and stiffness coefficients as a function of airgap for different heave velocities at $v_x = 20\text{ms}^{-1}$, $\omega_m = 0\text{RPM}$, v_y varied.	131
FIGURE 4.42: The thrust, lift and stiffness coefficients as a function of airgap for different heave velocities at $v_x = 100\text{ms}^{-1}$, $\omega_m = 0\text{RPM}$, v_y varied.	132
FIGURE 4.43: The thrust, lift and damping coefficients as a function of translational velocity for different angular velocities at $v_y = 0\text{ms}^{-1}$, $g = 10\text{mm}$, ω_m varied.	132
FIGURE 4.44: The thrust, lift and damping coefficients as a function of translational velocity for different heave velocities at $\omega_m = 0\text{RPM}$, $g = 10\text{mm}$, v_y varied.	133
FIGURE 4.45: The thrust, lift and damping coefficients as a function of heave velocity for different translational velocities at $\omega_m = 0\text{RPM}$, $g = 10\text{mm}$, v_x varied.	133
FIGURE 4.46: The thrust, lift and damping coefficients as a function of heave velocity for different angular velocities at $v_x = 0\text{ms}^{-1}$, $g = 10\text{mm}$, ω_m varied.	134
FIGURE 4.47: The contour plot for (a) Lift stiffness k_{yy} ($\partial F_y^{ss}/\partial g$) and (b) thrust stiffness k_{xy} ($\partial F_x^{ss}/\partial g$) as a function of slip and translational velocity at $g = 10\text{mm}$ and $v_y = 0\text{ms}^{-1}$.	135
FIGURE 4.48: (a) Damping coefficient D_{yy} (b) damping coefficient D_{xx} , (c) damping coefficient D_{xy} and (d) damping coefficient D_{yx} all as a function of slip and translational velocity at $g = 10\text{mm}$ and $v_y = 0\text{ms}^{-1}$.	136
FIGURE 4.49: The thrust, lift and stiffness coefficients as a function of slip for different translational velocities at $v_y = 0\text{ms}^{-1}$, $g = 10\text{mm}$.	137
FIGURE 4.50: The thrust, lift and stiffness coefficients as a function of slip for different heave velocities at $v_x = 0\text{ms}^{-1}$, $g = 10\text{mm}$.	137
FIGURE 4.51: The damping coefficients as a function of translational velocity for different heave velocities at $\omega_m = 0\text{RPM}$, $g = 10\text{mm}$.	138
FIGURE 4.52: The damping coefficients as a function of translational velocity for different rotational velocities at $v_y = 0\text{ms}^{-1}$, $g = 10\text{mm}$.	138

FIGURE 4.53: The damping coefficients as a function of translational velocity for different airgap at $v_y = 0\text{ms}^{-1}$ and $\omega_m = 0\text{RPM}$.	139
FIGURE 4.54: The damping coefficients as a function of slip for different translational velocities at $v_y = 0\text{ms}^{-1}$, $g = 10\text{mm}$.	139
FIGURE 4.55: The damping coefficients as a function of slip for different heave velocities at $v_x = 0\text{ms}^{-1}$, $g = 10\text{mm}$.	140
FIGURE 4.56: The damping coefficients as a function of slip for different heave velocities at $v_x = 100\text{ms}^{-1}$, $g = 10\text{mm}$.	140
FIGURE 5.1: The photograph of the experimental setup of a single EDW pendulum setup.	143
FIGURE 5.2: Picture of experimental four pole-pair EDW using 16 segmented NdFeB magnets.	144
FIGURE 5.3: Halbach rotor magnet assembly showing magnetization direction.	145
FIGURE 5.4: The schematic diagram of the pendulum setup showing guideway and EDW.	147
FIGURE 5.5: Experimental setup showing EDW, BLDC motors and batteries pack.	148
FIGURE 5.6: The schematic drawing for Figure 5.5. Both front-view and top-view are shown.	148
FIGURE 5.7: The diameter error plot of the circular guideway when rotated at the translational speed of 1.631ms^{-1} for 10 seconds of time.	149
FIGURE 5.8: A sample plot of air-gap as a function of time from a free oscillation test.	150
FIGURE 5.9: A comparison between the experimental and estimated air-gap for a free oscillation test of an EDW pendulum setup-Test-I.	152
FIGURE 5.10: A comparison between the experimental and estimated air-gap for a free oscillation test of an EDW pendulum setup-Test-II.	152
FIGURE 5.11: The measured ω_m of EDW for Test-A.	155

FIGURE 5.12: The measured v_y of the EDW for Test-A.	155
FIGURE 5.13: An air-gap profile using 2-D forces, 3-D forces and experimental results for Test-A.	156
FIGURE 5.14: 2-D and 3-D lift force at the operating points of Test-A.	156
FIGURE 5.15: 2-D and 3-D thrust force at the operating points of Test-A.	156
FIGURE 5.16: The measured ω_m of EDW for Test-B.	158
FIGURE 5.17: The measured v_x of the guideway for Test-B.	158
FIGURE 5.18: The measured v_y of the EDW for Test-B.	158
FIGURE 5.19: An air-gap profile using 2-D-forces, 3-D-forces and experimental results for Test-B.	159
FIGURE 5.20: 2-D and 3-D lift forces at the operating points of Test-B.	159
FIGURE 5.21: 2-D and 3-D thrust forces at the operating points of Test-B.	159
FIGURE 5.22: The measured ω_m of EDW for Test-C.	161
FIGURE 5.23: The measured v_y of the EDW for Test-C.	161
FIGURE 5.24: An air-gap profile using 3D forces and experimental results for Test-C.	161
FIGURE 5.25: 2-D and 3-D lift forces at the operating points of Test-C.	161
FIGURE 5.26: 2-D and 3-D thrust forces at the operating points of Test-C.	162
FIGURE 5.27: The measured ω_m of EDW for Test-D.	163
FIGURE 5.28: The measured v_x of the guideway for Test-D.	163
FIGURE 5.29: The measured v_y of the EDW for Test-D.	163
FIGURE 5.30: An air-gap profile using 3-D forces and experimental results for Test-D.	164
FIGURE 5.31: The measured ω_m of EDW for Test-E.	165
FIGURE 5.32: The measured v_x of the guideway for Test-E.	165
FIGURE 5.33: The measured v_y of the EDW for Test-E.	165

FIGURE 5.34: An air-gap profile using 3-D forces and experimental results for Test-E.	166
FIGURE 6.1: Complete setup of a multi-DOF EDW Maglev system.	168
FIGURE 6.2: Maglev vehicle. (a) Photograph of Maglev. (b) Autocad bottom view of Maglev.	169
FIGURE 6.3: Experimental 2 pole-pair Halbach rotor: (a) Magnetization direction. (b) The side view of the Halbach rotor.	169
FIGURE 6.4: (a) Halbach rotor assembly fixture. (b) Scorpion brushless DC motor.	170
FIGURE 6.5: Assembled 16-segment 2 pole-pairs Halbach rotor.	170
FIGURE 6.6: Phoenix ICE HV 120 brushless speed controller.	171
FIGURE 6.7: Silicon Sensing DMU02 IMU sensor.	172
FIGURE 6.8: The bottom view of an EDW Maglev vehicle.	172
FIGURE 6.9: The top view of an EDW Maglev vehicle.	173
FIGURE 6.10: Magnetic flux density, B_y comparison of front left rotor.	174
FIGURE 6.11: Magnetic flux density, B_y comparison of front right rotor.	174
FIGURE 6.12: Magnetic flux density, B_y comparison of rear left rotor.	174
FIGURE 6.13: Magnetic flux density, B_y comparison of rear right rotor.	175
FIGURE 6.14: The SimMechanics TM Maglev vehicle (Convex hull).	177
FIGURE 6.15: The Maglev co-ordinate system and force directions.	178
FIGURE 6.16: The 3-D lift force for one experimental EDW.	178
FIGURE 6.17: The 3-D thrust force for one experimental EDW.	178
FIGURE 6.18: The 3-D lift force contour plot for one experimental EDW at $g = 4mm$.	179
FIGURE 6.19: The 3-D lift force contour plot for one experimental EDW at $g = 5mm$.	179

FIGURE 6.20: The 3-D lift force as a function of z -offset at 4000RPM and $g = 5mm$.	180
FIGURE 6.21: The 3-D thrust force as a function of z -offset at 4000RPM and $g = 5mm$.	180
FIGURE 6.22: The 3-D lateral force as a function of z -offset at 4000RPM and $g = 5mm$.	180
FIGURE 6.23: The 3-D lift force as a function of z -offset at $v_x = 5ms^{-1}$ and $g = 5mm$.	181
FIGURE 6.24: The 3-D thrust force as a function of z -offset at $v_x = 5ms^{-1}$ and $g = 5mm$.	181
FIGURE 6.25: The 3-D lateral force as a function of z -offset at $v_x = 5ms^{-1}$ and $g = 5mm$.	181
FIGURE 6.26: Maglev sketch showing the pitch.	182
FIGURE 6.27: Maglev sketch front view with z -offset = 0mm.	182
FIGURE 6.28: The vehicle air-gap for zero z -offset simulation.	183
FIGURE 6.29: The translational velocity of the front and the rear rotors for zero z -offset simulation.	183
FIGURE 6.30: The pitch angle of the Maglev for zero z -offset simulation.	183
FIGURE 6.31: The yaw angle of the Maglev for zero z -offset simulation.	184
FIGURE 6.32: The roll angle of the Maglev for zero z -offset simulation.	184
FIGURE 6.33: The lift force of the front and rear rotors for zero z -offset simulation.	185
FIGURE 6.34: The thrust force of the front and rear rotors for zero z -offset simulation.	185
FIGURE 6.35: The lateral force of the front and rear rotors for zero z -offset simulation.	185
FIGURE 6.36: The airgap plot of the front and rear rotors for zero z -offset simulation.	186

FIGURE 6.37: The v_y plot of the front and rear rotors for zero z -offset simulation.	186
FIGURE 6.38: The z -offset of the front and rear rotors for zero z -offset simulation.	186
FIGURE 6.39: The Maglev sketch with the tether along the thrust axis.	187
FIGURE 6.40: A 4-wheeled EDW Maglev hanging setup with adjustable hight mechanism.	188
FIGURE 6.41: The bottom view of the experimental Maglev vehicle with lateral stability.	190
FIGURE 6.42: The EDW and guideway lateral configuration for lateral stability.	190
FIGURE 6.43: The lift force of an experimental EDWs at $g = 5\text{mm}$ and $z\text{-offset} = 31.5\text{mm}$.	190
FIGURE 6.44: The thrust force of an experimental EDWs at $g = 5\text{mm}$ and $z\text{-offset} = 31.5\text{mm}$.	191
FIGURE 6.45: The lateral force as a function of z -offset at 4000RPM and $g = 5\text{mm}$.	191
FIGURE 6.46: The rear left EDW air-gap measurement from initial $g = 4\text{mm}$.	192
FIGURE 6.47: The rear right EDW air-gap measurement from initial $g = 4\text{mm}$.	192
FIGURE 6.48: The front left EDW air-gap measurement from initial $g = 4\text{mm}$.	192
FIGURE 6.49: The front right EDW air-gap measurement from initial $g = 4\text{mm}$.	193
FIGURE B.1: An air-gap profile using 2-D and 3-D forces and experimental results for Test-C.	217
FIGURE B.2: An air-gap profile usign 2-D and 3-D forces and experimental results for Test-D.	217
FIGURE B.3: 2-D and 3-D lift forces at the operating points of Test-D.	218

FIGURE B.4: 2-D and 3-D thrust forces at the operating points of Test-D.	218
FIGURE B.5: An air-gap profile using 2-D and 3-D forces and experimental results for Test-E.	218
FIGURE B.6: 2-D and 3-D lift forces at the operating points of Test-E.	219
FIGURE B.7: 2-D and 3-D thrust forces at the operating points of Test-E.	219
FIGURE B.8: The measured ω_m of the EDW for Test-F.	219
FIGURE B.9: The measured v_y of the EDW for Test-F.	220
FIGURE B.10: An air-gap profile using 2-D-forces, 3-D forces and experimental results for Test-F.	220
FIGURE B.11: 2-D and 3-D lift forces at the operating points of Test-F.	220
FIGURE B.12: 2-D and 3-D thrust forces at the operating points of Test-F.	221
FIGURE B.13: The measured ω_m of the EDW for Test-G.	221
FIGURE B.14: The measured v_y of the EDW for Test-G.	221
FIGURE B.15: An air-gap profile using 2-D forces, 3-D forces and experimental results for Test-G.	222
FIGURE B.16: 2-D and 3-D lift forces at the operating points of Test-G.	222
FIGURE B.17: 2-D and 3-D thrust forces at the operating points of Test-G.	222
FIGURE B.18: The measured ω_m of the EDW for Test-H.	223
FIGURE B.19: The measured v_y of the EDW for Test-H.	223
FIGURE B.20: The measured v_x of the guideway for Test-H.	223
FIGURE B.21: An air-gap profile using 2-D forces, 3-D forces and experimental results for Test-H.	224
FIGURE B.22: 2-D and 3-D lift forces at the operating points of Test-H.	224
FIGURE B.23: 2-D and 3-D thrust forces at the operating points of Test-H.	224
FIGURE B.24: The measured ω_m of the EDW for Test-I.	225
FIGURE B.25: The measured v_y of the EDW for Test-I.	225

FIGURE B.26: The measured v_x of the guideway for Test-I.	225
FIGURE B.27: An air-gap profile using 2-D forces, 3-D forces and experimental results for Test-I.	226
FIGURE B.28: 2-D and 3-D lift forces at the operating points of Test-I.	226
FIGURE B.29: 2-D and 3-D thrust forces at the operating points of Test-I.	226
FIGURE B.30: The measured ω_m of the EDW for Test-J.	227
FIGURE B.31: The measured v_y of the EDW for Test-J.	227
FIGURE B.32: The measured v_x of the guideway for Test-J.	227
FIGURE B.33: An air-gap profile using 2-D forces, 3-D forces and experimental results for Test-J.	228
FIGURE B.34: 2-D and 3-D lift forces at the operating points of Test-J.	228
FIGURE B.35: 2-D and 3-D thrust forces at the operating points of Test-J.	228
FIGURE B.36: The measured ω_m of the EDW for Test-K.	229
FIGURE B.37: The measured v_y of the EDW for Test-K.	229
FIGURE B.38: The measured v_x of the guideway for Test-K.	229
FIGURE B.39: An air-gap profile using 2-D forces, 3-D forces and experimental results for Test-K.	230
FIGURE B.40: 2-D and 3-D lift forces at the operating points of Test-K.	230
FIGURE B.41: 2-D and 3-D thrust forces at the operating points of Test-K.	230
FIGURE C.1: Simulink block diagram of the Maglev vehicle with experimental setup parameters.	231
FIGURE C.2: Simulink diagram of the Maglev Vehicle Subsystem.	232
FIGURE C.3: Simulink block diagram of the batteries, controllers, laser sensor holders and sensors subsystems.	232
FIGURE C.4: Simulink block diagram of the bottom front right section subsystem.	233

FIGURE C.5: Simulink block diagram of the bottom front left section subsystem.	233
FIGURE C.6: Simulink block diagram of the bottom rear right section subsystem.	233
FIGURE C.7: Simulink block diagram of the bottom rear left section subsystem.	233
FIGURE C.8: Simulink block diagram of the front right force calculation subsystem.	233
FIGURE C.9: Simulink block diagram of the 3-D forces calculation lookup table subsystem.	234

LIST OF ABBREVIATIONS

ANL	Argonne National Laboratory
BLDC	Brushless Direct Current Motor
DLIM	Double Sided Linear Induction Motor
DOF	Degree of Freedom
EDS	Electrodynamic Suspension
EDW	Electrodynamic Wheel
EMS	Electromagnetic Suspension
ER	Electromagnetic River
ESC	Electronic Speed Controller
FEA	Finite Element Analysis
LIM	Linear Induction Motor
LRM	Linear Reluctance Motor
LSM	Linear Synchronous Motor
Maglev	Magnetic Levitation
MRI	Magnetic resonance imaging
NASA	National Aeronautics and Space Administration
NdFeB	Neodymium, Iron, and Boron
NDT	Non-destructive Testing
NI	National Instruments
PM	Permanent Magnet
RTW	Real Time Windows
SCM	Superconducting Magnets
SLIM	Single Sided Linear Induction Motor

LIST OF SYMBOLS

σ	Conductivity (Sm^{-1})
\mathbf{E}	Electric field intensity vector (Vm^{-1})
\mathbf{B}	Magnetic flux density vector (T)
\mathbf{H}	Magnetic field intensity vector (Am^{-1})
\mathbf{v}	Velocity vector (ms^{-1})
\mathbf{J}	Current density vector (Am^{-2})
ϕ	Magnetic scalar potential (A)
\mathbf{B}^r	Reflected magnetic flux density vector (T)
μ_o	Permeability of the free space (Hm^{-1})
\mathbf{B}^s	Source magnetic flux density vector (T)
ϕ_n	Magnetic scalar potential in region n (A)
Ω_i	Problem region i
\mathbf{A}	Magnetic vector potential vector (Wbm^{-1})
A_z	Magnetic vector potential in z -direction (Wbm^{-1})
v_y	Velocity in y -direction (ms^{-1})
v_x	Velocity in x -direction (ms^{-1})
ω_e	Electrical angular velocity (rads^{-1})
ω_m	Mechanical angular velocity (rads^{-1})
A_z^{ss}	Steady state z -component vector potential (Wbm^{-1})
E_z^{ss}	Steady state z -component electric field intensity (Vm^{-1})
\hat{x}	Unit vector in x -direction
\hat{y}	Unit vector in y -direction
\hat{z}	Unit vector in z -direction
\mathbf{n}_c	Normal vector to the conducting surface
ξ	Fourier frequency of the space variable x

j	Complex number
b	Thickness of the guideway (m)
g	Air-gap (m)
T^{ss}	Steady state transmission function
t	Time (s)
F_x	Thrust force (N)
F_y	Lift force (N)
$(.)^{ss}$	Steady state of $(.)$
$(.)^*$	Complex conjugate of $(.)$
w	Width of rotor (m)
$\text{Re}(\cdot)$	Real part of (\cdot)
$\text{Im}(\cdot)$	Imaginary part of (\cdot)
P_{Loss}	Power loss in the guideway (W)
P	Number of pole-pairs
η_{Thrust}	Thrust efficiency (%)
τ	Torque (N-m)
s_l	Slip (ms^{-1})
r_o	Outer radius of rotor (m)
B_r	Radial flux density (T)
B_θ	Azimuthal flux density (T)
B_r^m	Remanence of the magnet (T)
μ_r	Relative permeability of the magnet
r_i	Rotor inner radius (m)
y_o	y -axis rotor offset (m)
$u(\cdot)$	Unit step function
F_g	Gravitational force (N)
m	Mass (Kg)

F_d	Aerodynamic drag force (N)
ρ	Density of air (Kg m^{-3})
C_d	Aerodynamic drag coefficient (Kgs^{-1})
A	Frontal Area of the vehicle (m^2)
$\delta(t)$	Unit impulse function
k	Stiffness coefficient (Nm^{-1})
D	Damping coefficient (Ns^2m^{-1})
μ	Sliding friction coefficient (Ns^2m^{-1})
c	Viscous damping coefficient (Ns^2m^{-1})

CHAPTER 1: INTRODUCTION AND LITERATURE REVIEW

1.1 Introduction

As the world's population grows, the demand for fast and reliable public transportation has also been steadily increasing. It is most likely that conventional forms of transportation such as automobiles and air services will not be able to fulfill the demands placed on them by the increased population densities.

The innovative form of transportation using magnetic levitation (Maglev) that utilizes magnetic fields in order to create suspension, propulsion and guidance forces has been proposed as a viable alternative to existing transportation, more specifically to the conventional wheel-on-rail trains. Maglev technology offers several benefits such as reliability, safety, convenience, and compactness to name a few that are now becoming the basic requirements for the 21st century's modern transportation systems. Maglev's non-contact nature of lift, thrust and guidance force production enables this technology to operate at speeds higher than 500km/h with low guideway maintenance cost, relatively low energy consumption and low vibrations, therefore producing low noise and pollution to the environment [1]. Since Maglev does not operate on wheels, the technology is immune to slippage and is less susceptible to adverse weather conditions. In addition, Maglev vehicles can operate on steep gradients and small curve radii [2].

Maglev vehicle technology has been studied for several decades [3–14] and numerous experimental as well as theoretical investigations, have been undertaken [2, 7, 9, 15–32]. Maglev technology is not just limited to theory and laboratory scale setups, full scale Maglev vehicles have been successfully implemented in countries such as China [33], Japan [34, 35] and South Korea [12]. The interest in this technology is increasing

within the USA and several companies are trying to build commercially viable Maglev operations [36, 37]. The full scale demonstration systems have shown that Maglev is safe, reliable and affordable to the public. Unfortunately, the current Maglev technology has not been commercially successful and this is likely due to the expense involved with building the infrastructure for this technology.

Different methods for the electromagnetic suspension or levitation, propulsion and guidance are proposed by various authors utilizing electromagnets [38], permanent magnets [39–41] and superconducting magnets [34, 42, 43]. Each of these concepts has its own advantages and disadvantages; each will briefly be discussed in the following sections.

1.2 Types of Suspension Technologies

Maglev systems can be broadly classified into two types. An attractive type called electromagnetic suspension (EMS) and a repulsive type called electrodynamic suspension (EDS). Each of these types of Maglev will be briefly discussed.

1.2.1 Electromagnetic Suspension

Electromagnetic suspension (EMS) is achieved by utilizing the force of attraction between the electromagnets on a vehicle and a ferromagnetic rail placed on the underside of an elevated guideway as shown in Figure 1.1 and Figure 1.2. Maglev using EMS generally operates with a small air-gap at around 10mm. The separated type suspension and guidance EMS used by the German Transrapid is shown in Figure 1.1. Although the ferromagnetic body cannot be suspended in stable equilibrium in a static magnetic field [44], stability of EMS can be achieved by actively controlling the current in the electromagnets to maintain a nominally constant gap between the magnets and ferromagnetic guideway [45].

An integrated suspension and guidance type EMS, as shown in Figure 1.2 has been used by the Japanese HSST [2] and South Korean UTM [2]. The guidance force is created via the lateral reluctance force of attraction between the electromagnets and

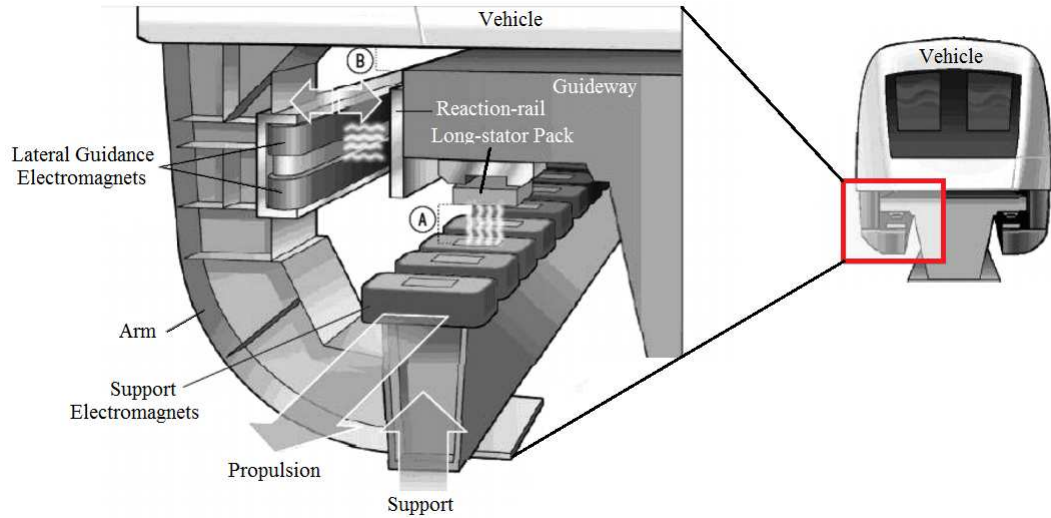


Figure 1.1: *Transrapid EMS with levitation and guidance electromagnets separated* [2].

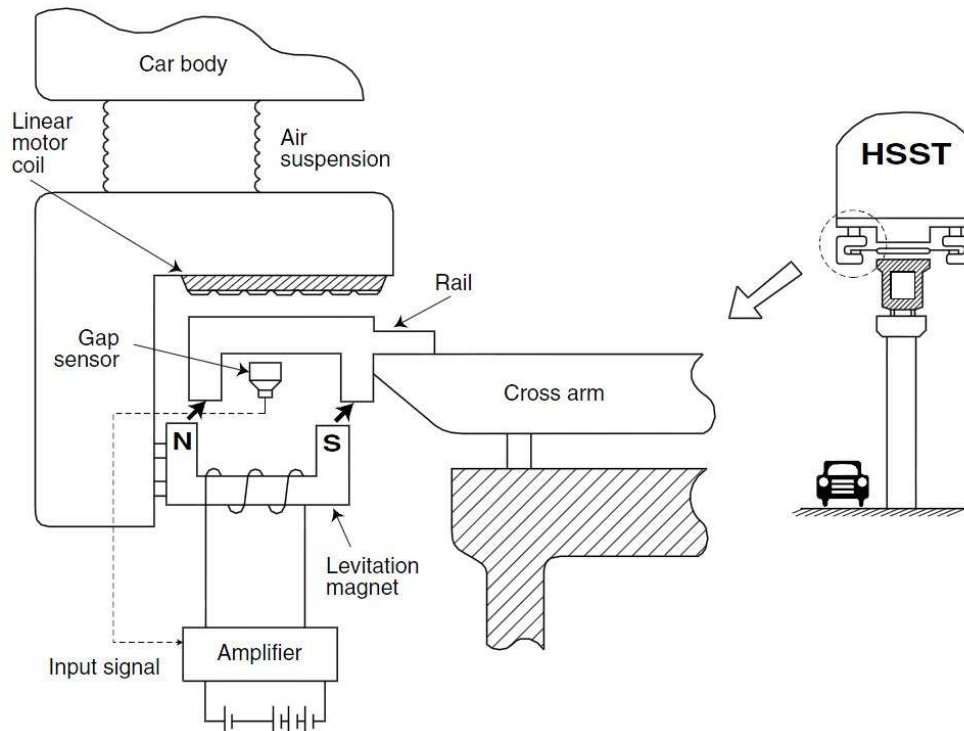
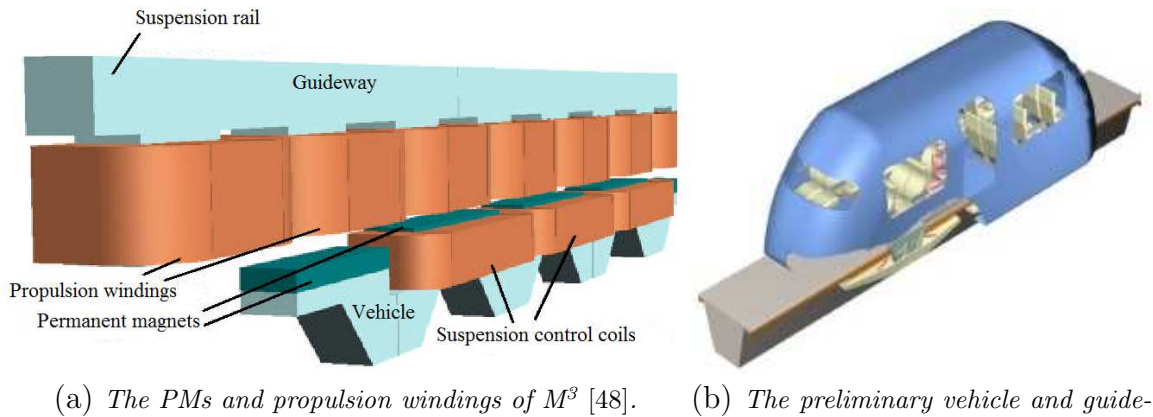


Figure 1.2: *Japanese HSST with levitation and guidance electromagnets integrated* [46].

the iron-rail. The interaction between the guidance and suspension for the integrated suspension and guidance type EMS increase at high speed, making the active control of the air-gap more challenging [2, 47]. Therefore, the system is better suited for low speed whereas the separated guidance and suspension system is preferred for high speed operation [2].

MagneMotion's M^3 vehicle as illustrated in Figure 1.3, has an array of permanent magnets (PMs) in addition to electromagnets. The PMs provide suspension and guidance forces as well as provide the field for the linear synchronous motor for propulsion [37, 48]. The M^3 Maglev use the PM in conjunction with control coils to achieve a magnetic air-gap of 20mm [37]. The use of superconductors for EMS has



(a) *The PMs and propulsion windings of M^3 [48].* (b) *The preliminary vehicle and guideway design of M^3 Maglev [37].*

Figure 1.3: *MagneMotion M^3 Maglev system.*

also been proposed by various authors [43, 49, 50]. The magnetic fields produced by high temperature superconductors will be strong compared with electromagnets but will require a separate cooling system, therefore, this is likely to be very expensive.

1.2.2 Electrodynamic Suspension

When magnets located on a vehicle are translationally moved above a conductive sheet guideway or coils, currents are induced in the coils or guideway that creates an opposing magnetic field. This induced magnetic field interacts with the field produced by the magnet to create a repulsive force and lifts the vehicle. Thus EDS is achieved by the repulsive force between the source field and this induced field. The demerit of EDS is that the induced current in the guideway results in a magnetic drag force and power loss. The magnetic drag force increases with the increase in speed until it reaches a peak value and then slowly decreases as the speed further increases. This is illustrated in Figure 1.4. Although the drag force decreases at high speed,

aerodynamic drag is increasing at the square of the velocity. The propulsion system should therefore be capable of overcoming this magnetic drag plus aerodynamic drag. Since, the EDS system can produce enough lift (to overcome the weight) only at sufficient speed, a system should be propelled on rubber-wheels like an airplane or secondary suspension is required during the starting.

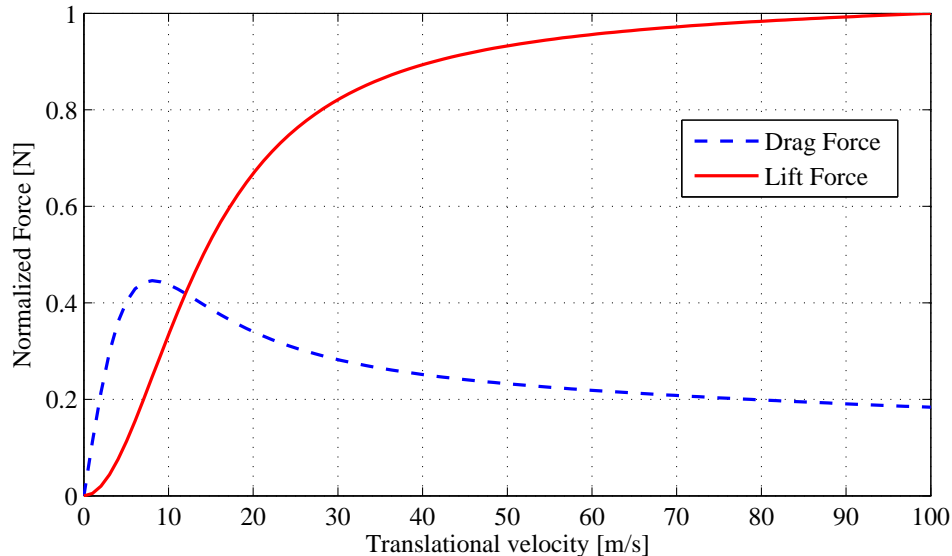


Figure 1.4: *Normalized force of EDS Maglev for different translational velocity.*

EDS using the superconducting coils mounted on the vehicle interacting with the conducting guideway was first proposed by Powell and Danby in 1966 [38, 51, 52]. Intensive analytical and experimental research, particularly in the 1970's, was undertaken to investigate the force produced by moving magnetic sources above a conductive guideway [53–57]. The finite conductive sheet edge-effect and channel-effects were also studied [58]. Most of these studies were carried out for high-speed Maglev applications.

Using a judicious guideway design EDS can be considered to be an inherently stable system at steady-state condition (according to Earnshaw's theorem) [44]. The EDS system have inherently low suspension and guidance damping coefficients and it decreases further at high speed. In fact, this damping can become negative [56, 59, 60].

Since the passive damping is inadequate, active control is always required for the operation on any un-steady state conditions to maintain the ride quality and passenger safety [61, 62]. Various damping techniques can be applied to maintain the stability of the vehicle. For example, passive or active electrodynamic primary suspension damping, passive or active mechanical secondary damping [63].

EDS using superconducting coils, as shown in Figure 1.5, has been developed by Central Japan Railways. The MLX01 high-speed system, operates at a suspension height of about 11cm above the guideway using a vertical null-flux structure that provides both lift and guidance force for the vehicle [64]. This MLX01 system is the world fastest Maglev system with a record-high speed of 581km/h [35].

Rare earth PMs have also been used for EDS. For example, General Atomic's Inductrack as shown in Figure 1.6 use a dual-Halbach array of PMs for suspension and linear synchronous motor for the propulsion [18, 36].

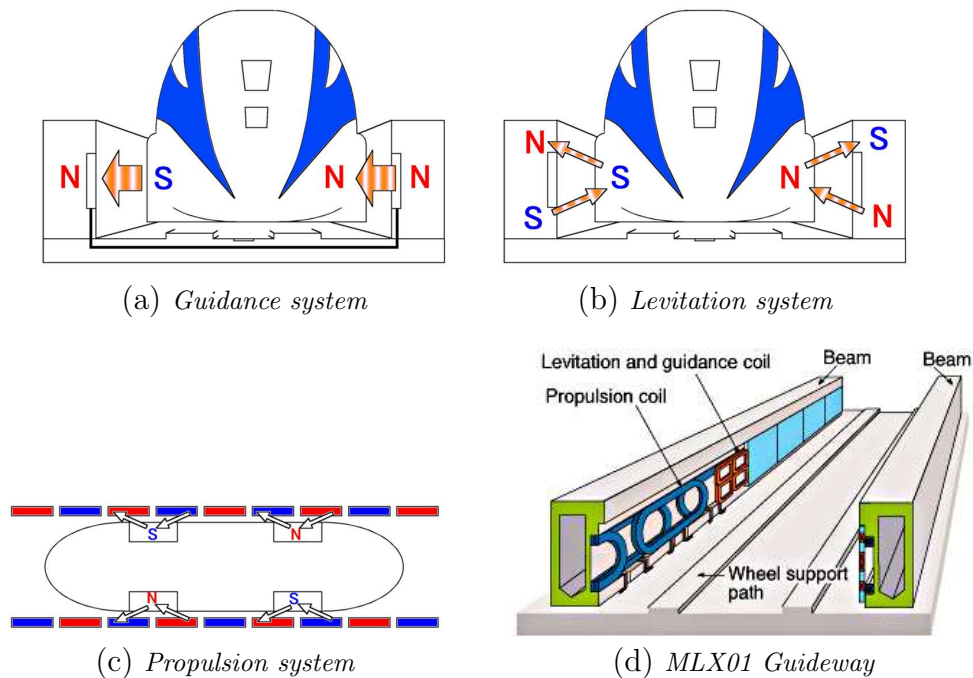
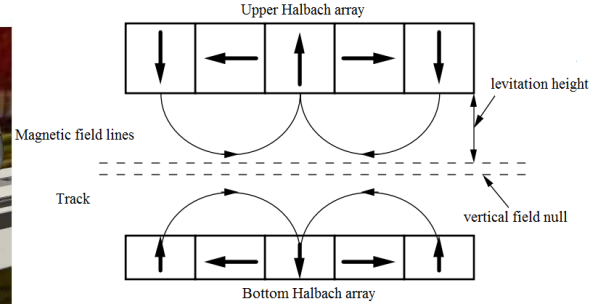


Figure 1.5: The Japanese MLX01 Maglev using null-flux structure [65].



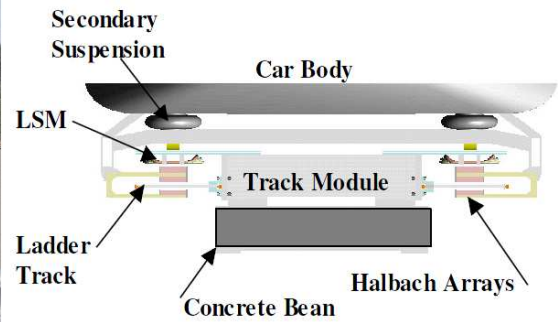
(a) *Urban Maglev Vehicle and Guideway* [17].



(b) *Dual-Halbach Array Configuration*.



(c) *Inductrack Test Vehicle* [17].



(d) *Vehicle-to-Guideway Arrangement* [17].

Figure 1.6: *The Inductrack Maglev model using dual-Halbach array and linear synchronous motor.*

1.3 Types of Propulsion Technologies

The techniques that have been proposed for the propulsion of a Maglev vehicle are the linear induction motor (LIM) [3, 66–69], the linear synchronous motor (LSM) [70–72], the linear reluctance motor [73–77], the DC linear motor [24, 78–81] and the segmented rail phase induction motor [82–84]. Only the most common techniques such as LIM and LSM will be discussed in detail in the following sub-sections.

1.3.1 Linear Induction Motor

The LIM is similar to the conventional rotary induction motor except that the stator (primary) and rotor (secondary) are cut open and flattened such that it produces a linear force instead of torque. Unlike a rotary induction motor, the LIM has an open air-gap and a finite length which causes “end-effects” [66, 67]. The basic opera-

tion principle of the LIM is similar to its rotary counterpart. Time-varying magnetic fields are produced in the air-gap by the primary side which induces eddy-currents in the secondary. The induced eddy-currents interact with the air-gap flux to produce the thrust force by Lorentz's law. LIMs are broadly divided into two different types: single sided (SLIM) and double sided (DLIM) as shown in Figure 1.7 and Figure 1.8. The primary of the SLIM is typically placed horizontally flat on to the guideway. The SLIMs can be further divided into two classifications depending on the length of the primary compared to the secondary as the long-stator and the short-stator LIMs as shown in Figure 1.7. The primary is composed of a conductive plate such as aluminum placed on top of back iron. This conductive plate provides a low resistance path for the induced currents and the back iron improves the magnetic circuit path.

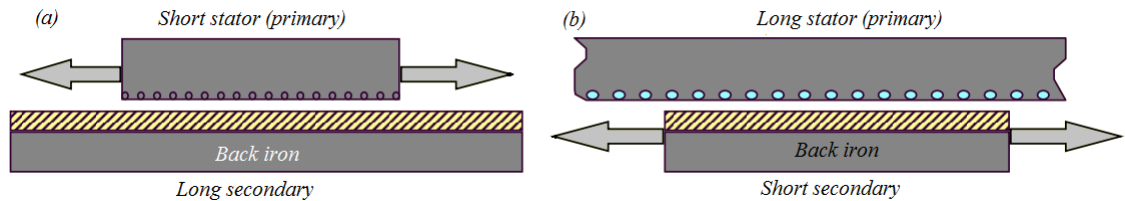


Figure 1.7: Single sided linear induction motor (a) short-stator SLIM (b) long-stator SLIM.

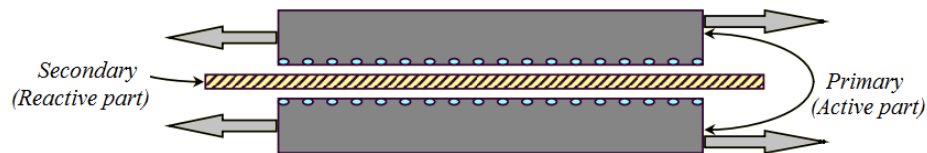


Figure 1.8: Double sided linear induction motor.

DLIM usually has a vertically positioned conducting secondary on the guideway and the short dual primary attached to the vehicle on either side [69]. In the SLIM, the inherently large attractive force between the primary and the secondary back-iron is significantly reduced and sometimes becomes repulsive at high-speed due to the induced current in the secondary [41]. Although LIMs are considered the best low cost solution for the production of direct linear motion, they suffer from a low power factor, when operating at large airgap, heavy weight and the necessity of a very long primary

to overcome the end-effects problems at high-speed [70, 85]. These problems are more pronounced in high-powered and high-speed applications [68]. However, the use of LIMs for propulsion has the structural advantage as it is simple and strong. Therefore, LIMs are only being used for low and medium-speed transportation applications.

The concept of using LIMs for the propulsion was proposed a century ago [69, 86]. However the concept was not developed for several decades. The first big transportation research project using LIMs was perhaps the Westinghouse ‘Electropult’ aircraft launcher developed in 1946 [87]. However this project was not continued because of the associated initial capital cost [88]. The interest in the application of DLIMs for high-speed transportation gained momentum during the sixties and seventies [3, 86]. This is because the DLIMs has a better thrust performance than the SLIMs for the same weight and because of its sandwich structure the attractive force between the primary and secondary is cancelled in DLIMs. However, the guideway structure for DLIM is complicated compared to SLIM. Recently there has been a renewed interest in using LIMs for aircraft launch applications in the USA [89–91]. A summary of recent and proposed projects using different types of propulsion system is presented in Table 1.1.

Table 1.1: *Current status of Maglev projects around the world* [85].

System	Location	Country	Motor type	Suspension type	Operation / test velocity	Status
Transrapid	Emsland	Germany	Long-stator LSM	EMS	400 / 451 km/h	Test facility
Transrapid	Shanghai	China	Long-stator LSM	EMS	430 / 501 km/h	In operation
MLU	Yamanashi	Japan	Air-core long-stator LSM	EDS	n/a / 581 km/h	Test facility
HSST	Nagoya	Japan	Short-stator LIM	EMS	n/a / 80 km/h	Test facility
Linimo	Nagoya	Japan	Short-stator LIM	EMS	100 km/h / n/a	In operation
Korean Maglev	Daejeon	South Korea	Short-stator LIM	EMS	n/a / 110 km/h	Test facility
	Changsha	China	Short-stator LIM	EMS	n/a / 150 km/h	Test facility
	Tangshan	China	Short-stator LIM	EMS	Planned up to 150 km/h	Test facility under construction
Magplane	Dalian	China	Wheels and PM	EDS with PM	Planned up to 320 km/h	Test facility under construction
	Shanghai	China	Long-stator LSM	EDS	Planned up to 550 km/h	Abandoned
				EMS with PM, control coils		
MagneMotion M3	Massachusetts	USA	Long-stator LSM	EDS with PM	n/a / 160 km/h	Test facility
General Atomics	Pennsylvania	USA	Long-stator LSM	EDS with PM	n/a / 160 km/h	Test facility
American Maglev	Virginia, Georgia	USA	Short-stator LIM	EMS	n/a / 60-70 km/h	Test facility
Maglev 2000	Florida	USA	Long-stator LIM	EDS	Planned up to 500 km/h	In research
Swissmetro		Switzerland	Short-stator LIM or long-stator LSM	EMS	Planned up to 500 km/h	Abandoned

1.3.2 Linear Synchronous Motor

The linear synchronous motor (LSM) is a type of linear motor in which the mechanical speed is in synchronism with the magnetic field motion. This is analogous to its rotary counterpart. The propulsive force is produced by the interaction of a travelling electromagnetic field on the guideway with an array of permanent magnets, electromagnets or a variable reluctance rail on the vehicle [71]. The guideway's travelling field is created by either a sinusoidally distributed current carrying poly-phase windings or by an electronically switched direct current circuit [71]. For high-speed Maglev applications, sinusoidally distributed 3-phase windings packed in the guideway are typically used. The speed is continuously adjusted by controlling the frequency of the guideway alternating current through the poly-phase windings. Electromagnetic braking can be achieved by reversing the direction of current in the windings. The motor actually acts as a generator during this reverse operation and the energy generated can be re-used and fed back to the grid [1].

The German Transrapid system uses a LSM with steel core excitation electromagnets embedded in the vehicle and the poly-phase stationary windings on the guideway, as illustrated in Figure 1.9. Whereas the Japanese MLX001 Maglev test system uses air-core superconducting electromagnets mounted on the vehicle and three-phase stationary windings on the guideway [71].

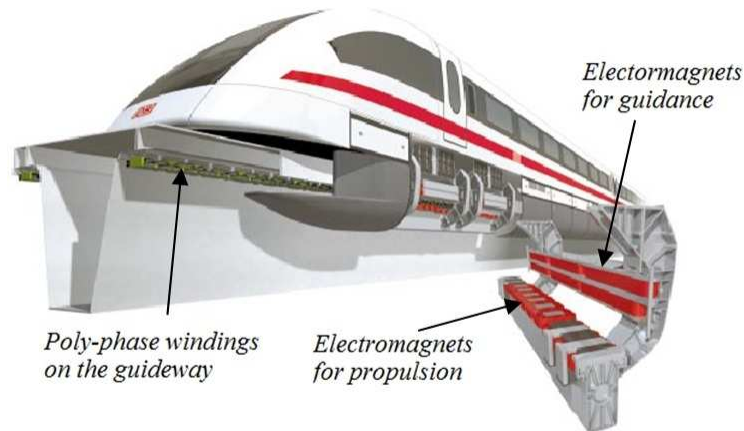


Figure 1.9: *The LSM propulsion used for German Transrapid [72].*

Various excitation systems can be used in LSMs such as PMs in the reaction rail, PMs in the armature (passive reaction rail), electromagnetic excitation system (with winding), superconducting excitation system and passive reaction rail with saliency (variable reluctance motor) [71].

The LSM can be divided into two types, the long-stator and short-stator [85, 92]. For high-speed applications, long-stator LSM is preferred because it has a higher efficiency as well as higher power factor compared with the LIM [2]. Laminated iron is used within the guideway stator windings in order to reduce eddy-current loss. Most current and proposed high-speed Maglev projects are using LSM for the generation of thrust force as illustrated in Table 1.1.

1.4 Integrated Propulsion and Suspension Techniques

Integrated propulsion and suspension techniques use the same passive guideway to achieve two forces; thrust and lift simultaneously. Since the same guideway is used for thrust and lift, construction cost could be significantly reduced using this technique. However, the design of the motor that can generate the desired suspension and propulsion forces simultaneously is challenging and complicated. Various methods have been proposed to obtain the simultaneous lift and thrust using a passive guideway [38, 93, 94].

1.4.1 LIM Using Magnetic Attraction

Rohr Inc. demonstrated an integrated method in which a LIM was used for propulsion and the normal attraction between the LIM primary and secondary was used for suspension. The 3.4 ton ROMAG vehicle system was demonstrated in 1972 [93]. This test vehicle used two linear induction motors, one on each side of the vehicle such that both traction and dynamic active suspension was provided. The disadvantage with this approach is that the system can only operate at low-speeds since the attractive force is dramatically reduced at high-speeds and can become repulsive. Hence, this method is not efficient and safe for high-speed applications.

This method has more recently been considered for steel plate transportation using a transverse flux LIM [93].

1.4.2 Linear Reluctance Motor

Ross proposed that a linear reluctance motor (LRM) could be used to provide both a lift force and propulsion force. The lift force would be provided by attraction of the iron and the propulsion by the reluctance forces created between the salient guideway poles [93]. Unfortunately, this approach suffers from a low power factor since only AC excitation is used [93].

1.4.3 Iron Cored LSM

An iron cored linear synchronous motor was proposed by Levi in 1973 using both a DC and AC excitation system on the same LRM primary [95]. This combined approach could overcome the low power factor problem associated with LRM [95, 96]. Different guideway configurations such as homopolar [97], heteropolar [98] and zig-zag [99] have been proposed for iron cored LSM in which the lift force and magnetization fields are produced by DC excitation whereas the thrust is produced by the synchronous interaction of the AC windings with the salient pole guideway [98–100]. The concept was demonstrated experimentally by Boldea using a 4-ton, 4-m long research vehicle, Magnibus-01 using a transverse-flux iron cored LSM [7, 8].

The homopolar LSM has been considered for high-speed Maglev use in Switzerland (called Swissmetro) [101]. The concept involved using partially evacuated tunnels in order to reduce the aerodynamic drag. Unfortunately, the Swissmetro went into liquidation in November 2009 due to the lack of federal funding [102].

1.4.4 Electromagnetic River

Electromagnetic River (ER) concept was proposed by Eastham and Laithwaite [103, 104]. As mention in section 1.3.1, when the LIM secondary is used without the back-iron a significant amount of repulsive force between the primary and secondary is produced, particularly at high-speed. In addition, a large propulsion force can be

produced if the slip is controlled [103]. Therefore, ER can be used for integrated suspension and propulsion applications. However, the ER concept has several disadvantages such as having an extremely low power factor, a low lift-to-weight ratio and it suffer from edge-effect problems therefore a very long primary is required for efficient operation [105, 106]. Although various methods have been proposed to improve the performance like using superconducting windings for greater lift-to-weight ratio or cooling the windings, the ER concept has never progressed past the small scale experimental setup tested by Eastham [104].

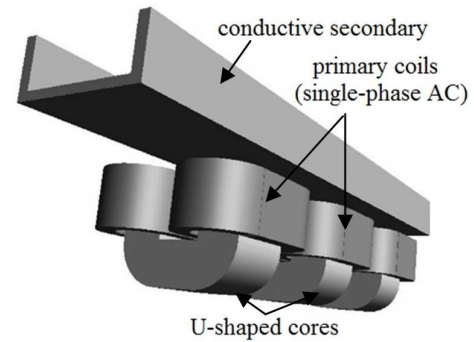
Recently the National Aeronautics and Space Administration (NASA) placed a contract with PRT Advanced Maglev Systems in association with the University of Sussex to develop a prototype electromagnetic accelerator based on the ER concept [107]. In [107] the authors claim that the ER concept is not suitable for the high-speed accelerator because both the levitation and propulsion forces are highly coupled and a function of the vehicle speed and the primary supply frequency. Therefore, a sophisticated control law is required to precisely control the frequency. The demonstration accelerator guideway with a model vehicle mounted is shown in Figure 1.10-(a). For this project, the ER has been modified with separate induction levitation and propulsion sub-systems. The induction levitation sub-system as shown in Figure 1.10-(b) provides the levitation independent of velocity with no propulsion effect. Whilst a DLIM provides the propulsion with no levitation effects.

1.4.5 Electrodynamic Wheels

The mechanical rotation of a magnetic source such as a radially magnetized magnetic rotor above a passive conductive guideway, such as aluminum, will induce eddy-currents in the guideway. This will result in an opposing magnetic field being created that interacts with the source magnetic field to produce lift and thrust forces simultaneously. Since the airgap flux is associated with the magnetic source field, this concept does not suffer from a low power factor issue like with the ER concept. How-



(a) Demonstration of electromagnetic launch assistance track of NASA [108].

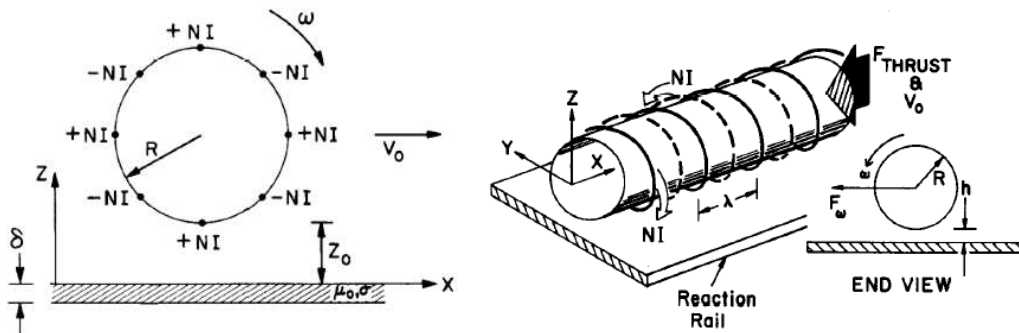


(b) The induction levitation of electromagnetic launch system [107].

Figure 1.10: The electromagnetic launch assistance system located at the NASA Marshall Space Flight Center.

ever, the system will have additional losses associated with the mechanical rotation of the magnetic source.

The inherent eddy-current drag in EMS and EDS can be converted to a thrust by rotating the magnetic source over the passive guideway [39, 41, 109]. Several methods have been proposed to rotate the magnetic source over the passive guideway [41, 110, 111]. For example, the concept of rotating magnetic rotor over a passive guideway for transportation was first investigated by Davis and Borcherts in 1973 using superconducting magnets with radial and helical configurations [110, 112] as shown in Figure 1.11.



(a) Radial rotor configuration [112].

(b) Helical rotor configuration [112].

Figure 1.11: Radial and helical superconducting rotor configurations.

After the discovery of rare-earth magnets, researchers have considered rotating

PM wheels over the conductive guideway instead of superconducting magnets. Fujii rotated an axial rotor using NdFeB magnets over a passive guideway to generate the integrated thrust and suspension [39, 40, 111]. Fujii investigated two different types of wheels; a tilted wheel rotating above an inclined guideway and an overlap type wheel rotating near the edge of a flat guideway. These topologies are shown in Figure 1.12. More recently a radially magnetized Halbach rotor rotating above a

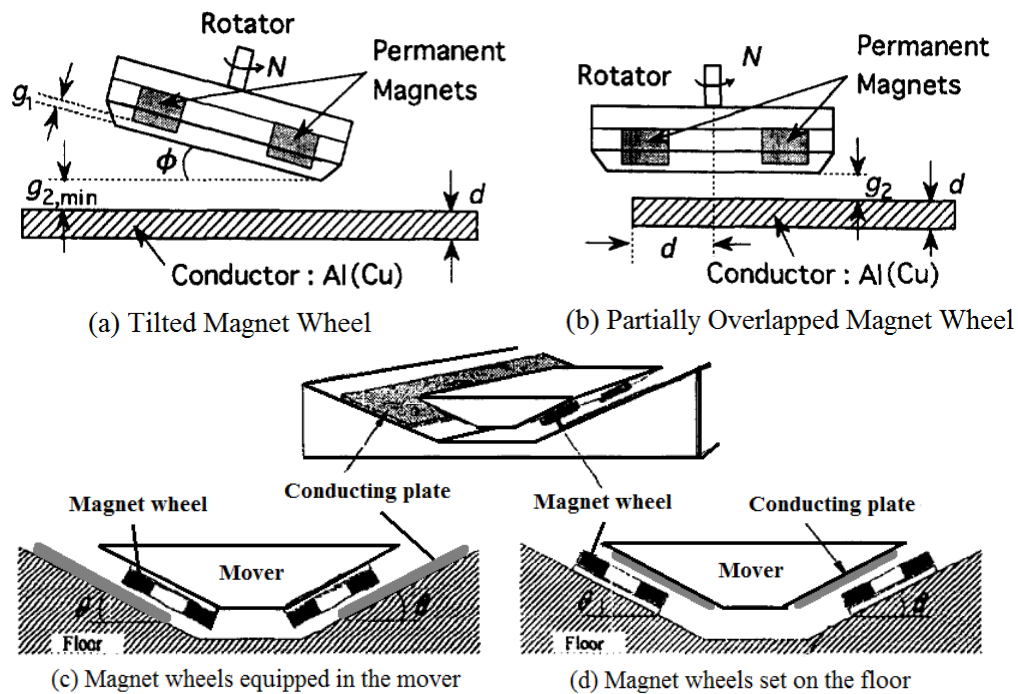


Figure 1.12: Magnet wheels rotating above a conductor [40, 113].

passive aluminum guideway was investigated and proposed as a low-cost alternative for high-speed ground transportation by Bird [41, 109, 114, 115]. The author called this device an Electrodynamic Wheel (EDW). The concept of an EDW for high-speed transportation is illustrated in Figure 1.13. The production of the thrust or braking depends on the relative slip speed, s_l , between circumferential speed, v_c , and the translational speed, v_x . The slip speed is defined as

$$s_l = v_c - v_x \quad (1.1)$$

If the rotor is rotated at a circumferential speed greater than the translational speed i.e. at positive slip values, a thrust force can be generated and vice-versa.

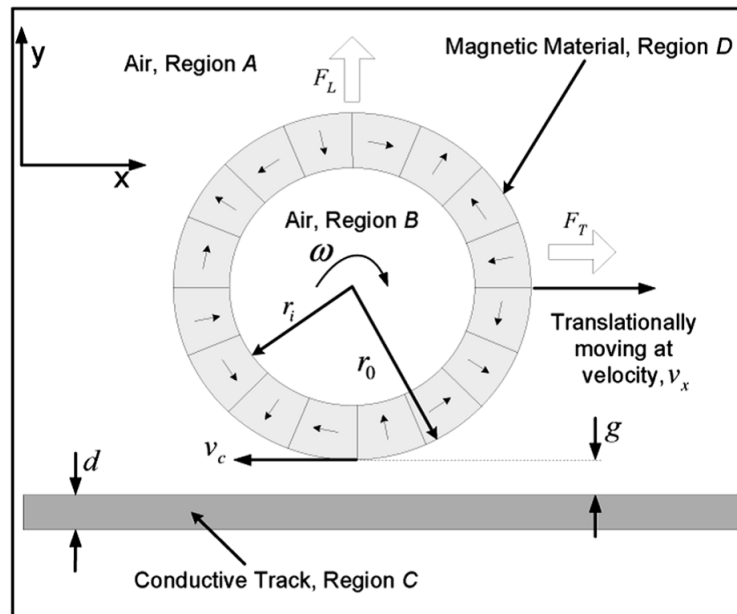


Figure 1.13: *The translationally moving and rotating EDW above a passive guideway* [41].

1.5 Research Goals

The goal of this research is to (1) derive 2-D analytic based steady-state and transient force equations for the case when a magnetic source such as Halbach rotor (or multiple Halbach rotors in series) is rotating and/or moving above a conductive passive aluminum guideway (2) investigate both numerically and experimentally the dynamics of a sub-scale EDW Maglev. In order to achieve these goals, the following tasks have been performed:

- A 2-D analytic based steady-state eddy-current model has been developed and validated.
- A 2-D analytic based transient eddy-current model has been developed and validated.
- The dynamic electromechanical suspension behavior of a 2-degree of freedom EDW Maglev has been investigated.

- A 1-degree of freedom pendulum style experimental setup has been used to experimentally investigate the dynamic suspension behavior of the EDW Maglev.
- A 4-wheeled sub-scale EDW Maglev vehicle experimental setup has been constructed and tested for lateral stability. This setup could be used for the investigation of the dynamic behavior of an EDW Maglev and design appropriate control laws.

1.6 Organization of the Thesis

This dissertation is organized in the following format.

Chapter 1 includes the background on different types of Maglev systems including a discussion on the various techniques used to create magnetic suspension and propulsion. The research goals of this dissertation are also outlined.

Chapter 2 includes a review of different techniques for 2-D electromagnetic steady-state modeling. This is followed by a complete derivation of the steady-state analytical model for force and power loss. The derived force and power loss equations are validated by using a steady-state finite element analysis (FEA) model using a Halbach rotor as a magnetic source.

Chapter 3 presents a brief review of transient eddy-current modeling techniques. This is followed by a detailed derivation of the transient force and power loss calculations using the spatial Fourier and temporal Laplace transform method. The performance of the derived analytic equations has been verified by using a transient FEA models developed in COMSOL and Magsoft.

Chapter 4 presents a detailed review of the dynamics of EDS Maglev systems and their magnetic damping and stiffness characteristics. It also investigates the dynamic suspension behavior of the EDS Maglev using EDWs with both steady-state and transient models developed in Chapter 2. The 2-degree of freedom EDW Maglev has been simulated. In addition, the analytic equations for the magnetic stiffness and damping constants are derived using the steady-state force equations.

In Chapter 5 a 1-degree of freedom EDW pendulum experimental setup is presented. The various experimental test results has been compared with the analytic results in this chapter.

Chapter 6 includes the details on the multi-degree of freedom sub-scale EDW Maglev setup. The dynamic simulation of the experimental Maglev setup are included in this chapter.

Chapter 7 presents the summary of the thesis and outlines the future direction of research for the successful control of a sub-scale EDW Maglev vehicle.

CHAPTER 2: A 2D STEADY-STATE ANALYTIC EDDY-CURRENT MODEL

2.1 Introduction

In this chapter the two-dimensional (2-D) analytic steady-state model is developed for a magnetic source simultaneously moving and/or rotating above a conducting guideway. The general equation for the tangential and normal components of the forces as well as the power loss in the guideway is developed. The developed equations are verified by using the electrodynamic wheel as a magnetic source which is both rotated and/or translationally moved above a conductive (aluminum) guideway. In section 2.2 a review of 2-D eddy-current modeling techniques is presented. In section 2.3 a 2-D analytic based steady-state model is developed using the quasi-static Maxwell's equations. The model has been derived using the vector potential in the conducting guideway region and the scalar potential in the non-conducting air region. The physical presence of the magnetic source is accounted for by including the source fields on the conducting boundary. The governing equations are solved using the spatial Fourier transform technique. The derived forces and power loss equations are verified by using a 2-D finite element analysis (FEA) model developed using COMSOL FEA software [116]. A summary of the chapter is provided in section 2.4.

2.2 A Review of 2-D Eddy-Current Modeling Techniques

The most common techniques that have been utilized for modeling 2-D eddy-current problems are the equivalent-circuit method, thick and thin conductive sheet approximation methods, numerical methods and the Fourier transform method. Each of these techniques will be reviewed in the following sub-sections.

2.2.1 Equivalent-Circuit Model

The equivalent-circuit modeling technique has been successfully applied by several authors to develop models for linear induction motors [117–120]. Most of these models utilize a modified version of general machine theory for rotatory machines. Several authors have successfully developed complicated equivalent-circuit models of LIMs including the various effects such as end-effects, skin-effects and longitudinal end-effects [121–123]. Most recently, an improved T-model equivalent circuits of a single-sided LIM has been developed and verified experimentally [124, 125]. The electrodynamic wheel configuration has a conductive guideway, a finite width, a non-uniform air-gap, and is not symmetric in 2-D therefore, the 2-D equivalent-circuit modeling technique would be highly inaccurate [41].

2.2.2 Thick and Thin Conductive Sheet Approximation

The thick conductive sheet technique is based on the assumptions that the guideway thickness, b , will always be greater than the magnetic skin depth, δ_s . i.e. $b > \delta_s$. where the skin depth, δ_s , is related to the source frequency, ω_e , and relative permeability of the material, μ_r , by [41]

$$\delta_s = \sqrt{\frac{2}{\mu_o \mu_r \sigma \omega_e}}. \quad (2.1)$$

The use of this technique is limited because it can only be used when the guideway is very thick compared to the magnetic skin depth or when the source is travelling at very low speed [41]. Nevertheless, this thick conductive sheet approximation method for eddy current modeling has been used by several authors [126–129] with various magnetic sources.

The thin sheet approximation is based on the assumption that the guideway thickness, b , is thin compared to the magnetic skin depth of the dominant frequencies of the source field i.e. $b < \delta_s$. Therefore, the induced eddy-current in the conductor is uniform throughout the guideway thickness.

Maxwell first proposed the concept of thin sheet approximations based on the principle of images [130, 131]. Smythe [132] used the method to calculate the torque produced by magnets or electromagnets moving above a rotating disk. Reitz [54] expanded on this technique to model the magnetic force on the magnets and coils moving parallel to and above a conducting plate of infinite length and width. Several other authors have considered this method for eddy-current modeling for Maglev applications [131, 133]. The thin sheet approximation has also been used to model linear induction motors by Yamamura and Ooi [3, 134]. These eddy-current problems are often solved using the vector potential, \mathbf{A} [3]. In general the current is uniform throughout the conductor thickness at low speed but at high speed this is not true. Therefore, this approach is not applicable for EDW applications where accurate force prediction across the full range of translational speeds will be needed [41].

2.2.3 Numerical Methods

2-D steady-state eddy-current models have been successfully developed by using a range of numerical methods such as the finite element method [135–138], finite difference method [135], boundary element method [135] and the hybrid boundary element method [139]. Numerical methods are extremely useful since they can be used to solve complex geometric eddy-current problems. In this research, the model developed in [41] using the finite element method will be used to validate the performance of the proposed analytical models. The FEA model was developed in COMSOL v3.5 software where both the rotational and the translational motion are included at the same time. The FEA model is described in detail in [41]. Almost all commercial FEA software cannot model both the rotational and translational motion. However, COMSOL is an exception in which both motions are possible. Therefore, the COMSOL software is used to develop the FEA model in this research.

2.2.4 The Spatial Fourier Transform Method

The spatial Fourier transform technique involves Fourier transforming one of the spatial variables in the direction of motion. This reduces the 2-D partial differential equations into a 1-D Fourier transformed equation, thus enabling a simple solution to be derived. The spatial Fourier transform technique has been used to calculate the force produced when moving an infinitely long coil [140] and also rectangular coil [55] above a infinitely thick conductor (conducting half-space). The spatial Fourier transform technique has also been used by several authors to model the linear induction motor in both 2-D and 3-D [3, 141] and study their performance for high-speed maglev transportation. 3-D end-effects have also been considered [66, 67]. Excellent agreement between the experimental measurements and the Fourier transform method were presented in [55, 66, 67].

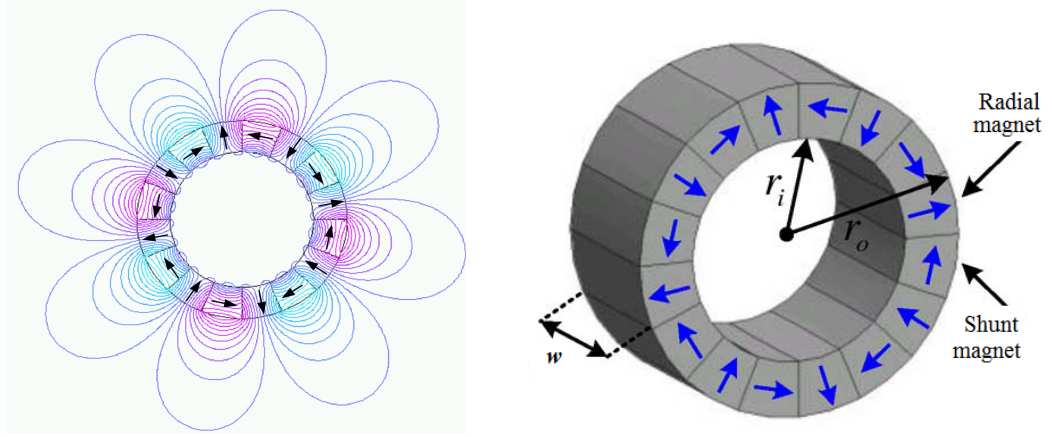
The spatial Fourier transform technique will be used in this research to represent the 2-D steady-state model of the EDW rotating and/or moving above a conductive guideway. This method is adapted because the governing equations as well as the source field were Fourier transformable and the 2-D model significantly simplified in the Fourier domain. The detail of this modeling is presented in the following section.

2.3 Fourier Transform 2-D Analytical Steady-State Solution

A computationally fast model is essential if active control of an eddy-current device is to be implemented. Deriving the 2-D eddy-current forces is a first step towards the development of such control laws. Since a 2-D model ignores the source edge-effect and a guideway edge effect; the performance will be different from the actual experimental results (as shown in section 5.4). However, for the special case in which the source and conductive guideway are sufficiently wide and uniform then 2-D modeling of the forces can be utilized [142].

Exact modeling approaches often model current sources using simple filament coils or current sheets that can be easily incorporated into the conductive region's geometry

[55, 143]. However, when a current or magnet source has a complex geometric shape and/or complex motion it is difficult to easily obtain the direct analytic solution by calculating the forces on the source. An EDW source as illustrated in Figure 2.1 is an example of one such complex source.



(a) A 2-D Halbach rotor showing magnetic field lines

(b) A 3-D Halbach rotor with a finite width

Figure 2.1: A four pole-pair Halbach rotor.

2.3.1 Governing Subdomain Equations

The model used for this analytic based solution is shown in Figure 2.2. It is composed of three subdomains; a conducting guideway region Ω_2 and two non-conducting air regions Ω_1 and Ω_3 . The magnetic source is present only in the upper non-conducting region Ω_1 . The material of the conductive guideway is assumed to be isotropic and linear.

The electromagnetic fields can be accurately modeled using the quasi-static Maxwell's equations, where the displacement current is neglected and a moving conductor is present. The applicable equations are:

$$\nabla \times \mathbf{E} = -\frac{\partial \mathbf{B}}{\partial t} \quad (2.2)$$

$$\nabla \cdot \mathbf{B} = 0 \quad (2.3)$$

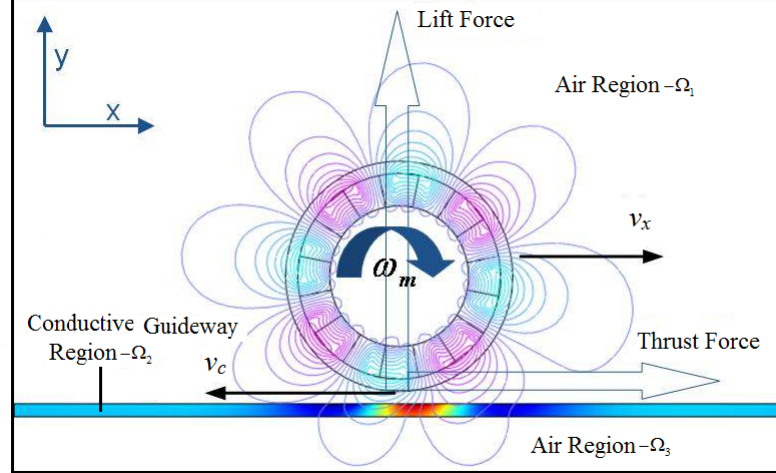


Figure 2.2: A FEA COMSOL model of a four-pole pair Halbach rotor rotating and translationally moving above a long conducting guideway. The induced guideway eddy-current are also shown in the guideway.

$$\nabla \times \mathbf{H} = \mathbf{J} \quad (2.4)$$

$$\mathbf{J} = \sigma(\mathbf{E} + \mathbf{v} \times \mathbf{B}) \quad (2.5)$$

where

σ = conductivity of the guideway (Sm^{-1})

\mathbf{v} = velocity vector of the guideway (ms^{-1})

\mathbf{E} = electric field intensity (Vm^{-1})

\mathbf{H} = magnetic field intensity (Am^{-1})

\mathbf{B} = magnetic flux density (T).

3-D FEA eddy-current formulations are often solved by utilizing the magnetic scalar potential in the air region and the vector potential in the conducting region. This formulation is often used because the number of unknowns in the non-conducting region is reduced and the source field only needs to be incorporated on the conducting boundary region [144, 145]. This is also advantageous for 2-D modeling because it enables the field and forces to be neatly formulated with respect to only the conducting boundary. In this thesis a novel formulation using the magnetic scalar potential in the air region and magnetic vector potential in the conducting region will be used.

The formulations for both regions are discussed in the following sections.

2.3.2 Non-Conducting Regions

There is no external current in the non-conducting region therefore Ampere's law (2.4) reduces down to

$$\nabla \times \mathbf{H} = 0 \quad (2.6)$$

Since the curl of a gradient is zero the magnetic field intensity, \mathbf{H} can be written in terms of the magnetic scalar potential, ϕ as

$$\mathbf{H} = -\nabla\phi \quad (2.7)$$

Therefore, the reflected magnetic flux density, \mathbf{B}^r due to the induced eddy-current in the conducting guideway becomes

$$\mathbf{B}^r = -\mu_0\nabla\phi \quad (2.8)$$

The source field within the non-conducting region will be

$$\mathbf{B}^s = B_x^s(x, y)\hat{x} + B_y^s(x, y)\hat{y} \quad (2.9)$$

and the total field in the non-conducting region, Ω_1 , is then

$$\mathbf{B} = \mathbf{B}^s - \mu_0\nabla\phi_1 \text{ in } \Omega_1 \quad (2.10)$$

where ϕ_1 is the magnetic scalar potential due to the induced guideway currents in region Ω_1 . Assuming that the magnetic source material is linear then after taking the divergence of both sides of (2.10) and noting that

$$\nabla \cdot \mathbf{B}^s = 0 \quad (2.11)$$

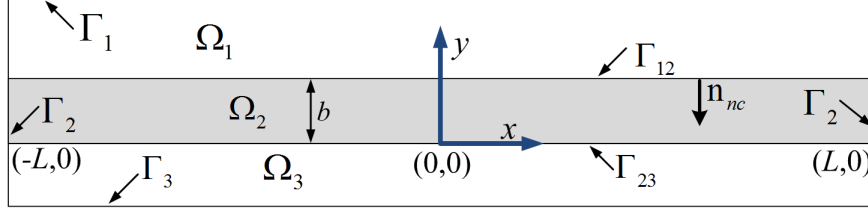


Figure 2.3: *Illustration of the conductive and non-conductive regions and boundaries used by the analytic based 2-D steady-state model.*

the formulation in the non-conducting region Ω_1 simply reduces to Laplace's equation:

$$\nabla^2 \phi_1 = 0 \text{ in } \Omega_1 \quad (2.12)$$

The analogous equation can be obtained for the non-conducting region Ω_3 . Hence, the governing equation for non-conducting regions can be obtained by expanding (2.12) to yield

$$\frac{\partial^2 \phi_n}{\partial x^2} + \frac{\partial^2 \phi_n}{\partial y^2} = 0 \text{ in } \Omega_n \text{ for } n = 1, 3 \quad (2.13)$$

Due to (2.11) it is not necessary to model the rotor's field within the non-conducting region [114, 138]. However, the presence of the magnetic source (Halbach rotor in this case) is analytically accounted for by incorporating the magnetic fields due to the rotor at the boundary interface Γ_{12} . Thus the problem region that will be solved for will be devoid of the source within the subdomain. Figure 2.3 shows the subdomains and boundary conditions that will be used by this model.

2.3.3 Conducting Guideway Region

Since the divergence of a curl is zero, the magnetic flux density can be written in terms of the cross product of a vector quantity

$$\mathbf{B} = \nabla \times \mathbf{A} \quad (2.14)$$

The quantity \mathbf{A} is called the magnetic vector potential or simply vector potential. The conducting region Ω_2 will be solved using this vector potential, \mathbf{A} . Substituting

(2.5) into (2.4) and noting that

$$\mathbf{B} = \mu_0 \mathbf{H} \quad (2.15)$$

the following expression is obtained

$$\nabla \times \mathbf{B} - \mu_0 \sigma (\mathbf{E} + \mathbf{v} \times \mathbf{B}) = 0 \quad (2.16)$$

The magnetic flux density and electric field intensity can be written in terms of vector potential \mathbf{A} and electric scalar potential ϕ by using

$$\mathbf{B} = \nabla \times \mathbf{A} \quad (2.17)$$

$$\mathbf{E} = -\frac{\partial \mathbf{A}}{\partial t} - \nabla \phi \quad (2.18)$$

Substituting (2.17) and (2.18) into (2.16) gives

$$\nabla \times (\nabla \times \mathbf{A}) + \mu_0 \sigma \left(\frac{\partial \mathbf{A}}{\partial t} + \nabla \phi - \mathbf{v} \times \nabla \times \mathbf{A} \right) = 0 \quad (2.19)$$

Now using the vector identity:

$$\nabla \times (\nabla \times \mathbf{A}) = \nabla \cdot (\nabla \cdot \mathbf{A}) - \nabla^2 \mathbf{A} \quad (2.20)$$

and Coulomb gauge law

$$\nabla \cdot \mathbf{A} = 0 \quad (2.21)$$

allows the relation (2.19) to be re-written as

$$\mu_0 \sigma \frac{\partial \mathbf{A}}{\partial t} - \nabla^2 \mathbf{A} - \mu_0 \sigma \mathbf{v} \times (\nabla \times \mathbf{A}) + \mu_0 \sigma \nabla \phi = 0 \quad (2.22)$$

In 2-D modeling, the current \mathbf{J} and therefore the vector potential \mathbf{A} flows only in the z -direction and hence \mathbf{B} and \mathbf{H} have only an x -component and y -component but no z -component. In 2-D the relationship between the vector potential and the magnetic field component is therefore

$$\nabla \times A_z = \begin{vmatrix} \hat{x} & \hat{y} & \hat{z} \\ \frac{\partial}{\partial x} & \frac{\partial}{\partial y} & \frac{\partial}{\partial z} \\ 0 & 0 & A_z \end{vmatrix} = \hat{x} \frac{\partial A_z}{\partial y} - \hat{y} \frac{\partial A_z}{\partial x} = \hat{x} B_x + \hat{y} B_y \quad (2.23)$$

where \hat{x} , \hat{y} and \hat{z} are the unit vectors in the x , y and z directions and B_x and B_y are the projections of the magnetic flux densities along the x and y directions. Since for 2-D modeling, $\nabla \cdot A_z = 0$, $\nabla \cdot J_z = 0$ there is no source to produce the electric scalar potential, its value is zero in (2.22) [41]. The detail explanation of this can be found on section 2.3.1 and section 5.3 of reference [41]. After neglecting the electrical scalar potential the 2-D equation for a moving conductive media in terms of A_z will be

$$\mu_0 \sigma \frac{\partial A_z}{\partial t} - \nabla^2 A_z - \mu_0 \sigma \mathbf{v} \times (\nabla \times A_z) = 0 \quad (2.24)$$

The motional effect of the source translationally moving above the conductive guideway is incorporated into the conductive region by using the convective term in (2.24) [114]. Most steady-state based models incorporate only one velocity term, typically the velocity in the direction of translational motion [3, 114, 138]. However, in this research both a translational velocity, v_x , and heave velocity, v_y , will be considered. In this case the convective term will be

$$\mathbf{v} \times (\nabla \times A_z) = (\hat{x} v_x + \hat{y} v_y) \times \left(\hat{x} \frac{\partial A_z}{\partial y} - \hat{y} \frac{\partial A_z}{\partial x} \right) \quad (2.25)$$

Using the vector cross product on (2.25), one obtains

$$\mathbf{v} \times (\nabla \times A_z) = - \left(v_x \frac{\partial A_z}{\partial x} + v_y \frac{\partial A_z}{\partial y} \right) \quad (2.26)$$

Substituting (2.26) into (2.24) gives

$$\mu_0 \sigma \frac{\partial A_z}{\partial t} - \nabla^2 A_z = -\mu_0 \sigma \left(v_x \frac{\partial A_z}{\partial x} + v_y \frac{\partial A_z}{\partial y} \right) \quad \text{in } \Omega_2 \quad (2.27)$$

If the model is steady-state in which ω_e is the source frequency then the vector potential can be written as

$$A_z(x, y, t) = A_z^{ss}(x, y) e^{j\omega_e t} \quad \text{in } \Omega_2 \quad (2.28)$$

where the superscript ‘ss’ denote ‘steady-state’. Substituting (2.28) into (2.27) and expanding, one obtain

$$\frac{\partial^2 A_z^{ss}}{\partial x^2} + \frac{\partial^2 A_z^{ss}}{\partial y^2} = \mu_0 \sigma \left(j\omega_e A_z^{ss} + v_x \frac{\partial A_z^{ss}}{\partial x} + v_y \frac{\partial A_z^{ss}}{\partial y} \right) \quad \text{in } \Omega_2 \quad (2.29)$$

2.3.4 Boundary Conditions

The boundary conditions for the electromagnetic fields at the top boundary interface between the non-conducting and conductive guideway regions, Γ_{12} are [146]

$$\mathbf{n}_c \cdot (\mathbf{B}_{\Omega_1} - \mathbf{B}_{\Omega_2}) = 0 \quad , \text{ on } \Gamma_{12} \quad (2.30)$$

$$\mathbf{n}_c \times (\mathbf{H}_{\Omega_1} - \mathbf{H}_{\Omega_2}) = 0 \quad , \text{ on } \Gamma_{12} \quad (2.31)$$

Since the permeability of the non-conducting and conducting regions is the same, the boundary condition (2.31) can be written as

$$\mathbf{n}_c \times (\mathbf{B}_{\Omega_1} - \mathbf{B}_{\Omega_2}) = 0 \quad , \text{ on } \Gamma_{12} \quad (2.32)$$

where \mathbf{B}_{Ω_1} is the magnetic flux density at the boundary Γ_{12} due to scalar potential and source field

$$\mathbf{B}_{\Omega_1} = \mathbf{B}^s - \mu_0 \nabla \phi_n \quad (2.33)$$

\mathbf{B}_{Ω_2} is the magnetic flux density in region Ω_2 due to the vector potential

$$\mathbf{B}_{\Omega_2} = \nabla \times \mathbf{A} \quad (2.34)$$

Substituting (2.33) and (2.34) into (2.30) and (2.32) one obtains [144, 147, 148]

$$\mathbf{n}_c \cdot (\mathbf{B}^s - \mu_0 \nabla \phi_1) = \mathbf{n}_c \cdot (\nabla \times \mathbf{A}) \quad , \text{ on } \Gamma_{12} \quad (2.35)$$

$$\mathbf{n}_c \times (\mathbf{B}^s - \mu_0 \nabla \phi_1) = \mathbf{n}_c \times (\nabla \times \mathbf{A}) \quad , \text{ on } \Gamma_{12} \quad (2.36)$$

Utilizing the relation (2.23) and vector algebra on (2.35) and (2.36), the boundary condition equations simplify down to

$$-\mu_0 \frac{\partial \phi_1(x, b)}{\partial x} + B_x^s(x, b) = \frac{\partial A_z^{ss}(x, y)}{\partial y} \Big|_{y=b} \quad , \text{ on } \Gamma_{12} \quad (2.37)$$

$$-\mu_0 \frac{\partial \phi_1(x, y)}{\partial y} \Big|_{y=b} + B_y^s(x, b) = -\frac{\partial A_z^{ss}(x, b)}{\partial x} \quad , \text{ on } \Gamma_{12} \quad (2.38)$$

If the source is only present in Ω_1 then the bottom conducting surface, Γ_{23} has no direct connection to the source field. Therefore, the normal and tangential components at the $A_z - \phi$ interface are

$$-\mu_0 \frac{\partial \phi_3(x, b)}{\partial x} = \frac{\partial A_z^{ss}(x, y)}{\partial y} \Big|_{y=b} \quad , \text{ on } \Gamma_{23} \quad (2.39)$$

$$-\mu_0 \frac{\partial \phi_3(x, y)}{\partial y} \Big|_{y=b} = -\frac{\partial A_z^{ss}(x, b)}{\partial x} \quad , \text{ on } \Gamma_{23} \quad (2.40)$$

The source field is assumed to be centrally located at $x = 0$ and the guideway is sufficiently long to ensure that the field is zero at the guideway ends, $x = \pm L$, such that

$$B_x^s(\pm L, y) = 0 \quad , \text{ on } \Gamma_2 \quad (2.41)$$

$$B_y^s(\pm L, y) = 0 \quad , \text{ on } \Gamma_2 \quad (2.42)$$

$$A_z(\pm L, y) = 0 \quad , \text{ on } \Gamma_2 \quad (2.43)$$

Also, on the outer non-conducting boundaries, one has

$$\phi_1 = 0 \quad , \text{ on } \Gamma_1 \quad (2.44)$$

$$\phi_3 = 0 \quad , \text{ on } \Gamma_3 \quad (2.45)$$

2.3.5 Fourier Transformed Governing Subdomain Equations

The governing equations for the problem regions are given by (2.27) and (2.13). These equations must satisfy the boundary conditions (2.37)-(2.45). The governing equations are solved by utilizing the Fourier transform technique. The spatial Fourier transform [149] for the vector potential and scalar potential with respect to the x -axis are defined as [150]

$$A_z^{ss}(\xi, y) = \int_{-\infty}^{\infty} A_z^{ss}(x, y) e^{-j\xi x} dx \quad (2.46)$$

$$\phi_n(\xi, y) = \int_{-\infty}^{\infty} \phi_n(x, y) e^{-j\xi x} dx \quad \text{for } n = 1, 3 \quad (2.47)$$

Noting that

$$\frac{\partial A_z(\xi, y)}{\partial x} = j\xi A_z(\xi, y) \quad (2.48)$$

$$\frac{\partial^2 A_z(\xi, y)}{\partial x^2} = -\xi^2 A_z(\xi, y) \quad (2.49)$$

and taking the Fourier transform on either side of (2.29), will be

$$\begin{aligned}
 -\xi^2 A_z^{ss}(\xi, y) + \frac{\partial^2 A_z^{ss}(\xi, y)}{\partial y^2} &= \mu_0 \sigma (j\omega_e A_z^{ss}(\xi, y) + j\xi v_x A_z^{ss}(\xi, y)) \\
 &\quad + \mu_0 \sigma v_y \frac{\partial A_z^{ss}(\xi, y)}{\partial y}
 \end{aligned} \tag{2.50}$$

Rearranging (2.50), one obtains

$$\frac{\partial^2 A_z^{ss}(\xi, y)}{\partial y^2} - \mu_0 \sigma v_y \frac{\partial A_z^{ss}(\xi, y)}{\partial y} - (\xi^2 + j\mu_0 \sigma (\omega_e + \xi v_x)) A_z^{ss}(\xi, y) = 0 \tag{2.51}$$

Defining

$$\gamma = \sqrt{\xi^2 + j\mu_0 \sigma (\omega_e + v_x \xi)} \tag{2.52}$$

$$2\lambda = \mu_0 \sigma v_y \tag{2.53}$$

allows (2.51) to be written as:

$$\frac{\partial^2 A_z^{ss}(\xi, y)}{\partial y^2} - 2\lambda \frac{\partial A_z^{ss}(\xi, y)}{\partial y} - \gamma^2 A_z^{ss}(\xi, y) = 0 \tag{2.54}$$

The general solution of $A_z^{ss}(\xi, y)$ can be obtained by solving (2.54) by using

$$A_z^{ss}(\xi, y) = M(\xi)e^{\beta_1 y} + N(\xi)e^{\beta_2 y} \quad \text{in } \Omega_2 \tag{2.55}$$

where

$$\beta_1 = \lambda + \sqrt{\lambda^2 + \gamma^2} \quad \text{and} \quad \beta_2 = \lambda - \sqrt{\lambda^2 + \gamma^2} \tag{2.56}$$

and $M(\xi)$ and $N(\xi)$ are unknowns constants. These unknowns $M(\xi)$ and $N(\xi)$ are evaluated by solving the boundary condition equations.

The Fourier transform of (2.13) in the non-conducting regions is

$$\frac{\partial^2 \phi_n(\xi, y)}{\partial y^2} = \xi^2 \phi_n(\xi, y) \quad \text{in } \Omega_n \tag{2.57}$$

where $n = 1$ and 3 . Solving (2.57) and noting that when moving away from the guideway along the y -axis in Ω_1 and Ω_3 the field must reduce to zero, one obtains the solutions

$$\phi_1(\xi, y) = X_1(\xi)e^{-\xi y} \quad \text{in } \Omega_1 \quad (2.58)$$

$$\phi_3(\xi, y) = X_3(\xi)e^{\xi y} \quad \text{in } \Omega_3 \quad (2.59)$$

2.3.6 Fourier Transformed Boundary Conditions

Fourier transforming the boundary conditions, (2.37) and (2.38), on the top guideway surface one obtains

$$-j\xi\mu_0\phi_1(\xi, b) + B_x^s(\xi, b) = \left. \frac{\partial A_z^{ss}(\xi, y)}{\partial y} \right|_{y=b} \quad \text{on } \Gamma_{12} \quad (2.60)$$

$$\mu_0 \left. \frac{\phi_1(\xi, y)}{\partial y} \right|_{y=b} - B_y^s(\xi, b) = j\xi A_z^{ss}(\xi, b) \quad \text{on } \Gamma_{12} \quad (2.61)$$

Substituting (2.55) and (2.58) into (2.60) and (2.61) one can obtain

$$-j\xi\mu_0 X_1(\xi)e^{-\xi b} + B_x^s(\xi, b) = \beta_1 M(\xi)e^{\beta_1 b} + \beta_2 N(\xi)e^{\beta_2 b} \quad \text{on } \Gamma_{12} \quad (2.62)$$

$$-\mu_0 \xi X_1(\xi)e^{-\xi b} - B_y^s(\xi, b) = j\xi [M(\xi)e^{\beta_1 b} + N(\xi)e^{\beta_2 b}] \quad \text{on } \Gamma_{12} \quad (2.63)$$

Now multiplying (2.63) by j and subtracting (2.63) from (2.62) yields

$$B^s(\xi, b) = (\beta_1 + \xi) M(\xi)e^{\beta_1 b} + (\beta_2 + \xi) N(\xi)e^{\beta_2 b} \quad (2.64)$$

where $B^s(\xi, b)$ is an arbitrary source at $y = b$ given by

$$B^s(\xi, b) = B_x^s(\xi, b) + jB_y^s(\xi, b) \quad (2.65)$$

Fourier transforming the bottom boundary conditions, (2.39) and (2.40), gives

$$-j\xi\mu_0\phi_3(\xi, 0) = \left. \frac{\partial A_z^{ss}(\xi, y)}{\partial y} \right|_{y=0} \quad \text{on } \Gamma_{23} \quad (2.66)$$

$$\mu_0 \left. \frac{\phi_3(\xi, y)}{\partial y} \right|_{y=0} = j\xi A_z^{ss}(\xi, 0) \quad \text{on } \Gamma_{23} \quad (2.67)$$

Substituting (2.55) and (2.59) into (2.66) and (2.67) one can obtain

$$-j\xi\mu_0 X_3(\xi) = \beta_1 M(\xi) + \beta_2 N(\xi) \quad \text{on } \Gamma_{23} \quad (2.68)$$

$$\mu_0 \xi X_3(\xi) = j\xi [M(\xi) + N(\xi)] \quad \text{on } \Gamma_{23} \quad (2.69)$$

Now multiplying (2.69) by j and adding (2.68) and (2.69) yields

$$0 = (\beta_1 - \xi) M(\xi) + (\beta_2 - \xi) N(\xi) \quad (2.70)$$

The unknowns $M(\xi)$ and $N(\xi)$ can be determined by solving (2.64) and (2.70) as

$$M(\xi) = \frac{(\beta_2 - \xi)}{e^{\beta_1 b}(\beta_2 - \xi)(\beta_1 + \xi) - e^{\beta_2 b}(\beta_1 - \xi)(\beta_2 + \xi)} B^s(\xi, b) \quad (2.71)$$

$$N(\xi) = -\frac{(\beta_1 - \xi)}{e^{\beta_1 b}(\beta_2 - \xi)(\beta_1 + \xi) - e^{\beta_2 b}(\beta_1 - \xi)(\beta_2 + \xi)} B^s(\xi, b) \quad (2.72)$$

2.3.7 The Vector Potential Solution

The complete steady-state solution of the magnetic vector potential in the conducting region can be obtained by substituting the values of $M(\xi)$ and $N(\xi)$ into (2.55); one obtains

$$A_z^{ss}(\xi, y) = \frac{(\beta_2 - \xi)e^{\beta_1 y} - (\beta_1 - \xi)e^{\beta_2 y}}{e^{\beta_1 b}(\beta_2 - \xi)(\beta_1 + \xi) - e^{\beta_2 b}(\beta_1 - \xi)(\beta_2 + \xi)} B^s(\xi, b) \quad (2.73)$$

Substituting (2.73) into the Fourier transform of (2.28) gives

$$A_z^{ss}(\xi, y, t) = T^{ss}(\xi, y)B^s(\xi, b)e^{j\omega_e t} \quad (2.74)$$

where

$$T^{ss}(\xi, y) = \frac{(\beta_2 - \xi)e^{\beta_1 y} - (\beta_1 - \xi)e^{\beta_2 y}}{e^{\beta_1 b}(\beta_2 - \xi)(\beta_1 + \xi) - e^{\beta_2 b}(\beta_1 - \xi)(\beta_2 + \xi)} \quad (2.75)$$

can be interpreted as the transmission function for an arbitrary source field, $B^s(\xi, b)$, imparted on the guideway surface, Γ_{12} . This has a similar form to the reflection coefficient that is used for non-destructive testing [151, 152]. If the heave velocity is not included in the model, then the transmission function reduces to

$$T_0^{ss}(\xi, y) = \frac{(\gamma + \xi)e^{\gamma y} + (\gamma - \xi)e^{-\gamma y}}{e^{\gamma b}(\gamma + \xi)^2 - e^{-\gamma b}(\gamma - \xi)^2} \quad (2.76)$$

This transmission function (2.76) will be used in the next chapter for transient modeling.

The Fourier transformed magnetic flux density within the conductive guideway is obtained by differentiating (2.74) with respect to x and y . Using (2.23), one obtains

$$B_y^{ss}(\xi, y) = -\frac{\partial A_z^{ss}(\xi, y)}{\partial x} = -j\xi T^{ss}(\xi, y)B^s(\xi, b) \quad (2.77)$$

$$B_x^{ss}(\xi, y) = \frac{\partial A_z^{ss}(\xi, y)}{\partial y} = \frac{\partial T^{ss}(\xi, y)}{\partial y}B^s(\xi, b) \quad (2.78)$$

These steady-state magnetic flux densities will be utilized to calculate the power loss and forces in section 2.3.9.

2.3.8 Reflected Field in the Non-Conducting Region

The value of the unknown $X_1(\xi)$ in the reflected field for region Ω_1 (2.58) can be obtained by substituting (2.74) and (2.58) into (2.61). After rearranging one obtains

$$X_1(\xi) = -\frac{1}{\mu_0\xi}[B_y^s(\xi, b) + j\xi T^{ss}(\xi, b)B^s(\xi, b)]e^{\xi b} \quad (2.79)$$

The scalar potential equation (2.59) in the non-conducting region is therefore given by

$$\phi_1(\xi, y) = -\frac{1}{\mu_0\xi}[B_y^s(\xi, b) + j\xi T^{ss}(\xi, b)B^s(\xi, b)]e^{\xi(b-y)} \quad (2.80)$$

The reflected magnetic flux density in Ω_1 due to the induced current in Ω_2 is then

$$B_x^r(\xi, y) = -\mu_0 \frac{\partial \phi_1(\xi, y)}{\partial x} = j[B_y^s(\xi, b) + j\xi T^{ss}(\xi, b)B^s(\xi, b)]e^{\xi(b-y)} \quad (2.81)$$

$$B_y^r(\xi, y) = -\mu_0 \frac{\partial \phi_1(\xi, y)}{\partial y} = -[B_y^s(\xi, b) + j\xi T^{ss}(\xi, b)B^s(\xi, b)]e^{\xi(b-y)} \quad (2.82)$$

where the superscript ‘r’ denotes the reflected component. Hence, the x -component and y -component of the reflected magnetic flux densities are related by

$$B_y^r(\xi, y) = jB_x^r(\xi, y) \quad (2.83)$$

This result is not dependent on the property of the source field. Also from (2.77) and (2.82), one obtains

$$B_y^r(\xi, y) = [B_y^{ss}(\xi, b) - B_y^s(\xi, b)]e^{\xi(b-y)} \quad (2.84)$$

Therefore at $y = b$, the y -component of the reflected field, B_y^r , the source field, B_y^s and the steady-state flux density, B_y^{ss} , are related by

$$B_y^r(\xi, b) = B_y^{ss}(\xi, b) - B_y^s(\xi, b) \quad (2.85)$$

Similarly, the analogous relation for the x -component of the flux density can be obtained as

$$B_x^r(\xi, b) = B_x^{ss}(\xi, b) - B_x^s(\xi, b) \quad (2.86)$$

2.3.9 Force and Power Equations

The steady-state electric field intensity, E_z^{ss} due to the vector potential, A_z^{ss} can be obtained by differentiating (2.74) with respect to time, t . Thus giving

$$E_z^{ss}(\xi, y) = -\frac{dA_z^{ss}(\xi, y, t)}{dt} = -j\omega_\epsilon T^{ss}(\xi, y)B^s(\xi, b)e^{j\omega_\epsilon t} \quad (2.87)$$

The value of electric field intensity and flux density equations will be utilized to calculate the power loss and forces in the following sub-sections.

2.3.9.1 Tensor Force Calculation

In 2-D, the normal force, F_y , and tangential force, F_x , per-unit width can be determined by evaluating Maxwell's stress tensor [130] over the surface of the conducting guideway:

$$F_x^{ss} = \frac{1}{2\mu_0} \operatorname{Re} \int_{-\infty}^{\infty} B_x^{ss}(x, b)B_y^{ss*}(x, b)dx \quad \text{on } \Gamma_{12} \quad (2.88)$$

$$F_y^{ss} = \frac{1}{4\mu_0} \operatorname{Re} \int_{-\infty}^{\infty} (B_y^{ss*}(x, b)B_y^{ss}(x, b) - B_x^{ss*}(x, b)B_x^{ss}(x, b)) d\xi \quad \text{on } \Gamma_{12} \quad (2.89)$$

where the star superscript denotes complex conjugation. These force equations can be evaluated in the Fourier domain. Consider the two functions $g_1(x)$ and $g_2(x)$ which are limited and integrable across the range $x(-\infty, +\infty)$. The Fourier transform of $g_1(x)$ and $g_2(x)$ is given by

$$g_i(\xi) = \int_{-\infty}^{\infty} g_i(x)e^{-j\xi x}dx \quad \text{for } i = 1, 2 \quad (2.90)$$

Parseval's theorem [150] states that the following integral relation holds

$$\int_{-\infty}^{\infty} g_1^*(x)g_2(x)dx = \frac{1}{2\pi} \int_{-\infty}^{\infty} g_1^*(\xi)g_2(\xi)d\xi \quad (2.91)$$

where $g_1^*(x)$ is the complex conjugate of $g_1(x)$. Therefore, by utilizing Parseval's theorem, (2.91), the normal and tangential forces can be obtained directly within the Fourier domain, thereby circumventing the need for inverse Fourier transforming [66]. Hence, utilizing (2.91) allows (2.88) and (2.89) to be expressed as

$$F_x^{ss} = \frac{1}{4\pi\mu_0} \operatorname{Re} \int_{-\infty}^{\infty} [B_x^{ss}(\xi, b)B_y^{ss*}(\xi, b)]d\xi \quad \text{on } \Gamma_{12} \quad (2.92)$$

$$F_y^{ss} = \frac{1}{8\pi\mu_0} \operatorname{Re} \int_{-\infty}^{\infty} [B_y^{ss*}(\xi, b)B_y^{ss}(\xi, b) - B_x^{ss*}(\xi, b)B_x^{ss}(\xi, b)] d\xi \quad \text{on } \Gamma_{12} \quad (2.93)$$

where $B_y^{ss*}(\xi, b)$ and $B_x^{ss*}(\xi, b)$ are the complex conjugates of (2.77) and (2.78) respectively evaluated at $y = b$. Substituting (2.85) and (2.86) into (2.92) enables the thrust force to be written in terms of the reflected and source magnetic flux densities as

$$F_x^{ss} = \frac{w}{4\pi\mu_0} \operatorname{Re} \int_{-\infty}^{\infty} [B_x^r B_y^{s*} + B_x^s B_y^{r*} + B_x^s B_y^{s*} + B_x^r B_y^{r*}]d\xi \quad (2.94)$$

Each magnetic flux densities term in (2.94) is a function of ξ and b . The detail (ξ, b) is dropped from each term for convenience. Substituting (2.83) into (2.94) gives

$$F_x^{ss} = \frac{w}{4\pi\mu_0} \operatorname{Re} \int_{-\infty}^{\infty} [B_x^r B_y^{s*} + B_x^s B_y^{r*} + B_x^s B_y^{s*} - jB_x^r B_x^{r*}]d\xi \quad (2.95)$$

Noting the following two relations

$$\operatorname{Re}[-jB_x^r B_x^{r*}] = \operatorname{Re}[-j|B_x^r|^2] = 0 \quad (2.96)$$

$$\operatorname{Re}[B_x^s B_y^{s*}] = \operatorname{Re}[B_x^{s*} B_y^s] \quad (2.97)$$

allows the conjugate terms in the thrust equation to be only applied on the source

$$F_x^{ss} = \frac{w}{4\pi\mu_0} \operatorname{Re} \int_{-\infty}^{\infty} [B_x^r B_y^{s*} + B_x^{s*} B_y^r + B_x^s B_y^{s*}] d\xi \quad (2.98)$$

Again substituting (2.83) into (2.98) gives

$$F_x^{ss} = \frac{w}{4\pi\mu_0} \operatorname{Re} \int_{-\infty}^{\infty} [B_y^r (B_x^{s*} - jB_y^{s*}) + B_x^s B_y^{s*}] d\xi \quad (2.99)$$

Substituting (2.82) into (2.99) gives

$$F_x^{ss} = \frac{w}{4\pi\mu_0} \operatorname{Re} \int_{-\infty}^{\infty} [-[B_y^s + j\xi T^{ss}(\xi, b) B^s] (B_x^{s*} - jB_y^{s*}) + B_x^s B_y^{s*}] d\xi \quad (2.100)$$

Noting the fact that

$$\operatorname{Re}[jB_y^s B_y^{s*}] = 0 \quad (2.101)$$

$$\operatorname{Re}[B_x^s B_y^{s*}] = \operatorname{Re}[B_x^{s*} B_y^s] \quad (2.102)$$

enables (2.100) to reduce down to

$$F_x^{ss} = \frac{w}{4\pi\mu_0} \operatorname{Re} \int_{-\infty}^{\infty} -(j\xi T^{ss}(\xi, b) B^s) (B_x^{s*} - jB_y^{s*}) d\xi \quad (2.103)$$

where $B^{s*} = (B_x^{s*} - jB_y^{s*})$ is the complex conjugate of B^s . Therefore, the tangential force in terms of transmission function and the source magnetic flux density is

$$F_x^{ss} = \frac{w}{4\pi\mu_0} \operatorname{Re} \int_{-\infty}^{\infty} -j\xi T^{ss}(\xi, b) |B^s|^2 d\xi \quad (2.104)$$

The force equation in terms of vector potential is

$$F_x^{ss} = \frac{w}{4\pi\mu_0} \operatorname{Re} \int_{-\infty}^{\infty} -j\xi A_z^{ss}(\xi, b) B^{s*} d\xi \quad (2.105)$$

The lift force can also be written in terms of the reflected and source field by substituting (2.85) and (2.86) into (2.93) and rearranging gives

$$F_y^{ss} = \frac{w}{8\pi\mu_0} \operatorname{Re} \int_{-\infty}^{\infty} [B_y^{s*} B_y^r + B_y^{r*} B_y^s - B_x^{s*} B_x^r - B_x^{r*} B_x^s + |B_y^s|^2 + |B_y^r|^2 - |B_x^s|^2 - |B_x^r|^2] d\xi \quad (2.106)$$

Using the relation (2.83) it can be noted that

$$\operatorname{Re}[|B_y^r|^2] = \operatorname{Re}[|B_x^r|^2] \quad (2.107)$$

and also

$$\operatorname{Re}[B_y^{s*} B_y^r] = \operatorname{Re}[B_y^s B_y^{r*}] \quad (2.108)$$

$$\operatorname{Re}[B_x^{s*} B_x^r] = \operatorname{Re}[B_x^s B_x^{r*}] \quad (2.109)$$

these three relations allow the normal force to be written as

$$F_y^{ss} = \frac{w}{8\pi\mu_0} \operatorname{Re} \int_{-\infty}^{\infty} [2(B_y^{s*} B_y^r - B_x^r B_x^{s*}) + |B_y^s|^2 - |B_x^s|^2] d\xi \quad (2.110)$$

where the conjugate is only applied to the source field terms. Again substituting (2.83) into (2.110) gives

$$F_y^{ss} = \frac{w}{8\pi\mu_0} \operatorname{Re} \int_{-\infty}^{\infty} [-2B_x^r (B_x^{s*} - jB_y^{s*}) + |B_y^s|^2 - |B_x^s|^2] d\xi \quad (2.111)$$

Substituting (2.81) into (2.111) the steady-state normal force is

$$F_y^{ss} = \frac{w}{8\pi\mu_0} \operatorname{Re} \int_{-\infty}^{\infty} [2\xi T^{ss}(\xi, b) |B^s|^2 - 2jB_y^s B_y^{s*} - j2B_y^s B_x^{s*} - |B_y^s|^2 - |B_x^s|^2] d\xi \quad (2.112)$$

Since

$$\operatorname{Re}[(B_x^s + jB_y^s)(B_x^s + jB_y^s)^*] = |B_y^s|^2 + |B_x^s|^2 + j2B_y^s B_x^{s*} = |B^s|^2 \quad (2.113)$$

$$\operatorname{Re}[jB_y^s B_y^{s*}] = \operatorname{Re}[j|B_y^s|^2] = 0 \quad (2.114)$$

the normal force can be written in terms of the transmission function as

$$F_y^{ss} = \frac{w}{8\pi\mu_0} \operatorname{Re} \int_{-\infty}^{\infty} (2\xi T^{ss}(\xi, b) - 1) |B^s|^2 d\xi \quad (2.115)$$

From (2.104) and (2.115), it can be concluded that the normal and tangential forces can be obtained by evaluating the real part and imaginary part respectively using a single equation.

$$F_y^{ss} = \frac{w}{8\pi\mu_0} \operatorname{Re} \int_{-\infty}^{\infty} (2\xi T^{ss}(\xi, b) - 1) |B^s(\xi, b)|^2 d\xi \quad (2.116)$$

$$F_x^{ss} = -\frac{w}{8\pi\mu_0} \operatorname{Im} \int_{-\infty}^{\infty} (2\xi T^{ss}(\xi, b) - 1) |B^s(\xi, b)|^2 d\xi \quad (2.117)$$

This eliminates the need of evaluating two separate equations for the lift and thrust force and thus reduces the computational time by half.

The integral term $(2\xi T^{ss}(\xi, b) - 1)$ can be simplified further and can be written as

$$2\xi T^{ss}(\xi, b) - 1 = \frac{-\mu_0\sigma(s_0 + \xi v_y)(e^{\alpha b} - e^{-\alpha b})}{(e^{\alpha b} - e^{-\alpha b})(2\xi^2 + \mu_0\sigma s_0) + 2\alpha\xi(e^{\alpha b} + e^{-\alpha b})} \quad (2.118)$$

Further simplifying (2.118) one can obtain

$$2\xi T^{ss}(\xi, b) - 1 = \frac{-\mu_0\sigma[s_o + \xi v_y]}{2\xi^2 + \mu_0\sigma s_o + 2\alpha\xi \coth(\alpha b)} \quad (2.119)$$

where

$$\alpha = \sqrt{\lambda^2 + \gamma^2} \quad (2.120)$$

$$s_o = j(\omega_{eo} + \xi v_{xo}) \quad (2.121)$$

and the variables v_{xo} and ω_{eo} are the steady-state velocity and the angular velocity respectively.

2.3.9.2 Lorentz Force Calculation

The tangential and normal forces can also be evaluated by using the Lorentz formula [146, 153]. The force density is defined by

$$\mathbf{F} = \mathbf{J} \times \mathbf{B} \quad (2.122)$$

where \mathbf{J} is defined in (2.5) and is re-written here for convenience

$$\mathbf{J} = \sigma(\mathbf{E} + \mathbf{v} \times \mathbf{B}) \quad (2.123)$$

In this 2-D formulation the current has only a z -component. The electric field intensity, E_z is given by (2.87) and noting that

$$\mathbf{v} \times \mathbf{B} = \begin{vmatrix} \hat{x} & \hat{y} & \hat{z} \\ v_x & v_y & 0 \\ B_x & B_y & 0 \end{vmatrix} = \hat{z}(v_x B_y - v_y B_x) \quad (2.124)$$

allows the z -component of the steady-state current density, J_z^{ss} , in region Ω_2 to be expressed as

$$J_z^{ss} = \sigma[v_x B_y^{ss}(\xi, y) - v_y B_x^{ss}(\xi, y) - E_z^{ss}(\xi, y)] \quad (2.125)$$

Now substituting (2.85), (2.78) and (2.79) into (2.121) one can obtain the current density in terms of vector potential as

$$J_z^{ss} = \sigma \left(-j\xi v_x A_z^{ss}(\xi, y) - v_y \frac{\partial A_z^{ss}(\xi, y)}{\partial y} - j\omega_e A_z^{ss}(\xi, y) \right) \quad (2.126)$$

Simplifying (2.126), current density becomes

$$J_z^{ss} = -\sigma \left(j(\xi v_x + \omega_e) A_z^{ss}(\xi, y) + v_y \frac{\partial A_z^{ss}(\xi, y)}{\partial y} \right) \quad (2.127)$$

Utilizing Parseval's theorem, the Lorentz force can be evaluated directly in Fourier domain and be written as

$$F_x^{ss} = -\frac{w}{4\pi} \int_{-\infty}^{\infty} \int_0^b \text{Re}[J_z^{ss} \cdot B_y^{ss*}] dy d\xi \quad (2.128)$$

$$F_y^{ss} = \frac{w}{4\pi} \int_{-\infty}^{\infty} \int_0^b \text{Re}[J_x^{ss} \cdot B_x^{ss*}] dy d\xi \quad (2.129)$$

The integration of these Lorentz force equations can be evaluated numerically in Matlab using the '*quad2d*' function.

2.3.9.3 Force Calculation Using Magnetic Charge

The thrust and lift forces can also be calculated using the magnetic charge model. The magnetic field due to the Halbach rotor can be modeled using a magnetic charge sheet. If the magnetic charge is distributed on a planar sheet at $y = b$ then the charge can be used to represent the source field. In this case the magnetic charge can be

defined in terms of magnetic flux density of the Halbach rotor by [154]

$$\rho_{ms}(x, b) = \frac{2}{\mu_0} B_y^s(x, b) \quad (2.130)$$

An expression of the force in terms of the magnetic charge can be written as [155]

$$\mathbf{F} = \frac{1}{2} \operatorname{Re} \int_{-\infty}^{\infty} \rho_{ms}(\mathbf{B}^r)^* dx \quad \text{on } \Gamma_{12} \quad (2.131)$$

Therefore, the force components are given by

$$F_x = \frac{1}{2} \operatorname{Re} \int_{-\infty}^{\infty} \rho_{ms}(B_x^r)^* dx \quad \text{on } \Gamma_{12} \quad (2.132)$$

$$F_y = \frac{1}{2} \operatorname{Re} \int_{-\infty}^{\infty} \rho_{ms}(B_y^r)^* dx \quad \text{on } \Gamma_{12} \quad (2.133)$$

The forces can be directly calculated in Fourier domain by using the Parseval's theorem. Substituting (2.130) into (2.132) and (2.133) and using Parseval's theorem, the force equations in Fourier domain are

$$F_x = \frac{1}{2\pi\mu_0} \operatorname{Re} \int_{-\infty}^{\infty} B_y^s(\xi, b)(B_x^r)^* d\xi \quad \text{on } \Gamma_{12} \quad (2.134)$$

$$F_y = \frac{1}{2\pi\mu_0} \operatorname{Re} \int_{-\infty}^{\infty} B_y^s(\xi, b)(B_y^r)^* d\xi \quad \text{on } \Gamma_{12} \quad (2.135)$$

Using the relation (2.83), the thrust forces can also be evaluated from the same integral by

$$F_x = \frac{1}{2\pi\mu_0} \operatorname{Im} \int_{-\infty}^{\infty} B_y^s(\xi, b)(B_y^r)^* d\xi \quad \text{on } \Gamma_{12} \quad (2.136)$$

2.3.10 Power Loss Calculation

In steady-state analysis the power loss within the guideway can be evaluated by using the Poynting vector [146]. In 2-D the average flow of power per-unit area through the top surface, Γ_{12} , of the guideway is given by

$$\mathbf{S} = \frac{1}{2} \mathbf{E} \times \mathbf{H}^* = \frac{1}{2\mu_0} \mathbf{E} \times \mathbf{B}^* = \frac{1}{2\mu_0} E_z^{ss} B_x^{ss*} \hat{y} \quad (2.137)$$

where \hat{y} is the unit vector in y -direction. The real power per-unit width transferred through Γ_{12} can be directly determined using Parseval's theorem. Therefore, substituting (2.87) into (2.137) and integrating along Γ_{12} one obtains

$$P_{Transferred} = \frac{1}{4\pi\mu_0} \operatorname{Re} \int_{-\infty}^{\infty} j\omega_e A_z^{ss}(\xi, b) B_x^{ss*}(\xi, b) d\xi \quad (2.138)$$

Taking the conjugate on both side of (2.86) and using (2.81), $B_x^{ss*}(\xi, b)$ can be expressed in terms of the source and reflected field as

$$B_x^{ss*}(\xi, b) = B_x^{s*}(\xi, b) + [jB_y^s(\xi, b) - \xi T^{ss}(\xi, b) B^s(\xi, b)]^* \quad (2.139)$$

Noting that

$$B_x^{s*}(\xi, b) = (B_x^s(\xi, b) - jB_y^s(\xi, b)) \quad (2.140)$$

(2.139) can be simplified to

$$B_x^{ss*}(\xi, b) = B_x^s(\xi, b) [1 - \xi T^{ss*}(\xi, b)] \quad (2.141)$$

Substituting (2.141) and (2.74) into (2.138) the power transfer can be written in terms of the transmission function and source field as

$$P_{Transferred} = \frac{1}{4\pi\mu_0} \operatorname{Re} \int_{-\infty}^{\infty} j\omega_e T^{ss}(\xi, b) B^s(\xi, b) [B^{s*}(\xi, b)(1 - \xi T^{sss}(\xi, b))] d\xi \quad (2.142)$$

Simplifying (2.142) one obtain

$$P_{Transferred} = \frac{1}{4\pi\mu_0} \operatorname{Re} \int_{-\infty}^{\infty} [j\omega_e T^{ss}(\xi, b) |B^s(\xi, b)|^2 - j\omega_e \xi |T^{sss}(\xi, b)|^2 |B^s(\xi, b)|^2] d\xi \quad (2.143)$$

Noting the fact that the second term of (2.143) is zero one obtain

$$P_{Transferred} = \frac{1}{4\pi\mu_0} \operatorname{Re} \int_{-\infty}^{\infty} j\omega_e T^{ss}(\xi, b) |B^s(\xi, b)|^2 d\xi \quad (2.144)$$

Consequently, the power loss per-unit width in the conductive region is

$$P_{Loss} = P_{Transferred} - F_x^{ss} v_x \quad (2.145)$$

Substituting the equation for the thrust force from (2.104) and (2.144) into (2.145) one obtain the power loss in the guideway in terms of transmission function and the source magnetic flux density as

$$P_{Loss} = \frac{1}{4\pi\mu_0} \operatorname{Re} \int_{-\infty}^{\infty} j(\omega_e + \xi v_x) T^{ss}(\xi, b) |B^s(\xi, b)|^2 d\xi \quad (2.146)$$

The power loss in terms of the vector potential will be

$$P_{Loss} = \frac{1}{4\pi\mu_0} \operatorname{Re} \int_{-\infty}^{\infty} j(\omega_e + \xi v_x) A_z^{ss}(\xi, b) B^{s*}(\xi, b) d\xi \quad (2.147)$$

In 2-D, the power loss can also be calculated using the surface integration (volume integration in 3D) over the region Ω_2 as

$$P_{Loss} = \frac{\sigma}{2} \iint_{\Omega_2} |J_z^{ss}|^2 d\Omega_2 \quad (2.148)$$

where J_z^{ss} is defined in (2.125). The thrust efficiency due to the force produced in the guideway can be calculated by using [3]

$$\eta_{Thrust} = \frac{F_x^{ss} v_x}{F_x^{ss} v_x + P_{Loss}} = \frac{F_x^{ss} v_x}{P_{Transferred}} \quad (2.149)$$

Alternatively, the thrust efficiency can be calculated in terms of the rotor torque as [110]

$$\eta_{Thrust} = \frac{F_x^{ss} v_x}{\tau \omega_m} \quad (2.150)$$

where ω_m is the rotor mechanical angular velocity and τ is the rotor torque given by

$$\tau = \frac{F_x^{ss} v_x + P_{Loss}}{\omega_m} = \frac{P_{Transferred}}{\omega_m} \quad (2.151)$$

Since the electrical angular velocity, ω_e , and mechanical angular velocity, ω_m , are related by

$$\omega_e = \omega_m P \quad (2.152)$$

where P is the number of pole-pairs, the final expression for the torque can be obtained by substituting (2.144) and (2.152) into (2.151)

$$\tau = \frac{P}{4\pi\mu_0} \operatorname{Re} \int_{-\infty}^{\infty} jT^{ss}(\xi, b) |B^s(\xi, b)|^2 d\xi \quad (2.153)$$

2.3.11 Halbach Rotor Source Field

The steady-state force and power loss equations were verified by comparing them with an FEA model in which a Halbach rotor such as shown in Figure 2.1 is both moved and rotated over a conductive guideway. In the analytic and FEA model the magnet eddy-current losses are neglected, however since the rotor magnets are highly segmented, the eddy-current loss within the magnets is relatively low [156, 157]. For such a problem where the source is moving and/or rotating at the same time the normal and tangential forces are dependent on a slip speed, s_l , defined as

$$s_l = \omega_m r_o - v_x \quad \text{ms}^{-1} \quad (2.154)$$

where r_o is the rotor outer radius. The 2-D analytical model for calculating the magnetic field distribution due to an air-cored Halbach rotor has been derived by Xia et al. [158]. The formulation was developed using the polar coordinate system and accounts for the relative permeability of the magnets. The equations for the magnetic flux densities are

$$B_r(r, \theta) = \frac{-\frac{2B_r^m P}{P+1}(1 + \mu_r) \left[1 - \left(\frac{r_i}{r_o} \right)^{P+1} \right] \left(\frac{r_o}{r} \right)^{P+1}}{(1 - \mu_r)^2 \left(\frac{r_i}{r_o} \right)^{2P} - (1 + \mu_r)^2} \sin(P\theta) \quad (2.155)$$

$$B_\theta(r, \theta) = \frac{\frac{2B_r^m P}{P+1}(1 + \mu_r) \left[1 - \left(\frac{r_i}{r_o} \right)^{P+1} \right] \left(\frac{r_o}{r} \right)^{P+1}}{(1 - \mu_r)^2 \left(\frac{r_i}{r_o} \right)^{2P} - (1 + \mu_r)^2} \cos(P\theta) \quad (2.156)$$

where

B_r^m = remanence of the magnet

r_i = inner rotor radius

μ_r = relative permeability of the magnet.

Defining

$$C = \left(\frac{2B_r^m P}{P+1} \right) \frac{(1 + \mu_r)r_o^{2P}(r_o^{P+1} - r_i^{P+1})}{(1 - \mu_r)^2 r_i^{2P} - (1 + \mu_r)^2 r_o^{2P}} \quad (2.157)$$

the source magnetic flux densities equations (2.155) and (2.156) becomes

$$B_r(r, \theta) = -\frac{C}{r^{P+1}} \sin(P\theta) \quad (2.158)$$

$$B_\theta(r, \theta) = \frac{C}{r^{P+1}} \cos(P\theta). \quad (2.159)$$

Noting that the relation between the magnetic flux density and vector potential in the polar coordinate system is given by

$$B_r(r, \theta) = \frac{1}{r} \frac{\partial A_z^s}{\partial \theta} \quad (2.160)$$

$$B_\theta(r, \theta) = -\frac{\partial A_z^s}{\partial r}. \quad (2.161)$$

The vector potential field exterior to the Halbach rotor source can be determined by using (2.158) and (2.160) as

$$A_z^s(r, \theta) = \frac{C \cos(P\theta)}{P r^P}. \quad (2.162)$$

Since the eddy current formulation is steady-state based, the rotor field must be complex in order to impart the rotational source field information onto the conductor. In order to achieve this the Halbach rotor field's angular information is made complex

$$A_z^s(r, \theta) = \frac{C}{P} \frac{e^{jP\theta}}{r^P}. \quad (2.163)$$

The expression of the vector potential (2.163) is analogous to using a complex current sheet [115]. Since the relative permeability of the magnet is included in (2.163), the field model is more accurate than using a current sheet [41, 115]. The magnetic vector

potential source field can be directly converted into Cartesian coordinates by utilizing the complex analysis relation

$$\frac{e^{jP\theta}}{r^P} = \frac{1}{(x - jy)^P}. \quad (2.164)$$

Utilizing (2.164) the Cartesian magnetic flux density source field components are then

$$B_y^s(x, y) = -\frac{\partial A_z}{\partial x} = \frac{C}{(x - jy)^{P+1}} \quad (2.165)$$

$$B_x^s(x, y) = \frac{\partial A_z}{\partial y} = \frac{jC}{(x - jy)^{P+1}}. \quad (2.166)$$

The magnetic flux density in (2.165) and (2.166) are developed for the coordinate system with the origin being at the center of the rotor. However, the coordinate system in the 2-D analytic formulation has the origin at the bottom of the guideway as shown in Figure 2.4. Therefore, a coordinate offset is required for the y -axis in order to express the magnetic flux density in the guideway coordinate system. Referring to Figure 2.4 it can be seen that the y -axis offset needs to be

$$y_o = r_o + g + b \quad (2.167)$$

where

g = the air-gap distance between the rotor and conducting guideway

b = the thickness of the guideway.

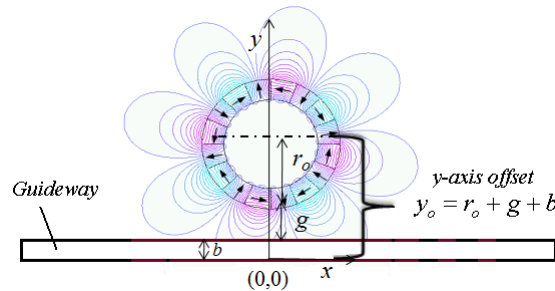


Figure 2.4: *Halbach rotor source fields with y -axis offset.*

The flux densities of the Halbach rotor can now be written as

$$B_y^s(x, y) = \frac{C}{(x - j(y - y_o))^{P+1}} \quad (2.168)$$

$$B_x^s(x, y) = jB_y^s(x, y) \quad (2.169)$$

and the total source field, $B^s(x, y)$ is given by

$$B^s(x, y) = B_x^s(x, y) + jB_y^s(x, y) = \frac{j2C}{(x - j(y - y_o))^{P+1}}. \quad (2.170)$$

2.3.11.1 The Fourier Transform for the Rotor Source Field

Since the 2-D formulation is using the Fourier transform and the source field needs to be included only at the boundary of the guideway, $y = b$, the flux densities of the Halbach rotor source field given by (2.168) and (2.169) must be evaluated at $y = b$. The Fourier transformed for the x -component of the source field is [150]

$$B_x^s(\xi, b) = \int_{-\infty}^{\infty} B_x^s(x, b) e^{-j\xi x} dx. \quad (2.171)$$

Substituting (2.168) into (2.171), one obtains

$$B_x^s(\xi, b) = \int_{-\infty}^{\infty} \left(\frac{jC}{(x - j(-r_o - g))^{P+1}} \right) e^{-j\xi x} dx. \quad (2.172)$$

Evaluating (2.172) by using the Fourier transform table given in [150] yields

$$B_x^s(\xi, b) = (-j)^P \frac{2}{P!} C \pi \xi^P e^{-\xi(g+r_o)} \mathbf{u}(\xi) \quad (2.173)$$

Similarly, the y -component of a Fourier transformed source magnetic flux density is

$$B_y^s(\xi, b) = (-j)^{P+1} \frac{2}{P!} C \pi \xi^P e^{-\xi(g+r_o)} \mathbf{u}(\xi). \quad (2.174)$$

where $u(\xi)$ is the unit step function [149]. The relation (2.169) is also true in the Fourier domain as seen from (2.173) and (2.174). The total source field in the Fourier domain is therefore

$$B^s(\xi, b) = B_x^s(\xi, b) + jB_y^s(\xi, b) = [(-j)^P + j(-j)^{P+1}] \frac{2}{P!} C \pi \xi^P e^{-\xi(g+r_o)} u(\xi). \quad (2.175)$$

The absolute value of the total source field is therefore

$$|B^s(\xi, b)|^2 = |(-j)^P + j(-j)^{P+1}|^2 \left(\frac{2}{P!}\right)^2 \pi^2 C^2 \xi^{2P} e^{-2\xi(g+r_o)} u(\xi). \quad (2.176)$$

Noting that

$$|(-j)^P + j(-j)^{P+1}|^2 = |2(-j)^P|^2 = 4 \quad (2.177)$$

the source field (2.176) can be written as

$$|B^s(\xi, b)|^2 = \left(\frac{4}{P!}\right)^2 \pi^2 C^2 \xi^{2P} e^{-2\xi(g+r_o)} u(\xi). \quad (2.178)$$

2.3.12 Analytic Based Simulation Results and FEA Validations

An analytic eddy-current simulation was performed using a four pole-pair Halbach rotor as a source. With $P = 4$ in (2.178) becomes

$$|B^s(\xi, b)|^2 = \frac{\pi^2}{36} C^2 \xi^8 e^{-2\xi(g+r_o)} u(\xi) \quad (2.179)$$

The power loss and lift and thrust/braking forces have been calculated using (2.147), (2.116) and (2.117) respectively. The power loss and forces equations were evaluated by numerical integration using the Gauss-Kronrod quadrature [159] algorithm in Matlab. The simulation parameters are given in Table 2.1. A 2-D FEA model developed by J. Bird [114] was modified to incorporate the heave velocity, v_y , in the guideway. This model was also modified by replacing the current sheet with the magnetic source

given by (2.162). The analytical forces and the power loss equations were validated by comparing the results with the modified 2-D FEA model. A per-unit width force vs slip comparison at $v_y = 0\text{ms}^{-1}$ for different translational velocities is shown in Figure 2.5 and Figure 2.6 and per-unit width power loss vs slip at $v_y = 0\text{ms}^{-1}$ comparison for different translational velocities is shown in Figure 2.7. The error (in percentage) in force calculations between analytical and FEA based model is shown in Figure 2.8. The error is less than 1%.

Table 2.1: *Simulation parameters for 2-D steady-state model.*

Halbach Rotor	Outer radius, r_o	70 mm
	Inner radius, r_i	47.88 mm
	Width of rotor, w	1 m
	Magnet (NdFeB), B_r	1.42 T
	Magnet relative permeability, μ_r	1.08
	Pole-pairs, P	4
Conductive guideway	Guideway length ($\pm L$)	0.8 m
	Thickness, b	10 mm
	Guideway width	100 mm
	Air-gap between rotor and guideway, (g)	10 mm
	Conductivity, σ (Al)	$2.459 \times 10^7 \text{ Sm}^{-1}$

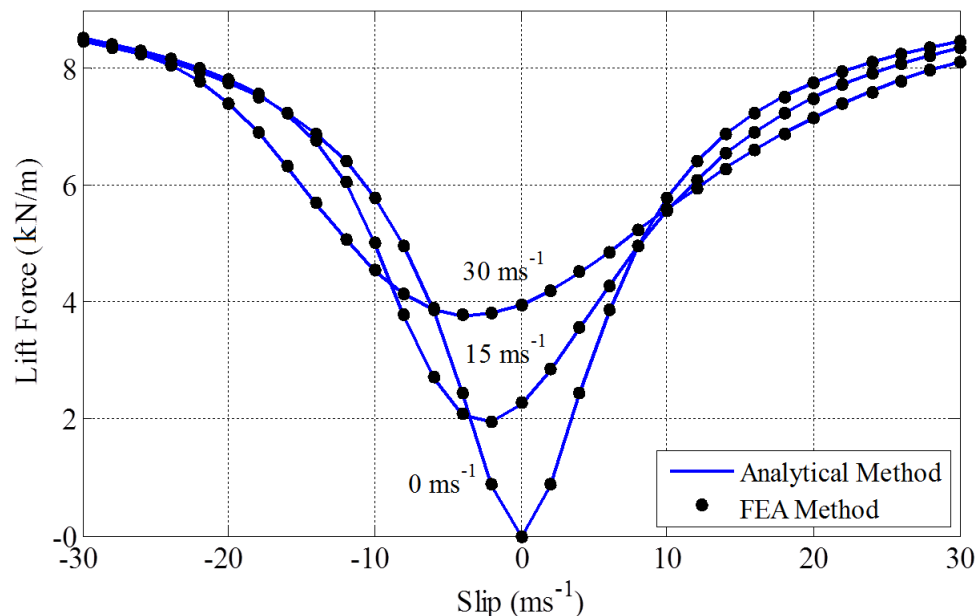


Figure 2.5: *Lift (normal) force as a function of slip and translational velocity at $v_y = 0\text{ms}^{-1}$.*

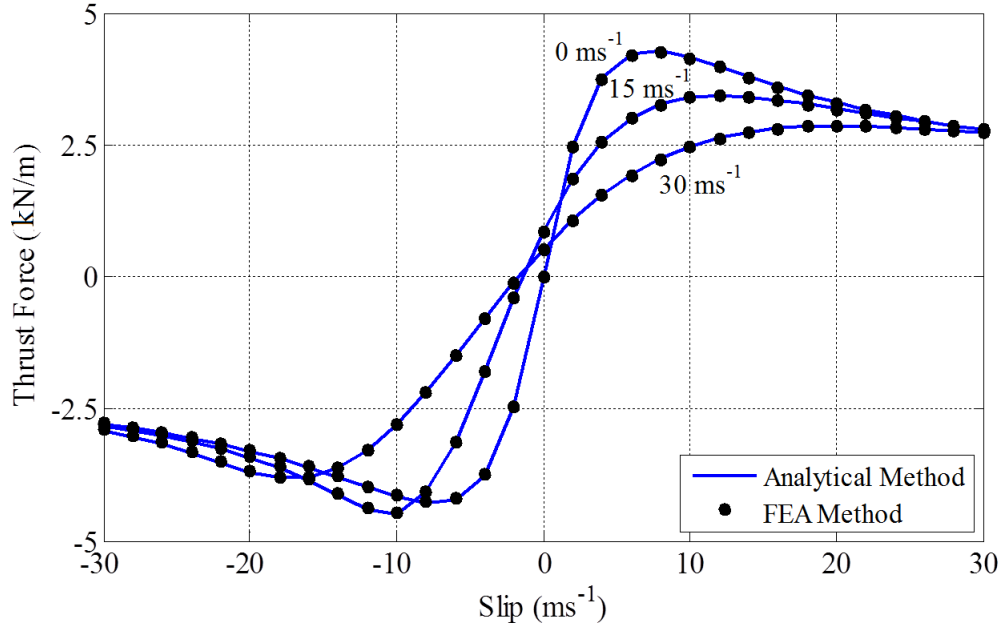


Figure 2.6: Thrust (tangential) force as a function of slip and translational velocity at $v_y = 0 \text{ ms}^{-1}$.

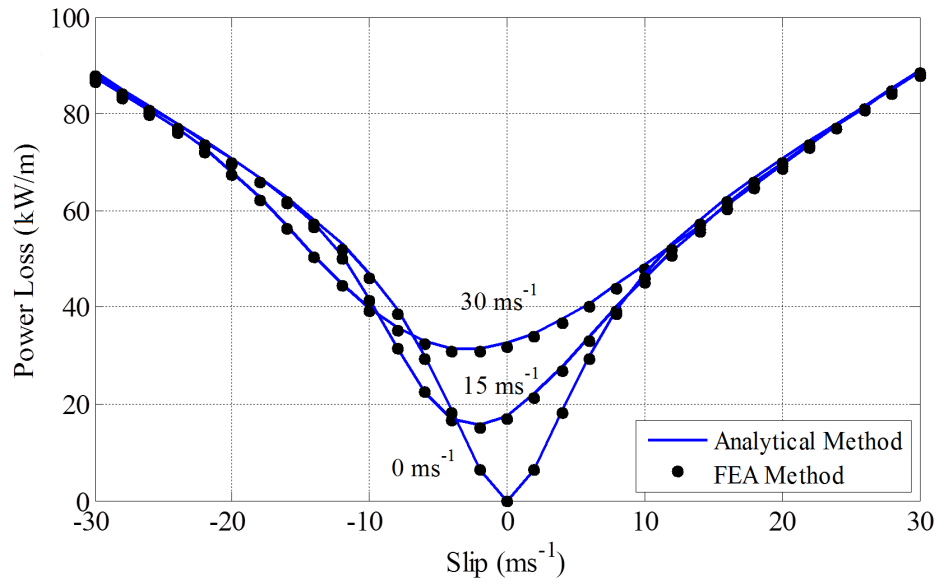


Figure 2.7: Power loss in the conducting guideway as a function of slip and translational velocity at $v_y = 0 \text{ ms}^{-1}$.

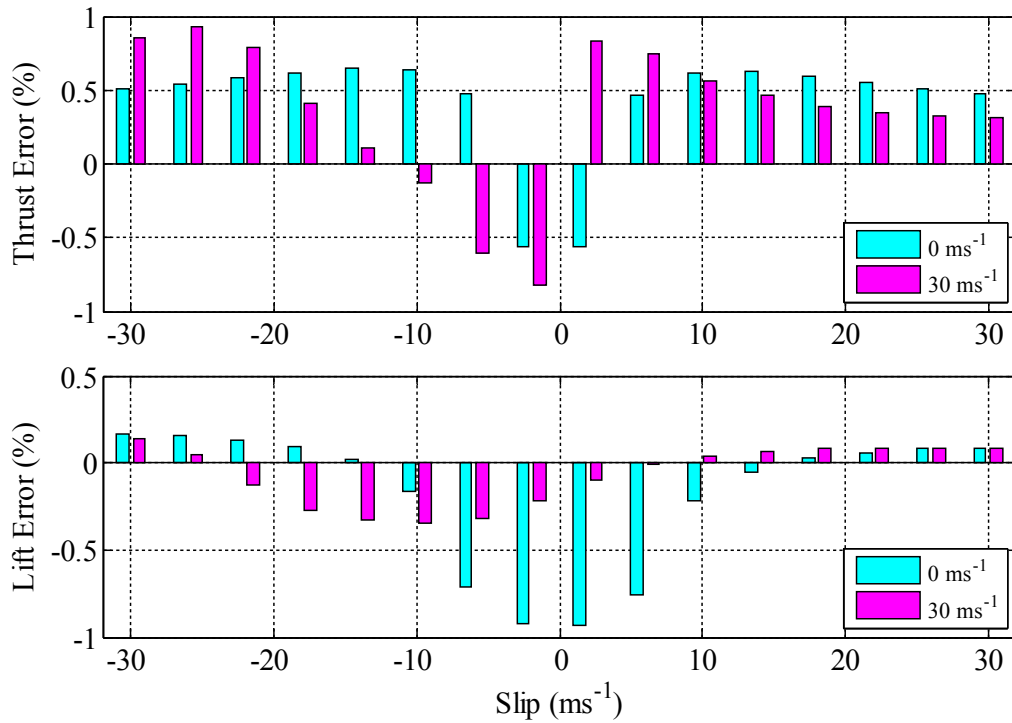


Figure 2.8: *The lift and thrust force percentage error between the FEA and analytical model as a function of slip for translational velocity, $v_x = 0\text{ms}^{-1}$ and 30ms^{-1} at $v_y = 0\text{ms}^{-1}$.*

A per-unit width lift force vs slip comparison at $v_x = 0\text{ms}^{-1}$ for different rotor heave velocities is shown in Figure 2.9. While Figure 2.10 illustrates the corresponding thrust force comparison. These results show that when the rotor is vertically moving away from the guideway, the lift force as well as thrust force decrease and vice-versa. Using a Dell T7400 computer the average force calculation time at one operating point using FEA was 5.22s while using this analytic based approach the calculation time was reduced to just 1.9ms.

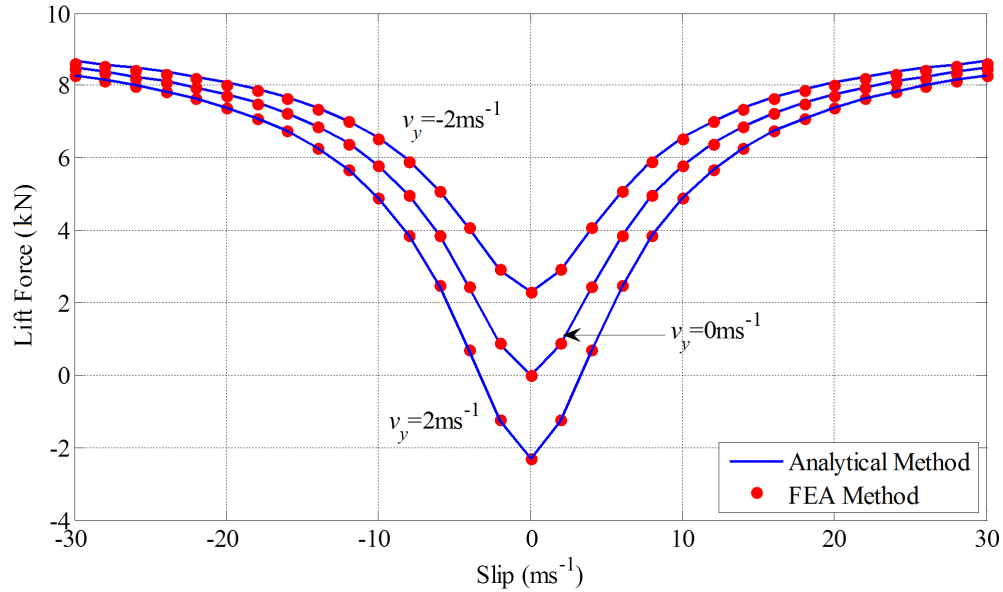


Figure 2.9: *Lift (normal) force in the conducting guideway as a function of slip and rotor heave velocity, v_y at translational velocity, $v_x = 0\text{ms}^{-1}$.*

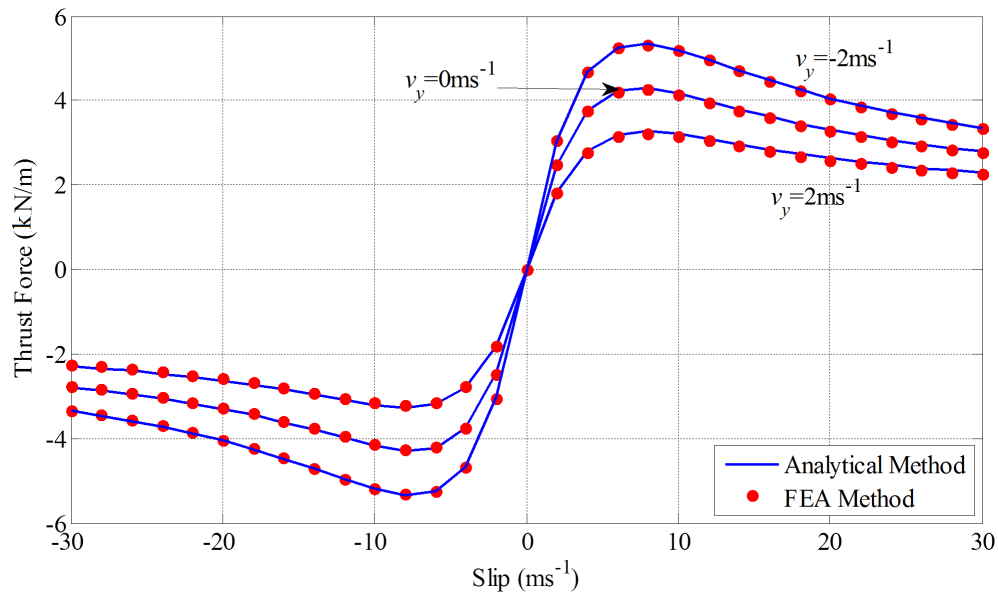


Figure 2.10: *Thrust (tangential) force in the conducting guideway as a function of slip and rotor heave velocity, v_y at translational speed, $v_x = 0\text{ms}^{-1}$.*

The 2-D FEA model presented in [114] was created in COMSOL (ver. 3.5) and solved using the linear stationary solver. The mesh had 154670 triangular elements and 273729 degrees of freedom. The FEA force calculation method used Maxwell's stress tensor method, evaluated along the surface of the guideway, and the FEA

calculated per-unit width power loss was computed using (2.148). The COMSOL FEA model showing a surface plot of the vector potential in the guideway and the contour plot of an x component of the magnetic flux density, B_x , in the non-conducting region is illustrated in Figure 2.11. An excellent agreement between the FEA and the analytical model has been obtained.

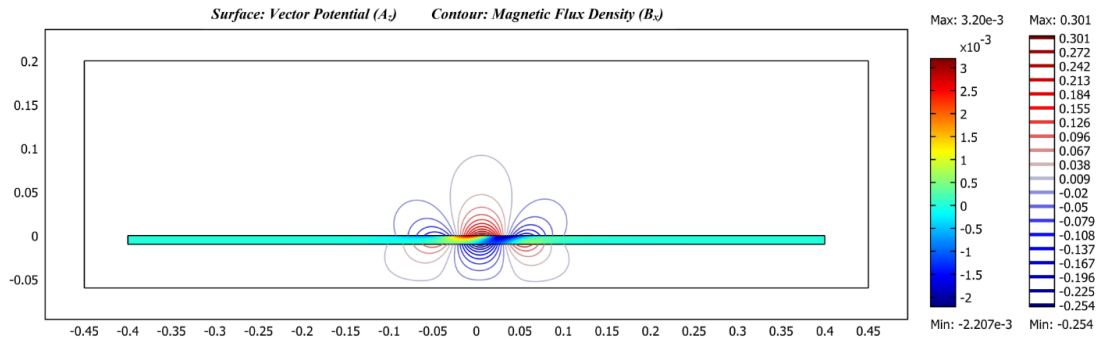


Figure 2.11: A COMSOL FEA result showing the surface plot of A_z in guideway and the contour plot of B_x in non-conducting region for $v_x = 20\text{ms}^{-1}$, $\text{slip} = 30\text{ms}^{-1}$ and $v_y = 0\text{ms}^{-1}$.

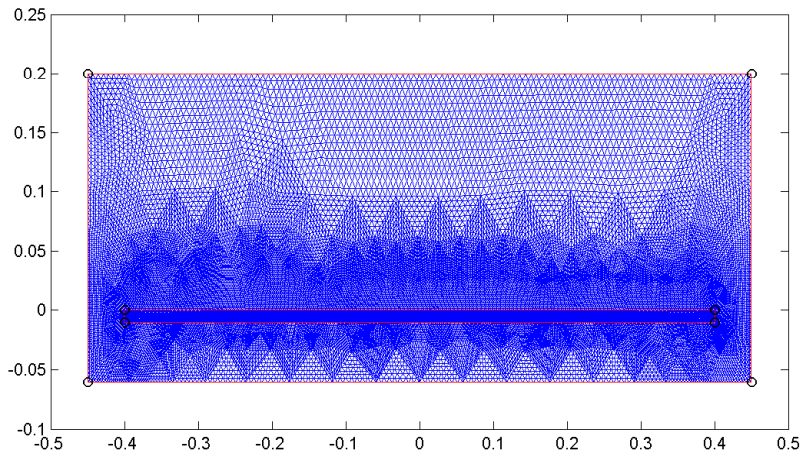


Figure 2.12: A mesh plot of a 2-D steady-state FEA model developed in COMSOL.

2.3.13 Electrodynamic Wheels in Series

The source field due to a single EDW Halbach rotor is derived in section 2.3.11 and validated in section 2.3.12. Using the spatial Fourier transform technique, the source field of the number of EDW Halbach rotors in series as shown in Figure 2.13 can be

derived. It has been found that when the EDWs are placed close to one another in series, the current induced by the first EDW can be utilized by the second, third and so on and therefore the Maglev vehicle needs less energy to create the same force [41]. The effect of EDW's in series has been investigated by Bird using the FEA model developed in COMSOL using a current sheet approach as shown in Figure 2.14. This model was later used by D. Bobba to investigate the effect of using multiple EDWs in series for possible application to a low-speed Maglev [160]. The analytical equations for the multiple EDW in series will be very fast and can be used for the optimization and investigation for both low and high-speed Maglev application.

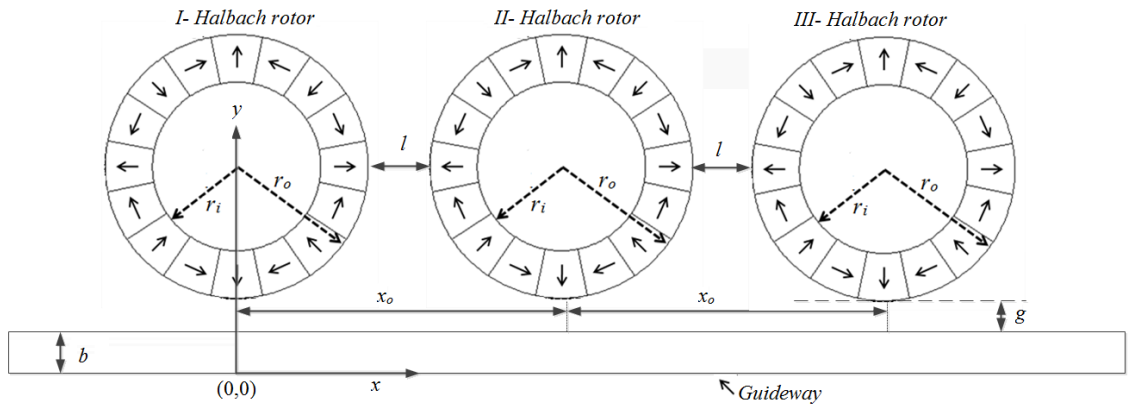


Figure 2.13: Multiple EDWs in series above a conductive guideway.

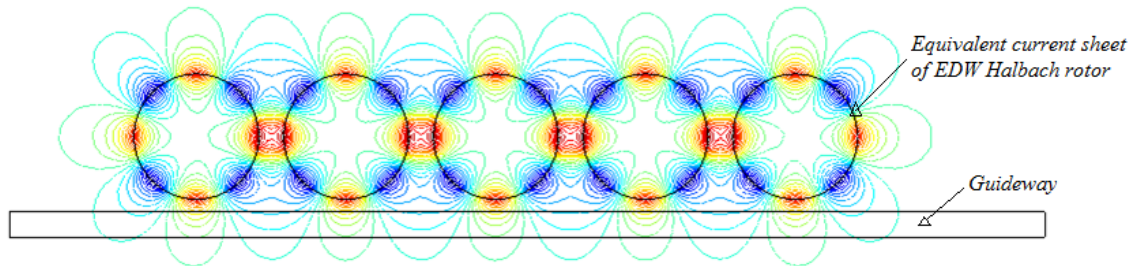


Figure 2.14: The vector potential contour plot for five EDWs in series using the steady-state FEA model developed in COMSOL [41].

From section 2.3.11, the flux densities of the first Halbach rotor can now be written as

$$B_y^I(x, y) = \frac{C}{(x - j(y - y_o))^{P+1}} \quad (2.180)$$

$$B_x^I(x, y) = jB_y^I(x, y) \quad (2.181)$$

If there are n Halbach rotors in series separated by the distance of x_o (center to center) in x direction, the field due to the corresponding Halbach rotors will be shifted by the x_o as given by

$$B_y^{II}(x, y) = \frac{C}{(x - x_o - j(y - y_o))^{P+1}} \quad (2.182)$$

$$B_y^{III}(x, y) = \frac{C}{(x - 2x_o - j(y - y_o))^{P+1}} \quad (2.183)$$

$$B_x^{II}(x, y) = jB_y^{II}(x, y) \quad (2.184)$$

$$B_x^{III}(x, y) = jB_y^{III}(x, y) \quad (2.185)$$

The Halbach rotor's field along the surface of the conducting plate can thus be obtained by setting $y = b$.

2.3.13.1 The Fourier Transform of the EDWs in Series

Fourier transform source field for the first Halbach rotor is obtained by using the Fourier transform given in [150]. Therefore, (2.180) and (2.181) when evaluated at $y = b$ becomes

$$B_y^I(\xi, b) = (-j)^{P+1} \frac{2}{P!} C \pi \xi^P e^{-\xi(g+r_o)} u(\xi) \quad (2.186)$$

$$B_x^I(\xi, b) = (-j)^P \frac{2}{P!} C \pi \xi^P e^{-\xi(g+r_o)} u(\xi) \quad (2.187)$$

Similarly, the Fourier transform fields due to the second and third Halbach rotor is given by

$$B_y^{II}(\xi, b) = (-j)^{P+1} \frac{2}{P!} C \pi \xi^P e^{-\xi(g+r_o)} e^{-j\xi x_o} u(\xi) \quad (2.188)$$

$$B_x^{II}(\xi, b) = (-j)^P \frac{2}{P!} C \pi \xi^P e^{-\xi(g+r_o)} e^{-j\xi x_o} u(\xi) \quad (2.189)$$

$$B_y^{III}(\xi, b) = (-j)^{P+1} \frac{2}{P!} C \pi \xi^P e^{-\xi(g+r_o)} e^{-j\xi 2x_o} u(\xi) \quad (2.190)$$

$$B_x^{III}(\xi, b) = (-j)^P \frac{2}{P!} C \pi \xi^P e^{-\xi(g+r_o)} e^{-j\xi 2x_o} u(\xi) \quad (2.191)$$

Therefore the total field due to the n number of Halbach rotors separated by a center to center distance of x_o is

$$B_x^s(\xi, b) = B_x^I(\xi, b) + B_x^{II}(\xi, b) + B_x^{III}(\xi, b) + \dots + B_x^n(\xi, b) \quad (2.192)$$

$$B_y^s(\xi, b) = B_y^I(\xi, b) + B_y^{II}(\xi, b) + B_y^{III}(\xi, b) + \dots + B_y^n(\xi, b) \quad (2.193)$$

Substituting the values from (2.186)-(2.191) into (2.192) and (2.193), one obtains

$$B_x^s(\xi, b) = (-j)^P \frac{2}{P!} C \pi \xi^P e^{-\xi(g+r_o)} u(\xi) [1 + e^{-j\xi x_o} + e^{-j\xi 2x_o} + \dots e^{-j\xi(n-1)x_o}] \quad (2.194)$$

$$B_y^s(\xi, b) = (-j)^{P+1} \frac{2}{P!} C \pi \xi^P e^{-\xi(g+r_o)} u(\xi) [1 + e^{-j\xi x_o} + e^{-j\xi 2x_o} + \dots e^{-j\xi(n-1)x_o}] \quad (2.195)$$

Simplifying (2.194) and (2.195), the source field due to n Halbach rotors in series will be

$$B_x^s(\xi, b) = (-j)^P \frac{2}{P!} C \pi \xi^P e^{-\xi(g+r_o)} u(\xi) \sum_{k=0}^{n-1} e^{-j\xi k x_o} \quad (2.196)$$

$$B_y^s(\xi, b) = (-j)^{P+1} \frac{2}{P!} C \pi \xi^P e^{-\xi(g+r_o)} u(\xi) \sum_{k=0}^{n-1} e^{-j\xi k x_o} \quad (2.197)$$

where

$$x_o = 2r_o + l \quad (2.198)$$

and l is the physical gap between the two Halbach rotors.

2.3.13.2 EDWs in Series: FEA and Analytic Comparison

The analytic model with multiple EDW in series has been validated with FEA COMSOL model. The comparison between these two models is based on the parameters as shown in the Table 2.2. The thrust force, lift force, power loss in the guideway and the thrust efficiency comparison between the analytic model and FEA COMSOL model are shown in Figure 2.15 - Figure 2.18. Very good match between FEA and analytic model has been observed. The peak values of the thrust point as well as the

minimum lift point are shifting with the increase in the gap-between the EDWs as observed in Figure 2.15 and Figure 2.16. This EDWs in series model is significantly faster than the FEA model. For one operating point the FEA took about 14.7452s whereas the analytic model took only about 20ms.

Table 2.2: *Simulation parameters for EDWs in series.*

Halbach Rotor	Outer radius, r_o	50 mm
	Inner radius, r_i	34.2 mm
	Width of rotor, w	50 mm
	Magnet (NdFeB), B_r	1.42 T
	Number of rotors, n	5
	Pole-pairs, P	4
	Translational velocity, v_x	140 ms^{-1}
Conductive guideway	Thickness, b	10 mm
	Guideway width	50 mm
	Air-gap between rotor and guideway, (g)	10 mm
	Conductivity, σ (Al)	$2.459 \times 10^7 \text{ Sm}^{-1}$

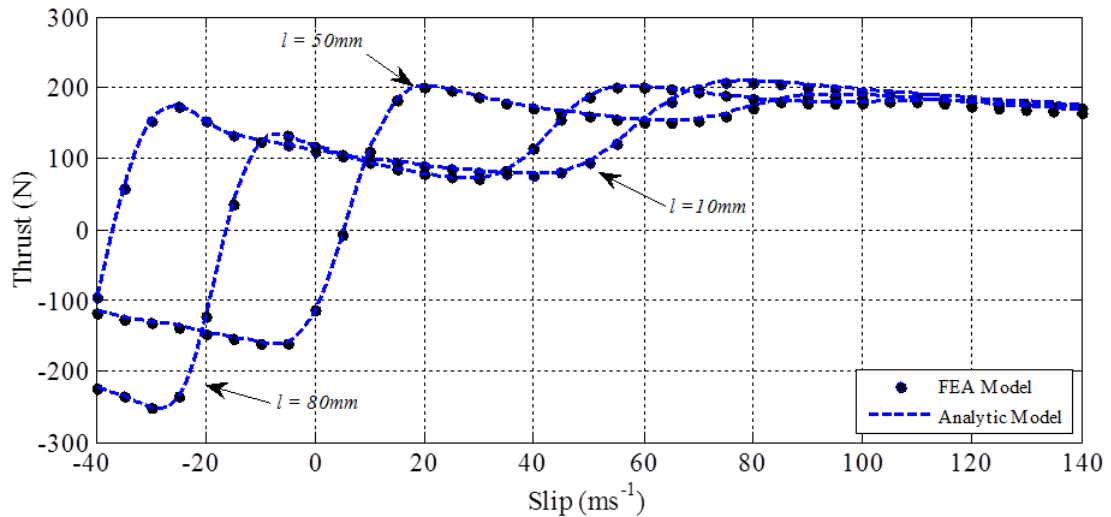


Figure 2.15: *The thrust force comparison between analytic and FEA for 5-EDWs in series above a conductive guideway.*

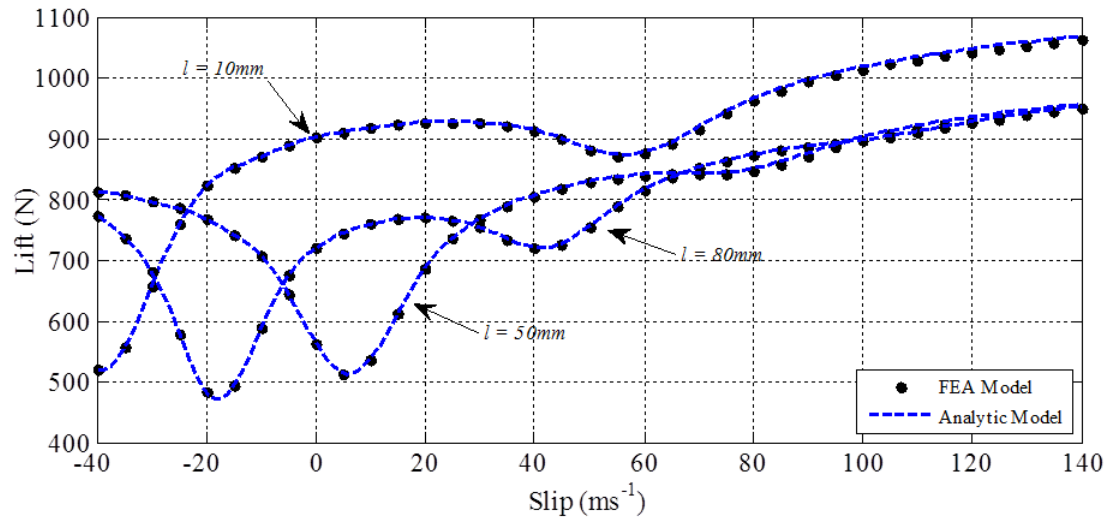


Figure 2.16: *The lift force comparison between analytic and FEA for 5-EDWs in series above a conductive guideway.*

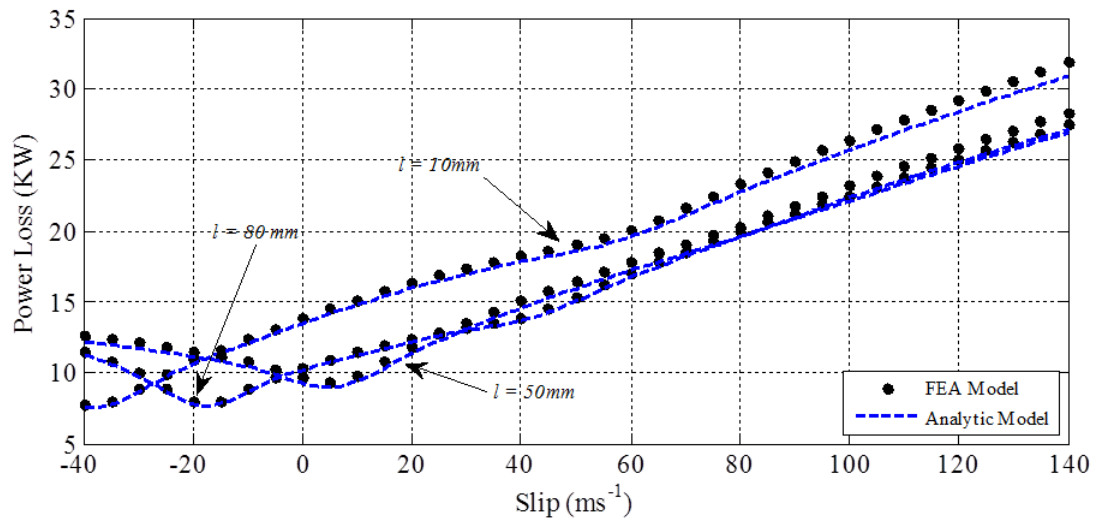


Figure 2.17: *The power loss comparison between analytic and FEA for 5-EDWs in series above a conductive guideway.*

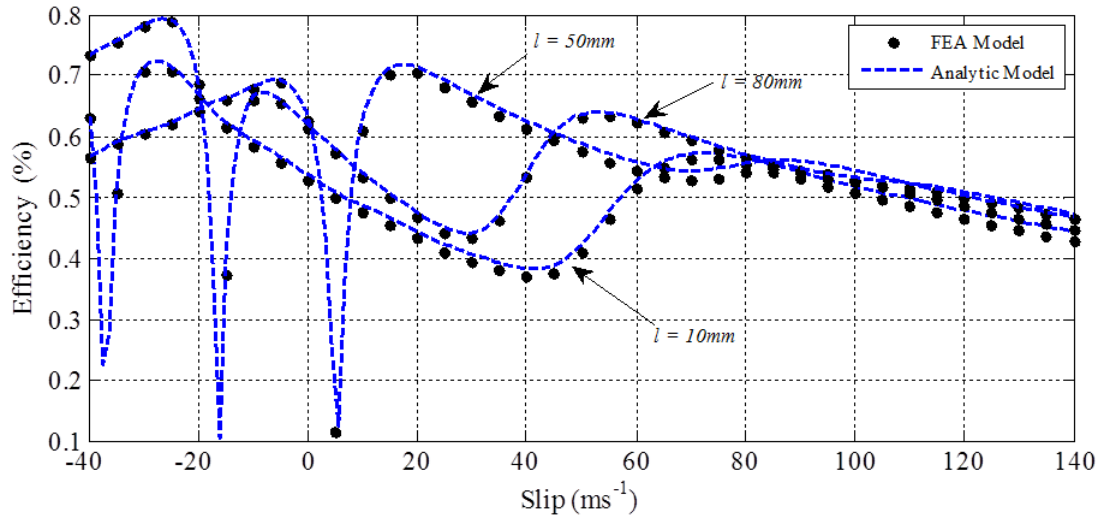


Figure 2.18: *The thrust efficiency comparison between analytic and FEA for 5-EDWs in series above a conductive guideway.*

2.4 Summary

The most commonly used 2-D eddy-current modeling techniques have been reviewed. The spatial Fourier transform method has been selected because the governing equations as well as the source field were easily Fourier transformable and the 2-D model simplifies in the Fourier domain. The force and power loss equations in two dimensions due to an arbitrary magnetic source oscillating and moving above a conductive guideway have been derived. The translational and heave velocity effect of the source have been included in the formulation. The solution has been verified by using a single EDW as well as multiple EDWs in series as a magnetic source. Only the magnitude of the steady-state source field on the top conductor surface needs to be provided. The calculation time using this analytic based approach is significantly faster than with FEA. The reflected magnetic flux density in the air region has also been derived.

CHAPTER 3: A 2-D TRANSIENT ANALYTIC EDDY-CURRENT MODEL

3.1 Introduction

In this chapter the 2-D transient analytic model for a magnetic source simultaneously rotating and/or moving above a conductive passive aluminum guideway is developed and validated. The analytical model is source independent so that any arbitrary magnetic source can be used. However, in order to validate the results and evaluate the performance of the developed model, a Halbach rotor has been used as a magnetic source. A review of the transient eddy-current modeling techniques is presented in section 3.2. This is followed by the presentation of the transient analytical model in section 3.3. As with the steady-state model the transient model is formulated in three different regions; two air regions and one conducting region. The analytical equations for the forces as well as for the power loss are validated with FEA models in section 3.4. The transient FEA model developed in COMSOL is presented in the Appendix A. A summary of the chapter is given in section 3.5.

3.2 A Review of 2-D Transient Eddy-Current Modeling

The transient eddy-current phenomenon has been utilized for a wide variety of applications such as non-destructive testing (NDT) [151, 152, 161–163], magnetic bearings [164, 165], magnetic resonance imaging (MRI) [166, 167], structural damping [168] and magnetic levitation [169–171] to name a few.

Most authors have solved transient eddy-current problems by using the Laplace transform technique. For instance, Fu and Bowler [152] studied the transient eddy-current response of a driver pickup probe above a conductive plate using a series expansion and inverse Laplace transform approach. Sapunov used the Laplace trans-

form technique to calculate the eddy-current density for the case when a filamentary circular coil is placed next to a conductive sheet and the excitation current in the coil has an increasing exponential form [172]. Waidelich examined the case of a long 2-D filamentary coil using the same technique [173]. Similarly, Panas and Kriezis used the Laplace transform technique to analyze the transient eddy-current distribution within a conducting plate when the excitation is a circular loop of current in air perpendicular or parallel to the surface dividing the two media [174]. This analysis has been done for infinite or finite plate thickness. In addition, they also considered the transient eddy-current problems in cylindrical shells. Hannakam used the Laplace transform technique to calculate the transient forces due to an arbitrary shaped coil [175].

The transient forces produced by eddy-currents have been studied by a variety of authors primarily for Maglev applications [56, 174, 176]. Davis and Wilkie derived the transient lift and thrust forces produced by moving a long wire above a thin conducting plate and analyzed the stability of such a system [56]. Fink and Hobrecht derived the forces for an infinitely long current loop moving parallel to a conductive sheet [176]. While, Panas and Kriezis calculated the transient eddy-current forces with two current filaments moving above a conducting plate of finite width [174].

A variety of numerical based 2-D transient eddy-current methods have been developed. For instance, Clemens et al. presents a transient numerical formulation for transient eddy current calculations with moving conductors based on finite integration method [177]. Yioultsis et al. developed a time domain eddy-current analysis method based on the finite difference time domain method [178].

3.3 A 2-D Transient Analytical Modeling

In order to understand the dynamics and design the active control for a maglev vehicle that contains a number of EDWs an accurate and computationally fast transient analytic based model is needed. Therefore, a fast transient analytic eddy-current

model has been developed in this section using the spatial Fourier transform and temporal Laplace transform. The model developed in this chapter will then be utilized in order to investigate the dynamic suspension behavior of an EDW Maglev vehicle.

In this transient analytical model, the same assumptions as used by the steady-state model have been made. Namely, the guideway conductor is assumed to be made up of a linear material, the displacement current has been neglected and the edge-effect due to the finite width of the source field and the guideway has been neglected. And lastly, the eddy-current within the magnetic source has been neglected.

The eddy-current forces are often calculated on the magnetic sources. However, if the magnetic source has a complex geometric configuration, such as, an EDW it is easier to formulate the problem with respect to the guideway. As with the steady-state model 2-D equations are derived by utilizing the magnetic scalar potential, ϕ , in the non-conducting region and the magnetic vector potential, A_z , in the conductive region.

3.3.1 Governing Subdomain Equations

The model for the 2-D transient analytic based solution is shown in Figure 3.1. The problem region is divided into one conducting region, Ω_2 and two non-conducting regions Ω_1 and Ω_3 . The magnetic source is not physically modeled in the air region. Instead the source field is evaluated analytically at the guideway surface and incorporated into the conducting boundary conditions.

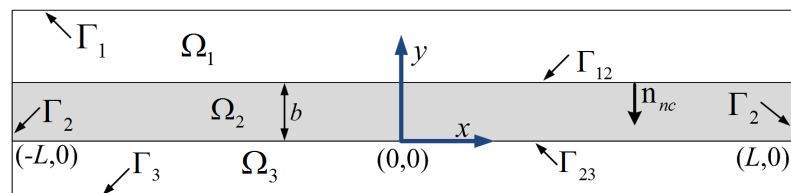


Figure 3.1: *Illustration of the conductive (Ω_2) and non-conductive (Ω_1 and Ω_3) regions and boundaries used by the analytic based transient eddy-current model.*

3.3.1.1 Conducting Guideway Region

The translational motion of a magnetic source can be modeled by either having the conductive region moving or magnetic source [179, 180]. In the case of 2-D steady-state modeling, the translational as well as heave motion of the magnetic source were incorporated into the conductive guideway. However, in this 2-D transient model, only the translational motion will be included within the rotor field. Since the transient model explicitly accounts for any change in the airgap with respect to time, the heave velocity, v_y , is not required. The derivation of the source field, including the translational velocity for a Halbach rotor, is presented in section 3.3.8. The governing transient guideway equation (2.24) in the conductive region, Ω_2 , for transient modeling is modified to

$$\mu_0\sigma \frac{\partial A_z}{\partial t} - \nabla^2 A_z = 0 \quad (3.1)$$

Expanding (3.1), the guideway governing equation becomes

$$\frac{\partial^2 A_z}{\partial x^2} + \frac{\partial^2 A_z}{\partial y^2} = \mu_0\sigma \left(\frac{\partial A_z}{\partial t} \right) \quad \text{in } \Omega_2 \quad (3.2)$$

3.3.1.2 Non-Conducting Regions

The governing equation in the non-conducting regions is exactly the same as used in the steady-state mode and will just be the Laplace equation given by (2.13). This equation is re-written below for convenience.

$$\frac{\partial^2 \phi_n}{\partial x^2} + \frac{\partial^2 \phi_n}{\partial y^2} = 0 \quad \text{in } \Omega_n \text{ for } n=1, 3 \quad (3.3)$$

3.3.1.3 Boundary Conditions

The boundary conditions are the same as derived in the steady-state model except now the source and the vector potential fields are a function of time, t . The boundary conditions on the top conductive surface, Γ_{12} , at the $A_z - \phi$ interface are therefore

given by [144]

$$-\mu_0 \frac{\partial \phi_1(x, b, t)}{\partial x} + B_x^{s1}(x, b, t) = \frac{\partial A_z(x, y, t)}{\partial y} \Big|_{y=b} \quad \text{on } \Gamma_{12} \quad (3.4)$$

$$-\mu_0 \frac{\partial \phi_1(x, y, t)}{\partial y} \Big|_{y=b} + B_y^{s1}(x, b, t) = -\frac{\partial A_z(x, b, t)}{\partial x} \quad \text{on } \Gamma_{12} \quad (3.5)$$

where $B_x^{s1}(x, b, t)$ and $B_y^{s1}(x, b, t)$ are the x and y components of the magnetic flux densities of the source at $y = b$. The boundary conditions on the bottom surface, Γ_{23} , for the continuity of tangential and normal components are respectively given by

$$-\mu_0 \frac{\partial \phi_3(x, 0, t)}{\partial x} = \frac{\partial A_z(x, y, t)}{\partial y} \Big|_{y=0} \quad \text{on } \Gamma_{23} \quad (3.6)$$

$$-\mu_0 \frac{\partial \phi_3(x, y, t)}{\partial y} \Big|_{y=0} = -\frac{\partial A_z(x, 0, t)}{\partial x} \quad \text{on } \Gamma_{23} \quad (3.7)$$

Again like with the steady-state model, the source field is assumed to be centrally located at $x = 0$ and the guideway is chosen to be sufficiently long in order to make the source fields zero at the guideway ends ($x = \pm L$). Therefore,

$$B_x^{s1}(\pm L, y) = 0 \quad \text{on } \Gamma_2 \quad (3.8)$$

$$B_y^{s1}(\pm L, y) = 0 \quad \text{on } \Gamma_2 \quad (3.9)$$

$$A_z(\pm L, y) = 0 \quad \text{on } \Gamma_2 \quad (3.10)$$

Also, the problem region is large enough so that scalar potentials on the outer non-conducting boundaries are zeros as

$$\phi_1 = 0 \quad \text{on } \Gamma_1 \quad (3.11)$$

$$\phi_3 = 0 \quad \text{on } \Gamma_3 \quad (3.12)$$

3.3.2 Fourier-Laplace Solution for Governing Subdomain Equations

Similar to the steady-state model, the solution to the transient problem has been obtained by using the spatial Fourier transform on variable- x . The Fourier transform for the vector and the scalar potentials are defined by [3, 150]

$$A_z(\xi, y, t) = \int_{-\infty}^{\infty} A_z(x, y, t) e^{-j\xi x} dx \quad (3.13)$$

$$\phi_n(\xi, y) = \int_{-\infty}^{\infty} \phi_n(\xi, y) e^{-j\xi x} d\xi \quad (3.14)$$

In addition to the Fourier transform, the transient equation for vector potential (3.13) is Laplace transformed with respect to time, t . Therefore, the vector potential becomes

$$A_z(\xi, y, s) = \int_0^{\infty} A_z(\xi, y, t) e^{-st} dt \quad (3.15)$$

3.3.2.1 Fourier and Laplace Transformed Conducting Region

The governing equation for the conducting region, Ω_2 given by (3.1) is Fourier transformed with respect to variable- x utilizing the Fourier definition (3.13). Therefore, the conducting region governing equation becomes

$$-\xi^2 A_z(\xi, y, t) + \frac{\partial^2 A_z(\xi, y, t)}{\partial y^2} = \mu_0 \sigma \frac{\partial A_z(\xi, y, t)}{\partial t} \quad (3.16)$$

Now taking the Laplace transform on either side of (3.16) by using the definition (3.15), the differential equation (3.16) reduces down to

$$\frac{\partial^2 A_z(\xi, y, t)}{\partial y^2} = \mu_0 \sigma [s A_z(\xi, y, s) - A_z(\xi, y, t_0)] + \xi^2 A_z(\xi, y, s) \quad (3.17)$$

where $A_z(\xi, y, t_0)$ is an initial value of the vector potential solution at time, $t = t_0$. If the initial value of the vector potential is the steady-state vector potential solution,

$A_z^{ss}(\xi, y, t_0)$ given in (2.73) then (3.17) becomes

$$\frac{\partial^2 A_z(\xi, y, s)}{\partial y^2} = (\mu_0 \sigma s + \xi^2) A_z(\xi, y, s) - \mu_0 \sigma A_z^{ss}(\xi, y, t_0) \quad (3.18)$$

Defining

$$\alpha = \sqrt{\xi^2 + \mu_0 \sigma s} \quad (3.19)$$

allows (3.18) to be written as

$$\frac{\partial^2 A_z(\xi, y, s)}{\partial y^2} = \alpha^2 A_z(\xi, y, s) - \mu_0 \sigma A_z^{ss}(\xi, y, t_0) \quad (3.20)$$

If the initial value of the steady-state vector potential is evaluated at translational velocity, v_{x0} , electrical angular velocity, ω_{e0} , and heave velocity, $v_y = 0$, the vector potential equation (2.74) at time $t = t_0$ can be rewritten as

$$A_z^{ss}(\xi, y, t_0) = T_0^{ss}(\xi, y, s_0) B^{s0}(\xi, b, t_0) \quad (3.21)$$

where $T_0^{ss}(\xi, y, s_0)$ is defined by (2.76) and γ (2.52) is defined in terms of v_{x0} and ω_{e0} as

$$\gamma = \sqrt{\xi^2 + j\mu_0 \sigma (\omega_{e0} - v_{x0} \xi)} = \sqrt{\xi^2 + \mu_0 \sigma s_0} \quad (3.22)$$

$$s_0 = j(\omega_{e0} - v_{x0} \xi) \quad (3.23)$$

The steady-state time dependence has been included into the source field function. The variable $B^{s0}(\xi, b, t_0)$ is the complex source field value at $t = t_0$ and is evaluated at the surface of the guideway, i.e. $y = b$

$$B^{s0}(\xi, b, t_0) = [B_x^{s0}(\xi, b) + jB_y^{s0}(\xi, b)] e^{j\omega_{e0} t_0} \quad (3.24)$$

Substituting (3.21) into (3.20) gives

$$\frac{\partial^2 A_z(\xi, y, s)}{\partial y^2} = \alpha^2 A_z(\xi, y, s) - \mu_0 \sigma T_o^{ss}(\xi, y, s_0) B^{s_0}(\xi, b, t_0) \quad (3.25)$$

The solution to (3.25) is given by

$$A_z(\xi, y, s) = \frac{\mu_0 \sigma}{(\alpha^2 - \gamma^2)} A_z^{ss}(\xi, y, s_0) + D_a(\xi, s) e^{\alpha y} + D_b(\xi, s) e^{-\alpha y} \quad (3.26)$$

Note that to obtain the solution to (3.25) the derivative of both A_z and A_z^{ss} must be considered. Substituting (3.22) and (3.19) into the denominator of (3.26) allows (3.26) to be expressed in compact form as

$$A_z(\xi, y, s) = \frac{A_z^{ss}(\xi, y, s_0)}{s - s_0} + D_a(\xi, s) e^{\alpha y} + D_b(\xi, s) e^{-\alpha y} \quad (3.27)$$

where the unknown constants $D_a(\xi, s)$ and $D_b(\xi, s)$ still need to be determined. They will be evaluated by solving the Fourier and Laplace transformed boundary conditions in section 3.3.3.

3.3.2.2 Fourier Transformed Non-Conducting Region

The governing equation for the non-conducting regions in the Fourier domain is the same as determined in the steady-state model and is given by

$$\frac{\partial^2 \phi_n(\xi, t)}{\partial y^2} = \xi^2 \phi_n(y, t) \quad \text{on } \Gamma_n \text{ for } n = 1, 3 \quad (3.28)$$

The solution of the differential equation (3.28) is given by

$$\phi_1(\xi, y, t) = \psi_1(\xi, t) e^{-\xi y} \quad \text{in } \Omega_1 \quad (3.29)$$

$$\phi_3(\xi, y, t) = \psi_3(\xi, t) e^{\xi y} \quad \text{in } \Omega_3 \quad (3.30)$$

where ψ_1 and ψ_3 are unknowns. As with the steady-state model, the solution of the scalar potentials in regions Ω_1 and Ω_3 are satisfying the fact that when moving away from the guideway along the y -axis in the field must reduce to zero. The change in ϕ_1 and ϕ_3 with respect to time will come from the boundary interface conditions.

3.3.2.3 Fourier and Laplace Transformed Boundary Conditions

The boundary condition equations along the top conducting surface given by (3.4) and (3.5) are Fourier transformed with respect to x and later Laplace transformed with respect to time, t , to yield

$$-j\mu_0\xi\phi_1(\xi, b, s) + B_x^{s1}(\xi, b, s) = \left. \frac{\partial A_z(\xi, y, s)}{\partial y} \right|_{y=b} \quad \text{on } \Gamma_{12} \quad (3.31)$$

$$-\mu_0 \left. \frac{\partial \phi_1(\xi, y, s)}{\partial y} \right|_{y=b} + B_y^{s1}(\xi, b, s) = -j\xi A_z(\xi, b, s) \quad \text{on } \Gamma_{12} \quad (3.32)$$

Substituting the value of the vector potential, $A_z(\xi, y, s)$, from (3.27) and scalar potential solution, $\phi_1(\xi, y)$, from (3.29) into the boundary condition equations (3.31) and (3.32) yields

$$-j\mu_0\xi\psi_1(\xi, s)e^{-\xi b} + B_x^{s1}(\xi, b, s) = \frac{B_x^{ss}(\xi, b, s_0)}{s - s_0} + \alpha (D_a(\xi, s)e^{\alpha b} - D_b(\xi, s)e^{-\alpha b}) \quad (3.33)$$

$$\mu_0\xi\psi_1(\xi, s)e^{-\xi b} + B_y^{s1}(\xi, b, s) = \frac{B_y^{ss}(\xi, b, s_0)}{s - s_0} + j\xi (D_a(\xi, s)e^{\alpha b} + D_b(\xi, s)e^{-\alpha b}) \quad (3.34)$$

Multiplying (3.34) by j and adding the above boundary conditions (3.33) and (3.34) will eliminate $\psi_1(\xi)$ from (3.33) and (3.34). Therefore, the combined boundary condition equation for the top conducting surface is given by

$$B^{s1}(\xi, b, s) = \frac{B^{s0}(\xi, b, s_0)}{s - s_0} + D_a(\xi, s)(\alpha + \xi)e^{\alpha b} + D_b(\xi, s)(\xi - \alpha)e^{-\alpha b} \quad (3.35)$$

where

$$B^{s1}(\xi, b, s) = B_x^{s1}(\xi, b, s) + jB_y^{s1}(\xi, b, s) \quad (3.36)$$

Rearranging (3.35), one can obtain

$$B^{s_1}(\xi, b, s) - \frac{B^{s_0}(\xi, b, s_0)}{s - s_0} = D_a(\xi, s)(\alpha + \xi)e^{\alpha b} + D_b(\xi, s)(\xi - \alpha)e^{-\alpha b} \quad (3.37)$$

Similarly, the bottom boundary condition given by (3.6) and (3.7) are Fourier transformed with respect to x to yield

$$-j\mu_0\xi\phi_3(\xi, 0, s) = \left. \frac{\partial A_z(\xi, y, s)}{\partial y} \right|_{y=0} \quad \text{on } \Gamma_{23} \quad (3.38)$$

$$-\mu_0 \left. \frac{\partial \phi_3(\xi, y, s)}{\partial y} \right|_{y=0} = -j\xi A_z(\xi, 0, s) \quad \text{on } \Gamma_{23} \quad (3.39)$$

Substituting the value of the vector potential, $A_z(\xi, y, s)$, from (3.27) and scalar potential solution, $\phi_3(\xi, y)$, from (3.30) into boundary condition equations (3.38) and (3.39) yields

$$-j\mu_0\xi\psi_3(\xi, s) = \alpha (D_a(\xi, s) - D_b(\xi, s)) \quad \text{on } \Gamma_{23} \quad (3.40)$$

$$-\mu_0\xi\psi_3(\xi, s) = -j\xi (D_a(\xi, s) + D_b(\xi, s)) \quad \text{on } \Gamma_{23} \quad (3.41)$$

Now combining (3.40) and (3.41) one can eliminate $\psi_3(\xi)$ to yield a combined boundary condition equation

$$0 = D_a(\xi, s)(\alpha - \xi) - D_b(\xi, s)(\xi + \alpha) \quad (3.42)$$

Therefore, $D_a(\xi, s)$ can be expressed in terms of $D_b(\xi, s)$ as

$$D_a(\xi, s) = D_b(\xi, s) \frac{\xi + \alpha}{\alpha - \xi} \quad (3.43)$$

3.3.3 Solution to Governing Equation

The top and bottom boundary conditions (3.37) and (3.43) are now solved for the two unknowns $D_a(\xi, s)$ and $D_b(\xi, s)$. Substituting (3.43) into (3.37) gives

$$D_a(\xi, s) = \frac{\alpha + \xi}{e^{\alpha b}(\alpha + \xi)^2 - e^{-\alpha b}(\alpha - \xi)^2} \left(B^{s_1}(\xi, b, s) - \frac{B^{s_0}(\xi, b, s_0)}{s - s_0} \right) \quad (3.44)$$

$$D_b(\xi, s) = \frac{\alpha - \xi}{e^{\alpha b}(\alpha + \xi)^2 - e^{-\alpha b}(\alpha - \xi)^2} \left(B^{s_1}(\xi, b, s) - \frac{B^{s_0}(\xi, b, s_0)}{s - s_0} \right) \quad (3.45)$$

Substituting (3.44) and (3.45) into (3.27) finally gives the vector potential solution as

$$A_z(\xi, y, s) = \frac{A_z^{ss}(\xi, y, s_0)}{s - s_0} + \left[B^{s_1}(\xi, b, s) - \frac{B^{s_0}(\xi, b, s_0)}{s - s_0} \right] T^t(\xi, y, s) \quad (3.46)$$

where

$$T^t(\xi, y, s) = \frac{(\alpha + \xi)e^{\alpha y} + (\alpha - \xi)e^{-\alpha y}}{e^{\alpha b}(\alpha + \xi)^2 - e^{-\alpha b}(\alpha - \xi)^2} \quad (3.47)$$

can be thought of as the source field transmission function and has the same form as obtained for the steady-state solution given by (2.76) where the superscript 't' in (3.47) refers to transient. The first term in (3.46) is the initial steady-state solution and the second term is the transient solution due to the change in the source field. The time term in the source field can be separated from the rest of the variables by noting that

$$B^{s_1}(\xi, b, t) = B^{s_1}(\xi, b)e^{s_1 t} \quad (3.48)$$

where

$$s_1 = j(\omega_{e1} + v_{x1}\xi) \quad (3.49)$$

The Laplace transform of (3.48) gives

$$B^{s_1}(\xi, b, s) = \frac{B^{s_1}(\xi, b)}{s - s_1} \quad (3.50)$$

Substituting (3.50) into the vector potential solution (3.46) yields

$$A_z(\xi, y, s) = \frac{A_z^{ss}(\xi, y, s_0)}{s - s_0} + \left[\frac{B^{s_1}(\xi, b)}{s - s_1} - \frac{B^{s_0}(\xi, b)}{s - s_0} \right] T^t(\xi, y, s) \quad (3.51)$$

Here the translational motion of the magnetic source has been accounted for by moving the magnetic source. While the steady-state model accounts for the motion of the source by including the velocity term within the transmission function. Either approach is possible when modeling the problem transiently [179, 180].

3.3.4 Transient Reflected Flux Density

The transient reflected eddy-current field can be determined by solving for unknown, $\psi_1(\xi, s)$ in Ω_1 . This can be achieved by substituting (3.29) into (3.32). The unknown, $\psi_1(\xi, s)$ can be written in terms of the vector potential, $A_z(\xi, b, s)$, and source field, $B_y^{s_1}(\xi, b, s)$ as

$$\psi_1(\xi, s) = \frac{-1}{\mu_0 \xi} [j\xi A_z(\xi, b, s) + B_y^{s_1}(\xi, b, s)] e^{\xi b} \quad (3.52)$$

The scalar potential, $\phi_1(\xi, y, s)$, in region Ω_1 is obtained by substituting (3.52) into (3.29)

$$\phi_1(\xi, y, s) = \frac{-1}{\mu_0 \xi} [j\xi A_z(\xi, b, s) + B_y^{s_1}(\xi, b, s)] e^{\xi(b-y)} \quad (3.53)$$

From (3.53) it can be noted that the reflected flux density values $B_x^r(\xi, y, s)$ and $B_y^r(\xi, y, s)$ are given by

$$B_x^r(\xi, y, s) = -\mu_0 \frac{\partial \phi_1(\xi, y, s)}{\partial x} = j [j\xi A_z(\xi, b, s) + B_y^{s_1}(\xi, b, s)] e^{\xi(b-y)} \quad (3.54)$$

$$B_y^r(\xi, y, s) = -\mu_0 \frac{\partial \phi_1(\xi, y, s)}{\partial y} = - [j\xi A_z(\xi, b, s) + B_y^{s_1}(\xi, b, s)] e^{\xi(b-y)} \quad (3.55)$$

Thus, as with the steady-state model the x and y components of the reflected flux densities in region, Ω_1 are related by

$$B_y^r(\xi, y, s) = jB_x^r(\xi, y, s) \quad (3.56)$$

Taking the inverse Laplace transform of (3.54) and (3.55) enables the transient reflected flux density components at $y = b$ to be obtain

$$B_x^r(\xi, b, t) = j[j\xi A_z(\xi, b, t) + B_y^{s1}(\xi, b, t)] \quad (3.57)$$

$$B_y^r(\xi, b, t) = -[j\xi A_z(\xi, b, t) + B_y^{s1}(\xi, b, t)] \quad (3.58)$$

The transient vector potential, $A_z(\xi, b, t)$ is derived in the next section and $B_y^{s1}(\xi, b, t)$ is the y -component of the magnetic source in the time domain.

3.3.5 Time Domain Solution

The time domain solution of the vector potential (3.51) can be obtained by determining the inverse Laplace transform of the transmission function (3.47). The inverse Laplace transforms of (3.47) could not be found in any known Laplace transform table. However, the inverse Laplace transform of complicated equations, such as (3.47), are possible by using the Heaviside expansion theorem [150, 151]. The transmission function is rearranged in order to facilitate this. Assuming a new variable h , such that, $b = 2h$, the transmission function (3.47) becomes

$$T^t(\xi, y, s) = \frac{(\alpha + \xi)e^{\alpha y} + (\alpha - \xi)e^{-\alpha y}}{e^{2\alpha h}(\alpha + \xi)^2 - e^{-2\alpha h}(\alpha - \xi)^2} \quad (3.59)$$

Simplifying the denominator of (3.59) one obtains

$$T^t(\xi, y, s) = \frac{(\alpha + \xi)e^{\alpha y} + (\alpha - \xi)e^{-\alpha y}}{[e^{\alpha h}(\alpha + \xi)]^2 - [e^{-\alpha h}(\alpha - \xi)]^2} \quad (3.60)$$

Further simplifying (3.60), the transmission function becomes

$$T^t(\xi, y, s) = \frac{\alpha(e^{\alpha y} + e^{-\alpha y}) + \xi(e^{\alpha y} - e^{-\alpha y})}{[\alpha(e^{\alpha h} + e^{-\alpha h}) + \xi(e^{\alpha h} - e^{-\alpha h})][\alpha(e^{\alpha h} - e^{-\alpha h}) + \xi(e^{\alpha h} + e^{-\alpha h})]} \quad (3.61)$$

Now using the trigonometric hyperbolic functions (3.61) can be written as

$$T^t(\xi, y, s) = \frac{2\alpha \cosh(\alpha y) + 2\xi \sinh(\alpha y)}{[2\alpha \cosh(\alpha h) + 2\xi \sinh(\alpha h)][2\alpha \sinh(\alpha h) + 2\xi \cosh(\alpha h)]} \quad (3.62)$$

Dividing the numerator and denominator by $\cosh(\alpha h) \sinh(\alpha h)$ i.e. by $0.5 \sinh(2\alpha h)$ gives

$$T^t(\xi, y, s) = \frac{\left(\frac{\alpha \cosh(\alpha y)}{\xi^2 \sin(2\alpha h)} + \frac{1 \sinh(\alpha y)}{\xi \sin(2\alpha h)} \right)}{\left(\frac{\alpha}{\xi} + \tanh(\alpha h) \right) \left(\frac{\alpha}{\xi} + \coth(\alpha h) \right)} \quad (3.63)$$

Let

$$\nu = \alpha h \quad \text{and} \quad \lambda = 1/(\xi h) \quad (3.64)$$

Therefore,

$$\nu \lambda = \alpha / \xi \quad (3.65)$$

Substituting (3.64) and (3.65) into the denominator of (3.63) gives

$$T^t(\xi, y, s) = \frac{\left(\frac{\alpha \cosh(\alpha y)}{\xi^2 \sin(2\alpha h)} + \frac{1 \sinh(\alpha y)}{\xi \sin(2\alpha h)} \right)}{(\lambda \nu + \tanh(\nu)) (\lambda \nu + \coth(\nu))} \quad (3.66)$$

For further simplification, let $\nu = jk$. Now substituting the value of $\nu = jk$ into (3.66) and using the trigonometric relations

$$\begin{aligned} \tanh(jk) &= j \tan(k) \\ \coth(jk) &= -j \cot(k) \end{aligned} \quad (3.67)$$

one obtains

$$T^t(\xi, y, s) = \frac{\left(\frac{2k \cos(2ky/b)}{b\xi^2 \sin(2k)} + \frac{\sin(2ky/b)}{\xi \sin(2k)} \right)}{(-\lambda k + \cot(k)) (\lambda k + \tan(k))} \quad (3.68)$$

Setting $y = b$ (3.47) can be algebraic manipulated to yield

$$T^t(\xi, b, s) = \frac{2k \cdot \cot(2k) + b\xi}{b\xi^2 (-\lambda k + \cot(k)) (\lambda k + \tan(k))} \quad (3.69)$$

The advantage of using (3.69) rather than (3.47) is that the roots in the denominator can be easily determined. They are given by

$$\tan(k) = -\lambda k \quad (3.70)$$

$$\cot(k) = \lambda k \quad (3.71)$$

The roots of (3.70) and (3.71) are calculated numerically by using the ‘*FindRoot*’ command in Mathematica software. The script used for the calculation of the roots for the guideway thickness of 6.3mm and is given below in Table 3.1 [151]. Only the first ten significant roots of (3.74) have been used. The sample plots of the *tan* and *cot* roots for $\xi = 250$ and $b = 6.3\text{mm}$ is illustrated in Figure 3.2.

Table 3.1: *Mathematica code for tan and cot root calculations.*

```
(* Cot Root Calculation *)
b = 6.3*10^-3;
h = b/2;
λ = Table[1/(ξh), {ξ, 1, 200, 1.99}];
L1 = Table[nπ, {n, 0, 9}];
L2 = L1 + π/2;
L0 = (L1+L2)/2;
CotRoot = Table[FindRoot[Cot[ξ] == λ[[i]]*ξ, {ξ, L0, L1, L2}, MaxIterations->500], {i, 10}];
NumberForm[MatrixForm[CotRoot], 10];

(* Tan Root Calculation *)
L1 = Table[nπ + π/2, {n, 0, 9}];
L2 = L1 + π/2;
L0 = (L1+L2)/2;
TanRoot = Table[FindRoot[Tan[ξ] == -λ[[i]]*ξ, {ξ, L0, L1, L2}, MaxIterations->500], {i, 10}];
NumberForm[MatrixForm[TanRoot], 10];
```

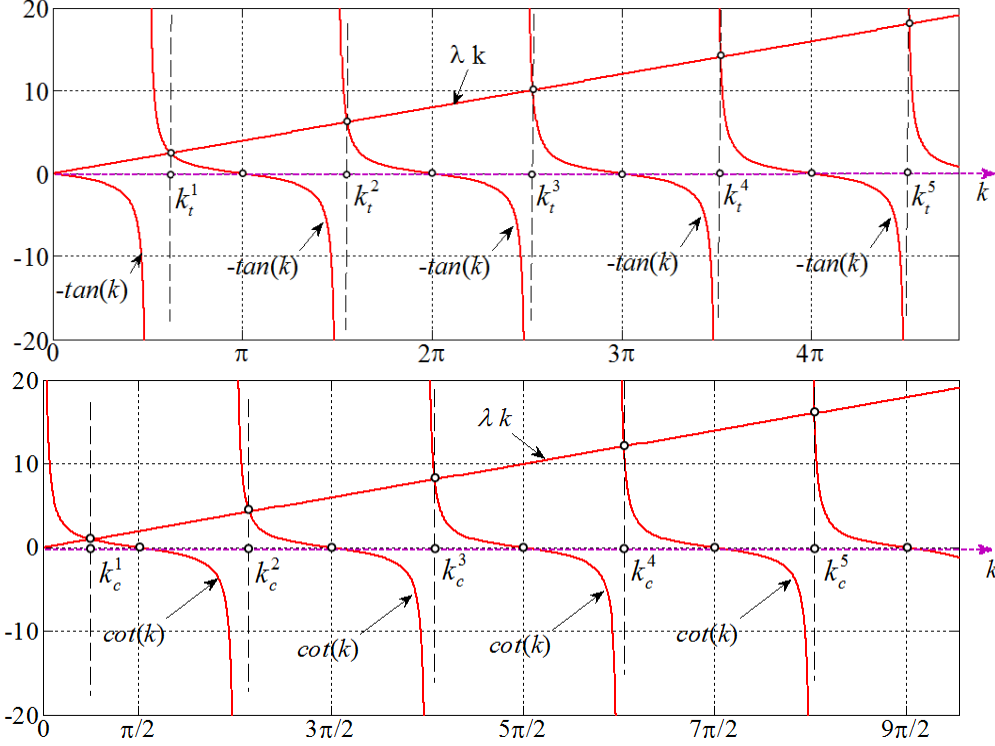


Figure 3.2: The sample tan and cot roots calculation for $\xi = 250$ and $b = 6.3\text{mm}$.

The n^{th} root of (3.70) is denoted by k_t^n and it lies between $n\pi + \pi/2$ and $n\pi + \pi$. The n^{th} root of (3.71) denoted by k_c^n , lie between $n\pi$ and $n\pi + \pi/2$. The poles corresponding to the roots and both are purely located at negative values, and are given by

$$s = [\alpha^2 - \xi^2] \frac{1}{\mu_o \sigma} \quad (3.72)$$

$$s_m^n = - \left[\left(\frac{2k_m^n}{b} \right)^2 + \xi^2 \right] \frac{1}{\mu_o \sigma} \quad (3.73)$$

where the subscript $m = t$ or c referring to $\tan(k)$ or $\cot(k)$ roots. With the roots of (3.69) identified the expression for the field transmission coefficient for the n^{th} root can be written as

$$T_k^t(\xi, b, k_m^n) = \frac{2k_m^n \cdot \cot(2k_m^n) + b\xi}{b\xi^2 (-\lambda k_m^n + \cot(k_m^n)) (\lambda k_m^n + \tan(k_m^n))} \quad (3.74)$$

Substituting (3.74) into (3.51) allows the vector potential, $A_z(\xi, y, s)$, to be written as

$$A_z(\xi, y, s) = \frac{A_z^{ss}(\xi, y, s_0)}{s - s_0} + \left[\frac{B^{s1}(\xi, b)}{s - s_1} - \frac{B^{s0}(\xi, s)}{s - s_0} \right] \times \left(\frac{(2k_m^n \cdot \cot(2k_m^n) + b\xi)}{b\xi^2 (-\lambda k_m^n + \cot(k_m^n)) (\lambda k_m^n + \tan(k_m^n))} \right) \quad (3.75)$$

The inverse Laplace transform of (3.75) is evaluated by using the Heaviside expansion theorem [150, 151]. The Heaviside expansion theorem states that ‘if $P(s)$ and $Q(s)$ are to be the polynomials of degree m and n respectively such that $n > m$ and $Q(s)$ has n distinct simple zeros at points s_1, s_2, \dots, s_n , then $P(s)/Q(s)$ is the Laplace transform of the function $g(t)$ ’ [150] where the time domain solution $g(t)$ is given by

$$g(t) = L^{-1} \left(\frac{P(s)}{Q(s)} \right) = \sum_{k=1}^n \frac{P(s_k)}{Q'(s_k)} e^{s_k t} \quad (3.76)$$

Utilizing (3.76), the inverse Laplace transform of the vector potential, (3.75) can be obtained. The resulting transient vector potential solution is

$$A_z(\xi, b, t) = B^{s0}(\xi, b) [T_o^{ss}(\xi, b, s_0) e^{s_0 t} + A_1(\xi) e^{s_0 t}] + B^{s1}(\xi, b) \left[A_2(\xi) e^{s_1 t} + \sum_{n=0}^9 (A_t^n(\xi) e^{s_t^n t} + A_c^n(\xi) e^{s_c^n t}) \right] \quad (3.77)$$

where, s_t^n and s_c^n are given by (3.73); the other constants in (3.77) are given as

$$A_1(\xi) = -T_o^{ss}(\xi, b, s_0) \quad (3.78)$$

$$A_2(\xi) = T_o^{ss}(\xi, b, s_1) \quad (3.79)$$

$$A_t^n(\xi) = \frac{-\frac{8k_t^n}{\mu_0 \sigma b^2} \left(\frac{2k_t^n \cos(2k_t^n y/b)}{b\xi^2 \sin(2k_t^n)} + \frac{\sin(2k_t^n y/b)}{\xi \sin(2k_t^n)} \right) Q_t^n}{(\cot(k_t^n) - \lambda k_t^n)(\lambda + \sec^2(k_t^n))(s_t^n - s_1)(s_t^n - s_0)} \quad (3.80)$$

$$Q_t^n = B^{s1}(s_t^n - s_0) - B^{s0}(s_t^n - s_1) \quad (3.81)$$

$$A_c^n(\xi) = \frac{\frac{8k_c^n}{\mu_0\sigma b^2} \left(\frac{2k_c^n \cos(2k_c^n y/b)}{b\xi^2 \sin(2k_c^n)} + \frac{\sin(2k_c^n y/b)}{\xi \sin(2k_c^n)} \right) Q_c^n}{(\cot(k_c^n) - \lambda k_c^n)(\lambda + \sec^2(k_c^n))(s_c^n - s_1)(s_c^n - s_0)} \quad (3.82)$$

$$Q_c^n = B^{s_1}(s_c^n - s_0) - B^{s_0}(s_c^n - s_1) \quad (3.83)$$

The vector potential solution (3.77) can be further simplified since substituting (3.78) into (3.77) results in the first two terms of (3.77) canceling each other out. Thus, (3.77) reduces down to

$$A_z(\xi, y, t) = B^{s_1}(\xi) \left[T_{new}^{ss}(\xi, b, s_1) e^{s_1 t} + \sum_{m=0}^9 (A_t^n(\xi) e^{s_t^n t} + A_c^n(\xi) e^{s_c^n t}) \right] \quad (3.84)$$

This is the transient solution of the vector potential for a step change in translational velocity from v_{x0} to v_{x1} , a step change in the electrical angular frequency from ω_{e0} to ω_{e1} or a step change in air-gap. The variable air-gap is embedded in the source field function $B^{s_1}(\xi)$ and $B^{s_1}(\xi)$ as shown in section 3.3.8. More than one of these inputs can change at the same time. The first term in (3.84) is the steady-state solution of the vector potential at v_{x1} , ω_{e1} and air-gap, g_1 . The following two terms are the transient decaying response terms due to a step change. Only the first ten roots are used because for the application studied in this thesis values for $n > 10$ leads to poles and that have very high negative values. As it can be noted from (3.84) the higher the negative values of s_t^n and s_c^n , the faster is the transient decay. Therefore, the fast decaying transient roots and their corresponding poles are neglected in this formulation.

3.3.6 Electric Field Intensity and Magnetic Flux Densities

The transient solution for the electric field intensity, $E_z(\xi, y, t)$, can be obtained from the vector potential, $A_z(\xi, y, t)$ by differentiating the vector potential with respect

to the time, t . Therefore, the electric field intensity, $E_z(\xi, y, t)$ is

$$E_z(\xi, y, t) = -\frac{dA_z(\xi, y, t)}{dt} = -B^{s_1}(\xi)[s_1 T_{new}^{ss}(\xi, y, s_1)e^{s_1 t} + \sum_{m=0}^9 (s_t^n A_t^n(\xi)e^{s_t^n t} + s_c^n A_c^n(\xi)e^{s_c^n t})] \quad (3.85)$$

The x and y components of the magnetic flux density developed on the conducting region Ω_2 can be obtained by differentiating the vector potential, $A_z(\xi, y, t)$ with respect to variables y and x respectively as

$$B_x(\xi, y, t) = \frac{\partial A_z(\xi, y, t)}{\partial y} \quad (3.86)$$

$$B_y(\xi, y, t) = -\frac{\partial A_z(\xi, y, t)}{\partial x} = -j\xi A_z(\xi, y, t) \quad (3.87)$$

The transient equation for $B_x(\xi, y, t)$ can be obtained by substituting the vector potential solution (3.84) into (3.86). Therefore, $B_x(\xi, y, t)$ is given by

$$B_x(\xi, y, t) = B^{s_1}(\xi) \left[C_1(\xi)e^{s_1 t} + \sum_{n=0}^9 (C_t^n(\xi)e^{s_t^n t} + C_c^n(\xi)e^{s_c^n t}) \right] \quad (3.88)$$

where the constants in (3.88) have been determined to be

$$C_1(\xi) = \frac{\left(-\frac{4k_1^2 \sin(2k_1 y/b)}{b^2 \xi^2 \sin(2k_1)} + \frac{2k_1 \cos(2k_1 y/b)}{b \xi \sin(2k_1)} \right)}{(\cot(k_1) - \lambda k_1)(\tan(k_1) + \lambda k_1)} \quad (3.89)$$

$$C_t^n(\xi) = \frac{\left(\frac{4(k_t^n)^2 \sin(2k_t^n y/b)}{b^2 \xi^2 \sin(2k_t^n)} - \frac{2k_t^n \cos(2k_t^n y/b)}{b \xi \sin(2k_t^n)} \right) \frac{Q_t^n 8k_t^n}{\mu_0 \sigma b^2}}{(\cot(k_t^n) - \lambda k_t^n)(\lambda + \sec^2(k_t^n))(s_t^n - s_0)(s_t^n - s_1)} \quad (3.90)$$

$$C_c^n(\xi) = -\frac{\left(\frac{4(k_c^n)^2 \sin(2k_c^n y/b)}{b^2 \xi^2 \sin(2k_c^n)} - \frac{2k_c^n \cos(2k_c^n y/b)}{b \xi \sin(2k_c^n)} \right) \frac{Q_c^n 8k_c^n}{\mu_0 \sigma b^2}}{(\lambda + \csc^2(k_c^n))(\lambda k_c^n + \tan(k_c^n))(s_c^n - s_0)(s_c^n - s_1)} \quad (3.91)$$

$$k_1 = j0.5b\sqrt{\xi^2 + \mu_0 \sigma s_1} \quad (3.92)$$

The transient solution of the vector potential, electric field intensity and the magnetic flux densities can be evaluated on the surface of the guideway by substituting $y = b$ in their respective equations. This will be used to calculate the transient forces on the guideway surface and the total power loss in the guideway in the following section.

3.3.7 Force and Power Loss Calculations

The thrust or braking force, F_x , and lift force, F_y , can be determined by either evaluating the stress tensor equations along the guideway surface ($y = b$) or by using the Lorenz equation. In 2-D, the stress tensor force calculation is a line integral whereas the Lorenz methods required a surface integral. In this section, the force equations for both the methods will be presented.

3.3.7.1 Tensor Force Calculation

As for the steady-state the transient normal and tangential force on the surface of the guideway ($y = b$) using Maxwell's stress tensor method are given by

$$F_x^t = \frac{w}{2\mu_0} \operatorname{Re} \int_{-\infty}^{\infty} [B_x^*(x, b, t)B_y(x, b, t)] d\xi \quad \text{on } \Gamma_{12} \quad (3.93)$$

$$F_y^t = \frac{w}{4\mu_0} \operatorname{Re} \int_{-\infty}^{\infty} [B_y^*(x, b, t)B_y(x, b, t) - B_x^*(x, b, t)B_x(x, b, t)] d\xi \quad \text{on } \Gamma_{12} \quad (3.94)$$

The transient thrust and lift force equations evaluated directly in the Fourier transform domain are

$$F_x^t = \frac{w}{4\pi\mu_0} \operatorname{Re} \int_{-\infty}^{\infty} [B_x^*(\xi, b, t)B_y(\xi, b, t)] d\xi \quad \text{on } \Gamma_{12} \quad (3.95)$$

$$F_y^t = \frac{w}{8\pi\mu_0} \operatorname{Re} \int_{-\infty}^{\infty} [B_y^*(\xi, b, t)B_y(\xi, b, t) - B_x^*(\xi, b, t)B_x(\xi, b, t)] d\xi \quad \text{on } \Gamma_{12} \quad (3.96)$$

where $B_y^*(\xi, b, t)$ and $B_x^*(\xi, b, t)$ are the complex conjugates of (3.87) and (3.86) respectively evaluated at $y = b$. The transient 2-D forces, F_x and F_y can also be written

directly in terms of the vector potential and source field components. These force equations are in the same form as for the steady-state model derived in section 2.3.9.1 except the vector potential and source fields are the function of time. The transient thrust and lift forces are given by

$$F_x^t = \frac{w}{4\pi\mu_0} \operatorname{Re} \int_{-\infty}^{\infty} [(j\xi A_z(\xi, b, t) B^{s*}(\xi, b, t))] d\xi \quad (3.97)$$

$$F_y^t = \frac{w}{8\pi\mu_0} \operatorname{Re} \int_{-\infty}^{\infty} [2\xi A_z(\xi, b, t) B^{s*}(\xi, b, t) - |B^s(\xi, b, t)|^2] d\xi \quad (3.98)$$

The thrust and lift forces are evaluated by substituting the vector potential (3.84) and the Fourier transformed source magnetic flux densities into (3.97) and (3.98) respectively.

3.3.7.2 Lorentz Force Calculation

The tangential force and normal force can also be evaluated by using the Lorentz formula [146, 153]. The force density in 2-D formulation where the current is assumed to have only z -components can be directly evaluated in the Fourier domain using the Parseval's theorem as

$$F_x^t = -\frac{w}{4\pi} \int_{-\infty}^{\infty} \int_0^b \operatorname{Re}[J_z(\xi, y, t) \cdot B_y^*(\xi, y, t)] dy d\xi \quad (3.99)$$

$$F_y^t = \frac{w}{4\pi} \int_{-\infty}^{\infty} \int_0^b \operatorname{Re}[J_z(\xi, y, t) \cdot B_x^*(\xi, y, t)] dy d\xi \quad (3.100)$$

where w is the width of the guideway and the current density, $J_z(\xi, y, t)$ is given by

$$J_z(\xi, y, t) = \sigma[v_x B_y(\xi, y, t) - E_z(\xi, y, t)] \quad (3.101)$$

3.3.7.3 Power Loss Calculation

The work done per unit time per unit volume which is the power delivered per unit volume is given by [153]

$$\frac{dW}{dt} = \int_v (\mathbf{E} \cdot \mathbf{J}) dV \quad (3.102)$$

Expanding (3.102), one can obtain [153]

$$\frac{dW}{dt} = -\frac{d}{dt} \int_v \frac{1}{2} \left(\epsilon_0 E^2 + \frac{1}{\mu_0} B^2 \right) dV - \frac{1}{\mu_0} \oint_s (\mathbf{E} \times \mathbf{B}) \cdot d\mathbf{S} \quad (3.103)$$

where \mathbf{E} and \mathbf{B} are the resultant electric and magnetic fields, V is the volume, ϵ_0 is the permittivity of free space and S is the close surface bounding V .

The steady-state power loss in the conductive guideway was evaluated in Chapter 2 by using the Poynting vector method and line integration. However, the same is not possible for the transient model because the total energy stored in the system which is given by the first integral on the right hand side of (3.103) is not constant during the transient. Unlike the steady-state model, the power transferred in the transient case is given by (3.103). Once the power transferred is known the power loss can be calculated using (2.145). However, the transient real power loss in the guideway in 2-D is not evaluated in this case using (3.103) instead it is evaluated using the surface integration (volume integration in 3D) over the conductive guideway region Ω_2 by using the following expression

$$P_{Loss}^t = \frac{\sigma}{2} \iint_{\Omega_2} |J_z(x, y, t)|^2 d\Omega_2 \quad (3.104)$$

The transient power loss can be directly evaluated in the Fourier domain using the

Parseval's theorem as

$$P_{Loss}^t = \frac{w\sigma}{4\pi} \int_{-\infty}^{\infty} \int_0^b \operatorname{Re}[J_z(\xi, y, t)J_z^*(\xi, y, t)] dy d\xi \quad (3.105)$$

3.3.8 Magnetic Source Field-A Halbach Rotor

The external rotor field created by the 2-D Halbach rotor for the steady-state modeling derived in section 2.3.11 is now modified by including the translational speed term into the rotor source field. Therefore, the time dependent magnetic flux densities of the Halbach rotor (2.168) and (2.169) becomes

$$B_y^{s1}(x, y, t) = \frac{C}{(x - v_{x1}t - j(y - y_o))^{P+1}} e^{j\omega_{e1}t} \quad (3.106)$$

$$B_x^{s1}(x, y, t) = \frac{jC}{(x - v_{x1}t - j(y - y_o))^{P+1}} e^{j\omega_{e1}t} \quad (3.107)$$

If the magnetic source is located at air-gap = g_1 , the y -axis offset given by (2.167) becomes

$$y_o = r_o + g_1 + b \quad (3.108)$$

then, the magnetic flux densities at $y = b$ (3.106) and (3.107) becomes

$$B_y^{s1}(x, b, t) = \frac{C}{(x - v_{x1}t + j(r_o + g_1))^{P+1}} e^{j\omega_{e1}t} \quad (3.109)$$

$$B_x^{s1}(x, b, t) = \frac{jC}{(x - v_{x1}t + j(r_o + g_1))^{P+1}} e^{j\omega_{e1}t} \quad (3.110)$$

3.3.8.1 Fourier and Laplace Transform for Rotor Source Field

The Fourier transform for the source field (3.109) and (3.110) is obtained by using the Fourier transform table given in [150]

$$B_x^s(\xi, b) = (-j)^P \frac{2}{P!} C \pi \xi^P e^{-\xi(g_1 + r_o)} e^{j(\omega_{e1} - \xi v_{x1})t} \mathbf{u}(\xi) \quad (3.111)$$

$$B_y^s(\xi, b) = (-j)^{P+1} \frac{2}{P!} C \pi \xi^P e^{-\xi(g_1+r_o)} e^{j(\omega_{e1}-\xi v_{x1})t} \mathbf{u}(\xi) \quad (3.112)$$

where $u(\xi)$ is the step function [149]. Laplace transforming (3.111) and (3.112) one can obtain

$$B_x^{s1}(\xi, b, s) = \frac{1}{2} \frac{B^{s1}(\xi, b)}{s - s_1} \quad (3.113)$$

$$B_y^{s1}(\xi, b, s) = -j B_x^{s1}(\xi, b, s) \quad (3.114)$$

where

$$B^{s1}(\xi, b) = B_x^{s1}(\xi, b) + j B_y^{s1}(\xi, b) = 2(-j)^P \frac{2}{P!} C \pi \xi^P e^{-\xi(g_1+r_o)} e^{j(\omega_{e1}-\xi v_{x1})t} \mathbf{u}(\xi) \quad (3.115)$$

$$s_1 = j(\omega_{e1} - \xi v_{x1}) \quad (3.116)$$

Similarly, the source function at $t = t_0$ at air-gap = g_0 can be written in the same format as (3.115) by

$$B^{s0}(\xi, b) = \frac{\pi}{6} C \xi^4 e^{-(r_o+g_0)\xi} \mathbf{u}(\xi) \quad (3.117)$$

3.4 Simulation Results and FEA Validations

In this section the results obtained by the analytic model derived in section 3.3 have been compared with the COMSOL FEA model developed in Appendix A and with a transient JMAG FEA model [160]. The vector potential field for this transient FEA model is illustrated in Figure 3.3. The JMAG model can only model the rotational or the translational motion but not simultaneously. In this transient model, only the rotational speed has been included. The parameters shown in Table 3.2 have been used to make these comparisons. Figure 3.4 shows the comparison for the lift and thrust forces when $v_x = 0 \text{ms}^{-1}$ and a step change in angular velocity from 0 RPM to 3000 RPM occurs at time $t = 0\text{s}$; this is then followed by a second step change in velocity from 0ms^{-1} to 10ms^{-1} at 15ms with the angular velocity being kept constant at 3000 RPM. The reduction in lift and thrust force after 15ms corresponds to the

decrease in slip value. Figure 3.5 shows the force comparison for the case when $v_x = 0\text{ms}^{-1}$ and a step change in angular speed from 0 to 1000 RPM occurs followed by a step change to 2000 RPM at $t = 15\text{ms}$. The FEA result in this comparison was obtained using the transient JMAG FEA model.

A power loss comparison for the case when $v_x = 0\text{ms}^{-1}$ and a step change in angular speed from 0 to 3000 RPM occurs followed by a step change to 5000 RPM at $t = 15\text{ms}$ is shown in Figure 3.6. Excellent agreement between the analytic and the FEA results has been achieved. The air-gap between the rotor and conductive guideway is held constant in these simulations. The integral in (3.95), (3.96) and (3.105) were evaluated using the Simpson's integration algorithm in Matlab numerically. The integration over ξ is carried out from $\xi = 0$ to 250 because the source field is negligible for $\xi > 250$ and is zero for $\xi < 0$ due to the step function in (3.117).

The lift and thrust force comparison for a step change in air-gap at $t = 15\text{ms}$ for $\omega_m = 1000\text{RPM}$ and $v_x = 0\text{ms}^{-1}$ is illustrated in Figure 3.7. Similarly, the lift and thrust force comparison for a step change in air-gap at $t = 15\text{ms}$ for $\omega_m = 0\text{RPM}$ and $v_x = 10\text{ms}^{-1}$ is illustrated in Figure 3.8.

Table 3.2: *Simulation parameters for 2-D transient model.*

Halbach Rotor	Outer radius, r_o	50 mm
	Inner radius, r_i	34.20 mm
	Width of rotor, w	100 mm
	Magnet (NdFeB), B_r	1.42 T
	Magnet relative permeability	1.08
	Pole-pairs, P	4
Conductive guideway	Guideway length ($\pm L$)	0.3 m
	Thickness, b	10 mm
	Guideway width	100 mm
	Air-gap between rotor and guideway, (g)	10 mm
	Conductivity, σ (Al)	$2.459 \times 10^7 \text{ Sm}^{-1}$

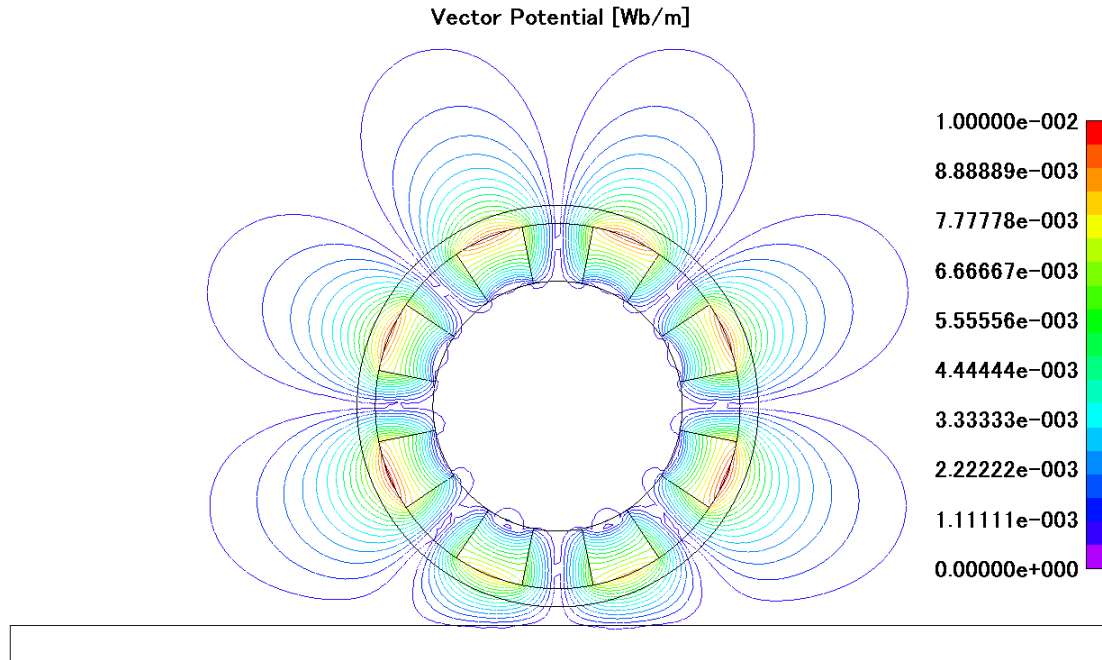


Figure 3.3: Vector potential fields for the transient JMAG model. The JMAG model could not model both rotational and translational motion of the rotor simultaneously. This model was used to verify the results in Figure 3.5.

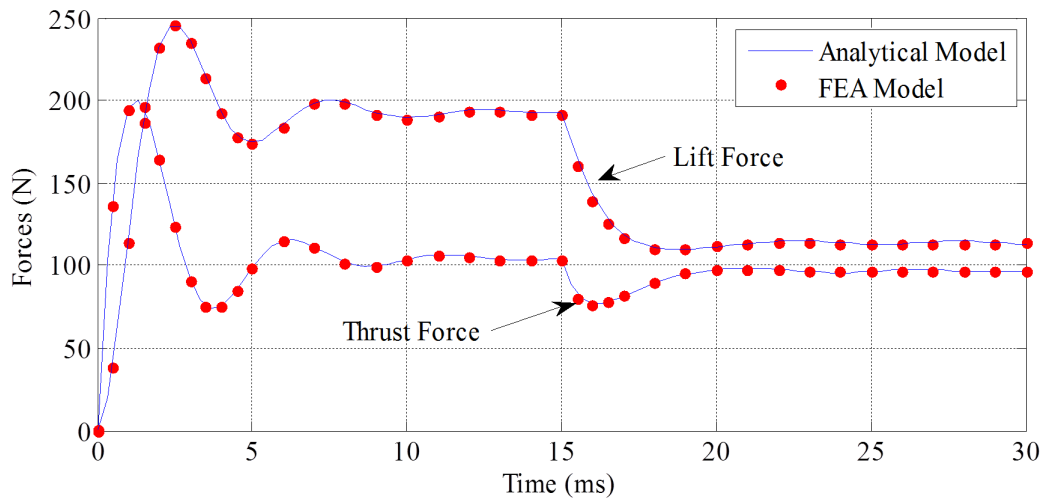


Figure 3.4: A comparison for the transient lift and thrust forces for a step change in angular velocity from 0 RPM to 3000 RPM with velocity 0 ms^{-1} at $t = 0 \text{ ms}$ and a second step change of velocity from $v_x = 0 \text{ ms}^{-1}$ to $v_x = 10 \text{ ms}^{-1}$ at $t = 15 \text{ ms}$ with angular velocity = 3000 RPM.

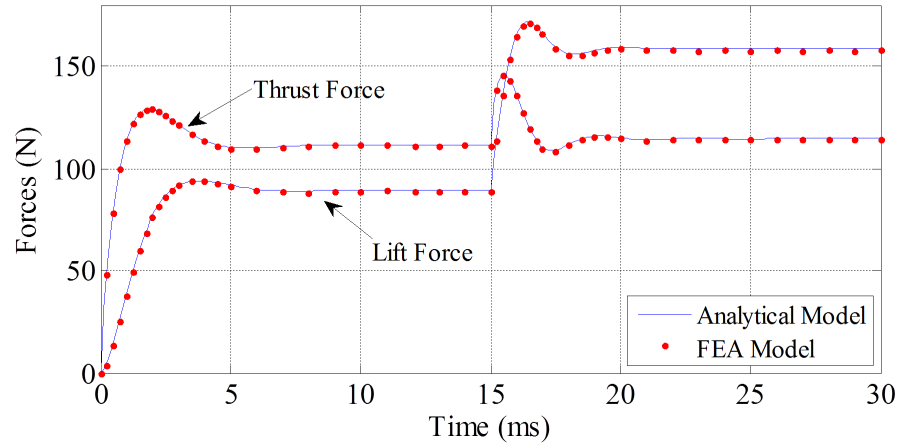


Figure 3.5: A comparison for the transient lift and thrust forces for a step change in angular speed from 0 RPM to 1000 RPM at $t = 0\text{ms}$ and step change from 1000 RPM to 2000 RPM at $t = 15\text{ms}$ at Velocity = 0ms^{-1} .

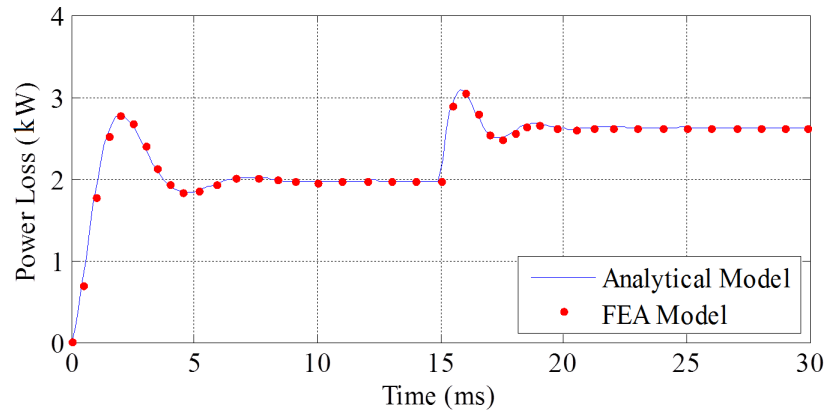


Figure 3.6: A comparison for the transient power loss for a step change in angular speed from 0 RPM to 3000 RPM at $t = 0\text{ms}$ and step change from 3000 RPM to 5000 RPM at $t = 15\text{ms}$. Velocity = 0ms^{-1} .

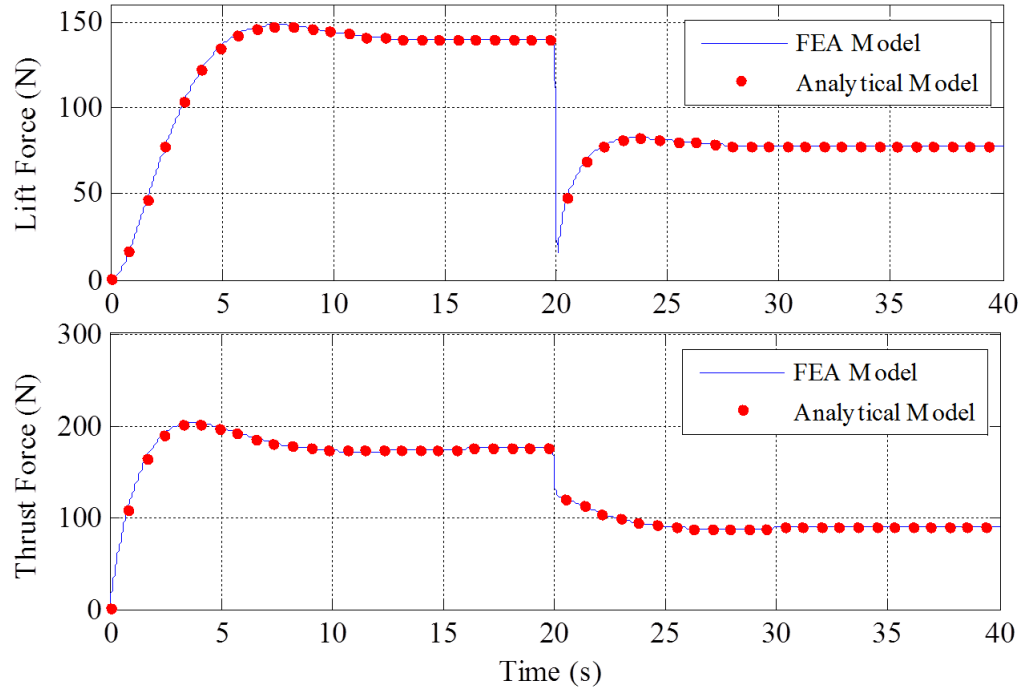


Figure 3.7: A comparison for the transient lift and thrust forces for a step change in air-gap from 10 mm to 15mm at $t = 15$ ms with $\omega_m = 1000\text{RPM}$, $v_x = 0\text{ms}^{-1}$.

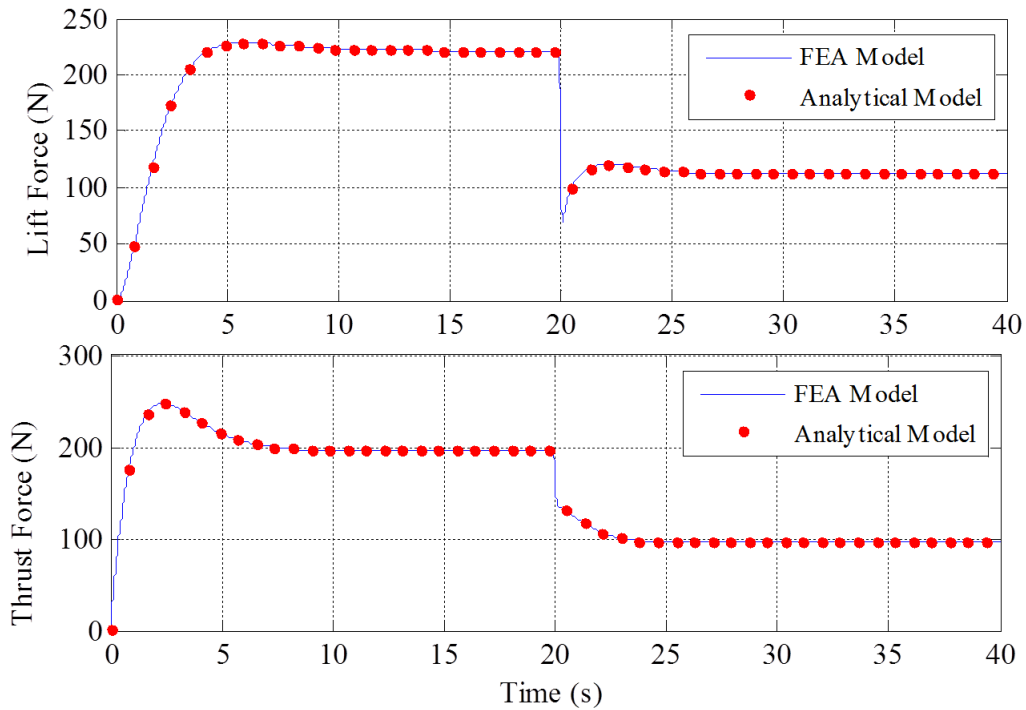


Figure 3.8: A comparison for the transient lift and thrust forces for a step change in air-gap from 10 mm to 15mm at $t = 15\text{ms}$ with $\omega_m = 0\text{RPM}$, $v_x = 10\text{ms}^{-1}$.

The COMSOL FEA surface plots of the vector potential, A_z in the guideway and

the contour plots of the magnetic flux density, B_x in non-conducting region for a step change in velocity, v_x from 0ms^{-1} to 10ms^{-1} while keeping the angular speed, $\omega_m = 0\text{RPM}$ are shown in Figure 3.9 and Figure 3.10. These results has been obtained with $g = 10\text{mm}$ at time 1ms and 5ms . The vector potential distribution as well as the magnetic flux distribution is different in these figures. The maximum value of vector potential and the magnetic flux density are higher in Figure 3.9 compared to Figure 3.10 showing that high current is induced during the step change.

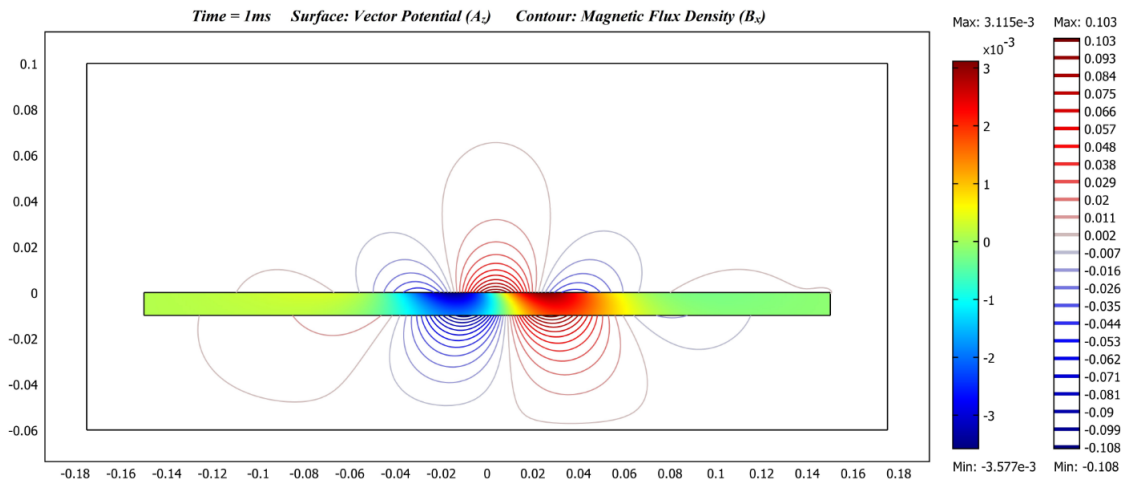


Figure 3.9: COMSOL FEA plot showing the surface plot of A_z in the guideway and contour plot of B_x in the air-region for a step change in v_x from 0ms^{-1} to 10ms^{-1} after 1ms . The angular speed is kept at 0RPM and $g = 10\text{mm}$.

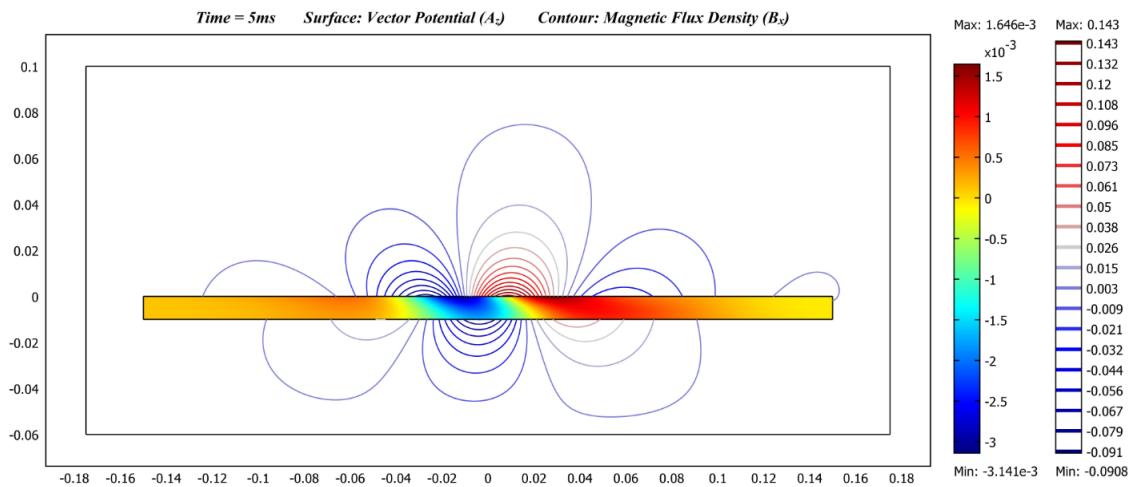


Figure 3.10: COMSOL FEA plot showing the surface plot of A_z in the guideway and contour plot of B_x in the air-region for a step change in v_x from 0ms^{-1} to 10ms^{-1} after 5ms . The angular speed is kept at 0RPM and $g = 10\text{mm}$.

3.4.1 FEA Model in Magsoft/Flux 2D

The 2D transient model of an EDW rotating above a conducting guideway has been created in a FEA software called Magsoft/Flux2D (v 10.4) in order to validate the analytic equations developed in section 3.3. In the analytic model, the Halbach rotor source field is considered as a smoothly varying sinusoidal waveform (refer section 3.3.8). However, in order to obtain an ideal sinusoidal waveform, a large number of magnet segments are required. In this section, three different configurations have been investigated. The 16 segments, 32 segments and 64 segments transient model of a 4 pole-pairs EDW as shown in Figures 3.11 - Figure 3.13 has been studied. The sample mesh plot of these EDW models has been illustrated in Figure 3.14. Since the Magsoft can model only one motion either rotation or translational at a time, only the rotational motion has been modeled. The model has been compared with the analytic model for step change in angular velocity of the EDW at constant air-gap and translational velocity, $v_x = 0\text{ms}^{-1}$. The material properties and the geometric properties of this model has been provided in the Table 3.3.

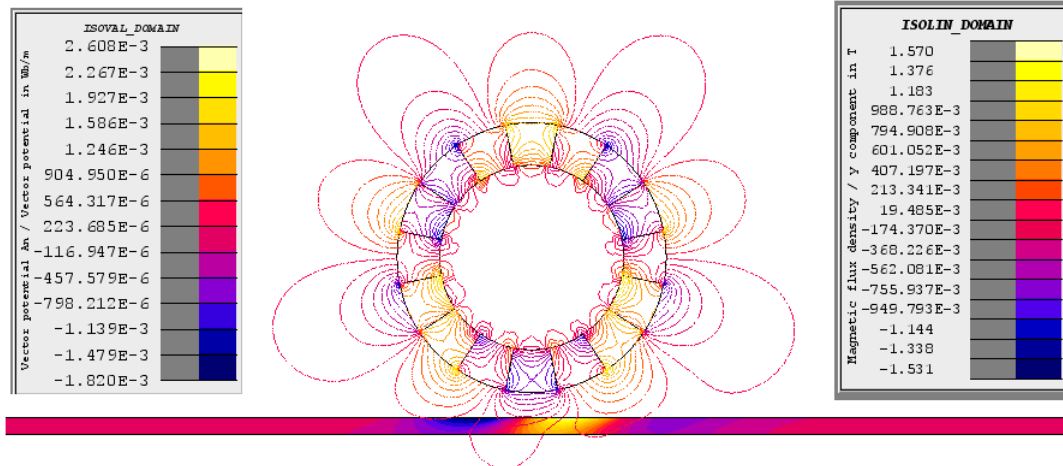


Figure 3.11: 2D FEA Magsoft model for a 16-segments 4 pole-pairs Halbach rotor rotating above an aluminum sheet guideway. The surface plot of the vector potential on the guideway region and the contour plot of the magnetic flux density, B_y in air and magnet region is shown in this figure.

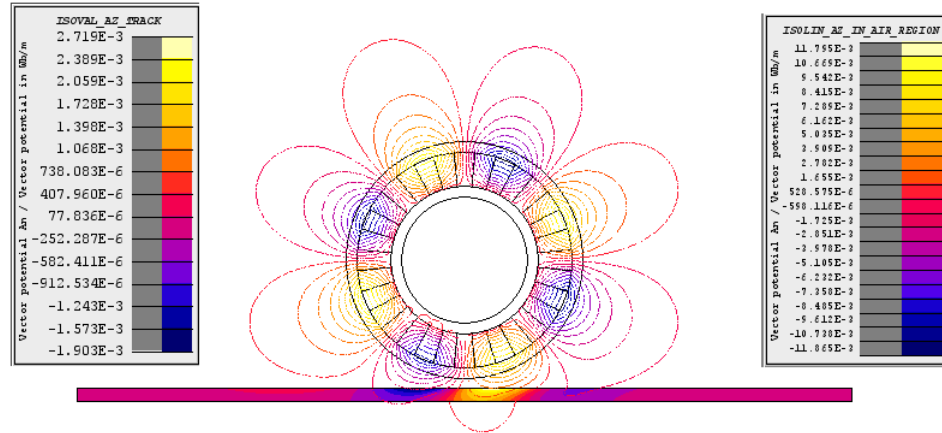


Figure 3.12: *FEA Magsoft model for a 32-segments 4 pole-pairs Halbach rotor rotating above an aluminum sheet guideway. The surface plot of vector potential in guideway region and the contour plot of the same on the air and magnet region is shown in this figure.*

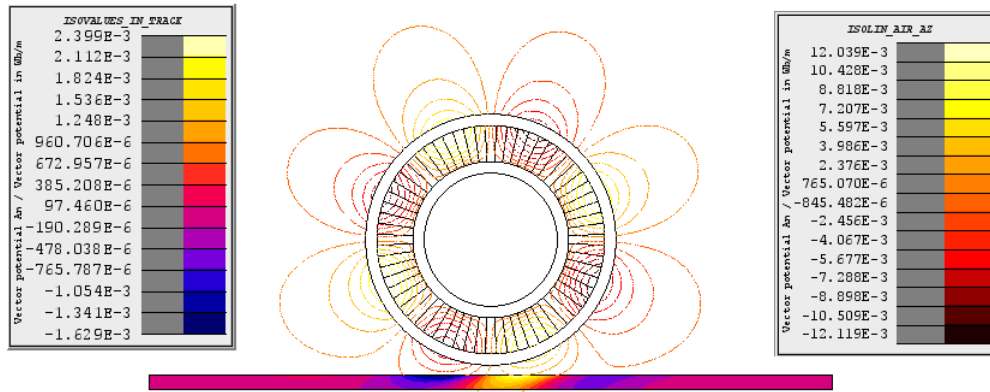


Figure 3.13: *FEA Magsoft model for a 64-segments 4 pole-pairs Halbach rotor rotating above an aluminum sheet guideway. The surface plot of vector potential in guideway region and the contour plot of the same on the air and magnet region is shown in this figure.*

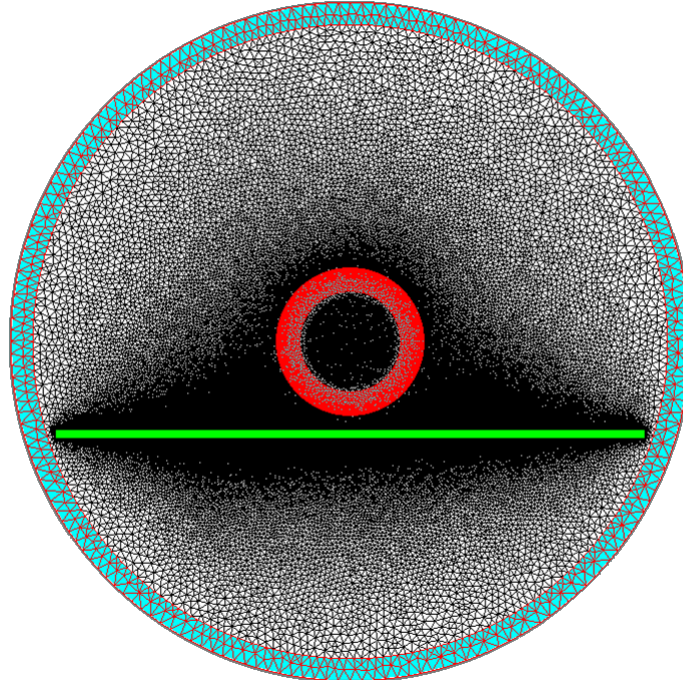


Figure 3.14: *The problem regions of the 2D transient Magsoft model with the mesh.*

Table 3.3: *Simulation Parameters for Magsoft Model.*

Halbach Rotor	Outer radius, r_o	50 mm
	Inner radius, r_i	34.20 mm
	Width of rotor, w	50 mm
	Magnet (NdFeB), B_r	1.42 T
	Magnet relative permeability	1.055
	Pole-pairs, P	4
Conductive guideway	Guideway length ($\pm L$)	0.4 m
	Thickness, b	10 mm
	Guideway width	50 mm
	Air-gap between rotor and guideway, (g)	9.5 mm
	Conductivity, σ (Al)	$2.459 \times 10^7 \text{ Sm}^{-1}$

The comparison between the force and power loss in the guideway between these three models has been done with the analytic model as well as COMSOL model. The 16 segments model is the most inaccurate model among the three Magsoft models. The 32 segments model is better than the 16 segments model. However, the 64 segments model is very close with the analytic model and COMSOL model because the source fields produced by this model are very smooth like an analytic fields equations

given by (3.113) and (3.114). In analytic model the Halbach rotor source field is modelled using only the fundamental component. With the 64 segments rotor, the fundamental components of the source field is very close to the fundamental component used in the analytic source fields. However, in the 16 segments and 32 segments rotors, the fundamental component is less compared with the analytic source fields. Therefore, these two models is giving less force compared with the 64 segments rotor.

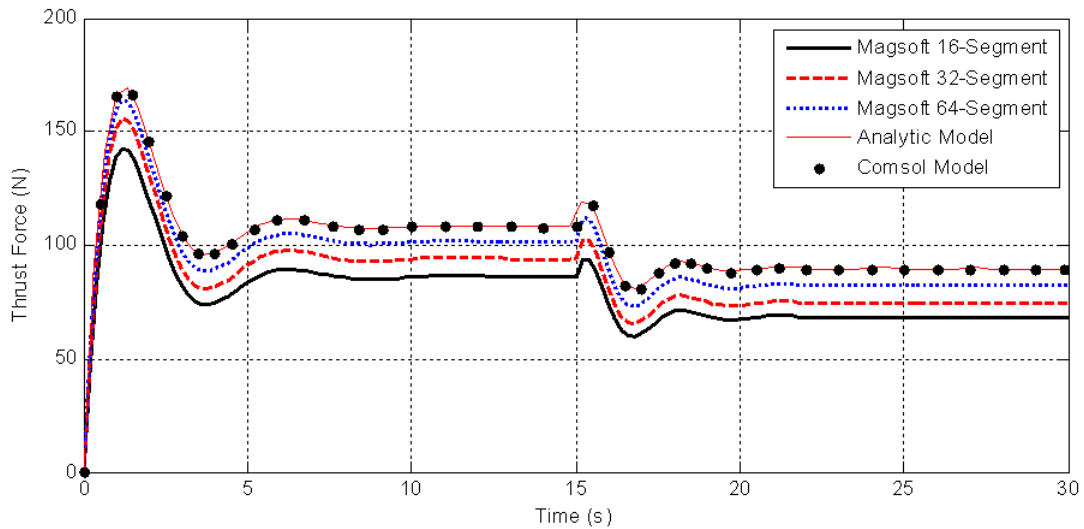


Figure 3.15: *The thrust force comparison between the Magsoft models, analytic model and COMSOL model for a step change in ω_m from 0 to 3000RPM at $t = 0s$ followed by the second step change in ω_m from 3000RPM to 5000RPM at $t = 15ms$.*

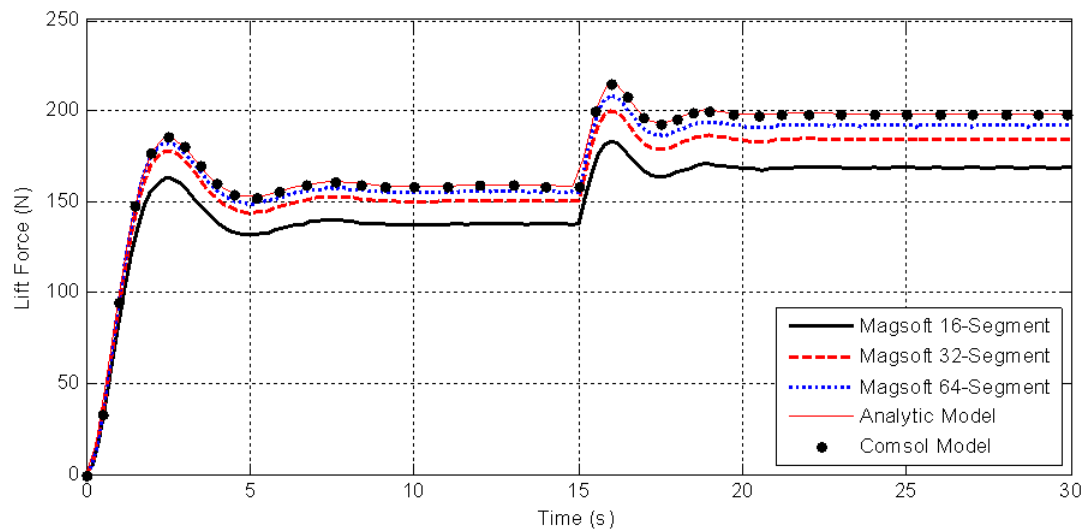


Figure 3.16: *The lift force comparison between the Magsoft models, analytic model and COMSOL model for a step change in ω_m from 0 to 3000RPM at $t = 0s$ followed by the second step change in ω_m from 3000RPM to 5000RPM at $t = 15ms$.*

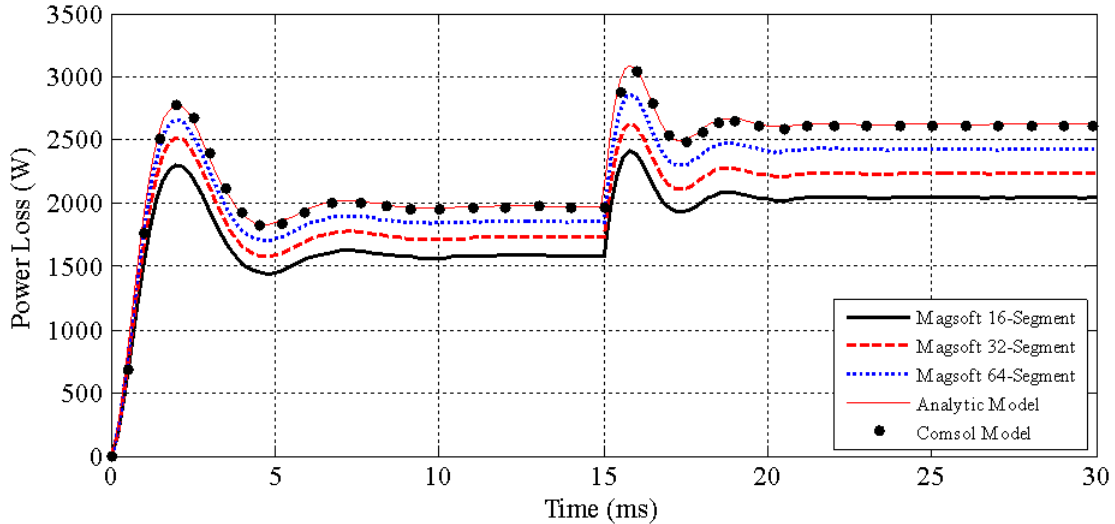


Figure 3.17: The power loss in the guideway comparison between the Magsoft models, analytic model and COMSOL model for a step change in ω_m from 0 to 3000RPM at $t = 0s$ followed by the second step change in ω_m from 3000RPM to 5000RPM at $t = 15ms$.

The comparison of the thrust force, lift force and the power loss in the guideway between the Magsoft models, Comsol model and the analytic model are illustrated in Figure 3.15 - Figure 3.17. These comparison plots were obtained for the case when air-gap is held constant at 9.5mm. The step change in ω_m from 0RPM to 3000RPM is applied at $t = 0s$ followed by the step change in the ω_m from 3000RPM to 5000RPM at $t = 15ms$ and $v_x = 0ms^{-1}$.

3.5 Summary

A 2-D transient formulation for a translationally moving and/or rotating Halbach rotor above a passive aluminum sheet guideway has been obtained by using the spatial Fourier transform and temporal Laplace transform method. The conductive region was solved for the vector potential whereas the air region was solved for the magnetic scalar potential. The time domain solution was obtained by utilizing the Heaviside expansion theorem to find the inverse Laplace transform.

The transient solution for the normal and tangential forces along the surface of the guideway was calculated by using Maxwell's stress tensor as well as Lorentz method. The force calculations were performed directly in the spatial Fourier domain by using

Parseval's theorem. This eliminates the need for inverse Fourier transforming. The performance of the derived equations were validated by comparing them with two different 2-D FEA transient models developed using COMSOL, JMAG and Magsoft softwares.

The eddy-current field equations are written in a general form so that other magnetic sources can be used. The computational time using this analytic model has been significantly reduced compared with the FEA model. Using a quad-core Dell precision T7400 PC the average force calculation time at one operating point using a COMSOL FEA was about 2.8522s while using the analytic based transient model the time was reduced to only 0.1026s. The developed transient model will be used to investigate the dynamic electromechanical simulation behavior of the EDW maglev vehicle.

CHAPTER 4: ELECTROMECHANICAL DYNAMIC SUSPENSION MODEL

4.1 Introduction

In this chapter, the dynamic behavior of the electromechanical model using EDW is presented. The electromagnetic part, the EDW model, is coupled with the mechanical part, the vehicle model, in order to investigate the dynamic behavior of the complete EDW Maglev vehicle. The steady-state and transient models of the EDW developed in Chapter 2 and Chapter 3 have been separately coupled to the mechanical vehicle model. The mechanical model has been developed in Matlab/Simulink using SimMechanicsTM and the analytical based wheel models are integrated in Simulink using s-functions. Both the steady-state as well as the transient coupled mechanical models have been studied for the step change in weight and the angular speed of the EDW.

In section 4.2 a brief review of the dynamic modeling for various maglev technologies published in different literature is presented. In section 4.3 a review of magnetic damping and stiffness is presented. The dynamic behavior of an EDW Maglev using the steady-state model is investigated in section 4.4. Similarly, the dynamic behavior of an EDW Maglev using the transient model is presented in section 4.5. The magnetic damping and stiffness of the EDW is evaluated analytically and investigated for a wide range of velocity, air-gap and RPM values in section 4.6. Finally, a summary of the chapter is presented in section 4.7.

4.2 Review on Dynamic Maglev Modeling

A comprehensive understanding of the vehicle dynamics is a crucial first step towards the design of an effective suspension system. It is also essential for the

development of the control laws for the successful operation of a Maglev system. Maglev system needs to satisfy the passenger safety and the ride quality requirements in order to be commercially viable. Therefore, it is essential to consider the dynamic as well as static stability as an integral part of Maglev design even for the concept development. The dynamic stability of EDS Maglev suspension systems have been investigated on large-scale vehicles, on linear test tracks, as well as on laboratory-scale setups. An excellent review of dynamic stability for EDS Maglev suspension systems is presented by Rote and Cai [63]. The dynamics and ride quality is often the last things that is considered in the design of a Maglev vehicle. If judiciously designed EDS Maglev systems are generally stable in steady-state operation; however, this is not true under the influence of nonsteady-state conditions. Therefore, various forms of active and passive damping mechanisms must be incorporated into the design to make the nonsteady-state operation stable.

The EDS Maglev as shown in Figure 4.1 used superconducting magnets and a continuous guideway. It was experimentally tested in 1970's by Coffey et al. [9] and it was determined to be stable within the operation velocity of 15ms^{-1} (three times the lift-off speed). Coffey also conducted experiments to compare the performance using active and passive damping coils and discovered that the active damping is more effective than passive damping and suggested that the passive damping could be used as a backup system in case of emergency when the active damping failed.

Several tests were performed by Iwahana et al. in 1980 [181] using the test vehicle with inverted-T cross-section guideway as shown in Figure 4.2. The vehicle contained 4 SCMs for propulsion and guidance and 4 SCMs for suspension. The vertically mounted coils for propulsion and null-flux for guidance were also included in the guideway. The vehicle was tested with a profile consisting of acceleration to a constant speed, running at constant speed and deceleration to rest. No instabilities were reported for the speed range of 38, 50 and 58ms^{-1} during these tests.

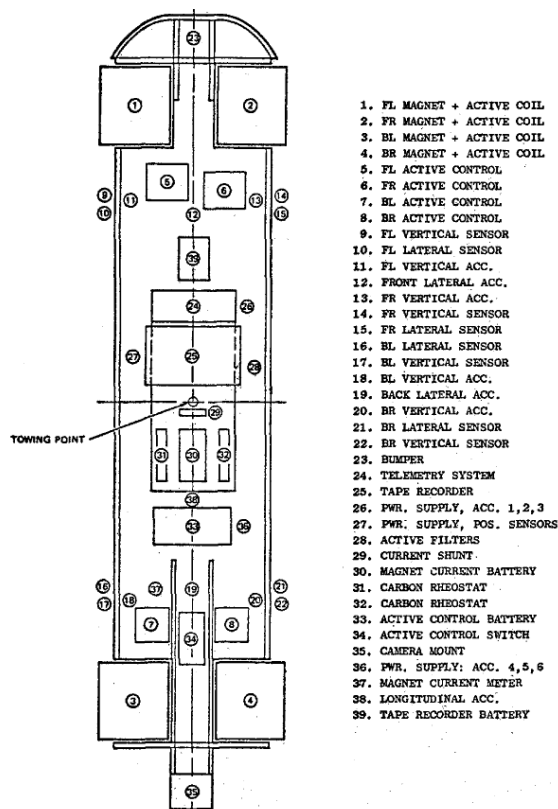


Figure 4.1: *The EDS Maglev using SCMs used by Coffey et al. [9].*

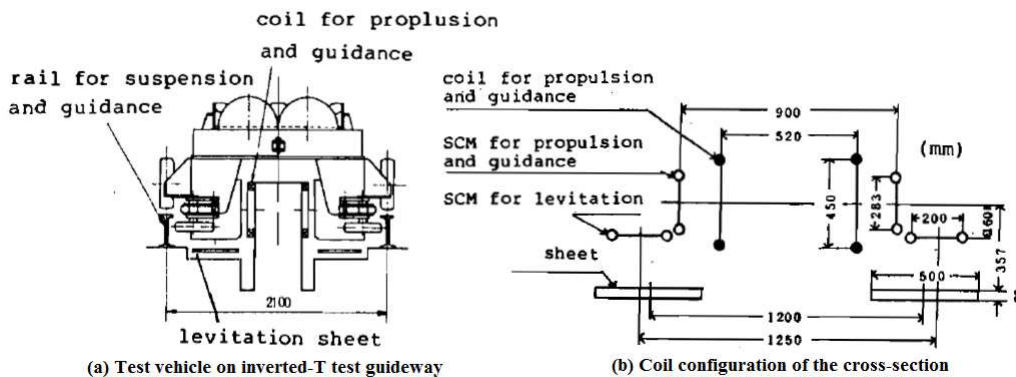


Figure 4.2: *Test vehicle using SCMs over a inverted-T test guideway [181].*

In the late 1970s, a 10-metric-ton test vehicle, ML-500 as shown in Figure 4.3, was tested over a discrete-coil guideway at the Miyazaki test track, Japan, in the speed range of 21ms^{-1} to 83ms^{-1} and no instabilities was observed. The Miyazaki test system was modified several times; different vehicle models such as MLU-001, MLU-002 and MLU-002N with additional passive damping were tested for guideway discontinuities

[182] as well. No instabilities were reported during these tests. The topologies and the pictures of these test vehicles are shown in Figure 4.4 - Figure 4.6.

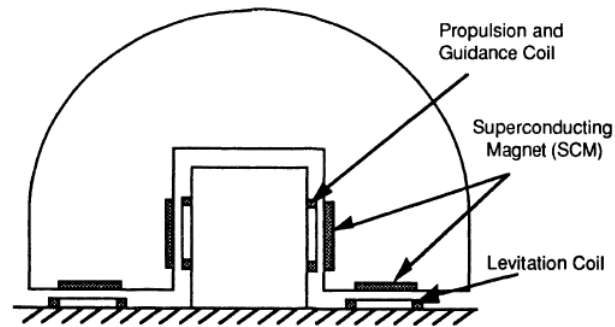


Figure 4.3: *Cross-section of ML-500 test vehicle with inverted-T-shaped guideway configuration* [14].

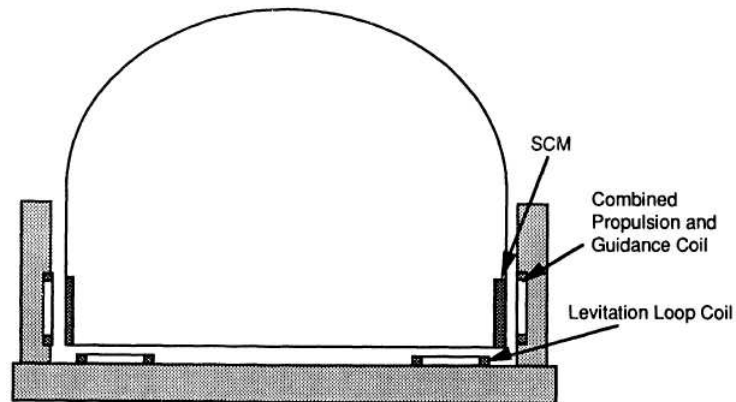


Figure 4.4: *Cross-section of MLU001 test vehicle with a U-shaped guideway configuration, levitation coils on the ground, and combined propulsion and guidance coils on the side wall* [14].

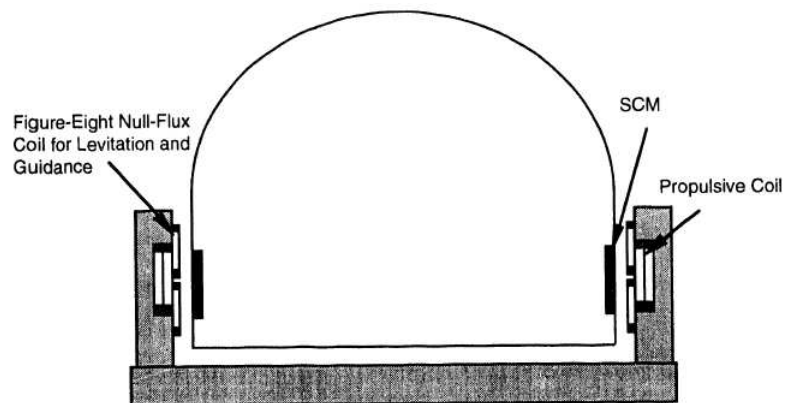


Figure 4.5: *Cross-section of MLU002 test vehicle with side wall null-flux levitation system* [14].

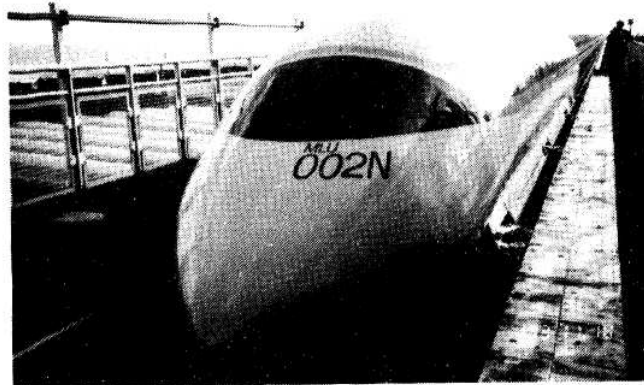


Figure 4.6: *MLU002N test vehicle photo* [14].

The full-scale passenger test Maglev vehicle, MLX01 (as shown in Figure 4.7 located at the Yamanashi test track was reported to have a coupled roll-lateral instability at low-speed. The authors defined this instability as a static instability and is due to the fact that guideway force is not sufficiently stiff to limit the coupled roll-lateral instability at low-speed. However, this kind of instability was not observed at high-speed [183].



Figure 4.7: *Photo of MLX01 test vehicle at Yamanashi test track* [65].

A coupled lateral roll-yaw instability was reported by Moon when the experimental vehicle as shown in Figure 4.8 modeled with 3-degree of freedom was levitated above a V-shaped rotating aluminum guideway [170, 184]. This instability was caused by a coupling of the lateral and roll motions to yaw through the magnetic drag.

The laboratory Maglev vehicle consisting of a segmented inverted T-shaped aluminum track and PMs moving above an adjustable speed guideway as shown in Figure 4.9 was investigated by Chu and Moon [186]. The authors found a coupled yaw-lateral

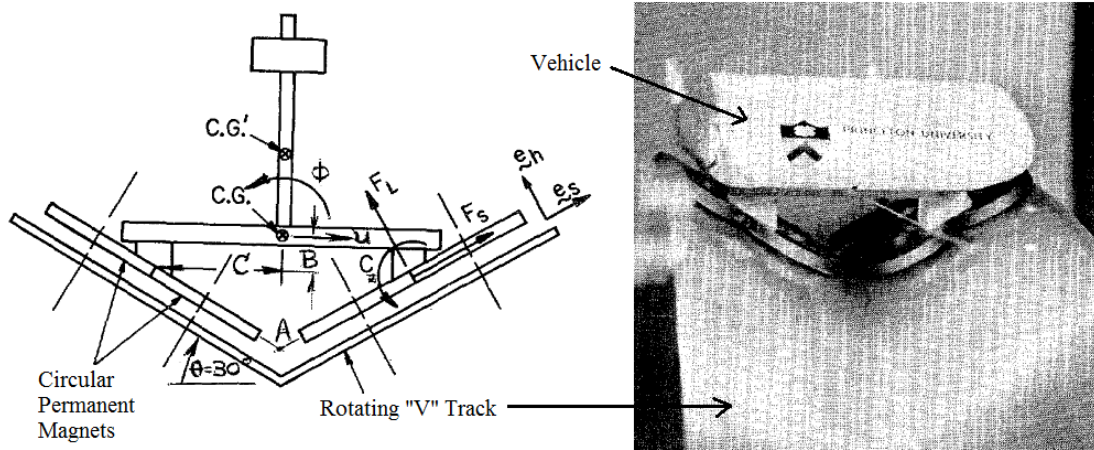


Figure 4.8: Sketch and a picture of a PM levitated Maglev in a V-shaped guideway [185].

vibration resulting in both divergence and flutter. The divergence lead to two stable equilibrium yaw positions whereas the flutter instability lead to a limit cycle oscillation coupling yaw and lateral motion around the drag-peak.

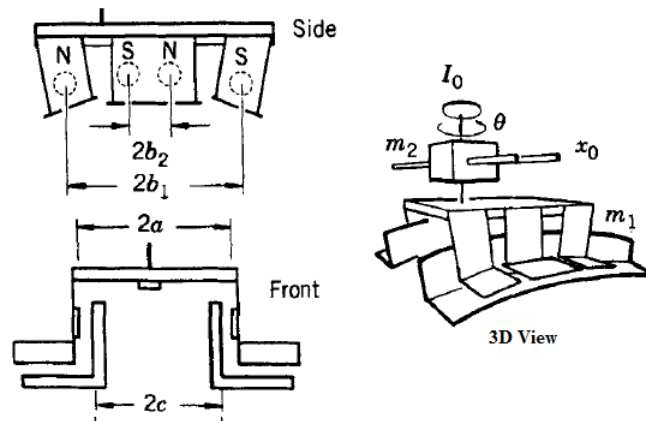


Figure 4.9: Sketch of Maglev model used by Chu and Moon [186].

The study of laboratory scale EDS Maglev at Argonne National Laboratory (ANL) in the 1990's demonstrated a variety of complex motions and instabilities experimentally [186–188]. Divergence and flutter motion was obtained analytically and numerically for coupled vibration of a 3-DOF Maglev vehicle shown in Figure 4.10. In addition, instabilities in five directions were observed when the 5-DOF (vertical heave, lateral slip, pitch, yaw and roll) vehicle system as shown in Figure 4.11 was translationally moved above a double L-shaped continuous aluminum guideway. In

this experiment, the system parameters such as system damping, vehicle geometry and the coupling effects between degrees of freedom were identified as key factors that caused the dynamic instabilities in the EDS Maglev [189].

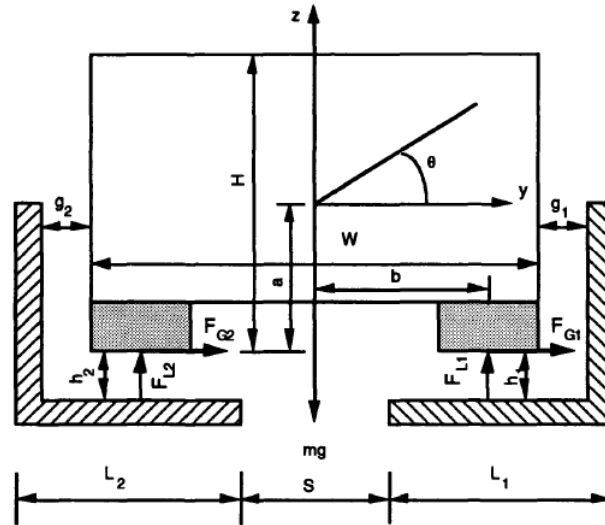


Figure 4.10: A 3-DOF Maglev system on a double L-shaped aluminum guideway [190].

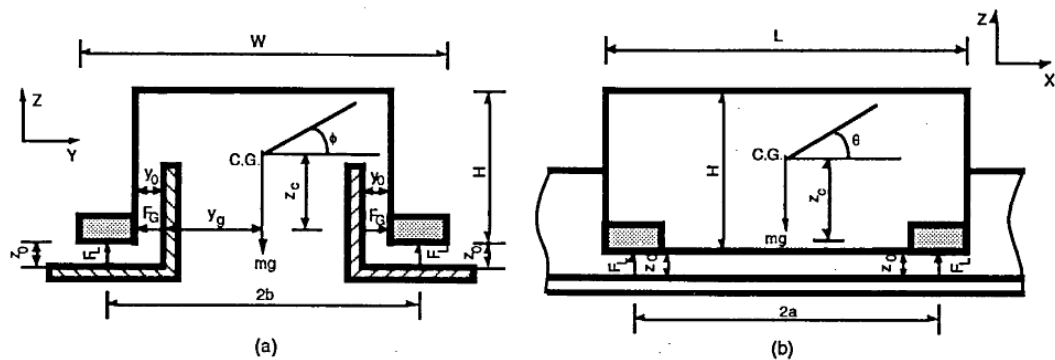


Figure 4.11: Maglev vehicle on double L-shaped aluminum sheet guideway: (a) Front view; (b) Side view.

Han theoretically investigated the dynamics of the EDS Maglev system using a linear permanent magnet Halbach array and proposed a control system to effectively stabilize the system [191, 192].

4.3 Magnetic Damping and Stiffness

Magnetic damping is one of the important parameters that determines the dynamic response and the stability of the Maglev system. The damping can be active

and passive. The magnetic damping inherent in a magnet-moving EDS or EMS system in the absence of any external damping is called intrinsic magnetic damping. A number of studies have found that the intrinsic magnetic damping decreases with increases in the translational velocity and it has been found to sometimes become negative for speeds greater than a characteristic velocity; resulting in self-excited vehicle oscillations [56, 59, 60, 184]. For example, Iwamoto et al. [59] theoretically examined the intrinsic magnetic damping between SCMs and a loop-guideway for a full scale EDS Maglev. The analysis was performed for both constant current and constant flux modes of the SCMs. The authors found that the damping was only not negative at extremely low velocities and suggested that the negative damping could be overcome by the addition of passive damper coils placed inside the cryostats [59].

Yamada et al. investigated the damping of superconducting coils aboard a Maglev vehicle and short-circuited coils arranged along a guideway [60]. The authors also demonstrated the existence of negative intrinsic damping using the experimental setup shown in Figure 4.12. This pendulum setup was comprised of a magnet array supported by a string that was free to move normal to the surface of the rotating aluminum guideway.

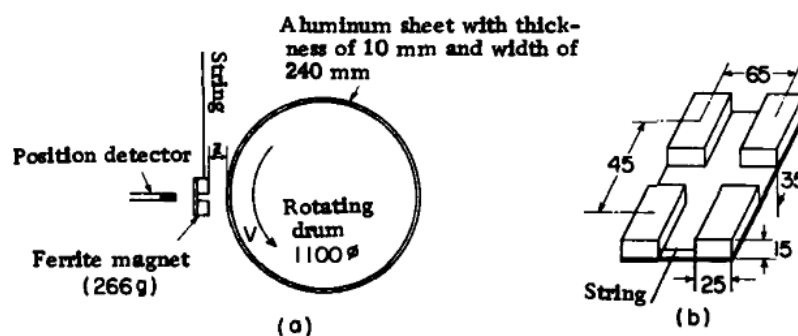


Figure 4.12: *Pendulum experimental setup to determine a magnetic damping* [60].

A similar pendulum setup used by Moon to investigate magnetic damping is illustrated in Figure 4.13-(a) [170, 184]. In this experiment a magnet was mounted to a stiff cantilevered bean of natural frequency 22Hz in order to keep the air-gap small

even when the normal force is developed. The aerodynamic as well as structural damping was also measured to accurately estimate the magnetic damping. Moon found that negative intrinsic damping existed at speeds higher than a critical velocity. Although the calculated critical velocity was less than the measured one, yet the result clearly showed the measured damping decreased and become negative with an increase in speed. The calculated result for damping vs speed showing negative intrinsic damping is illustrated in Figure 4.13-(b).

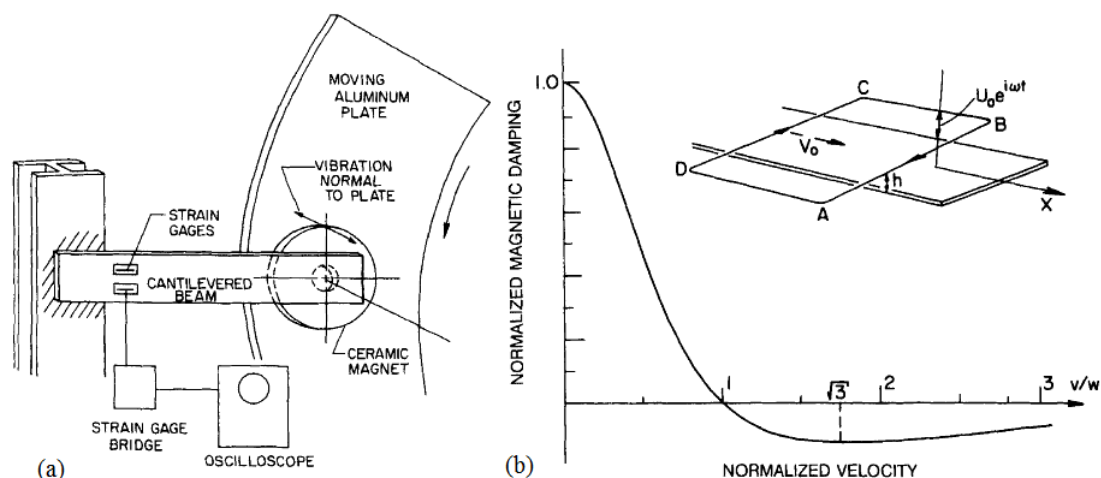


Figure 4.13: *Magnetic damping measurement (a) Experimental setup (b) Magnetic damping vs velocity* [184].

In these above mentioned investigations, the dynamic response of the system supported by or subjected to magnetic force were either measured or analyzed. The magnetic damping was calculated from the system response. This is called the indirect method of measuring magnetic damping [193]. The method to calculate the magnetic damping by using the eddy-current losses [194] or magnetic force due to an arbitrary motion [56] is a direct method based on quasi-steady motion.

The method used to measure the magnetic damping and stiffness at ANL is a direct method based on the unsteady-motion theory [187, 193, 195]. This method is capable of measuring the self and mutual magnetic damping. A series of tests were conducted in the 1990's at ANL to determine the effect of various parameters such as conductivity, air-gap, excitation amplitude and frequency on the magnetic damping

and stiffness. The experimental setup shown in Figure 4.14 consisted of a rotating drum, shaker, force transducer and magnet. The experiments again demonstrated that negative intrinsic damping for velocity greater than a characteristic velocity existed. It was suggested that the measured magnetic damping and stiffness could be used to investigate Maglev vehicle dynamics.

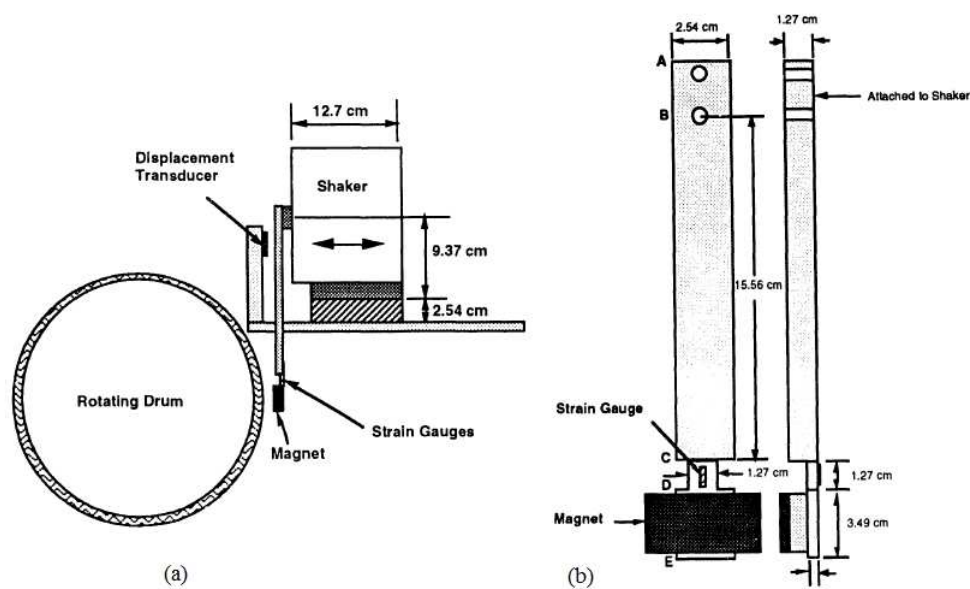


Figure 4.14: *Magnetic damping and stiffness calculation setup at ANL (a) Schematic diagram (b) Force transducer and magnet support [193].*

The magnetic damping forces and vehicle dynamic computer simulation model of a 1-D discrete coil has been developed [196]. The negative damping behavior has been reported in this computer simulation. The magnetic damping of a figure-eight-shaped null-flux coil was analytically studied by He and Coffey in 1997 [197]. The close form expression of the magnetic damping as a function of heave-and-sway was derived using dynamic circuit theory. The authors found that the vertical intrinsic magnetic damping existed and was maximum at the null-flux position and decreased with the heave velocity.

From the above review it is clear that the lift, drag and the guidance forces produced in EDS Maglev system are highly dependent on position and velocities. Therefore, it is very important to derive the forces equations in terms of the position

and velocity in order to investigate the motion-dependent force i.e. the intrinsic magnetic damping force. The motion-dependent forces of the EDW derived in earlier chapters are now coupled with the mechanical vehicle models in order to investigate the dynamic behavior of an EDS Maglev using EDWs.

4.4 Dynamic Modeling Using Steady-State Force Equations

The steady-state thrust and lift force equations developed in Chapter 2 will be utilized in this section in order to investigate the dynamic behavior of an EDW Maglev. An electromechanical model using four EDWs has been created in the Matlab Simulink environment. Each EDW is connected to the vehicle through a drive shaft. The traction motors have not been included in this model. However, the torque is directly applied to the drive shafts. The basic configuration of the vehicle is shown in Figure 4.15. The block diagram for the integration of the EDW model and vehicle model is shown in Figure 4.16. Since, the model is simulated using only 2-DOF, only the variation in the vehicle gap, g in the y -axis, and variation in x -direction is considered. The vehicle's y -axis motion acts like an electromechanical nonlinear spring mass system [198]

$$m \frac{d^2 g(t)}{dt^2} = F_y(t) - F_g \quad (4.1)$$

where

F_g = gravitational force

m = mass of vehicle and the rotor magnets.

The equation of motion in the x -direction is given by

$$m \frac{d^2 x(t)}{dt^2} = F_x(t) - F_d(t) \quad (4.2)$$

where $F_x(t)$ is the thrust force and F_d is the aerodynamic drag force. The aerodynamic drag force is proportional to the square of translational velocity and frontal area as

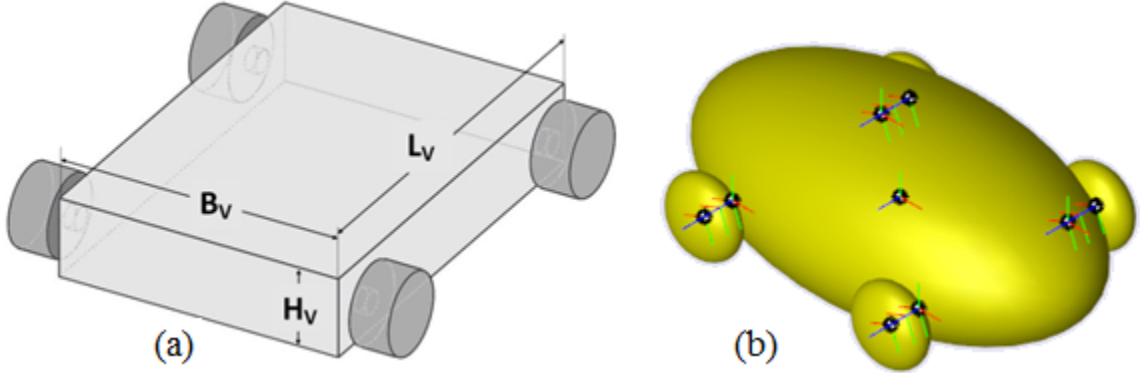


Figure 4.15: (a) The maglev vehicle used for simulation, where B_v , H_v and L_v are the breadth, height and length of the vehicle. (b) Simulink SimMechanicsTM EDW Maglev vehicle.

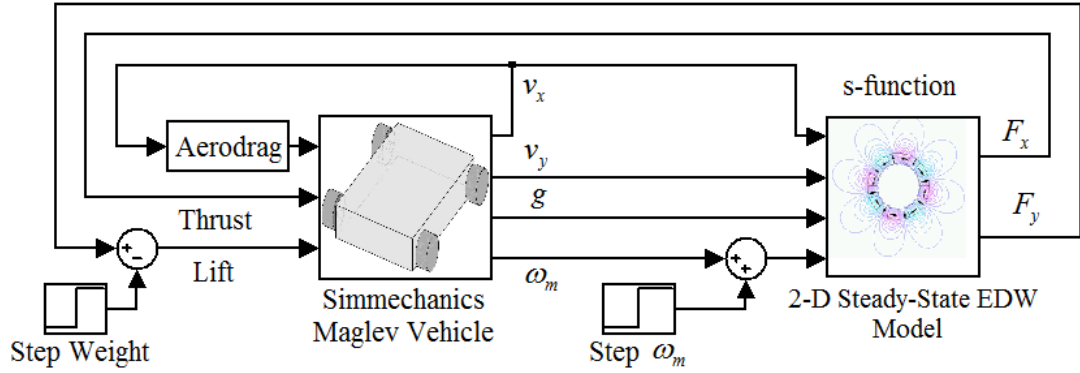


Figure 4.16: The block diagram showing EDW steady-state model coupled with the mechanical vehicle model. The heave velocity is also included in this model.

given by [198]

$$F_d = 0.5\rho C_d A v_x(t)^2 \quad (4.3)$$

where

ρ = density of air,

C_d = aerodynamic drag coefficient,

A = frontal area of the vehicle.

The aerodynamic and structural damping is not included in this model. The parameters used for the vehicle model and EDW model are given in Table 4.1. The steady-state thrust, (2.104), and lift, (2.115) are written as a s-function in Matlab and incorporated into Simulink. The F_x and F_y outputs from the EDW model have been

coupled to the Maglev vehicle model along with the aerodynamic drag. The vehicle outputs, v_x , v_y , g and ω_m are feed back into the EDW model block. Thus, the EDW model utilizes these parameters to calculate the forces, F_x and F_y at the next time step. In this way, a close loop is formed between the vehicle and the electromagnetic EDW model for each simulation time step.

Table 4.1: *Parameters for 2-DOF Maglev vehicle dynamic simulation.*

Vehicle	Length of the vehicle, L_V	40 cm
	Breadth of the vehicle, B_V	20 cm
	Height of the vehicle, H_V	10 cm
	Thickness of vehicle, T_V	4 cm
	Frontal area of the vehicle. A	0.0476 m ²
	Density of iron, ρ_{Fe}	7.93 gm-cm ⁻³
	Length of drive shaft, L_{DS}	4 cm
	Radius of drive shaft, R_{DS}	1cm
	Total Weight of vehicle of Figure 4.15	21.38 kg
	Aerodynamic drag coefficient, C_d	0.25 kgs ⁻¹
Halbach rotor	Outer radius, r_o	50 mm
	Inner radius, r_i	34.20 mm
	Width, w	50 mm
	Magnet (NdFeB), B_r	1.42 T
	Magnet relative permeability	1.08
	Pole-pairs, P	4
Conducting plate	Conductivity (Al)	2.459×10^7 Sm ⁻¹
	Single sheet width	50 mm
	Thickness, b	10 mm
	Air-gap between rotor and plate, g	10 mm

The dynamic simulation has been performed for two different step change disturbances. The first one is for a step change in angular speed and later for a step change in the weight of the vehicle. The simulation results obtained will be compared with the transient model in the following section.

4.5 Dynamic Modeling Using Transient Force Equations

In section 3.3 the 2-D transient eddy-current forces due to a step change in angular velocity, translational velocity or air-gap of a source field were derived. In order to form the dynamic electromechanical model the transient eddy-current model must

be coupled to the transient mechanical model. Therefore, the transient eddy-current model must be capable of predicting forces for continuous changes in the operating inputs such as ω_m , v_x or g from non-steady state initial conditions. In this section the transient model presented in section 3.3 will be extended so that it can account for continuous changes in the source input rather than just a single step change in the source input parameters.

Referring to section 3.3.2 it can be noted that the Fourier and Laplace transformed vector potential differential equation (3.20) in region Ω_2 , for the case when initially no field is present in the guideway, $A_z^{ss}(\xi, y, t_0) = 0$ at $t = 0$ s, will be

$$\frac{\partial^2 A_z(\xi, y, s)}{\partial y^2} = \alpha^2 A_z(\xi, y, s) \quad (4.4)$$

Following the same procedure as undertaken to derive the solution from (3.20) to (3.46), the solution of the vector potential in the Fourier-Laplace domain can be obtained for $A_z^{ss}(\xi, y, t_0) = 0$ as

$$A_z^t(\xi, y, s) = T^t(\xi, y, s)B^s(\xi, b, s) \quad (4.5)$$

where the transmission function $T^t(\xi, y, s)$ is defined in (3.47). The solution (4.5) is the vector potential solution for any arbitrary source $B^s(\xi, b, s)$. The step response of unity vector potential can therefore be obtained by making $B^s(\xi, b, s)$ a unit step input. The step response as well as impulse response of the vector potentials is derived in the following section.

4.5.1 Vector Potential Step and Impulse Response

If the source field is a unit-step

$$B^s(\xi, b, s) = \frac{1}{s} \quad (4.6)$$

then by using (4.5) and following the derivation method given in section 3.3.5 the vector potential field at $y = b$ is

$$A_z^{step}(\xi, b, t) = A_1 u(t) + \sum_{n=0}^9 (A_t^n e^{s_t^n t} + A_c^n e^{s_c^n t}) \quad (4.7)$$

where

$$A_1 = T(\xi, b, 0) = 1/(2\xi) \quad (4.8)$$

$$A_t^n = -\frac{8k_t^n}{\mu_o \sigma b^3 \xi^2} \frac{(2k_t^n \cot(2k_t^n) + b\xi)}{s_t^n (-\lambda k_t^n + \cot(k_t^n)) (\lambda + \sec^2(k_t^n))} \quad (4.9)$$

$$A_c^n = \frac{8k_c^n}{\mu_o \sigma b^3 \xi^2} \frac{(2k_c^n \cot(2k_c^n) + b\xi)}{s_c^n (\lambda + \csc^2(k_c^n)) (\lambda k_c^n + \tan(k_c^n))} \quad (4.10)$$

and the time constants are

$$s_q^n = - \left[\left(\frac{2k_q^n}{b} \right)^2 + \xi^2 \right] \frac{1}{\mu_o \sigma} \quad (4.11)$$

the subscript $q = t$ or c denoted for *tan* or *cot*. The impulse response can be obtained from the step response solution. Inverse Laplace transforming (4.7) and multiplying through by s gives

$$A_z^{imp}(\xi, b, s) = A_1 + \sum_{n=0}^9 \left(\frac{A_t^n s}{s - s_t^n} + \frac{A_c^n s}{s - s_c^n} \right) \quad (4.12)$$

inverse Laplace transforming (4.12) using the Heaviside expansion theorem, one obtains

$$A_z^{imp}(\xi, b, t) = A_1 \delta(t) + \sum_{n=0}^9 (A_t^n + A_c^n) \delta(t) + \sum_{n=0}^9 A_t^n s_t^n e^{s_t^n t} + A_c^n s_c^n e^{s_c^n t} \quad (4.13)$$

The transient response due to an arbitrary source change $\Delta B^s(\xi, b, \tau)$ at any point in time can be obtained by utilizing the convolution integral of the impulse response

[150]

$$A_z(\xi, b, t) = \int_0^t \Delta B^s(\xi, b, \tau) A_z^{imp}(\xi, b, t - \tau) d\tau \quad (4.14)$$

Substituting (4.13) into (4.14) gives

$$\begin{aligned} A_z(\xi, b, t) = & \int_0^t \Delta B^s(\xi, b, \tau) \left((A_1 + \sum_{m=0}^9 (A_t^m + A_c^m)) \delta(t - \tau) \right. \\ & \left. + \sum_{n=0}^9 (A_t^n s_t^n e^{s_t^n(t-\tau)} + A_c^n s_c^n e^{s_c^n(t-\tau)}) \right) d\tau \end{aligned} \quad (4.15)$$

The y -component flux density transient response on the conducting plate for an arbitrary input on Γ_{12} is obtained by using (2.77), this gives

$$B_y(\xi, b, t) = -\frac{\partial A_z(\xi, b, t)}{\partial x} = -j\xi A_z(\xi, b, t) \quad (4.16)$$

To find $B_x(\xi, b, t)$ for an arbitrary input on Γ_{12} the impulse response for B_x must first be obtained; it is given by

$$\begin{aligned} B_x^{imp}(\xi, b, t) &= \left. \frac{\partial A_z^{imp}(\xi, y, t)}{\partial y} \right|_{y=b} \\ &= \frac{\delta(t)}{2} + \sum_{m=0}^9 (C_t^m + C_c^m) \delta(t) + C_t^m s_t^m e^{s_t^m t} + C_c^m s_c^m e^{s_c^m t} \end{aligned} \quad (4.17)$$

where

$$C_t^m = \frac{-8k_t^m}{\mu_o \sigma b^2} \frac{(2k_t^m/b\xi)^2 - (2k_t^m/b\xi) \cot(2k_t^m)}{s_t^m [-\lambda k_t^m + \cot(k_t^m)] [\lambda + \sec^2(k_t^m)]} \quad (4.18)$$

$$C_c^m = \frac{8k_c^m}{\mu_o \sigma b^2} \frac{(2k_c^m/b\xi)^2 - (2k_c^m/b\xi) \cot(2k_c^m)}{s_c^m [-\lambda k_c^m + \cot(k_c^m)] [\lambda + \sec^2(k_c^m)]} \quad (4.19)$$

Using (4.17) the transient response for the x -component of the magnetic flux density due to any arbitrary input, $\Delta B^s(\xi, b, \tau)$ can be obtained by utilizing the convolution

integral of the impulse response as

$$B_x(\xi, b, t) = \int_0^t \Delta B^s(\xi, b, \tau) B_x^{imp}(\xi, b, t - \tau) d\tau \quad (4.20)$$

Substituting (4.17) into (4.20) gives

$$\begin{aligned} B_x(\xi, b, t) = & \int_0^t \Delta B^s(\xi, b, \tau) \left(\frac{\delta(t - \tau)}{2} + \sum_{m=0}^9 (C_t^m + C_c^m) \delta(t - \tau) \right. \\ & \left. + \sum_{m=0}^9 (C_t^m s_t^m e^{s_t^m(t-\tau)} + C_c^m s_c^m e^{s_c^m(t-\tau)}) \right) d\tau \end{aligned} \quad (4.21)$$

The transient forces are calculated from the equations derived in section 3.3.7.1 by using the vector magnetic flux densities given by (4.16) and (4.21).

4.5.2 Validation of Transient Analytic Model Using FEA

An electromechanical model used to investigate the dynamic suspension behavior of an EDW Maglev using 2-D transient analytic force is illustrated in Figure 4.17. As in the steady-state case (section 4.4) the vehicle is modeled using SimMechanics™ whereas the EDW is modeled as an s-function. All the other modeling assumptions are the same as for the steady-state case except that the heave velocity is not included in the transient EDW model and of course time, t , is included in the transient EDW model. This model is also investigated for a step change in weight as well as for a step change in angular velocity. The simulation results are presented in section 4.5.3 and section 4.5.4.

The transient model developed in section 4.5.1 for continuous changes in input conditions was validated by comparing it with an analogous FEA transient model. The FEA model developed in Appendix A has been modified to account for the continuous change in input conditions of v_x , g and ω_m . This modified FEA model was then integrated to the mechanical vehicle model developed in SimMechanics™. This FEA model developed in COMSOL V3.5 is integrated with the Matlab/Simulink in

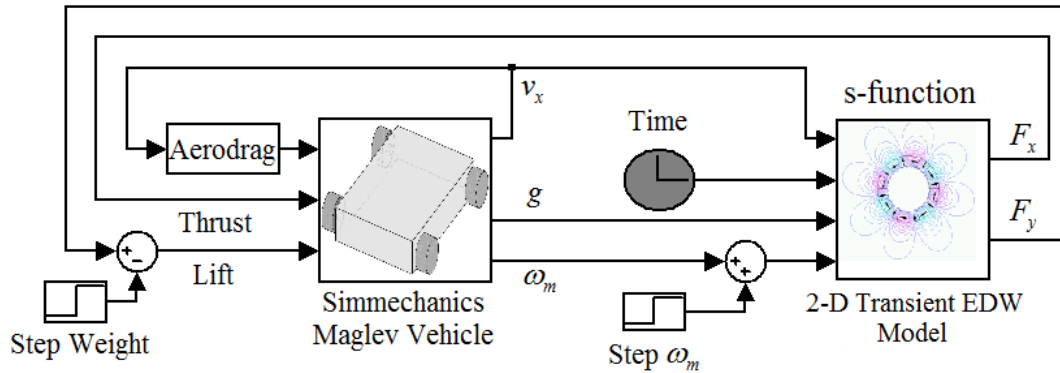


Figure 4.17: The block diagram showing EDW transient model coupled with the mechanical vehicle model.

the form of an s-function.

The following initial conditions have been used during the starting of the simulation. The vehicle initial airgap, g_o , is 10mm, initial velocity, v_{xo} , is 10ms^{-1} and initial angular velocity, ω_{mo} , is 400rads^{-1} . These initial conditions result in a positive slip $s_l = 10\text{ms}^{-1}$. The comparison is made by using the parameters given in Table 4.1 except that the equivalent current sheet of value $1.1814 \times 10^6 \text{ Am}^{-1}$ is used as for the source [114]. The comparison between the lift force, thrust force and the air-gap are illustrated in Figure 4.18, Figure 4.19 and Figure 4.20 respectively. An excellent agreement between the FEA model and the analytic based transient model for a continuously changing input condition was obtained. The integrated simulation between the transient FEA model and vehicle SimMechanicsTM model is extremely time intensive. For instance, to obtain the result shown in Figure 4.18 to Figure 4.20, the FEA integrated with the vehicle model took about 2 weeks. However, the computational time using the analytic based transient model could be completed within a few minutes.

4.5.3 Dynamic Simulation for Step Change in Weight of the Vehicle

This simulation was performed using the initial airgap, $g_o = 10\text{mm}$, initial velocity, $v_{xo} = 10\text{ms}^{-1}$ and initial angular velocity, $\omega_{mo} = 400\text{rads}^{-1}$. Therefore, with the initial positive slip, $s_l = 10\text{ms}^{-1}$. The dynamic response when using these initial conditions

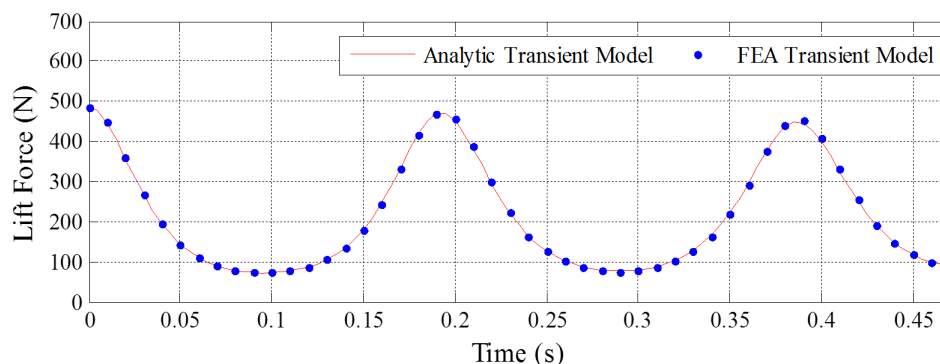


Figure 4.18: *The lift force plot comparison between the FEA transient model and analytical transient model when integrated with the Simulink SimMechanicsTM vehicle model.*

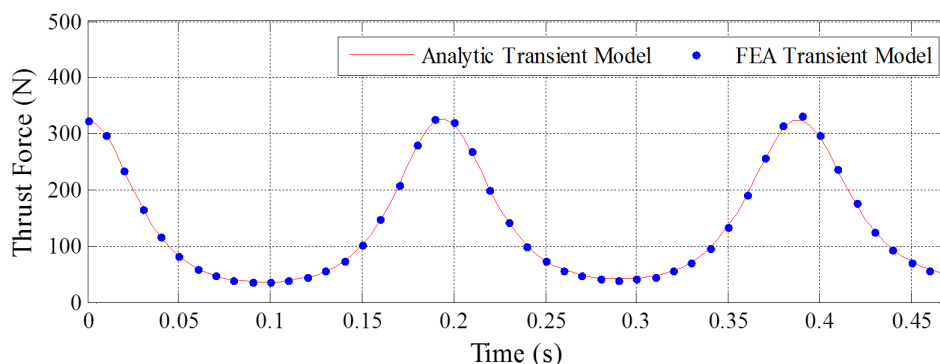


Figure 4.19: *The thrust force plot comparison between the FEA transient model and analytical transient model when integrated with the Simulink SimMechanicsTM vehicle model.*

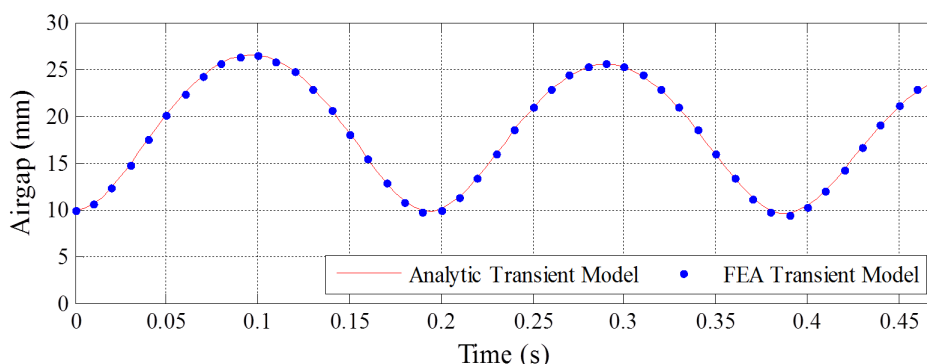


Figure 4.20: *The airgap plot comparison between the FEA transient model and analytical transient model when integrated with the Simulink SimMechanicsTM vehicle model.*

with the steady-state model (discussed in section 4.4) and transient model (derived in section 4.5) are compared in Figure 4.22 to Figure 4.28. The mechanical vehicle model is the same for both models. The parameters given in Table 4.1 were used. The large initial transient is due to the positive slip of the vehicle creating a thrust and lift force and consequently the vehicle accelerates in both the x and y directions at $t = 0$ s.

The results showed that the steady-state model tracks the transient response quite closely. This is because of the presence of the heave velocity term v_y in the steady-state EDW model. The sudden change in lift force creates a mechanical acceleration and consequently this is captured by the v_y term, without the feedback created by v_y the steady-state model cannot account for the dynamic variation in the airgap. As the the system mechanical time constant is much larger than the eddy-current time constants the resulting error in force estimation is relatively small, as shown in Figure 4.28. The dynamic simulation showed that the electromagnetic damping is clearly present. The vehicle stabilizes at the air-gap of 10mm after about 4s. However, the oscillation of the Maglev for 4s is not acceptable for ride quality. Therefore, an appropriate control laws has to be implemented to bring Maglev system in stable operation quickly. The lift and thrust forces are highly coupled. The translational velocity is smoothly increasing until the thrust and drag forces becomes constant.

At time $t = 5\text{s}$ a step change in mass of 50N is applied resulting in a second transient phase. Since the mass is increased, the vehicle now stabilizes at an air-gap of 8mm (lower than the previous stable air-gap). Therefore, more lift force is produced. The translational velocity is decreased slightly and this results in a decrease in the aerodynamic drag force. The electromechanical system using steady-state EDW calculated forces very closely tracks the transient eddy-current based model. The oscillation response to the second step change show that even for about 30% change in lift force the resulting error obtained when using the steady-state based force method is under 2%.

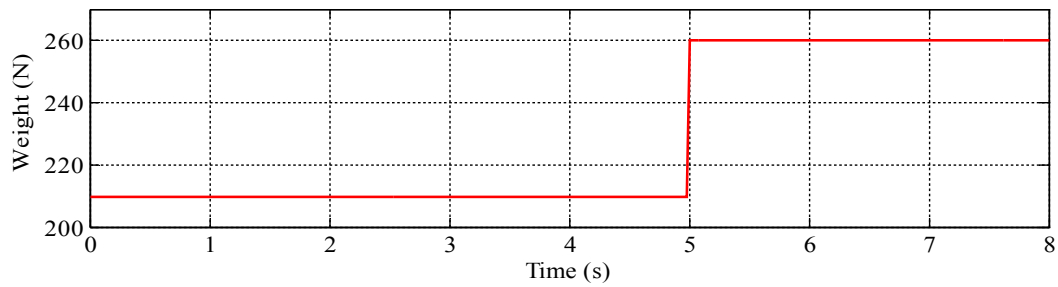


Figure 4.21: *The weight as a step input. The step change of 50N weight is applied at $t = 5s$.*

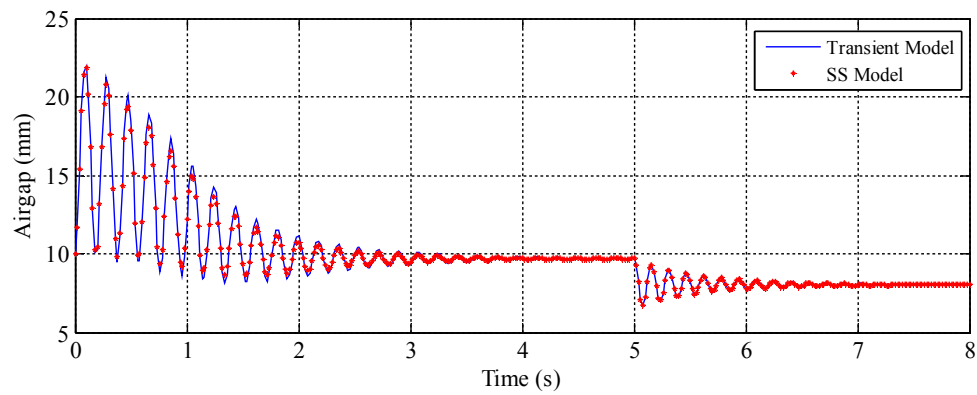


Figure 4.22: *Airgap comparison between the steady-state and transient dynamic model for a step change in weight of the vehicle.*

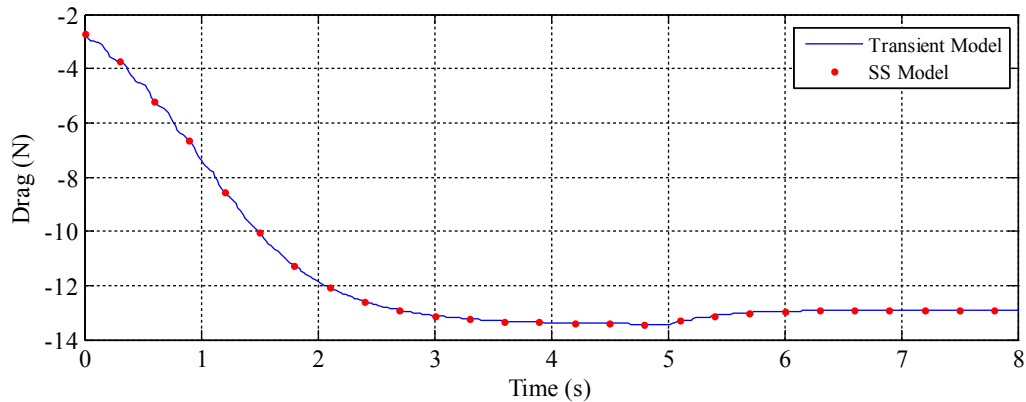


Figure 4.23: *Aerodynamic drag force comparison between the steady-state and transient dynamic model for a step change in weight of the vehicle.*

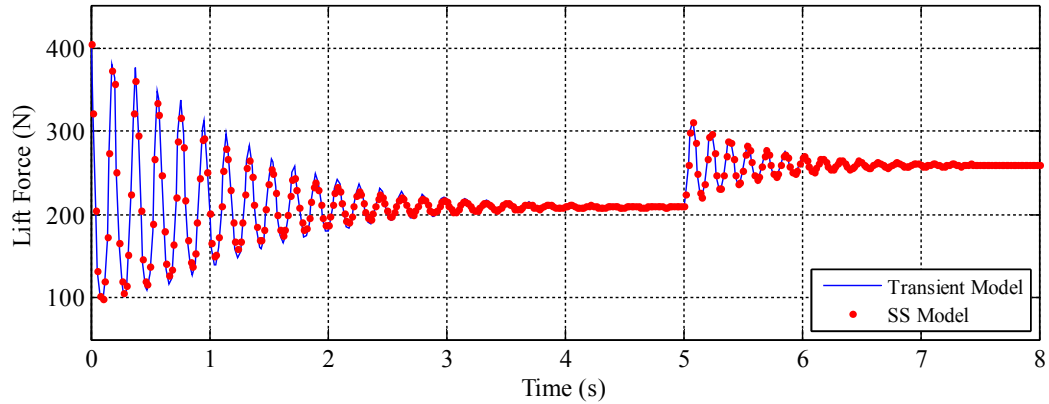


Figure 4.24: Lift force comparison between the steady-state and transient dynamic model for a step change in weight of the vehicle.

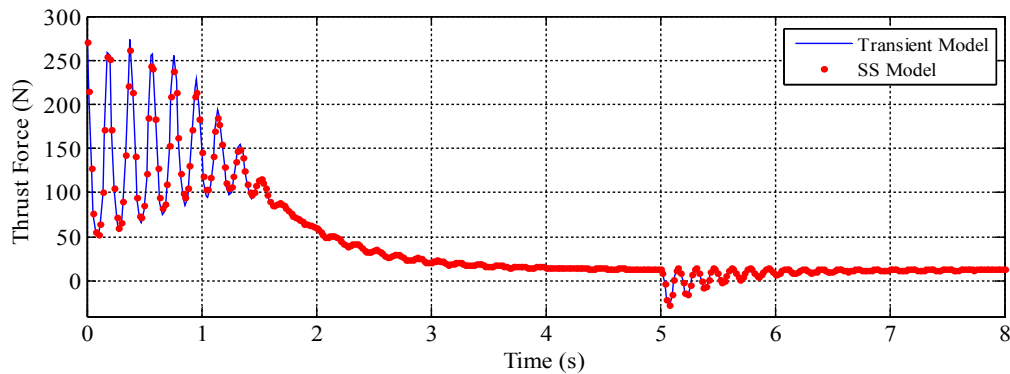


Figure 4.25: Thrust force comparison between the steady-state and transient dynamic model for a step change in weight of the vehicle.

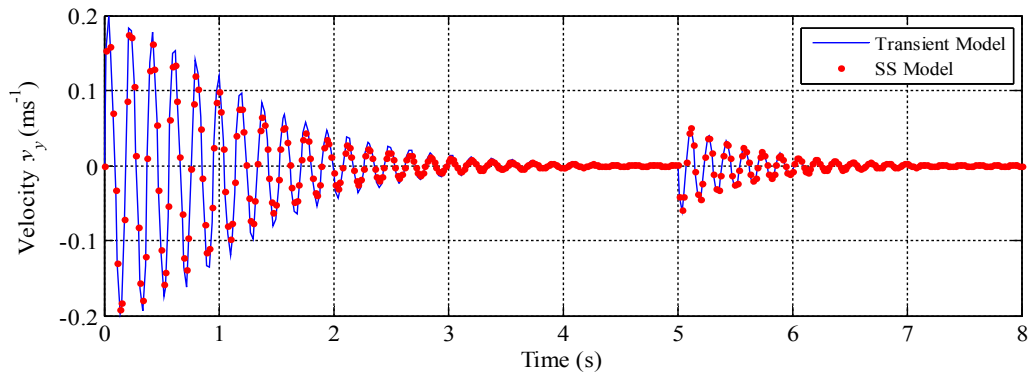


Figure 4.26: Heave velocity comparison between the steady-state and transient dynamic model for a step change in weight of the vehicle.

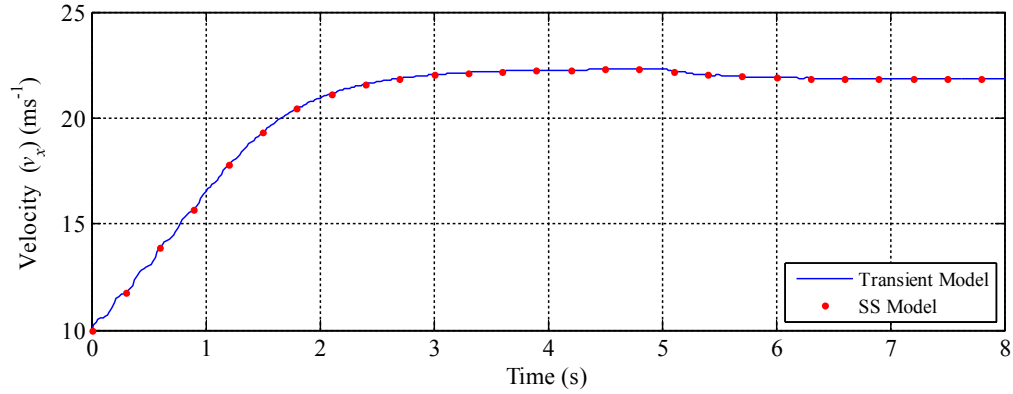


Figure 4.27: *Translational velocity comparison between the steady-state and transient dynamic model for a step change in weight of the vehicle.*

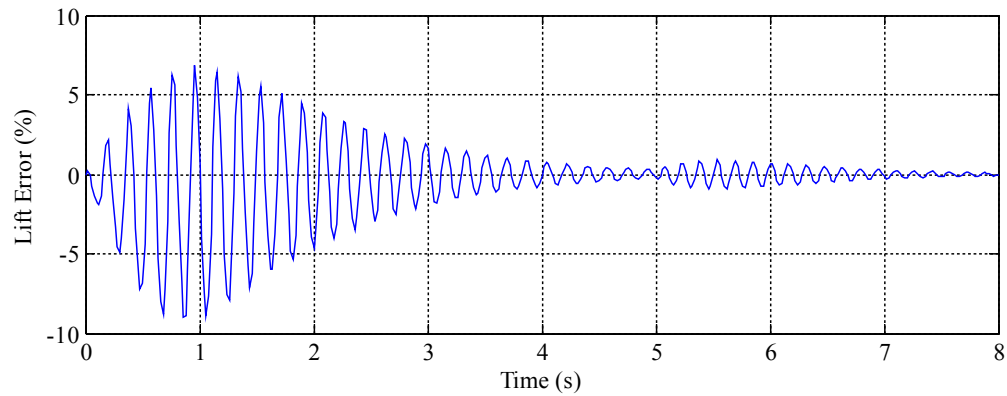


Figure 4.28: *The percentage error of lift force between the steady-state and transient dynamic model for a step change in weight of the vehicle.*

4.5.4 Dynamic Simulation for Step Change in Angular Speed of EDWs

The two models (as shown in Figure 4.16 and Figure 4.17) are simulated for a step change in angular velocity, ω_m . The comparison of various parameters for the step change in angular velocity is shown in Figure 4.30 to Figure 4.35. Both models start in a steady-state condition (i.e. the steady-state operation condition of the earlier simulation just before $t = 5$ s) and then a step change in ω_m from 400rads^{-1} to 600rads^{-1} as shown in Figure 4.29 occurs at $t = 1$ s. This results in an increased slip and consequently an increase in translational velocity. As the velocity is greater the new steady-state air-gap value increases (Figure 4.30). However, the new steady-state lift negligibly changes. This is because the increase in angular speed

is compensated by the increase in air-gap resulting in an almost equal amount of steady-state lift production. The thrust force, aerodynamic drag force are constantly increased until the vehicle reach the steady-state operation. The steady-state model again closely tracks the eddy-current based transient electromechanical model. The error in percentage between the two models is relatively small as illustrated in Figure 4.36.

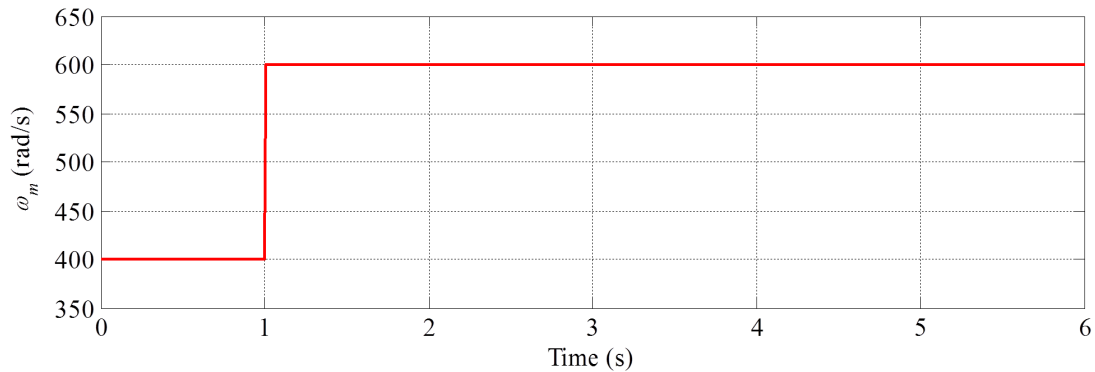


Figure 4.29: Step change in the angular speed from 400rad/s^{-1} to 600rad/s^{-1} at $t = 1\text{s}$

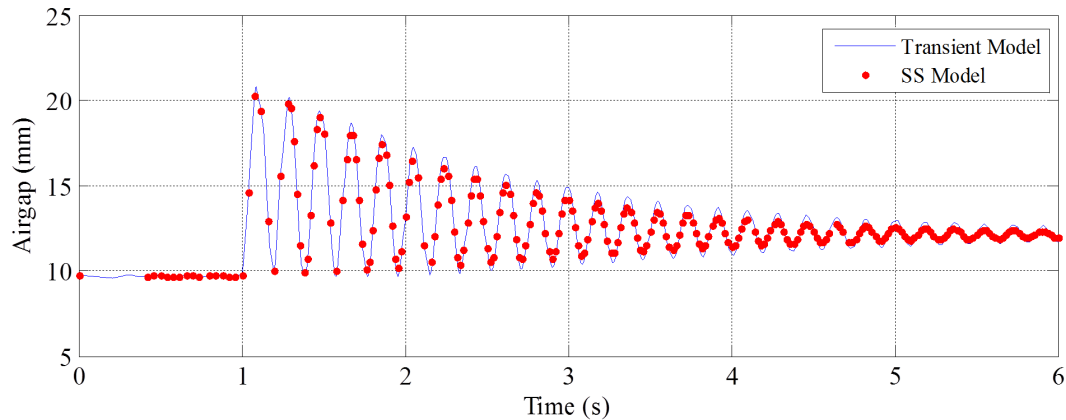


Figure 4.30: Air-gap comparison between the steady-state and transient dynamic model for a step change in ω_m of the EDWs.

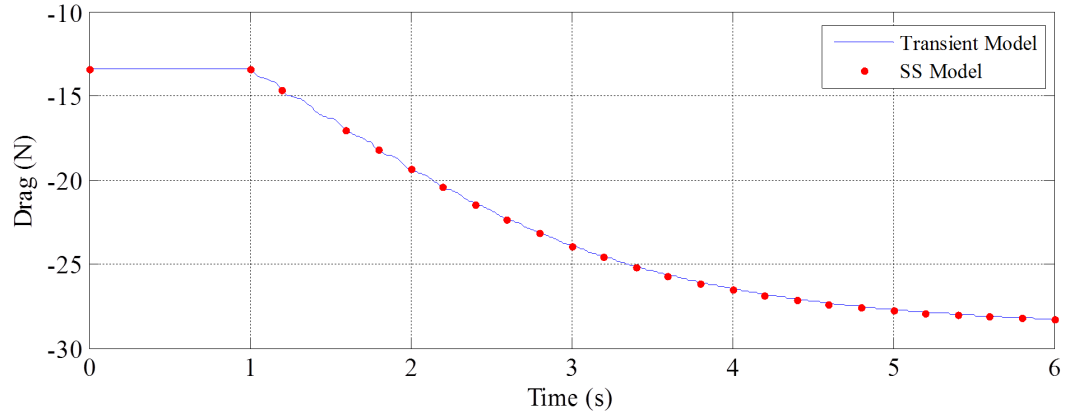


Figure 4.31: Aerodynamic drag force comparison between the steady-state and transient dynamic model for a step change in ω_m of the EDWs.

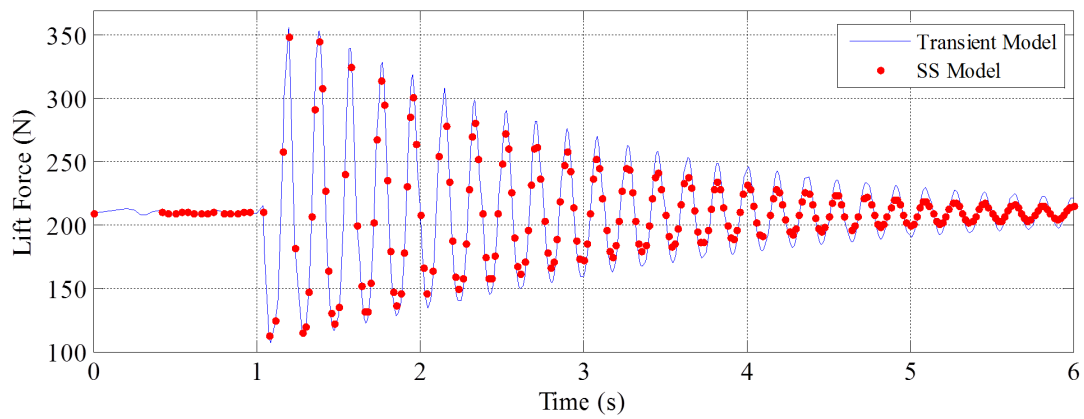


Figure 4.32: Lift force comparison between the steady-state and transient dynamic model for a step change in ω_m of the EDWs.

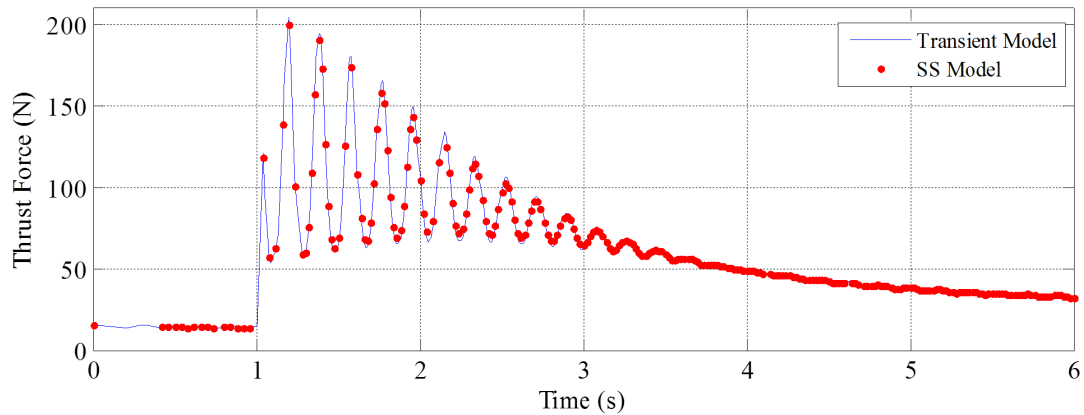


Figure 4.33: Air-gap comparison between the steady-state and transient dynamic model for a step change in ω_m of the EDWs.

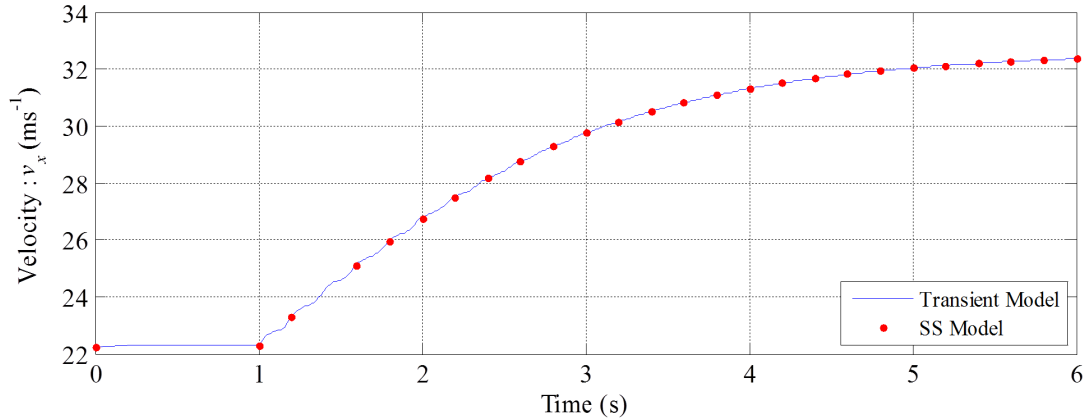


Figure 4.34: *Translational velocity comparison between the steady-state and transient dynamic model for a step change in ω_m of the EDWs.*

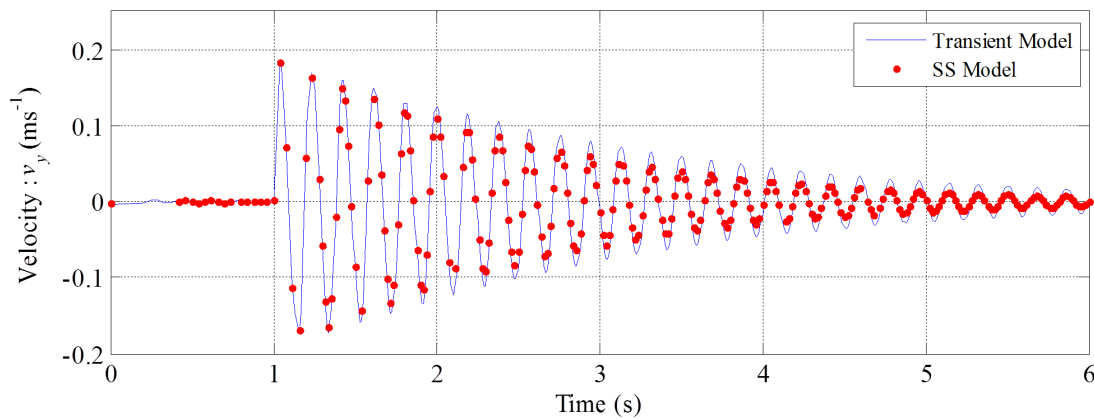


Figure 4.35: *Heave velocity comparison between the steady-state and transient dynamic model for a step change in ω_m of the EDWs.*

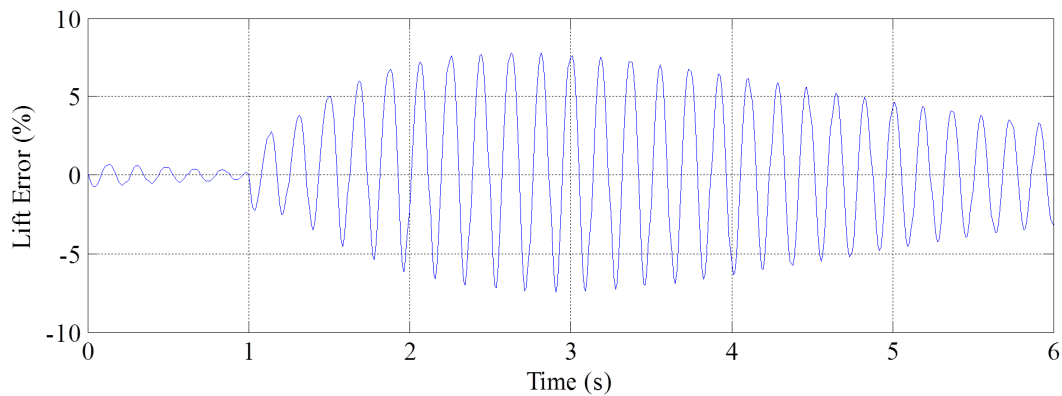


Figure 4.36: *The percentage error of lift force between the steady-state and transient dynamic model for a step change in ω_m of the EDWs.*

4.6 Magnetic Stiffness and Damping of an EDW

The one degree of freedom vehicle simulation results indicate that the eddy-current damping and stiffness characteristics of the electromechanical system can be relatively accurately predicted by using only the steady-state eddy-current force model (with v_y) [199]. The steady-state equations are significantly simpler to understand and less computationally expensive. Therefore, they have been used to study the stiffness and damping characteristics for this EDW Maglev system. The thrust and lift stiffness equations along the y -axis are dependent on the source location and therefore obtained by differentiating (2.104) and (2.116) with respect to the airgap, g . The thrust and lift force equations derived in section 2.3.9.1 are re-written here for convenience.

$$F_x = \frac{w}{4\pi\mu_0} \operatorname{Re} \int_{-\infty}^{\infty} j\xi T^{ss}(\xi, b) |B^s(\xi, b)|^2 d\xi \quad (4.22)$$

$$F_y = \frac{w}{8\pi\mu_0} \operatorname{Re} \int_{-\infty}^{\infty} (2\xi T^{ss}(\xi, b) - 1) |B^s(\xi, b)|^2 d\xi \quad (4.23)$$

The only term that is a function of airgap, g , is the source term, $|B^s(\xi, b)|^2$. The source term for a Halbach rotor is given by (2.175) and is also re-written for convenience

$$|B^s(\xi, b)|^2 = \left(\frac{4}{P!}\right)^2 \pi^2 C^2 \xi^{2P} e^{-2\xi(g+r_o)} u(\xi) \quad (4.24)$$

Differentiating the thrust force equation (4.22) with respect to air-gap gives

$$k_{xy} = \frac{\partial F_x}{\partial g} = \frac{w}{4\pi\mu_0} \operatorname{Re} \int_{-\infty}^{\infty} j\xi T(\xi, b) \frac{\partial |B^s(\xi, b)|^2}{\partial g} d\xi \quad (4.25)$$

The differentiation of magnetic flux density with respect to air-gap is

$$\frac{\partial |B^s(\xi, b)|^2}{\partial g} = \left(\frac{4}{P!}\right)^2 C^2 \pi^2 \xi^{2P} u(\xi) \frac{\partial e^{-2\xi(g+r_o)}}{\partial g} \quad (4.26)$$

or simply

$$\frac{\partial |B^s(\xi, b)|^2}{\partial g} = -2 \left(\frac{4}{P!} \right)^2 C^2 \pi^2 \xi^{2P+1} e^{-2\xi(g+r_o)} u(\xi) \quad (4.27)$$

Substituting (4.24) into (4.25) and noting (4.27) one obtains

$$k_{xy} = -\frac{8w}{\mu_0} \frac{C^2 \pi}{(P!)^2} \operatorname{Re} \int_0^\infty j T^{ss}(\xi, b) \xi^{2P+1} e^{-2\xi(g+r_o)} d\xi \quad (4.28)$$

Similarly, the lift stiffness coefficient, k_{yy} , can be obtained by differentiating (4.23) with respect to the air-gap, g as

$$k_{yy} = \frac{\partial F_y}{\partial g} = \frac{w}{8\pi\mu_0} \operatorname{Re} \int_{-\infty}^\infty (2\xi T^{ss}(\xi, b) - 1) \frac{\partial |B^s(\xi, b)|^2}{\partial g} d\xi \quad (4.29)$$

Substituting (4.24) into (4.29), and noting (4.26), the expression for the stiffness coefficient, k_{yy} becomes

$$k_{yy} = -\frac{w}{8\pi\mu_0} \operatorname{Re} \int_0^\infty 2\xi [(2\xi T(\xi, b) - 1) \left(\frac{4}{P!} \right)^2 C^2 \pi^2 \xi^{2P} e^{-2\xi(g+r_o)}] d\xi \quad (4.30)$$

Rearranging (4.30), the stiffness coefficient k_{yy} is

$$k_{yy} = -\frac{w}{\mu_0} \frac{4C^2 \pi}{(P!)^2} \operatorname{Re} \int_0^\infty [(2\xi T(\xi, b) - 1) \xi^{2P+1} e^{-2\xi(g+r_o)}] d\xi \quad (4.31)$$

As the conducting guideway is assumed to be infinitely long and uniform, the forces will not change with spatial motion along the x -axis. Therefore, the stiffness coefficients k_{xx} and k_{yx} are both zero.

$$k_{xx} = \frac{\partial F_x}{\partial x} = 0 \quad (4.32)$$

$$k_{yx} = \frac{\partial F_y}{\partial x} = 0 \quad (4.33)$$

The magnetic damping coefficients are dependent on the transmission functions. The thrust force damping coefficients can be determined by differentiating (4.22) with respect to velocities in the x and y direction, one obtains

$$D_{xx} = \frac{\partial F_x}{\partial v_x} = \frac{w}{4\pi\mu_0} \operatorname{Re} \int_{-\infty}^{\infty} (j\xi) \frac{\partial T^{ss}(\xi, b)}{\partial v_x} |B^s(\xi, b)|^2 d\xi \quad (4.34)$$

$$D_{xy} = \frac{\partial F_x}{\partial v_y} = \frac{w}{4\pi\mu_0} \operatorname{Re} \int_{-\infty}^{\infty} (j\xi) \frac{\partial T^{ss}(\xi, b)}{\partial v_y} |B^s(\xi, b)|^2 d\xi \quad (4.35)$$

where the derivative of the transmission function with respect to v_x and v_y is respectively

$$\frac{\partial T^{ss}(\xi, b)}{\partial v_x} = \frac{\mu_0\sigma\xi}{4\chi} \frac{\begin{pmatrix} -2j((\lambda - \xi + 2b\lambda\xi)\chi) + \sigma\mu(2b\chi + \sinh(2b\chi))(\omega_e + \xi v_x) \\ -2j((\lambda^2 - \lambda\xi + \xi^2)\sinh(2b\chi) + \chi(\xi - \lambda)\cosh(2b\chi)) \end{pmatrix}}{[2\xi\chi \cosh(b\chi) + (\gamma^2 + \xi^2)\sinh(b\chi)]^2} \quad (4.36)$$

$$\frac{\partial T^{ss}(\xi, b)}{\partial v_y} = \frac{\mu_0\sigma}{4\chi} \frac{\begin{pmatrix} 2b\lambda(\gamma^2 + (2\lambda - \xi)\xi)\chi + 2(\gamma^2 + \xi^2)\chi \sinh(b\chi)^2 \\ + (\lambda\xi^2 - \gamma^2(\lambda - 2\xi))\sinh(2b\chi) \end{pmatrix}}{[2\xi\chi \cosh(b\chi) + (\gamma^2 + \xi^2)\sinh(b\chi)]^2} \quad (4.37)$$

and

$$\chi^2 = \gamma^2 + \lambda^2 \quad (4.38)$$

Similarly, damping associated with the lift force can be determined by differentiating (4.23) with respect to velocities v_x and v_y as

$$D_{yx} = \frac{\partial F_y}{\partial v_x} = -\frac{w}{8\pi\mu_0} \operatorname{Re} \int_{-\infty}^{\infty} \frac{\partial(2\xi T^{ss}(\xi, b) - 1)}{\partial v_x} |B^s(\xi, b)|^2 d\xi \quad (4.39)$$

$$D_{yy} = \frac{\partial F_y}{\partial v_y} = -\frac{1}{8\pi\mu_0} \operatorname{Re} \int_{-\infty}^{\infty} \frac{\partial(2\xi T(\xi, b) - 1)}{\partial v_y} |B^s(\xi, b)|^2 d\xi \quad (4.40)$$

Since the derivative of constant term is zero, (4.39) and (4.40) can be further simplified

to

$$D_{yx} = -\frac{w}{8\pi\mu_0} \operatorname{Re} \int_{-\infty}^{\infty} (2\xi) \frac{\partial T^{ss}(\xi, b)}{\partial v_x} |B^s(\xi, b)|^2 d\xi \quad (4.41)$$

$$D_{yy} = -\frac{1}{8\pi\mu_0} \operatorname{Re} \int_{-\infty}^{\infty} (2\xi) \frac{\partial T(\xi, b)}{\partial v_y} |B^s(\xi, b)|^2 d\xi \quad (4.42)$$

where the derivative of the transmission function with respect to v_x and v_y are already defined by (4.36) and (4.37).

The stiffness and damping coefficients are the slopes of the force-displacement and force-velocity curves respectively. This is similar to the concept of the torsional spring stiffness and damping coefficients in synchronous machines in which the torsional spring stiffness is the slope of the torque-angle curve and the damping coefficient is the slope of the torque-speed curve [200]. The parameters used to perform the simulations in this section are specified in Table 4.2. The numerical correlation of the stiffness constants with the gradients of the force-displacement curves is shown in Figure 4.37 - Figure 4.42. The stiffness coefficients, k_{xy} and k_{yy} are calculated numerically using (4.28) and (4.31) respectively. Whilst the forces are evaluated using (4.22) and (4.23). The variation of the stiffness coefficients with airgap in these results clearly indicate that the vehicle is more stable at small airgap values. This type of stiffness characteristic has been observed by other authors [200]. The lift force and stiffness coefficient, k_{yy} are almost unchanged with the change in heave velocity at high angular velocity and translational velocity as illustrated in Figure 4.40 and Figure 4.42 respectively. However, the thrust and the stiffness coefficient, k_{xy} are still affected by the change in heave velocity at both high and low rotational and translational velocities.

Similarly the numerical correlation of the damping coefficients with the gradient of the force-velocity curves is shown in Figure 4.43 - Figure 4.46. The damping coefficients, D_{xx} , D_{xy} , D_{yx} and D_{yy} are evaluated numerically using (4.34), (4.35), (4.41) and (4.42) respectively. The damping coefficients are decreased with the increase in

translational speed as shown in Figure 4.43 and Figure 4.44.

Table 4.2: *Simulation parameters for stiffness and damping.*

	Outer radius, r_o	50 mm
	Inner radius, r_i	34.20 mm
	width, w	1 m
Halbach rotor	Magnet (NdFeB), B_r	1.42 T
	Magnet relative permeability	1.08
	Pole-pairs, P	4
	Conductivity (Al)	$2.459 \times 10^7 \text{ Sm}^{-1}$
Conducting plate	Single sheet width	1 m
	Thickness, b	10 mm
	Air-gap between rotor and plate, g	10 mm

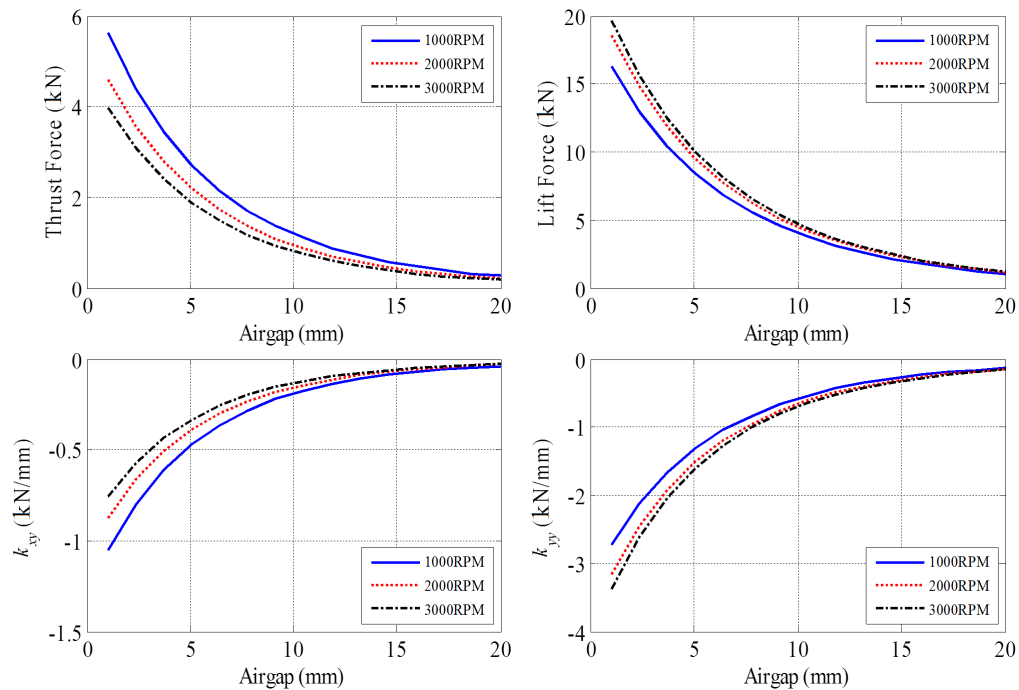


Figure 4.37: *The thrust, lift and stiffness coefficients as a function of airgap for different rotational velocities at $v_y = 0 \text{ ms}^{-1}$, ω_m varied.*

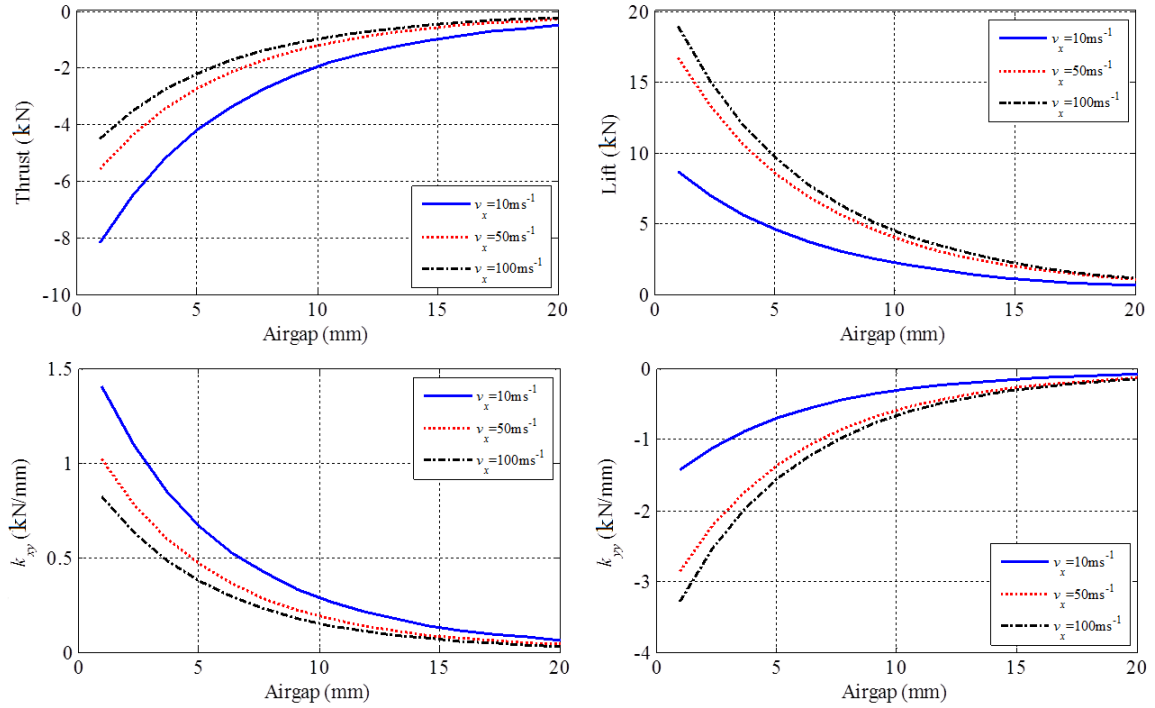


Figure 4.38: The thrust, lift and stiffness coefficients as a function of airgap for different translational velocities at $v_y = 0 \text{ ms}^{-1}$, $\omega_m = 0 \text{ RPM}$, v_x varied.

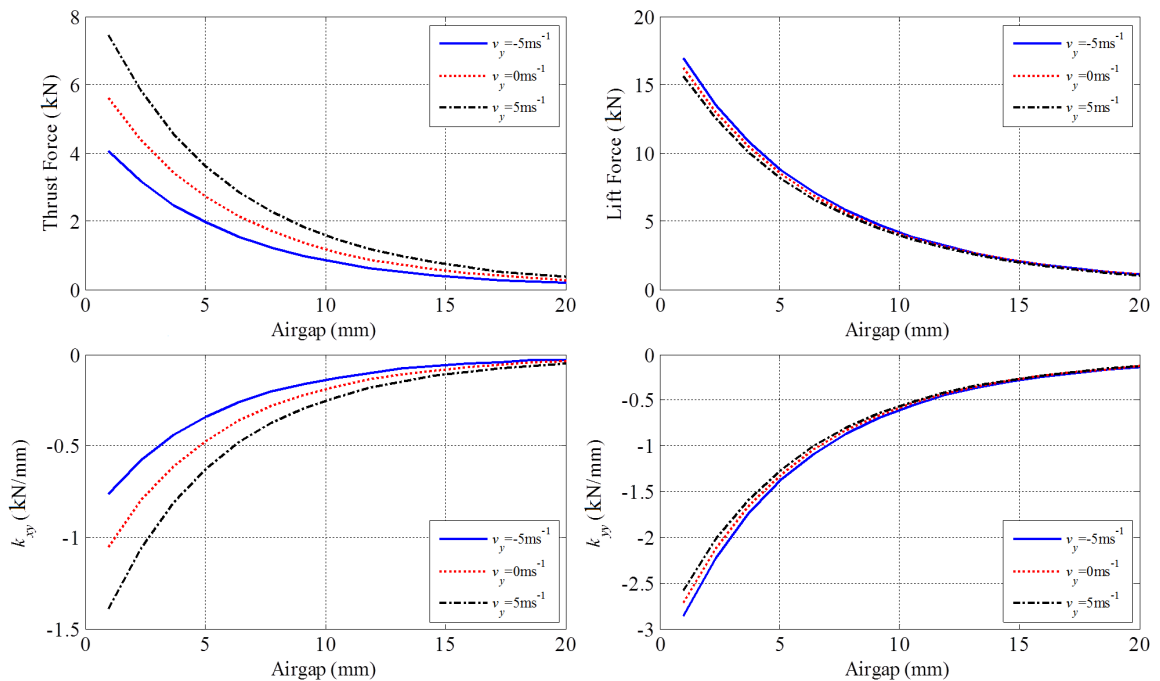


Figure 4.39: The thrust, lift and stiffness coefficients as a function of airgap for different heave velocities at $v_x = 0 \text{ ms}^{-1}$, $\omega_m = 1000 \text{ RPM}$, v_y varied.

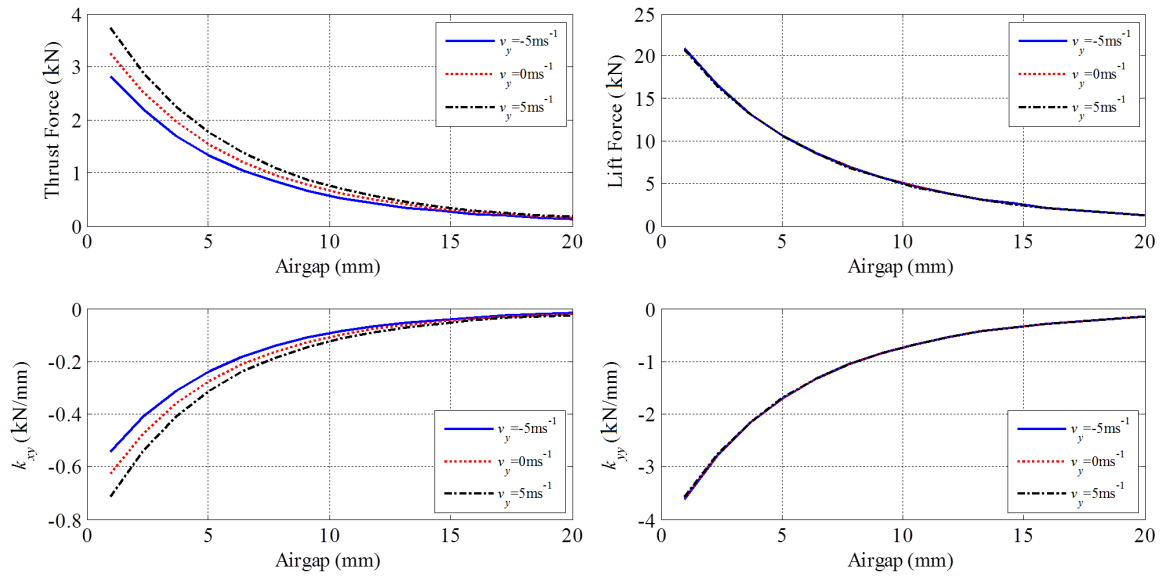


Figure 4.40: The thrust, lift and stiffness coefficients as a function of airgap for different heave velocities at $v_x = 0 \text{ ms}^{-1}$, $\omega_m = 6000 \text{ RPM}$, v_y varied.

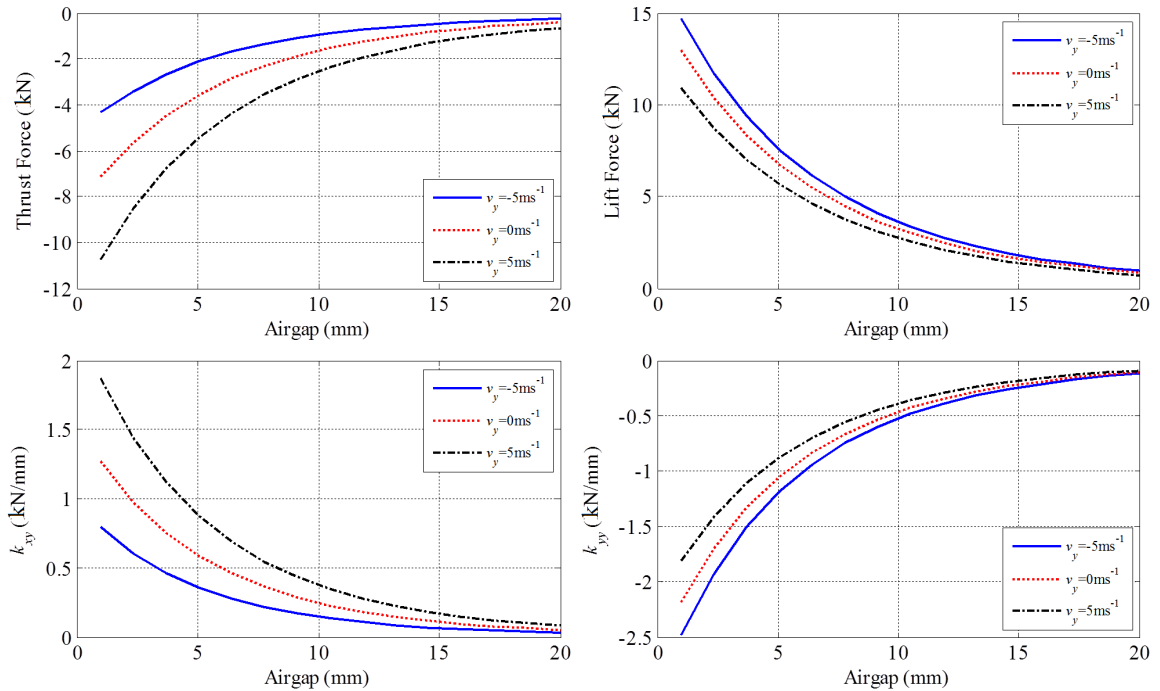


Figure 4.41: The thrust, lift and stiffness coefficients as a function of airgap for different heave velocities at $v_x = 20 \text{ ms}^{-1}$, $\omega_m = 0 \text{ RPM}$, v_y varied.

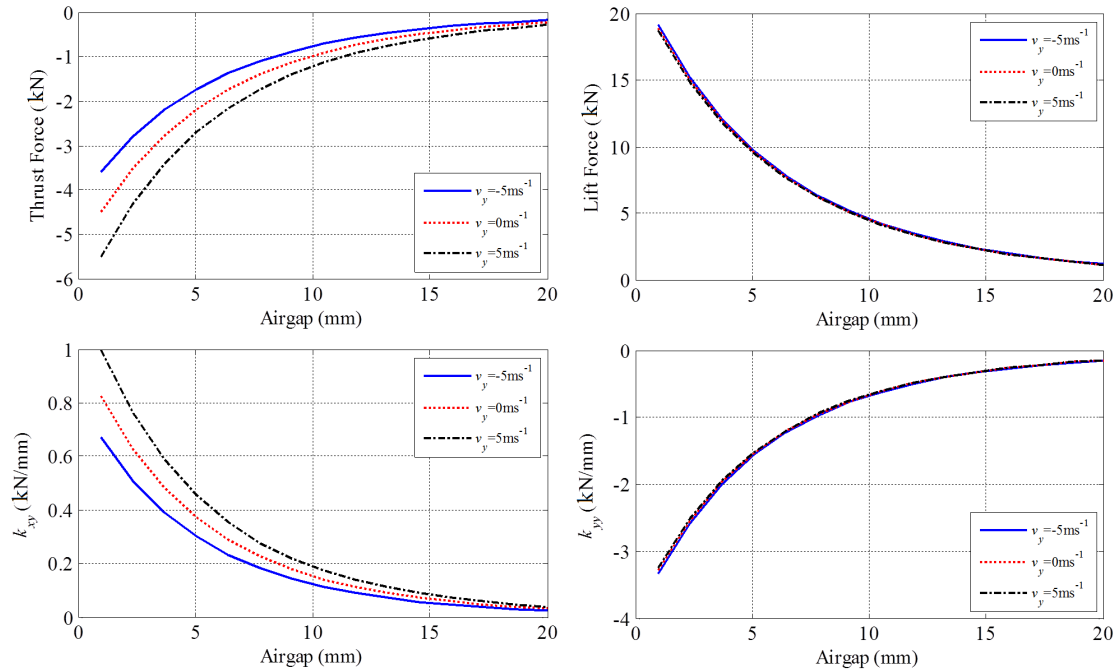


Figure 4.42: The thrust, lift and stiffness coefficients as a function of airgap for different heave velocities at $v_x = 100 \text{ ms}^{-1}$, $\omega_m = 0 \text{ RPM}$, v_y varied.

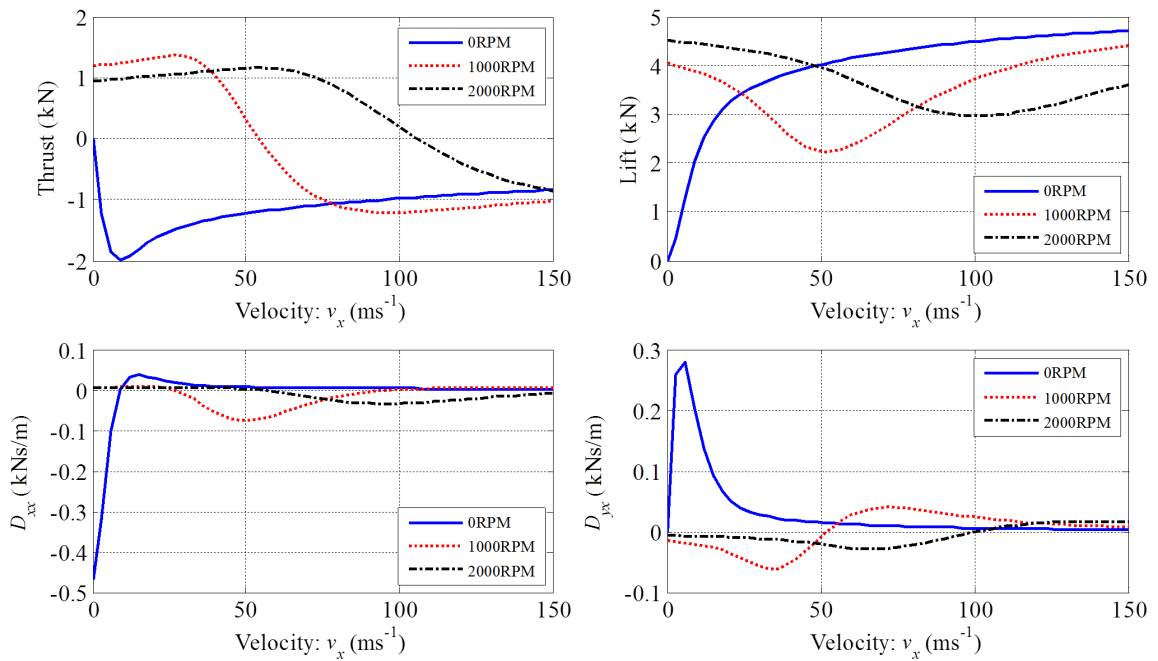


Figure 4.43: The thrust, lift and damping coefficients as a function of translational velocity for different angular velocities at $v_y = 0 \text{ ms}^{-1}$, $g = 10 \text{ mm}$, ω_m varied.

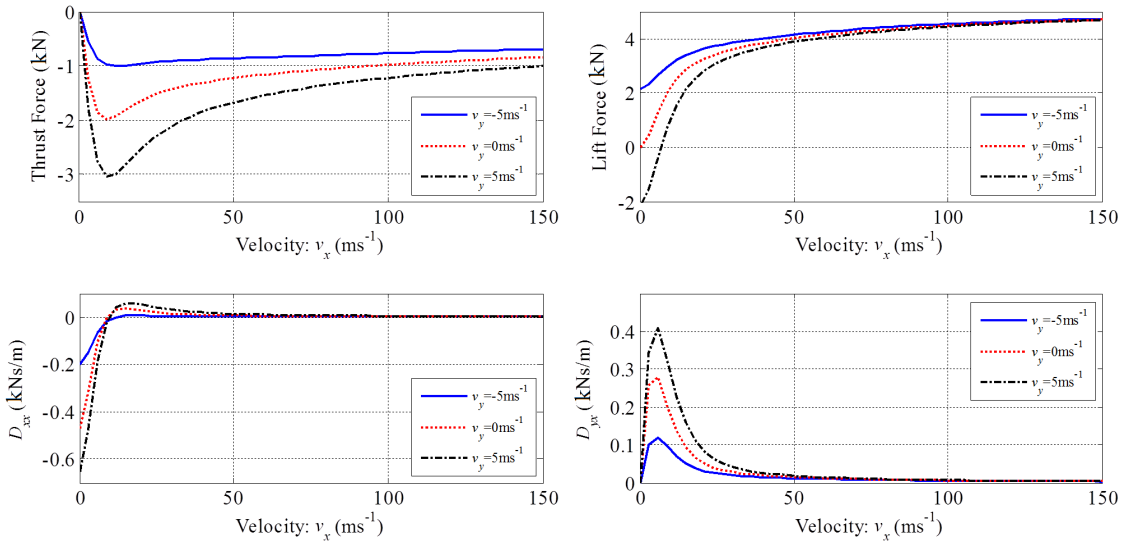


Figure 4.44: *The thrust, lift and damping coefficients as a function of translational velocity for different heave velocities at $\omega_m = 0\text{RPM}$, $g = 10\text{mm}$, v_y varied.*

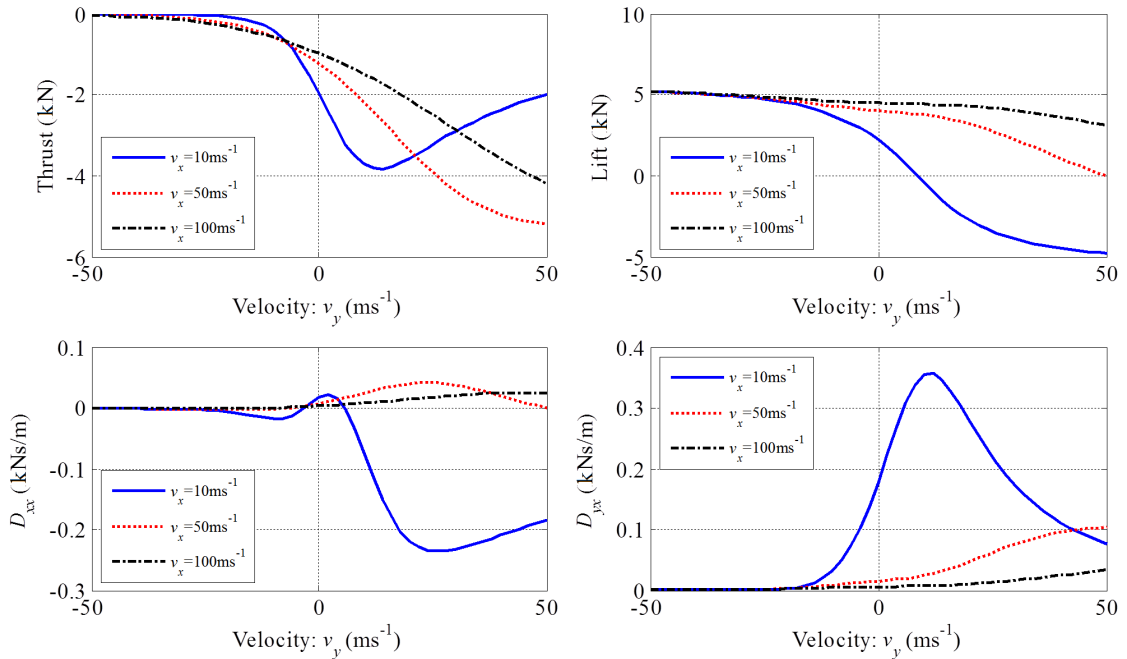


Figure 4.45: *The thrust, lift and damping coefficients as a function of heave velocity for different translational velocities at $\omega_m = 0\text{RPM}$, $g = 10\text{mm}$, v_x varied.*

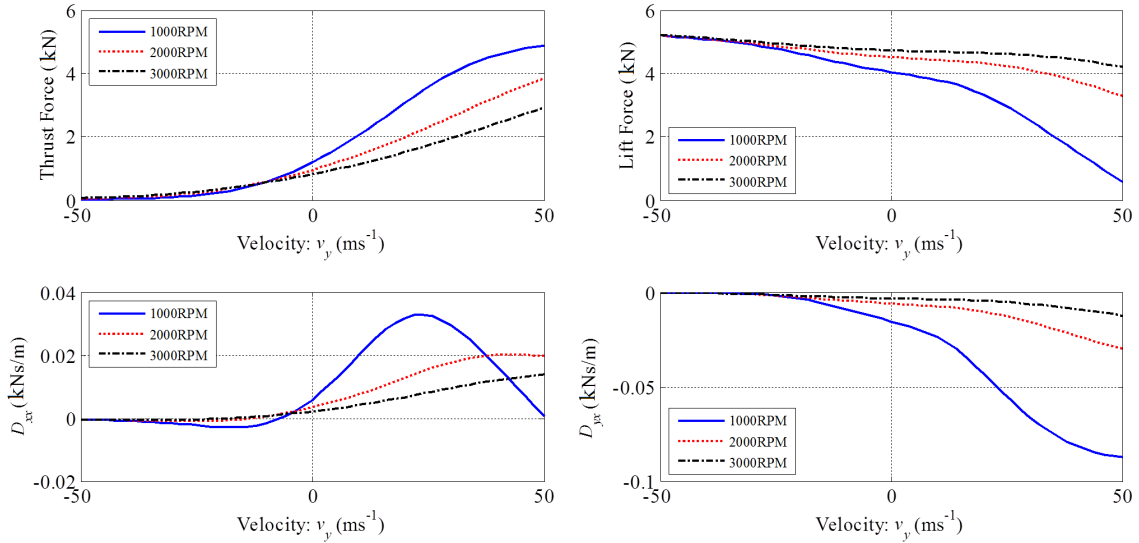


Figure 4.46: *The thrust, lift and damping coefficients as a function of heave velocity for different angular velocities at $v_x = 0\text{ms}^{-1}$, $g = 10\text{mm}$, ω_m varied.*

Using the parameters given in Table 4.2 the stiffness and damping contour plots shown in Figure 4.47 and Figure 4.48 were obtained. The plots indicate that the damping values for the system are particularly low, becoming extremely low at high velocities. Negative damping is clearly present under many conditions. The stiffness increases somewhat with increased velocity. Figure 4.49 and Figure 4.50 illustrate how the stiffness coefficients relate to thrust and lift force as a function of slip for different translational and heave velocities respectively. The variation of the damping coefficients as a function of the translational velocity for the variation of heave velocity, angular velocity and airgap are more clearly illustrated in Figure 4.51, Figure 4.52 and Figure 4.53 respectively. Similarly, the variation of damping coefficient as a function of slip for different translational velocities and heave velocities are shown in Figure 4.54 - Figure 4.56. The low damping indicates that active control of the EDWs using ω_m will be essential.

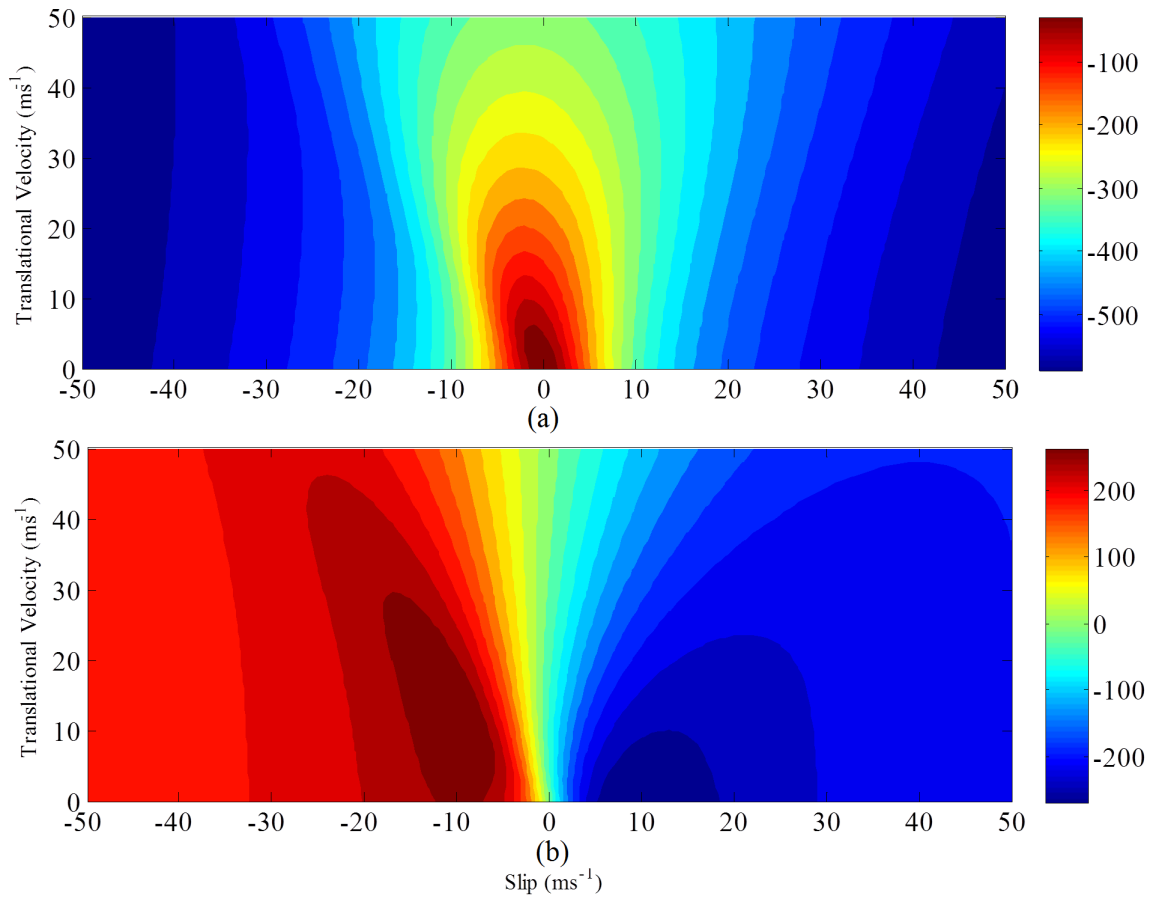


Figure 4.47: The contour plot for (a) Lift stiffness k_{yy} ($\partial F_y^{ss}/\partial g$) and (b) thrust stiffness k_{xy} ($\partial F_x^{ss}/\partial g$) as a function of slip and translational velocity at $g = 10\text{mm}$ and $v_y = 0\text{ms}^{-1}$.

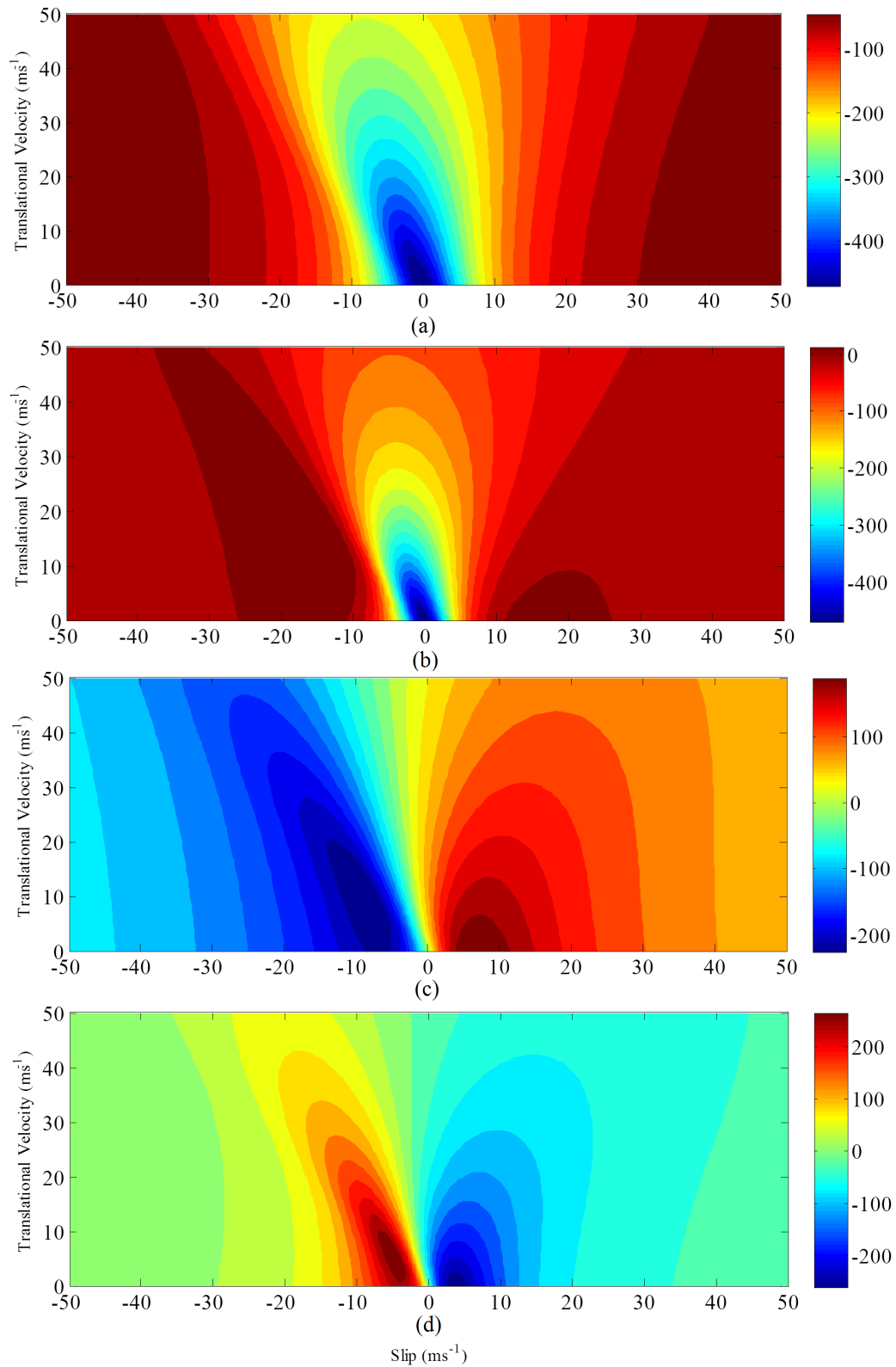


Figure 4.48: (a) Damping coefficient D_{yy} (b) damping coefficient D_{xx} , (c) damping coefficient D_{xy} and (d) damping coefficient D_{yx} all as a function of slip and translational velocity at $g = 10\text{mm}$ and $v_y = 0\text{ms}^{-1}$.

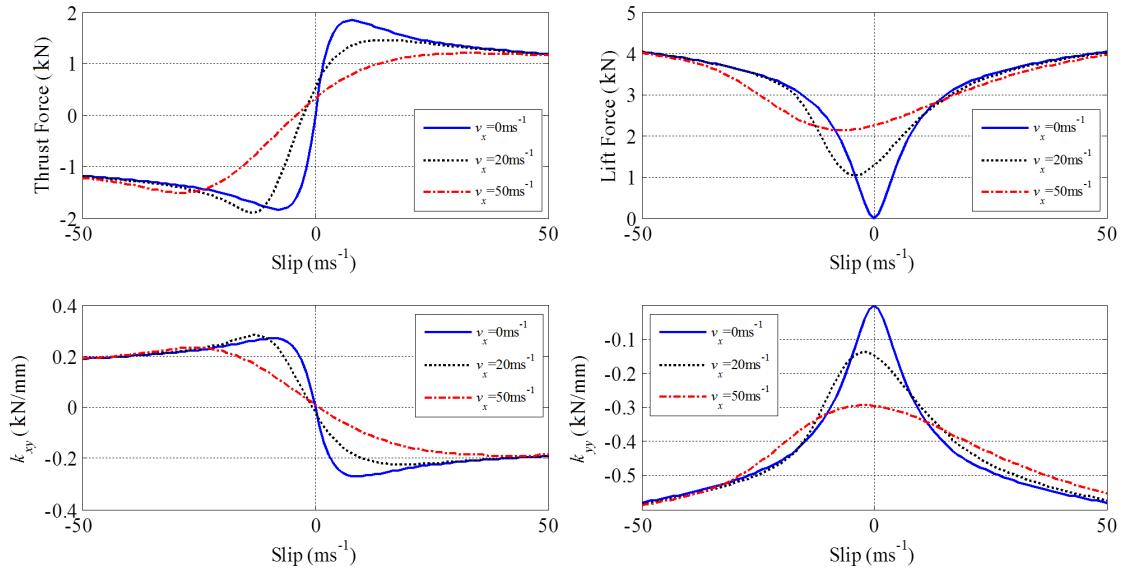


Figure 4.49: The thrust, lift and stiffness coefficients as a function of slip for different translational velocities at $v_y = 0 \text{ms}^{-1}$, $g = 10 \text{mm}$.

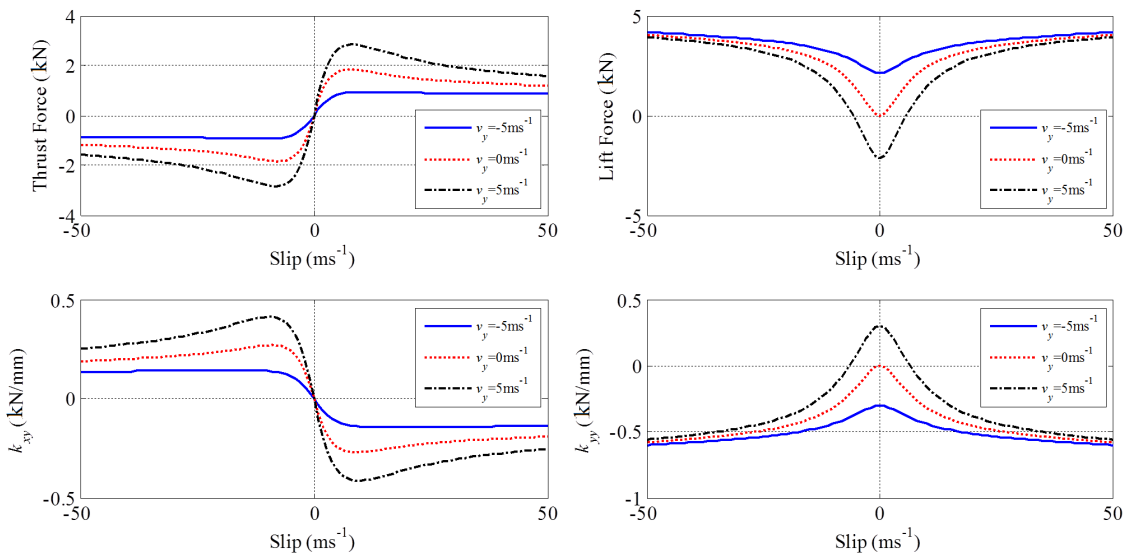


Figure 4.50: The thrust, lift and stiffness coefficients as a function of slip for different heave velocities at $v_x = 0 \text{ms}^{-1}$, $g = 10 \text{mm}$.

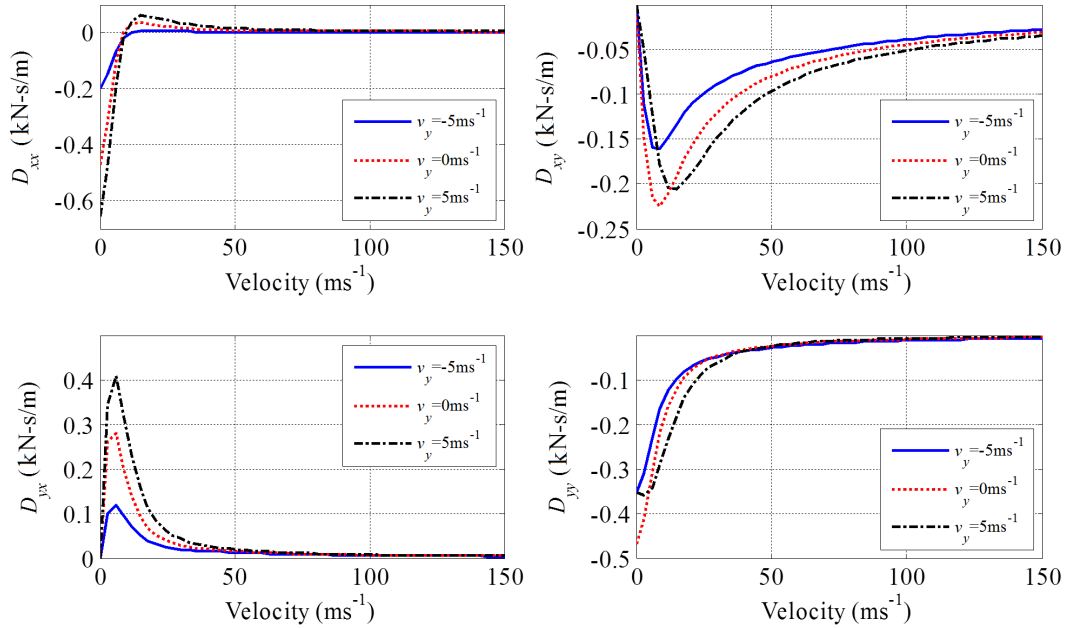


Figure 4.51: The damping coefficients as a function of translational velocity for different heave velocities at $\omega_m = 0$ RPM, $g = 10$ mm.

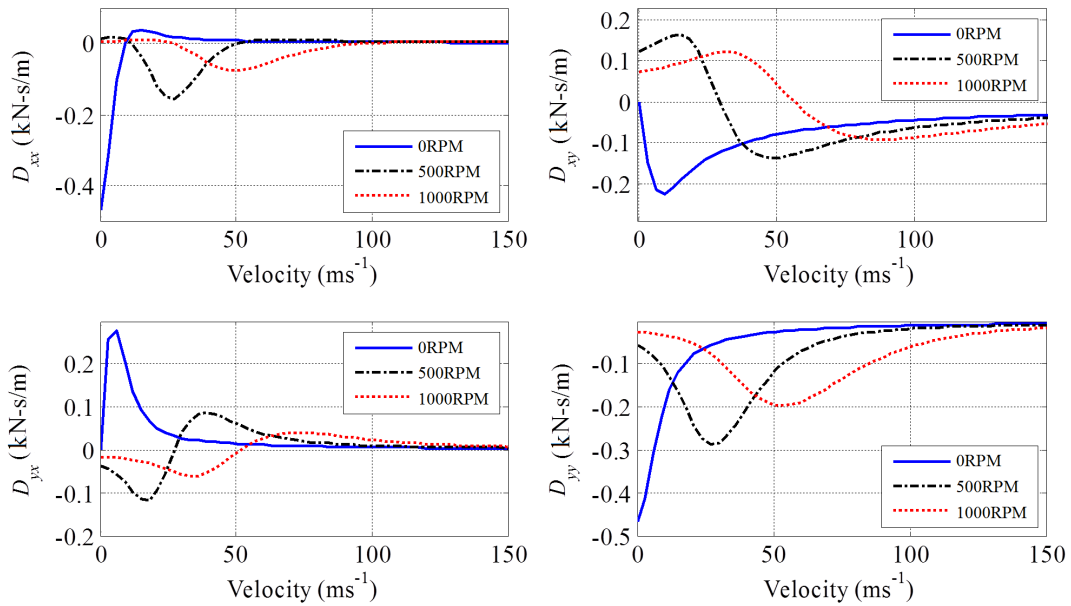


Figure 4.52: The damping coefficients as a function of translational velocity for different rotational velocities at $v_y = 0$ ms⁻¹, $g = 10$ mm.

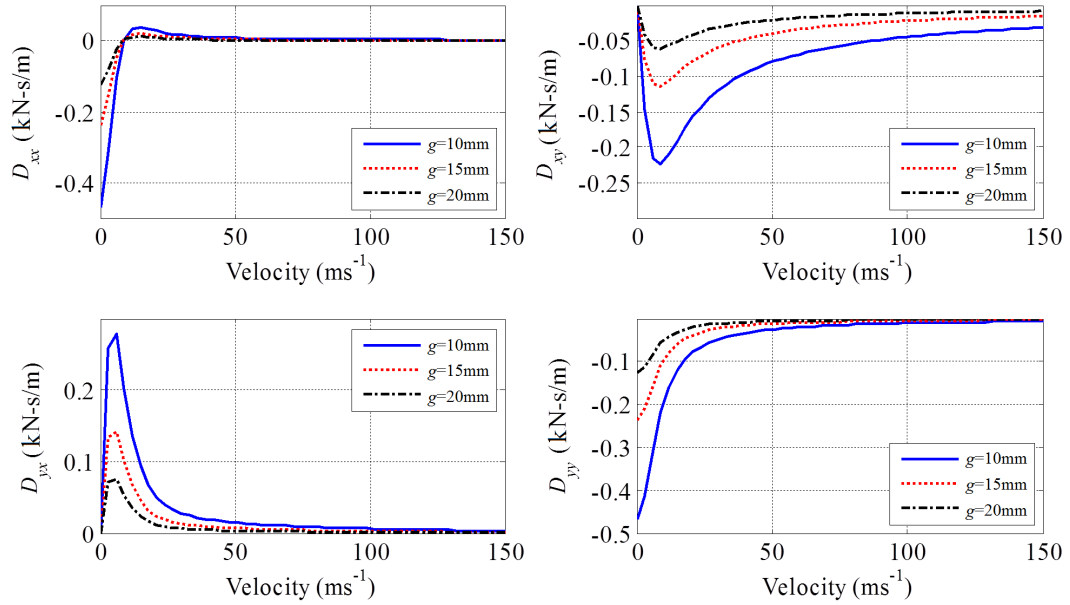


Figure 4.53: The damping coefficients as a function of translational velocity for different airgap at $v_y = 0\text{ms}^{-1}$ and $\omega_m = 0\text{RPM}$.

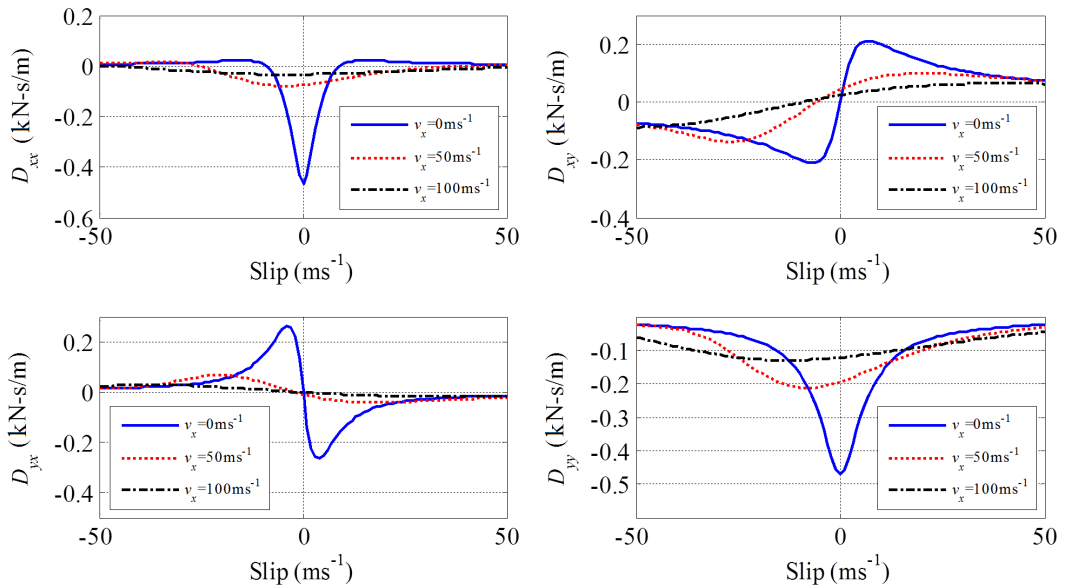


Figure 4.54: The damping coefficients as a function of slip for different translational velocities at $v_y = 0\text{ms}^{-1}$, $g = 10\text{mm}$.

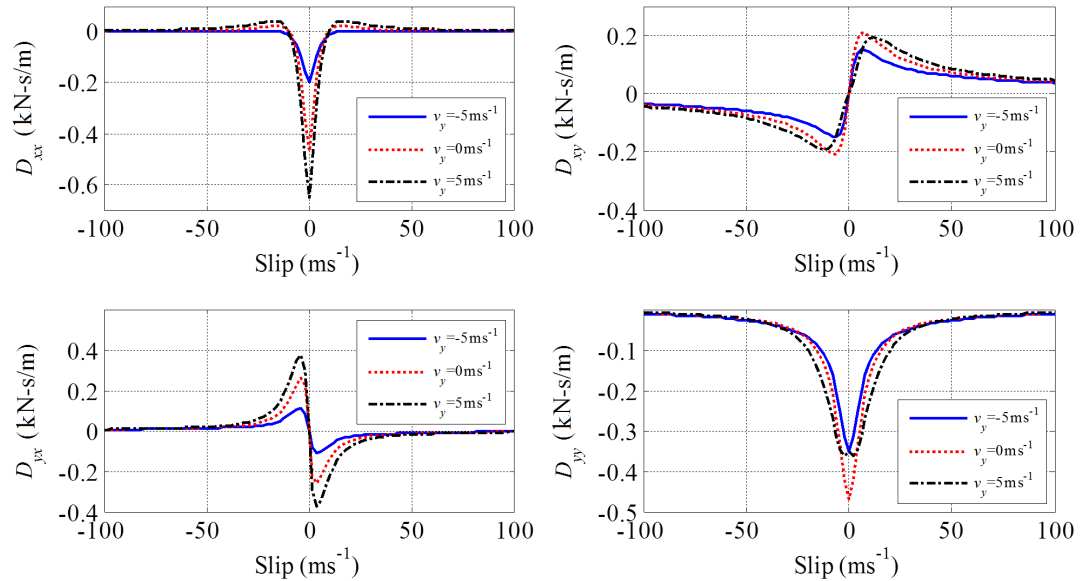


Figure 4.55: The damping coefficients as a function of slip for different heave velocities at $v_x = 0 \text{ ms}^{-1}$, $g = 10 \text{ mm}$.

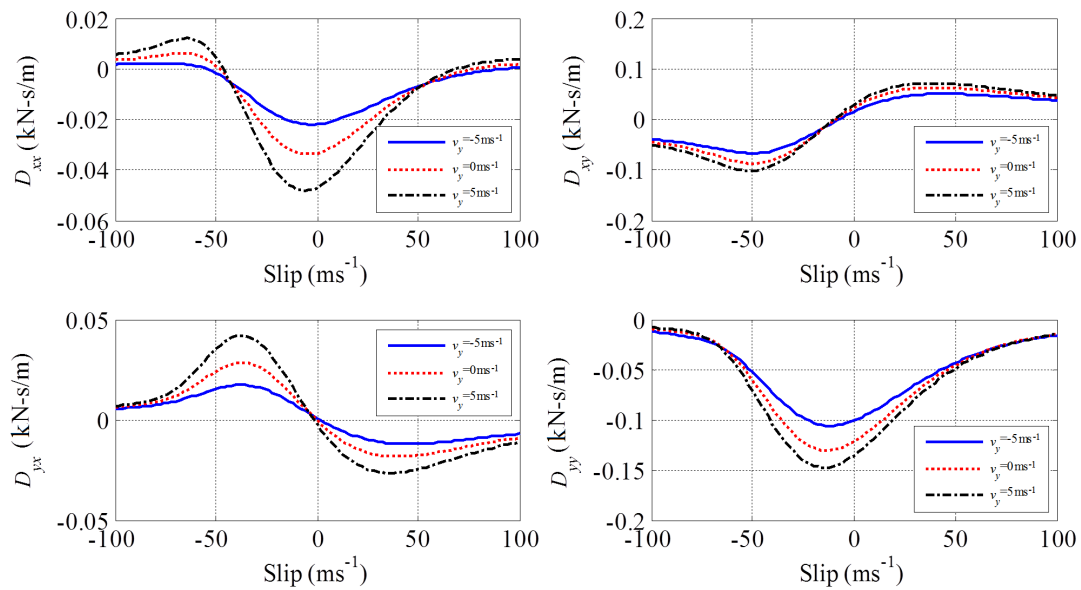


Figure 4.56: The damping coefficients as a function of slip for different heave velocities at $v_x = 100 \text{ ms}^{-1}$, $g = 10 \text{ mm}$.

4.7 Summary

The dynamic modeling of various EDS Maglev systems has been reviewed. A review of magnetic damping and stiffness is presented. The dynamics of an EDW Maglev has been investigated using an analytic steady-state EDW model including

a heave velocity and a fully transient EDW model. The transient analytic model developed in Chapter 3 has been modified to account for a continuous change in input conditions. This modified transient analytic model has been validated using a transient FEA model when integrated with a mechanical vehicle developed in SimMechanicsTM. A close match between the dynamics of the steady-state with v_y and transient analytic models has been observed for both step changes in the weight of vehicle and angular velocity of the EDWs. The simulation results indicate that the inclusion of the heave velocity, v_y , in the steady-state model creates a means for feedback in the electromechanical system and thereby enables the steady-state based force calculations to quite accurately track the dynamic behavior. The electromechanical simulation time is greatly reduced when the forces are computed using steady-state equations. These results indicate that under the conditions studied the steady state model can be used for dynamic electromechanical analysis.

The steady-state force equations (with v_y) have been used to obtain the analytic equations for magnetic stiffness and damping for the EDW Maglev system. The derived, magnetic damping and stiffness equations for this EDW Maglev are investigated for a wide range of velocities, air-gaps and RPMs. During this study it is confirmed that active control is essential for the successful operation of an EDW Maglev.

CHAPTER 5: EXPERIMENTAL VERIFICATION AND RESULTS

5.1 Introduction

In this chapter the dynamics of an EDW has been investigated using a 1-degree of freedom single EDW experimental pendulum setup. The dynamic equation of motion for a 1-DOF pendulum has been derived. The several dynamic tests has been performed. The damping due to the viscous as well as sliding friction has been experimentally determined from the free oscillation of the pendulum. The steady-state force equations for the lift and thrust force derived in Chapter 2 have been used to derive the dynamic nonlinear equation of motion for a forced EDW pendulum. This nonlinear dynamic equation of the forced pendulum is used to verify that the steady-state eddy-current force equations including the heave velocity can accurately predict the transient behavior of an eddy-current device such as an EDW.

The details of the experimental setup are presented in section 5.2. The damping coefficient due to air resistance and friction is experimentally evaluated in section 5.3. The experimental results from the dynamic test of a single EDW pendulum setup are presented in section 5.4. The comparison between the analytic model and the experimental results are also presented in this section. Finally, a summary of the chapter is provided in section 5.5.

5.2 Experimental Setup

In this experimental setup both the translational as well as rotational motion is considered. In order to make measurements more easily, a circular aluminum guideway is considered instead of a flat aluminum guideway. The circular wheel guideway as shown in Figure 5.1 is 1.2m in diameter and has two continuous aluminum (6061-

T06) rings affixed onto its outer surface. The width and thickness of these aluminum rings are 77mm and 6.7mm respectively. This guideway wheel was originally used at Argonne National Laboratory during the 1990's and later used by Bird at the University of Wisconsin-Madison and was brought to UNC Charlotte by Bird. Only one aluminum guideway is used for the pendulum setup.

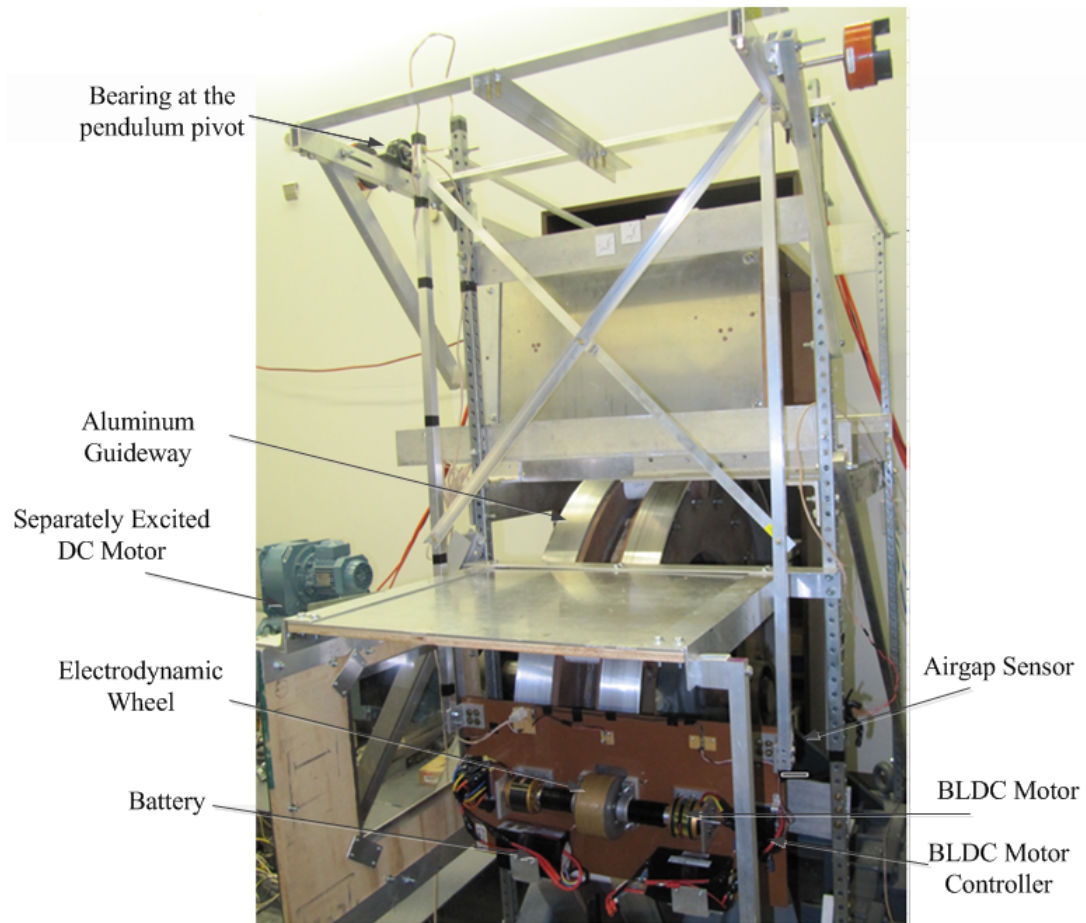
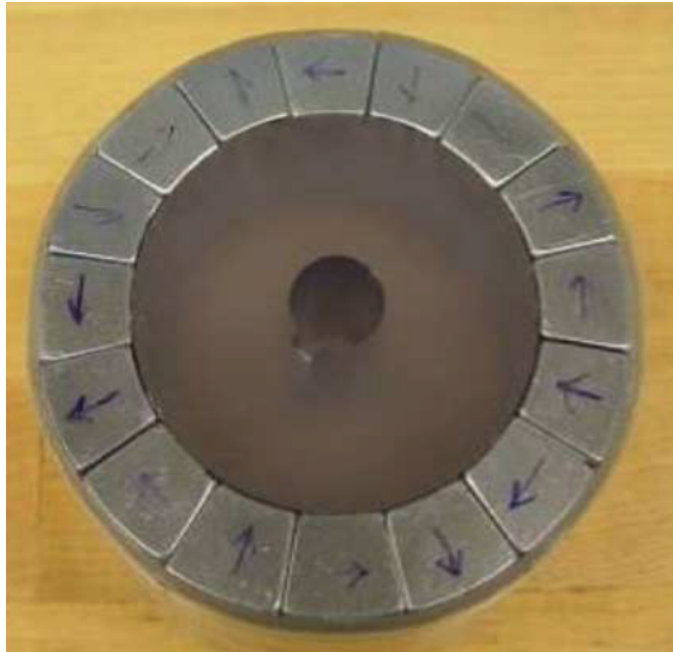


Figure 5.1: *The photograph of the experimental setup of a single EDW pendulum setup.*

The 16-segment 4 pole-pair EDW Halbach rotor is used in this experimental setup as shown in Figure 5.2. This rotor was assembled by Bird. The magnetization direction of the rotor assembly is shown in Figure 5.3. The outer and inner radius of the EDW is 50mm and 34.2mm respectively. The parameters for both the guideway and the EDW are given in Table 5.1. The experimental setup, as shown in Figure 5.1, has been constructed with the help from W. Bomela. The aluminum guideway,

Table 5.1: *Guideway and EDW parameters of the experimental setup.*

EDW rotor parameters	Outer radius, r_o	50 mm \pm 0.58 mm
	Inner radius, r_i	34.20 mm
	Width of rotor, w	50 m
	Sleeve thickness	2.6 mm \pm 0.1 mm
	Magnet (NdFeB), B_r	1.42 (T)
	Magnet relative permeability	1.08
	Pole-pairs, P	4
Guideway parameters	Outer radius (R_o)	600 mm \pm 0.58 mm
	Guideway width	77 mm
	Thickness, b	6.3 mm
	Conductivity (Al)	2.459×10^7 Sm ⁻¹

Figure 5.2: *Picture of experimental four pole-pair EDW using 16 segmented NdFeB magnets [41].*

EDW, Brushless DC (BLDC) motors as well as air-gap sensor are shown in this figure. The schematic diagram of this setup is shown in Figure 5.4. The EDW is rotated by two Axi-5330/24 BLDC motors rotating in the same direction. The parameters of these BLDC motor are given in Table 5.2. The two BLDC motors are used to get sufficient torque to rotate the EDW even at very small air-gap from the guideway.

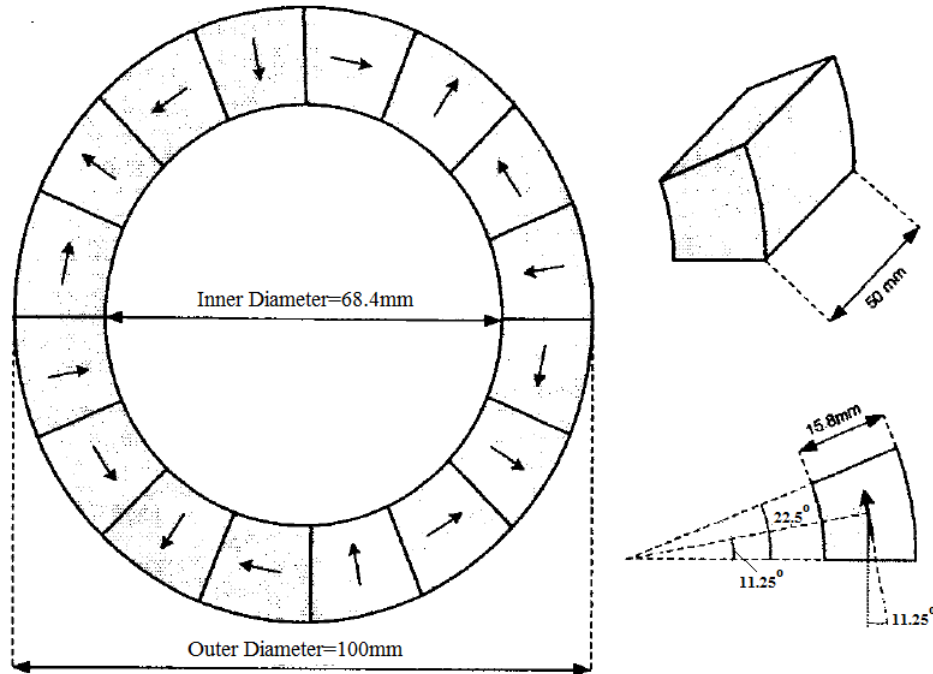


Figure 5.3: *Halbach rotor magnet assembly showing magnetization direction* [41].

The power is supplied by the battery pack onboard the pendulum as shown in Figure 5.5. The schematic of this EDW and BLDC motor configuration is shown in Figure 5.6. Turnigy 4.5Ah 6cell 19.8V batteries are used to drive the BLDC motors. The BLDC motors are driven by HobbyKing 150A Brushless Electronic Speed Controllers (ESC). The speed of the motors is controlled by varying the 5V pulse width to the ESC. The guideway is rotated by a separately excited DC motor. The parameters of this DC motor supplied by the manufacturer as well as parameters measured in the lab are given in Table 5.3. The RPM of the separately excited DC motor and EDW or (BLDC) motors has been measured using a rotary encoder sensor and Hall effect sensors respectively. These sensors output were connected to Matlab/Simulink Real Time Window (RTW) through a National Instrument (NI) PCIe-2659 board. The oscillation of the pendulum was measured using a Panasonic laser displacement sensor. The analog output of this displacement sensor was also connected to Matlab RTW through the same NI board.

The step change in the RPM of an EDW is achieved by a step change in the

duty cycle of the pulse width modulation (that is required for ESC) via the function generator. The field and armature of the guideway motor is powered using an Agilent Technologies DC power supply and a Chroma DC power supply respectively.

Table 5.2: *Axi-5330/24 brushless PM DC motor parameters.*

Measured parameters using RLC meter	Parameter supplied by manufacturer
Per-phase inductances $L_{p-p} = 30.17\mu\text{H}$	RPM/V = 197
Per-phase resistance $R_{p-p} = 0.0181\text{Ohms}$	Max. efficiency = 97%
	Max. efficiency current = 15-38A (> 85%)
	Current Capacity = 65A/30s
	No load current = 1.5A

Table 5.3: *ABB separately excited DC motor parameters.*

Armature Winding	Field Winding
$V_a = 440\text{V}$	$V_f = 340\text{V}$
$I_a = 69\text{A}$	$I_f = 2.44\text{A}$
$R_a = 0.71\text{Ohms}$	$R_f = 139.34\text{Ohms}$
$L_a = 10.5\text{mH}$	
Measured values (RLC-meter)	Measured values (RLC meter)
$L_a = 5.884\text{mH}$	$L_f = 10.8\text{H}$
$R_a = 1.0\text{Ohms}$	$R_f = 111.5\text{Ohms}$
Torque rating = 132Nm	RPM rating = 1895RPM
Power rating= 26.1KW	$J = 0.12\text{Kgm}^{-2}$

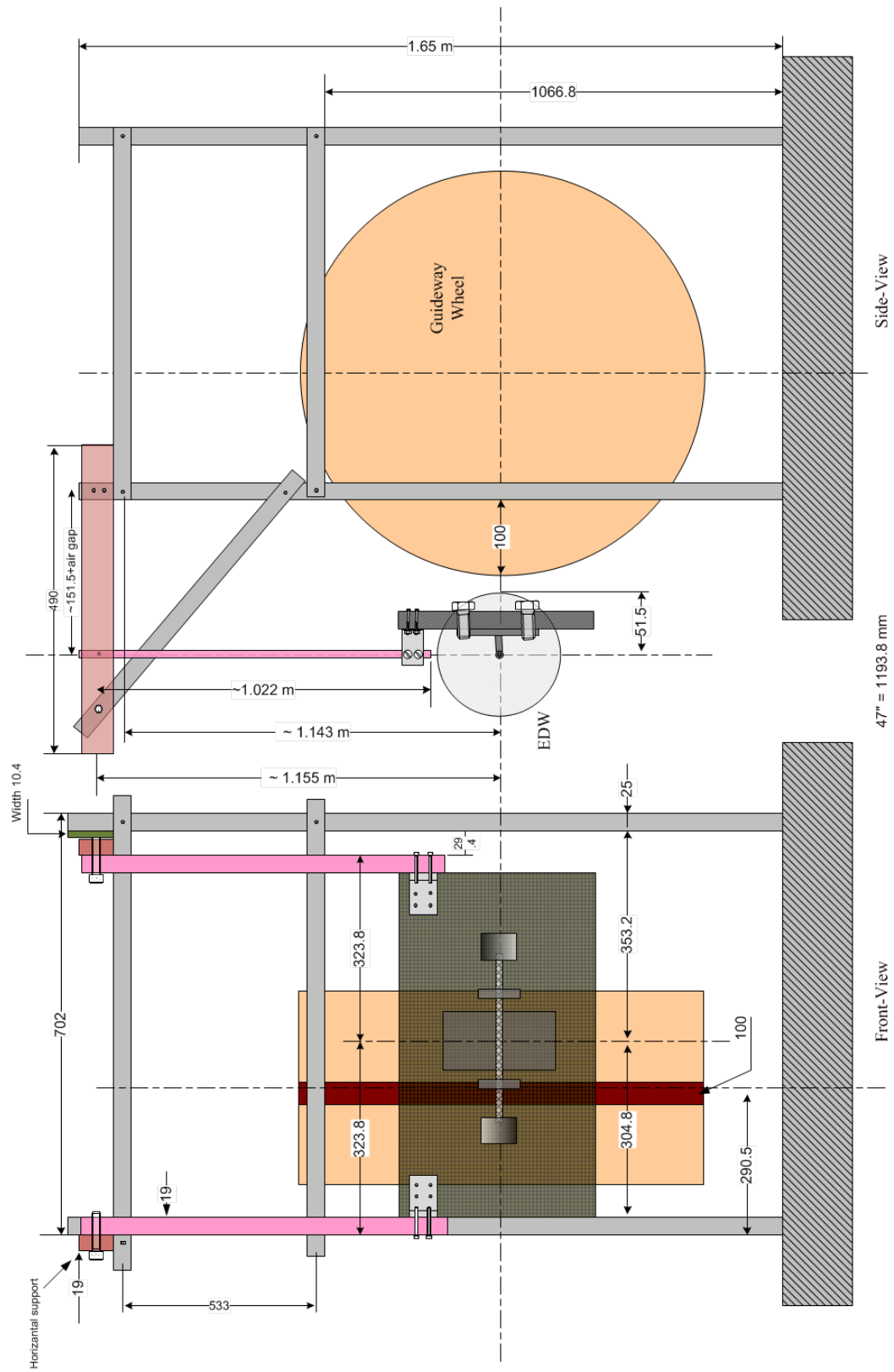


Figure 5.4: The schematic diagram of the pendulum setup showing guideway and EDW.

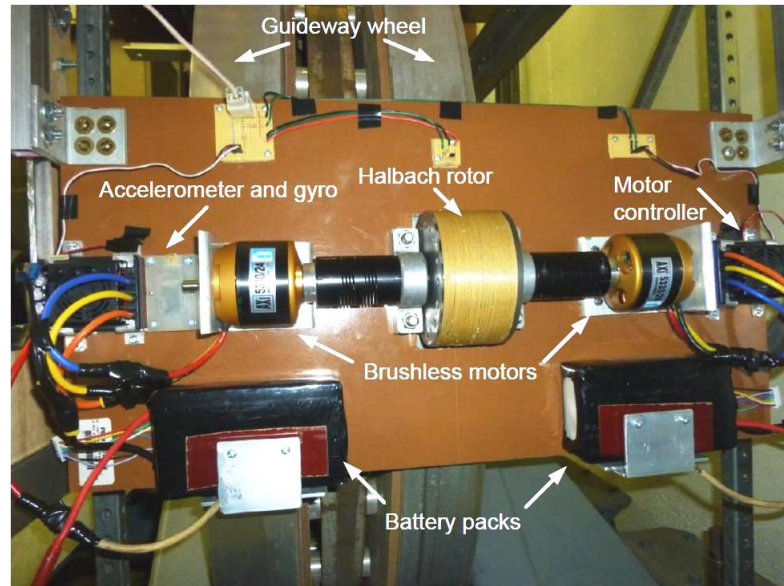


Figure 5.5: *Experimental setup showing EDW, BLDC motors and batteries pack.*

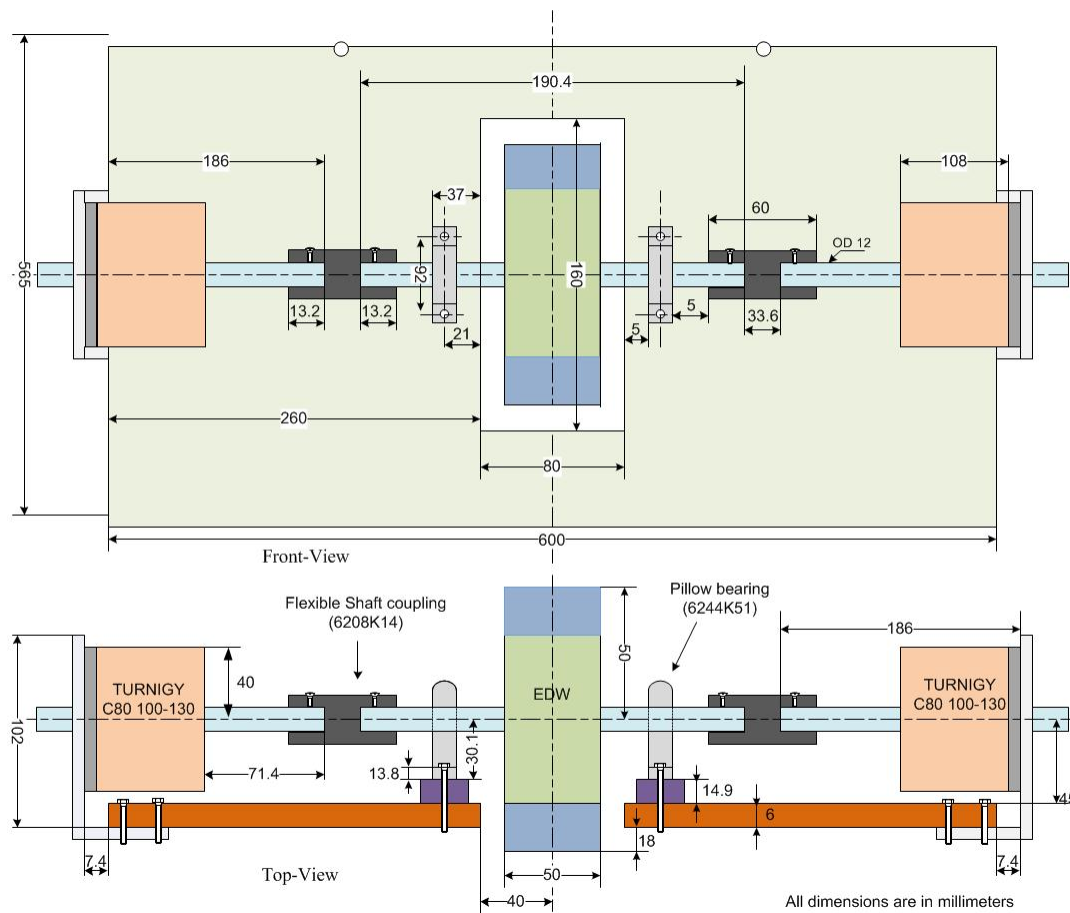


Figure 5.6: *The schematic drawing for Figure 5.5. Both front-view and top-view are shown.*

5.2.1 Measurement of guideway irregularities

The guideway irregularities were measured by using a Panasonic laser displacement sensor. The guideway was rotated at a speed of 1.631ms^{-1} and the air-gap was measured from a fixed position. It was observed that the guideway was not perfectly a circle. The plot of this is illustrated in Figure 5.7. The error was found to be $\pm 0.29\text{mm}$ (the peak to peak of this oscillation was 0.5875mm).

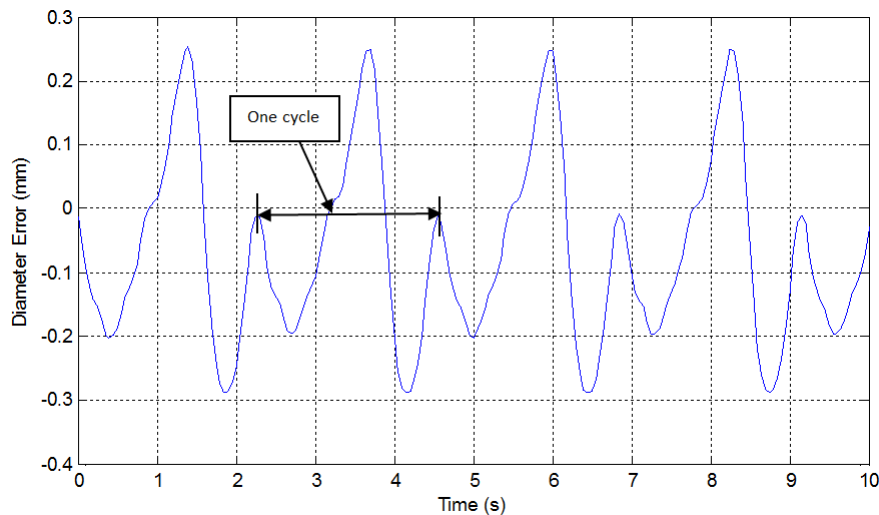


Figure 5.7: *The diameter error plot of the circular guideway when rotated at the translational speed of 1.631ms^{-1} for 10 seconds of time.*

5.3 Calculation of Air and Friction Damping Coefficients

Several tests have been performed in order to determine the damping characteristics of the EDW pendulum setup when there is no rotation of the EDW. In this case the damping is purely due to the air resistance and sliding friction at the pendulum pivot. A sample plot for the free oscillation of the EDW pendulum is shown in Figure 5.8.

If the angle of the pendulum is very small, the equation of motion for the free oscillation in the presence of a viscous force can be modeled using the well-known mass spring damper equation as [201, 202]

$$m \frac{d^2y(t)}{dt^2} + c \frac{dy(t)}{dt} + ky(t) = 0 \quad (5.1)$$

where

m = mass of the pendulum (kg)

c = viscous damping coefficient (Ns^2m^{-1})

k = stiffness coefficient (Nm^{-1})

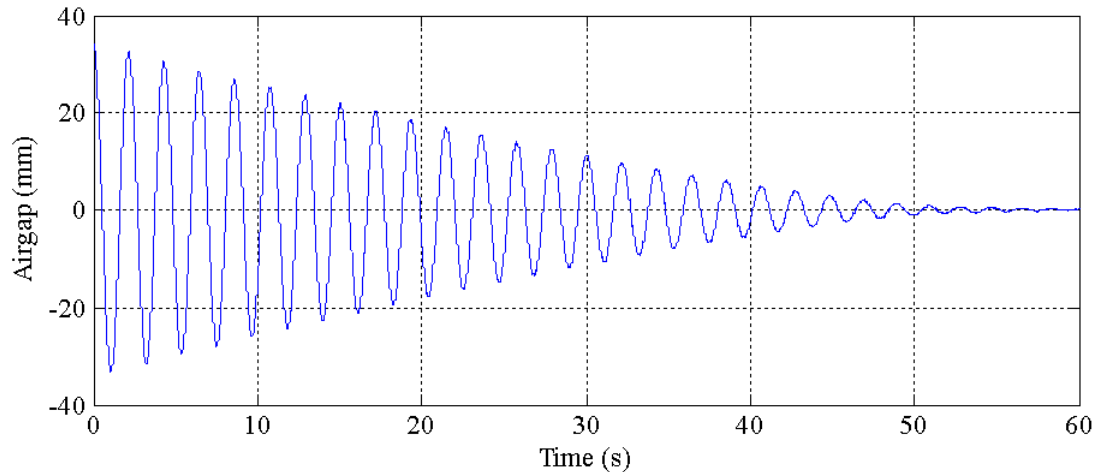


Figure 5.8: A sample plot of air-gap as a function of time from a free oscillation test.

Similarly, the equation of motion for the free oscillation in the presence of sliding (dry) friction is given by [201]

$$m \frac{d^2 y(t)}{dt^2} + \text{sgn} \left[\frac{dy(t)}{dt} \right] \mu m G + ky(t) = 0 \quad (5.2)$$

where

μ = sliding friction coefficient (Ns^2m^{-1})

G = acceleration due to gravity (ms^{-2})

$$\text{sgn}(x) = \begin{cases} +1 & \text{for } x > 0 ; \\ -1 & \text{for } x < 0 ; \\ 0 & \text{for } x = 0 . \end{cases}$$

In the pendulum setup of the EDW the viscous damping is present due to the air-resistance and the sliding friction is present at the pivot (bearing) where the pendulum is oscillating. Therefore, the equation free motion of the EDW pendulum

in the presence of both viscous as well as sliding friction can be modeled by combining (5.1) and (5.2) to get

$$m \frac{d^2 y(t)}{dt^2} + c \frac{dy(t)}{dt} + \operatorname{sgn} \left[\frac{dy(t)}{dt} \right] \mu m G + k y(t) = 0 \quad (5.3)$$

The damping coefficient due to air resistance, c , the damping coefficient due to friction, μ and the stiffness coefficient, k , are determined by using a least square error estimation technique on (5.3) in Matlab. A plot showing the comparison between the free oscillation experimental data air-gap variation and estimated air-gap variation when using (5.3) is shown in Figure 5.9 and Figure 5.10. Several other tests have been performed to obtain a good estimate of the parameters in (5.3). The estimated air-gap plot is matching very closely with the measured air-gap values until about 30s. However, the estimated air-gap is damping quickly after 30s compared with the measured air-gap. Since, the nonlinearities due to the vibrations are not included in this estimation, the small oscillation after 30s is not obtained in the estimated air-gap. The estimates of the parameters c , k and μ for various tests is shown in Table 5.4. The average of these parameters obtained in Table 5.4 is used in (5.3) to represent the dynamic equation of motion for the forced EDW pendulum.

Table 5.4: *Damping and stiffness coefficients from free oscillations.*

Test No.	Viscous Damping (Ns ² m ⁻¹)	Sliding Friction (Ns ² m ⁻¹)	Stiffness Coefficient (Nm ⁻¹)
Test-I	0.277	1.988x10 ⁻⁴	76.0697
Test-II	0.409	1.909x10 ⁻⁴	76.9649
Test-III	0.399	1.8408x10 ⁻⁴	76.7980
Test-IV	0.3223	2.1262x10 ⁻⁴	76.6677
Test-V	0.395	1.9345x10 ⁻⁴	77.5035
Average	0.361	1.9599x10 ⁻⁴	76.8008

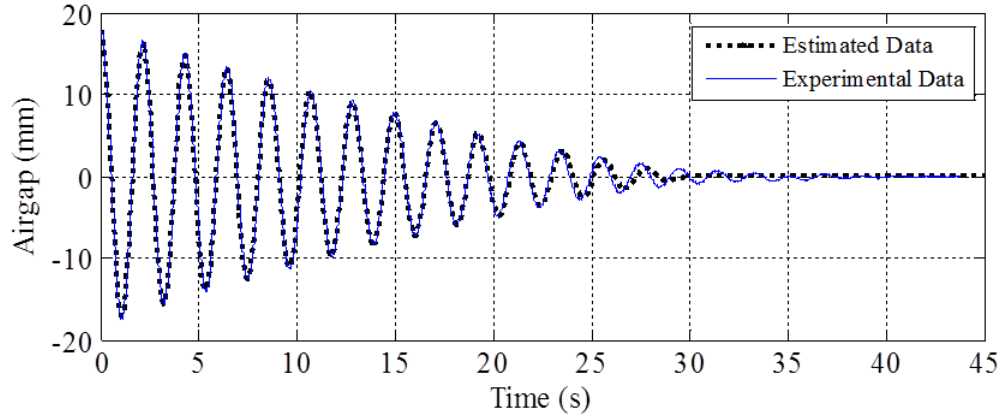


Figure 5.9: A comparison between the experimental and estimated air-gap for a free oscillation test of an EDW pendulum setup-Test-I.

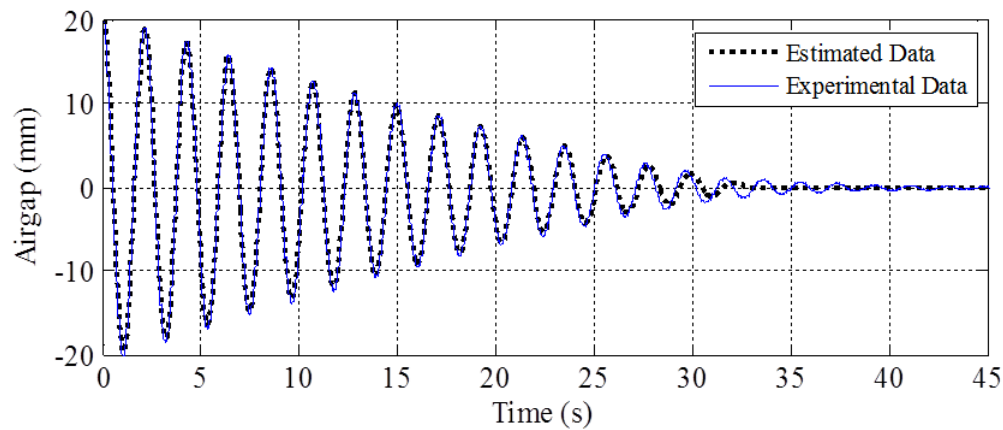


Figure 5.10: A comparison between the experimental and estimated air-gap for a free oscillation test of an EDW pendulum setup-Test-II.

5.4 Dynamics of the Forced Pendulum

In order to investigate the dynamic behavior of the EDW pendulum, the guideway wheel is moved (rotated in this experiment) by the separately excited DC motor as shown in Figure 5.1 and the EDW is rotated by the two BLDC motors as shown in Figure 5.5. When the rotational motion of the EDW and the guideway is added to the pendulum setup, the equation of motion becomes a forced pendulum motion. The equation of this forced pendulum system can be written as

$$m \frac{d^2 y(t)}{dt^2} + c \frac{dy(t)}{dt} + \left[\frac{dy(t)}{dt} \right] \mu m G + k y(t) = F_y^{EDW}(v_x, v_y, \omega_m, y) \quad (5.4)$$

where, the force term $F_y^{EDW}(v_x, v_y, \omega_m, y)$ on the right hand side of (5.4) is the lift force produced by the rotating EDW while interacting with the moving guideway. This lift force is a function of velocity (v_x and v_y), angular velocity (ω_m) and the air-gap (g or y in this case since the oscillation is only in y -direction). The steady-state and the transient equations for this lift force has already been derived in Chapter 2 and Chapter 3 respectively. The parameters g , v_x and ω_m are contineously measured using the laser displacement, rotary encoder and hall effect sensors respectively. The velocity, v_y has been obtained by differentiating the air-gap data with respect to time in Matlab.

In order to acqrately model the dynamic behaviour of the EDW pendulum, the effect of the translational force has also been included in the model. In this experimental setup, the translational force is acting vertically downward. The thrust force's effect can be included as the addition of an equivalent mass to the pendulum setup. Therefore, the effective mass of the pendulum becomes

$$m' = m + F_x^{EDW}/G \quad (5.5)$$

where F_x^{EDW} is the thrust force due to the EDW.

The dynamic equation of motion when including both the translational and lift force is therefore given by

$$m' \frac{d^2 y(t)}{dt^2} + c \frac{dy(t)}{dt} + \left[\frac{dy(t)}{dt} \right] \mu m' G + ky(t) = F_y^{EDW}(v_x, v_y, \omega_m, y) \quad (5.6)$$

Table 5.5: *Pendulum setup parameters.*

Mass of setup without batteries	7.04 (kg)
Mass of two Turnigy batteries	1.810 (kg)
Length of the pendulum	1.307 (m)

Using the steady-state lift force equations derived in Chapter 2 and the parameters given in Table 5.4 and Table 5.5, the dynamic equation given by (5.4) has been solve using the Matlab *ode45* function. The measured air-gap, g , velocity, v_x , heave velocity, v_y and EDW angular velocity, ω_m has been used as input parameters to calculate the lift force, F_y^{EDW} in (5.6). Only the initial value (at $t = 0s$) of the air-gap and the heave velocity has been used in order to solve (5.6) using *ode45*. Since the equation is solved for two state variables: air-gap and heave velocity, the air-gap and heave velocity required to evaluate F_y^{EDW} for the next time step will be obtained from the proceeding *ode45* solution. However, the *ode45* will be supplied with the measured v_x and ω_m for the entire solution time. In this way, the air-gap and v_y profile is obtained from *ode45*. This air-gap profile (obtained analytically solving (5.6)) is compared with the measured air-gap profile. Several tests have been performed and validated in this section.

5.4.1 Test-A

In this test case, the pendulum is initially at an equilibrium position such that the air-gap between the EDW and the guideway is 11.95mm. The guideway is fixed in this test ($v_x = 0ms^{-1}$). The EDW is initially at rest. The EDW is now rotated by a step change (at $t = 0s$) in angular velocity as shown in Figure 5.11. The pendulum starts to oscillate and settles at the steady-state position of 23.33mm. The experimental (measured) v_y and air-gap are shown in Figure 5.12 - Figure 5.13. The lift and thrust forces calculated using the steady-state analytic equations (2.116) and (2.117) for the corresponding parameters is shown in Figure 5.14 and Figure 5.15. With the initial air-gap (11.95mm), initial $v_y = 0ms^{-1}$ and measured ω_m , the dynamical equation (5.6) is solved via *ode45*. The air-gap profile obtained is compared with the experimental in Figure 5.14. The analytical air-gap profile is very high (32.34mm) compared with the experimental one. This is a consequence of the 2-D steady-state lift and thrust forces being very high compared with the actual experimental values because they

did not account for the finite width of the guideway as well as finite rotor source width. The 2-D model was based on the assumption that the rotor source as well as guideway is extended to infinite length in the z -direction. However, this is not true for the experimental setup. Therefore, in order to make a realistic comparison, the experimental results will be compared with the 3-D EDW force model which have been developed by S. Paul [203]. In this 3-D eddy-current model, the effect of the finite width of the rotor source as well as the guideway has been taken into account. Since, in the experimental setup, the rotor width (50mm) as well as guideway width (77mm) are finite, the 3-D force on the right side of (5.6) should be capable of predicting the dynamics of the experimental setup more accurately.

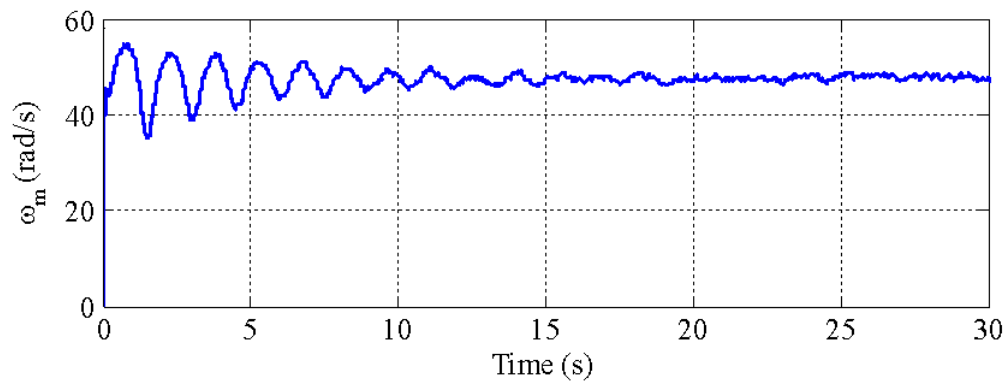


Figure 5.11: *The measured ω_m of EDW for Test-A.*

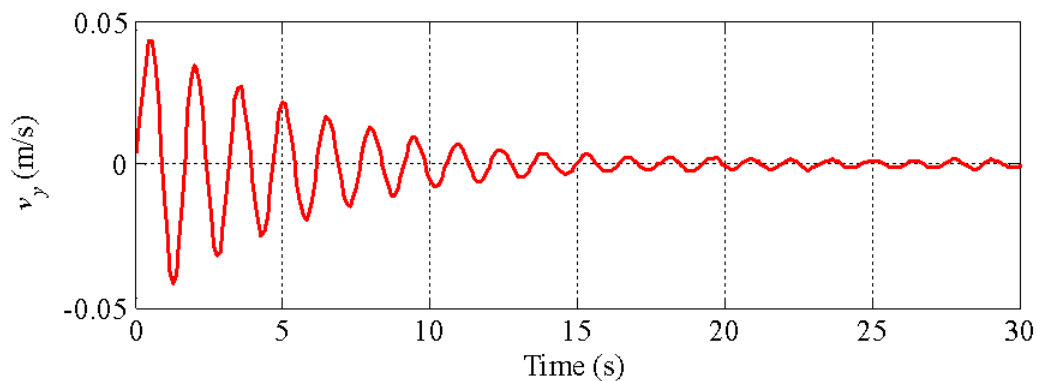


Figure 5.12: *The measured v_y of the EDW for Test-A.*

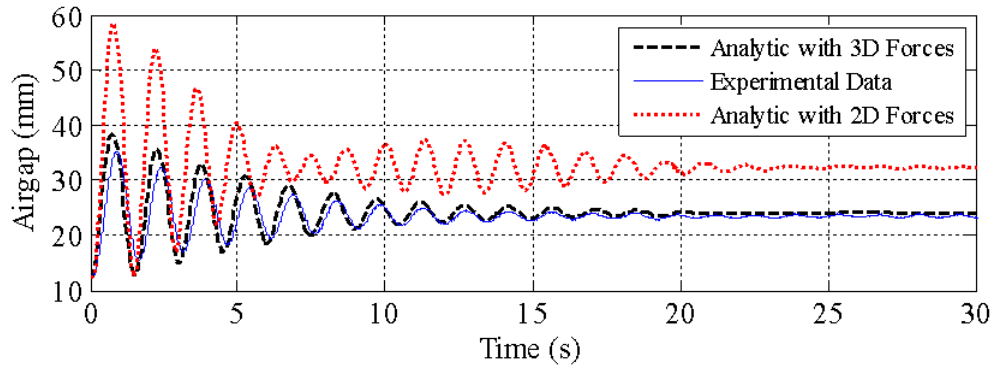


Figure 5.13: An air-gap profile using 2-D forces, 3-D forces and experimental results for Test-A.

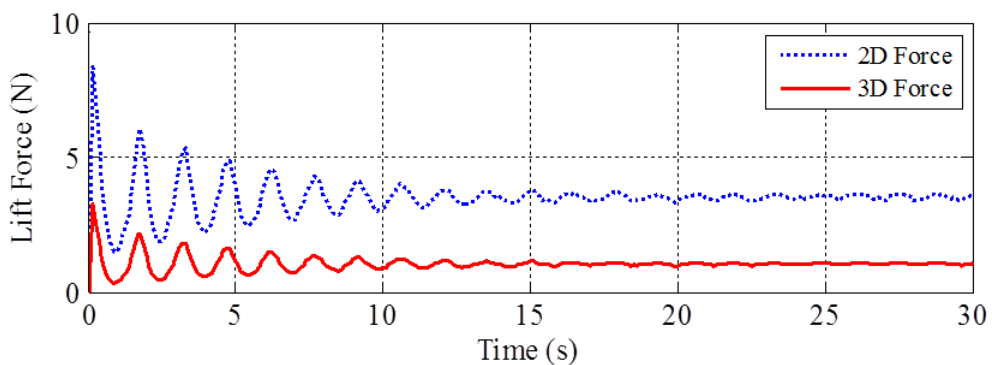


Figure 5.14: 2-D and 3-D lift force at the operating points of Test-A.

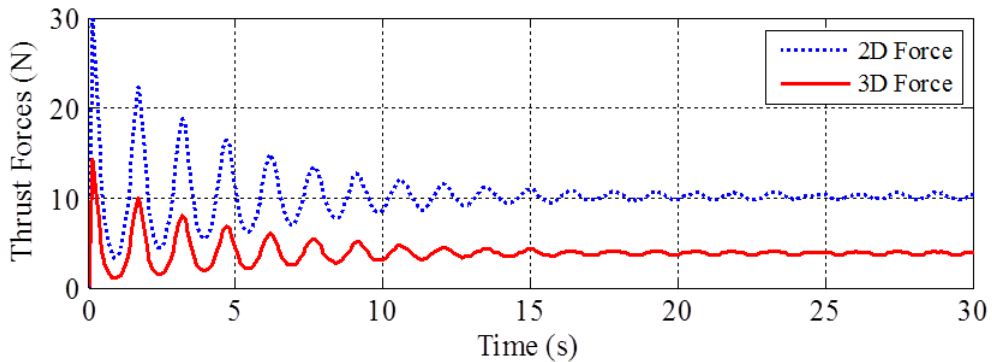


Figure 5.15: 2-D and 3-D thrust force at the operating points of Test-A.

The lift and thrust forces from the 3-D model is compared with the corresponding 2-D model forces in Figure 5.14 and Figure 5.15. The 3-D forces are almost three times smaller than the 2-D forces. The dynamic equation (5.6) is solved using ode45 by replacing 2-D forces with the 3-D forces (developed by S. Paul). The air-gap profile obtained is compared with the experimental as well as the air-gap profile from

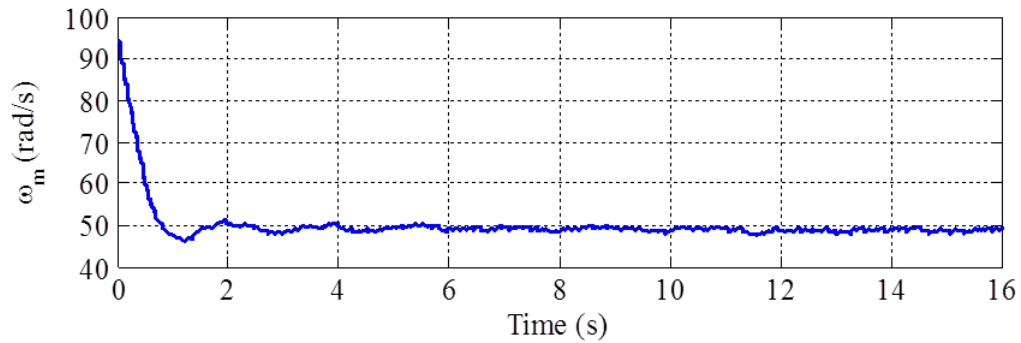
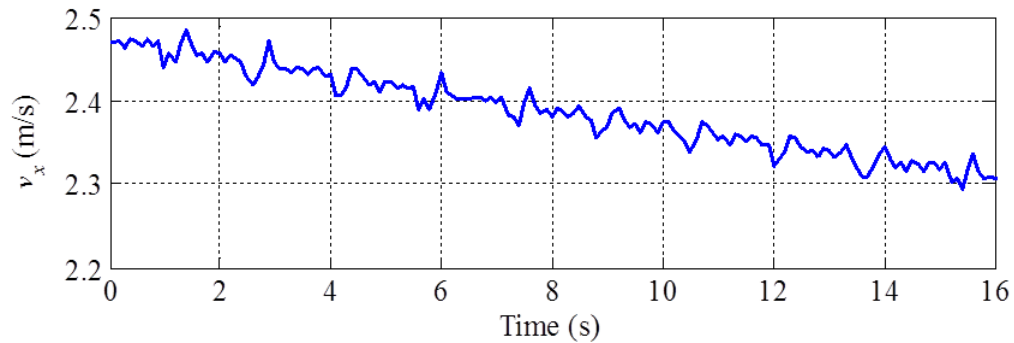
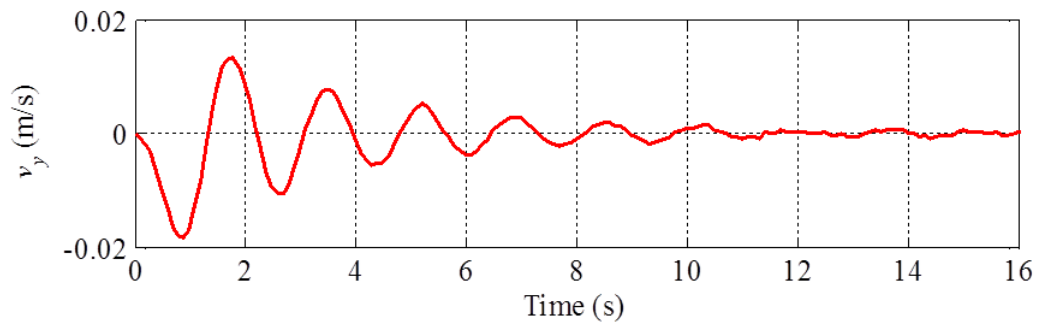
(5.6) with 2-D forces on Figure 5.13. The air-gap value using 3-D forces settled down to 24.1mm; slightly greater than the experimental values (23.33mm). The analytical 3-D air-gap profile is higher than the experimental one because the analytic force equations developed by S. Paul is based on the assumption that the guideway is flat. However, the guideway is circular in the experimental setup. This curved guideway setup produces less force compared with the flat guideway as investigated by J. Bird in [41]. The second reason for the difference between the measured and calculated air-gap using 3-D forces is because the steady-state force model (with v_y) has been used instead of transient model. As discussed in Chapter 4, there will be an error of about 5% while using steady-state force model instead of transient force model when integrated with the Maglev vehicle. The similar experimental test performed at $v_x = 0\text{ms}^{-1}$ (Test-F) is included in Appendix B.

5.4.2 Test-B

The pendulum equilibrium position and the initial conditions of the steady-state operation at $t = 0\text{s}$ are shown in Table 5.6. The EDW is now rotated by a step change (at $t = 0\text{s}$) in ω_m from 94.7rads^{-1} to 48.7rads^{-1} as shown in Figure 5.16. Since, the value of ω_m and slip is decreases the lift force also decreases. Therefore, the pendulum air-gap decreases and reaches to a new steady-state at $g = 17.86\text{mm}$. The experimental (measured) v_x , v_y and air-gap, g are shown in Figure 5.17 - Figure 5.19. The steady-state lift and thrust forces calculated using the corresponding parameters are shown in Figure 5.20 and Figure 5.21. With the initial air-gap (26.15mm), initial $v_y = 0\text{ms}^{-1}$ and measured ω_m and v_x , the dynamic equation (5.6) is solved via ode45. The air-gap value obtained from ode45 is compared with the experimental in Figure 5.19. The steady-state air-gap value using 2-D forces and 3-D forces are 23.87mm and 18.21mm respectively. As in the Test-A, the value of air-gap using 2-D forces is very high compared with experimental but the calculated air-gap using 3-D forces is close to the measured one. The results in this test is consistent with Test-A.

Table 5.6: *Initial conditions for Test-B at $t = 0s$.*

Parameters	Values
Pendulum equilibrium position	$g = 11.95\text{mm}$
Initial air-gap	$g = 26.15\text{mm}$
Initial translational velocity	$v_x = 2.46\text{ms}^{-1}$
Initial angular velocity	$\omega_m = 94.7\text{rads}^{-1}$
Initial heave velocity	$v_y = 0\text{ms}^{-1}$
Initial slip velocity	$s_l = 2.275\text{ms}^{-1}$

Figure 5.16: *The measured ω_m of EDW for Test-B.*Figure 5.17: *The measured v_x of the guideway for Test-B.*Figure 5.18: *The measured v_y of the EDW for Test-B.*

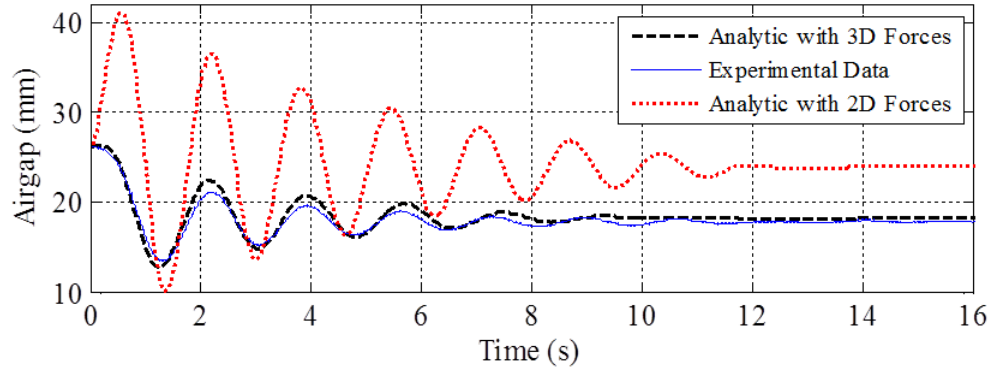


Figure 5.19: An air-gap profile using 2-D-forces, 3-D-forces and experimental results for Test-B.

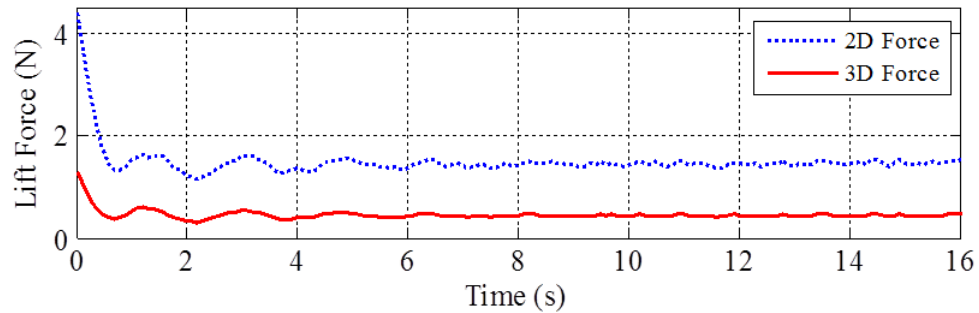


Figure 5.20: 2-D and 3-D lift forces at the operating points of Test-B.

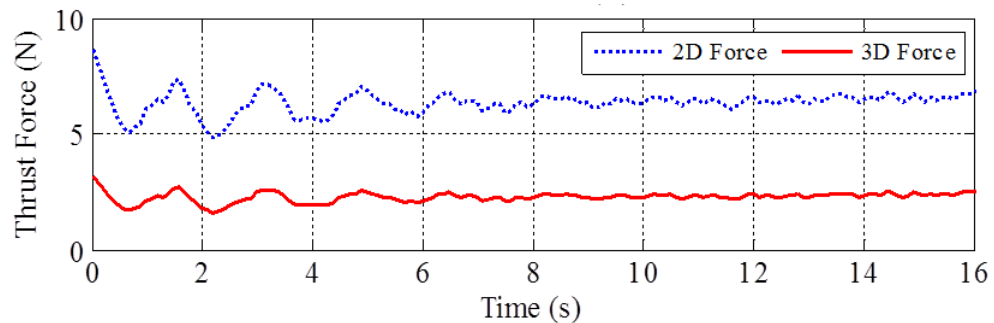


Figure 5.21: 2-D and 3-D thrust forces at the operating points of Test-B.

In the following tests the air-gap between the EDW and guideway at the equilibrium point is increased to $g = 21.5\text{mm}$. The comparison between the experimental result and solution using the 3-D forces will be included in this chapter. However, the comparison with the corresponding 2-D is included in the Appendix B.

5.4.3 Test-C

The pendulum equilibrium position and the initial conditions for this test are given in Table 5.7. The velocity of the guideway is kept zero in this test case. The EDW is now rotated by a step change (at $t = 0s$) in ω_m from 0 rads^{-1} to 51.50 rads^{-1} (steady-state) as shown in Figure 5.22. The pendulum starts to oscillate due to the lift force between the EDW and guideway. The pendulum air-gap increases and reaches to a steady-state air-gap of $g = 28.56 \text{ mm}$. The measured v_y and air-gap are shown in Figure 5.23 and Figure 5.24. The lift and thrust force calculated using the 3-D steady-state equations for the corresponding parameters is shown in Figure 5.25 and Figure 5.26. The air-gap value obtained from ode45 is compared with the experimental in Figure 5.24. The comparison of the air-gap for 2-D, 3-D and experimental is included in Appendix B (Figure B.1). The steady-state air-gap value using 2-D forces and 3-D forces are 36.8 mm and 29.13 mm respectively. As in the above test cases, the value of the air-gap using 2-D forces is very high compared with experimental values but the air-gap using 3-D forces is close to the measured values. The small oscillation that is present in the measured air-gap (refer Figure 5.24) is due to the vibration of the pendulum setup. This vibration is caused by the rotation of the EDW. Since, this vibration is not included in the dynamic equation of motion, the small oscillation is not obtained in the estimated air-gap values.

Table 5.7: *Initial conditions for Test-C at $t = 0s$.*

Parameters	Values
Pendulum equilibrium position	$g = 21.5 \text{ mm}$
Initial air-gap	$g = 21.5 \text{ mm}$
Initial translational velocity	$v_x = 0 \text{ ms}^{-1}$
Initial angular velocity	$\omega_m = 0 \text{ rads}^{-1}$
Initial heave velocity	$v_y = 0 \text{ ms}^{-1}$
Initial slip velocity	$s_l = 0 \text{ ms}^{-1}$

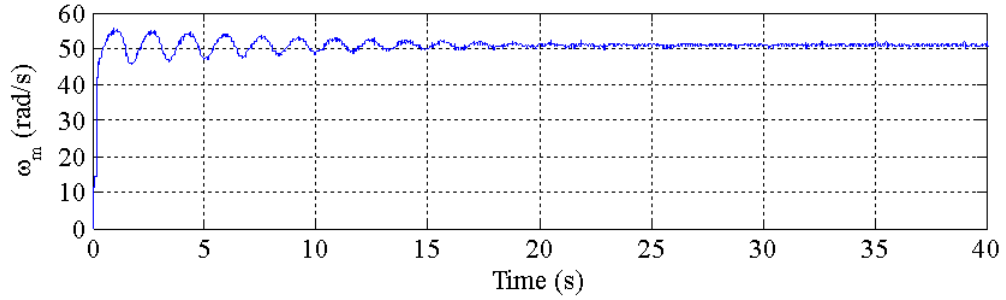


Figure 5.22: The measured ω_m of EDW for Test-C.

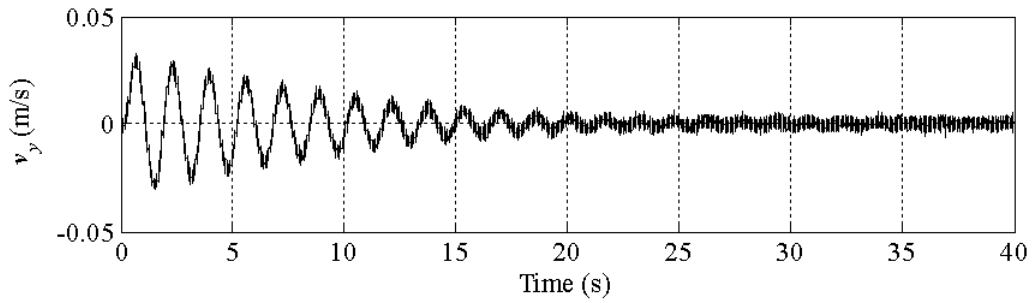


Figure 5.23: The measured v_y of the EDW for Test-C.

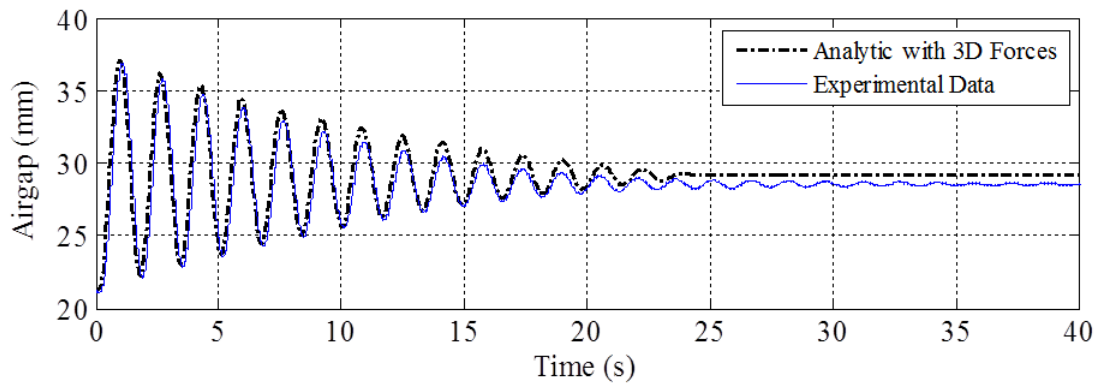


Figure 5.24: An air-gap profile using 3D forces and experimental results for Test-C.

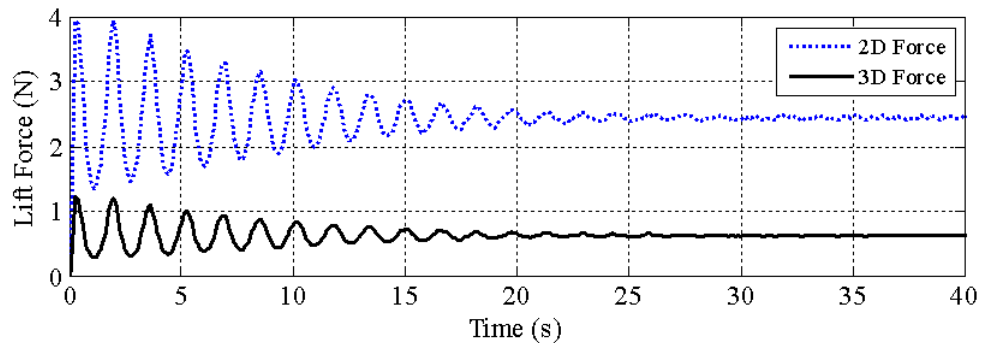


Figure 5.25: 2-D and 3-D lift forces at the operating points of Test-C.

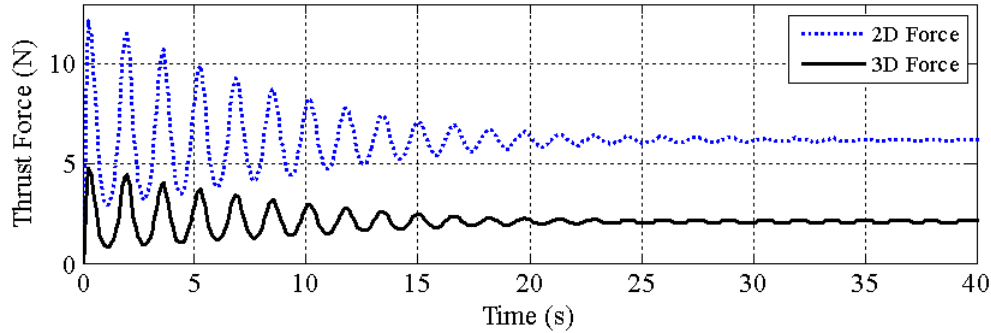


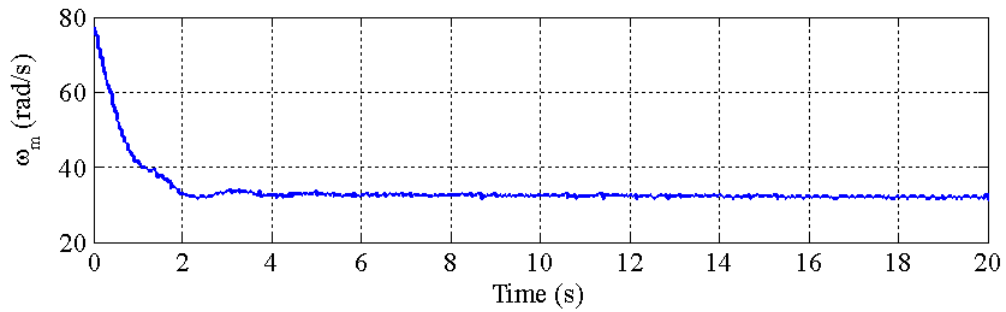
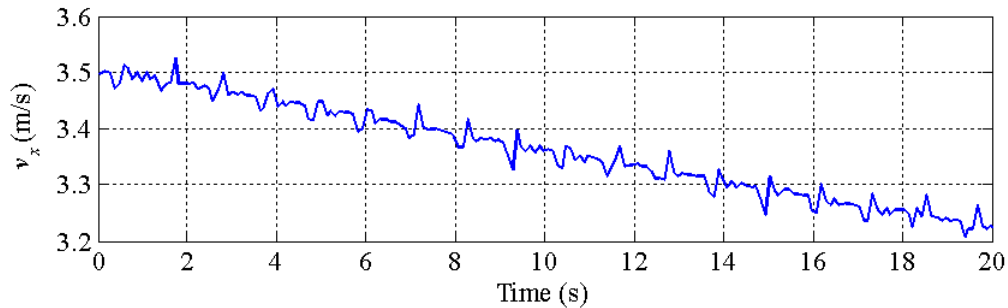
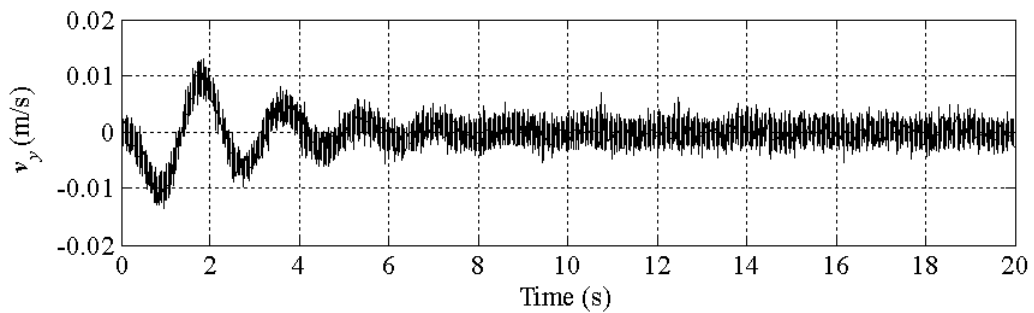
Figure 5.26: 2-D and 3-D thrust forces at the operating points of Test-C.

5.4.4 Test-D

The pendulum equilibrium position and the initial steady-state operating conditions for this test are shown in Table 5.8. The ω_m of EDW is stepped down (at $t = 0$ s) from 77.21 rads^{-1} to 31.54 rads^{-1} (steady-state) as shown in Figure 5.27. Since, the value of ω_m and slip is decreasing the lift force also decreases. Therefore, the pendulum air-gap decreases and reaches a new steady-state at $g = 22.8\text{mm}$. The experimental v_x , v_y and air-gap is shown in Figure 5.28 - Figure 5.30. With the initial air-gap (26.79mm), initial $v_y = 0\text{ms}^{-1}$ and measured ω_m and v_x , the dynamic equation (5.6) is solved via ode45 for both 2-D and 3-D cases. The air-gap value obtained from ode45 using 3-D is compared with the experimental in Figure 5.29. The air-gap comparison for the 2-D case is included in Appendix B (Figure B.2). The lift and thrust forces calculated using the steady-state analytical equations for these parameters v_x , v_y , g and ω_m are shown in Figure B.3 and Figure B.4. The steady-state air-gap value using 2-D forces and 3-D forces are 25.34mm and 23.22mm respectively. The value of air-gap 3-D forces is close to the measured one.

Table 5.8: *Initial conditions for Test-D at $t = 0s$.*

Parameters	Values
Pendulum equilibrium position	$g = 21.5\text{mm}$
Initial air-gap	$g = 26.79\text{mm}$
Initial translational velocity	$v_x = 3.5\text{ms}^{-1}$
Initial angular velocity	$\omega_m = 77.21\text{rads}^{-1}$
Initial heave velocity	$v_y = 0\text{ms}^{-1}$
Initial slip velocity	$s_l = 0.3605\text{ms}^{-1}$

Figure 5.27: *The measured ω_m of EDW for Test-D.*Figure 5.28: *The measured v_x of the guideway for Test-D.*Figure 5.29: *The measured v_y of the EDW for Test-D.*

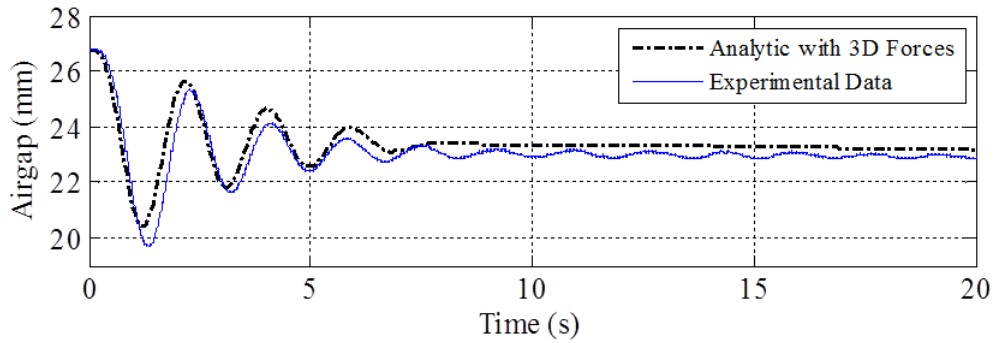


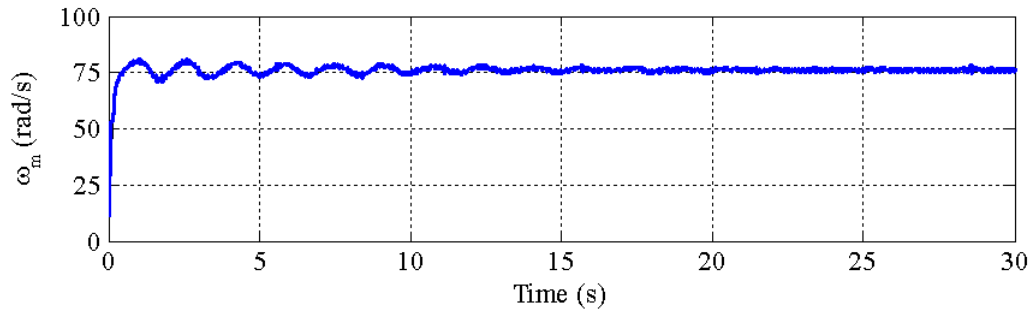
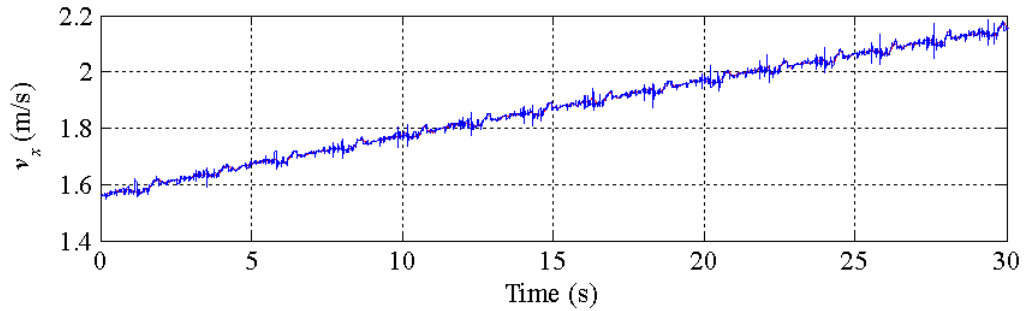
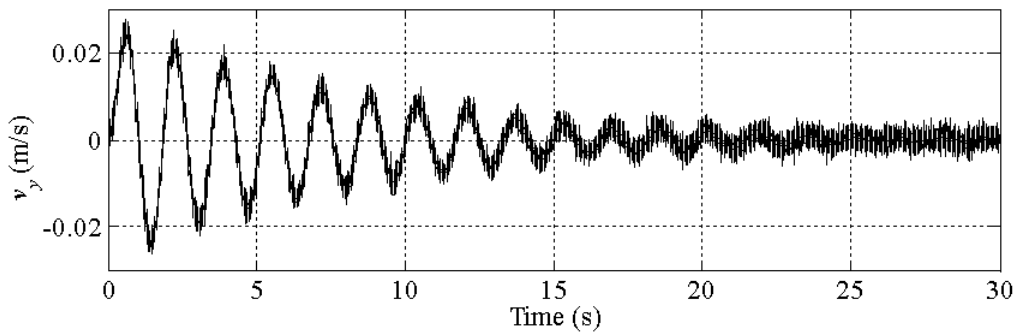
Figure 5.30: An air-gap profile using 3-D forces and experimental results for Test-D.

5.4.5 Test-E

The pendulum equilibrium position and the initial conditions of the parameters for this test are listed in Table 5.9. The step change in ω_m from 10.62 rads^{-1} to 75.47 rads^{-1} as shown in Figure 5.31 is applied at $t = 0\text{s}$. The value of ω_m and slip increases, therefore, the lift force also increases. The pendulum air-gap increases and reaches to a new steady-state air-gap at $g = 28.65\text{mm}$. The experimental v_x , v_y and air-gap are shown in Figure 5.32 - Figure 5.34. The dynamic equation (5.6) for both 2-D and 3-D cases with the initial air-gap (22.10mm), initial $v_y = 0\text{ms}^{-1}$ and measured ω_m and v_x . The air-gap value obtained from (5.6) using 3-D is compared with the experimental in Figure 5.33. The air-gap comparison for 2-D case is included in Appendix B (Figure B.5). The lift and thrust force calculated using the steady-state analytic equations for these parameters v_x , v_y , g and ω_m are shown in Figure B.6 and Figure B.7. The steady-state air-gap value using 2-D forces and 3-D forces are 37.0mm and 29.18mm respectively. The value of air-gap 3-D forces is close to the measured one. Several other tests are included in the Appendix ??.

Table 5.9: *Initial conditions for Test-E at $t = 0s$.*

Parameters	Values
Pendulum equilibrium position	$g = 21.5\text{mm}$
Initial air-gap	$g = 22.10\text{mm}$
Initial translational velocity	$v_x = 1.55\text{ms}^{-1}$
Initial angular velocity	$\omega_m = 10.62\text{rads}^{-1}$
Initial heave velocity	$v_y = 0\text{ms}^{-1}$
Initial slip velocity	$s_l = -1.019\text{ms}^{-1}$

Figure 5.31: *The measured ω_m of EDW for Test-E.*Figure 5.32: *The measured v_x of the guideway for Test-E.*Figure 5.33: *The measured v_y of the EDW for Test-E.*

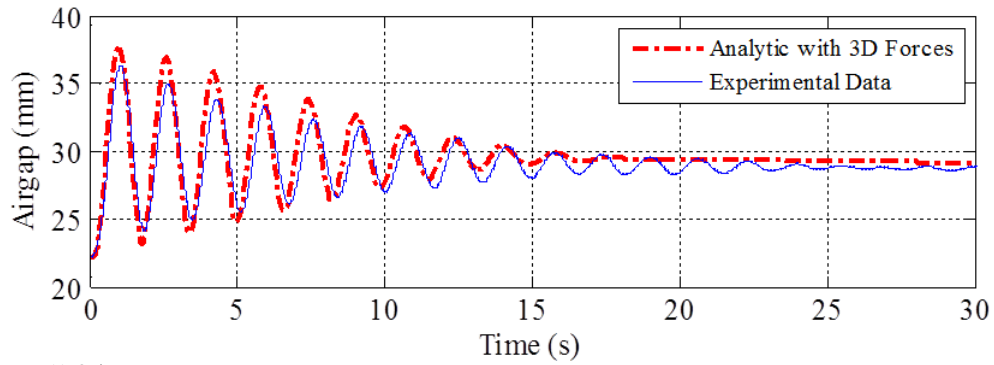


Figure 5.34: *An air-gap profile using 3-D forces and experimental results for Test-E.*

5.5 Summary

The 1-degree of freedom EDW pendulum setup has been constructed and tested. The irregularities of the circular guideway have been identified. The damping due to air resistance and friction has been experimentally evaluated. The dynamic equations of motion for the EDW pendulum setup have been developed. The experimental results showed that the 2-D model is predicting higher forces and therefore giving more oscillation compared to the experimentally measured one. However, the comparison of the measured air-gap of the 1-DOF pendulum during the forced oscillation using EDW with the analytic dynamic equations using the 3-D steady-state force equation is very closely matching. This experimental validates the simulation results in Chapter 4 that the steady-state force with v_y included model can accurately predict the transient behavior of the EDW Maglev.

CHAPTER 6: DYNAMICS OF MULTI-DOF EDW MAGLEV

6.1 Introduction

In this chapter the dynamics of a multi-degree of freedom sub-scale EDW Maglev vehicle has been investigated. A 6-DOF Maglev model has been simulated in Matlab Simulink/SimMechanicsTM. The experimental setup of a sub-scale Maglev vehicle has been built using 4-EDWs. This experiment setup has been simulated to investigate the dynamics in 6-DOFs (translational, x , heave, y , lateral, z , roll, θ_x , yaw, θ_y and pitch, θ_z).

The experimental setup of the multi-DOF sub-scale Maglev vehicle is described in detail in section 6.2. The Simulink model of the experimental EDW Maglev is presented in section 6.3. The 6-DOF simulation results of the EDW Maglev setup is included in section 6.4. The experimental results of EDW Maglev with lateral stability is presented in section 6.5. A summary of the chapter is presented in section 6.6.

6.2 Multi-DOF Maglev Experimental Setup

In order to investigate the dynamics of the EDW Maglev system in multi-DOF, an experimental setup as shown in the Figure 6.1 has been used. The guideway used for this setup is the same one as described in Chapter 5. The only difference is that in Chapter 5, only one sheet of the aluminum guideway was used. However, in this setup, both the sheets will be used.

A Maglev vehicle with four EDWs as shown in Figure 6.2 has been constructed. The EDW Halbach rotor has 16-magnets, is 52mm in diameter with 2 pole-pairs. This diameter was chosen so that the EDW torque could be met by the motor torque

while also having a greater diameter than the motor drive. The detail parameters of the Halbach rotor and guideway are presented in Table 6.1. The magnetization of the Halbach rotor is shown in Figure 6.3. The axial length of the rotor at the inner radius is 53.5mm whereas it is 52mm at the outer radius. This difference in the length was chosen such that the magnets could be held by the end plates more easily and give more mechanical strength to the rotor. The rotor yoke is made up of aluminum. The rotor was assembled by using the fixture as shown in Figure 6.4-(a). A Kevlar fiber was wrapped around the rotor to retain the magnet pieces in the EDW rotor. The assembled Halbach rotor with endplates and shaft is shown in Figure 6.5.

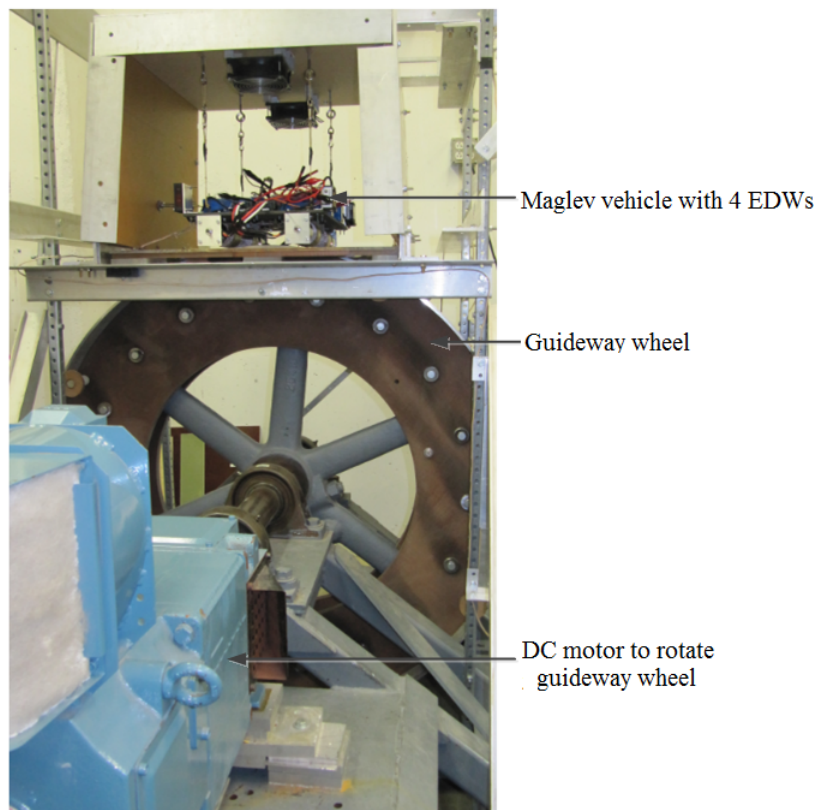


Figure 6.1: *Complete setup of a multi-DOF EDW Maglev system.*

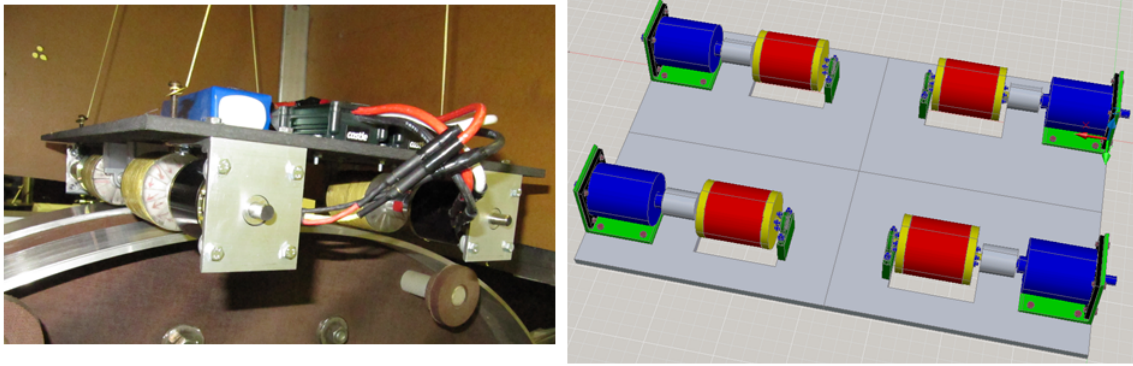


Figure 6.2: *Maglev vehicle. (a) Photograph of Maglev. (b) Autocad bottom view of Maglev.*

Table 6.1: *Guideway and EDW parameters for the 4-wheel Maglev setup.*

EDW Halbach rotor parameters	Outer radius, r_o	52 mm \pm 0.58 mm
	Inner radius, r_i	20 mm
	Width of rotor, w	52 mm
	Sleeve thickness	0.75 mm \pm 0.1 mm
	Magnet (NdFeB), B_r	1.42T
	Magnet relative permeability	1.08
Guideway parameters	Pole-pairs, P	2
	Outer radius, R_o	600 mm \pm 0.58 mm
	Guideway width, w	77 mm
	Thickness, b	6.3 mm
	Conductivity (Al), σ	2.459×10^7 Sm $^{-1}$
	Sheets separation	101 mm

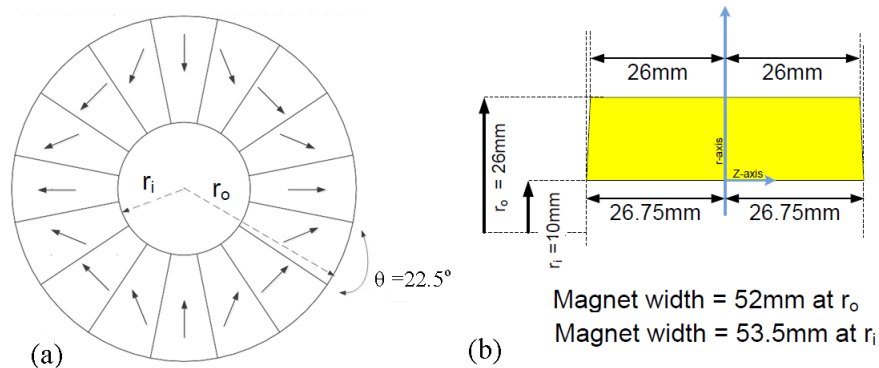


Figure 6.3: *Experimental 2 pole-pair Halbach rotor: (a) Magnetization direction. (b) The side view of the Halbach rotor.*

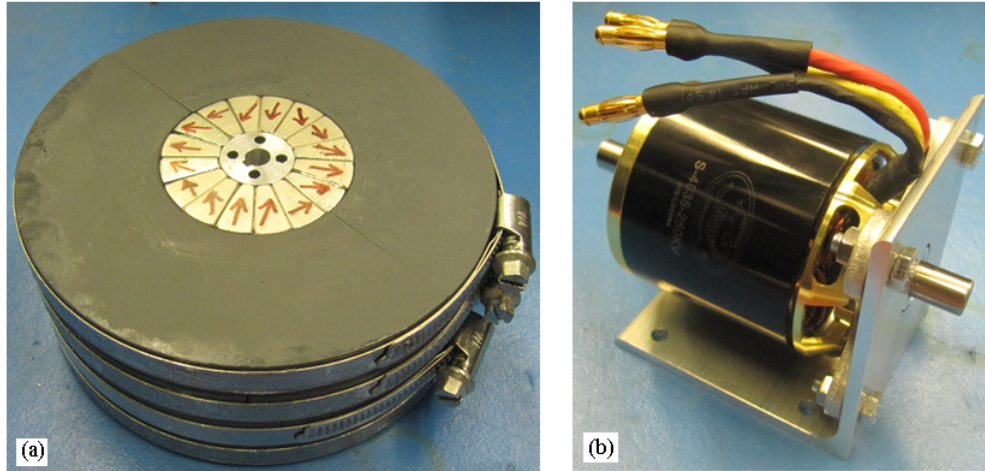


Figure 6.4: (a) Halbach rotor assembly fixture. (b) Scorpion brushless DC motor.

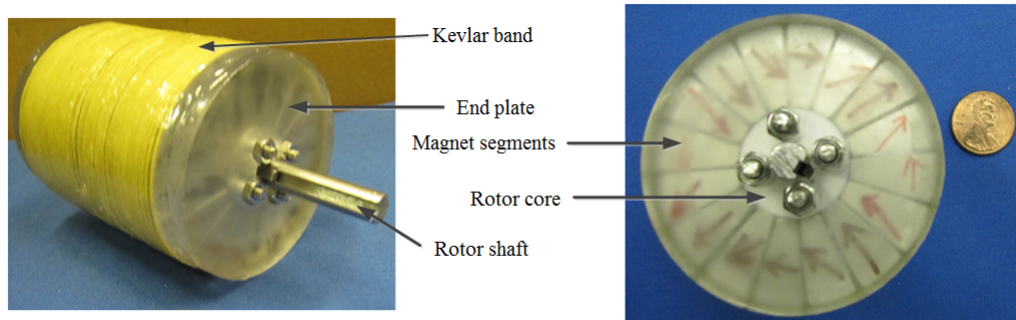


Figure 6.5: Assembled 16-segment 2 pole-pairs Halbach rotor.

Each EDW Halbach rotor is rotated by a Scorpion S-4035-250KV brushless DC motor as shown in Figure 6.4-(b). The parameters of this motor are given in Table 6.2. These motors are selected based on the torque and outer diameter requirement study performed using 3-D magnetic forces. The brushless motors are coupled with the Halbach rotors by flexible shaft couplers. The motors are rotated by Phoenix ICE HV 120 Brushless Speed Controller as shown in Figure 6.6. The parameters of this controller are given in Table 6.3. The speed of the brushless DC motors is controlled by changing the 5V pulse width to the ICE HV controller. The speed of each Halbach rotor is separately measured using a Hall effect sensor (part AH1751-PG-B-A).



Figure 6.6: *Phoenix ICE HV 120 brushless speed controller.*

Table 6.2: *Scorpion S-4035-250KV BLDC motor parameters.*

Motor parameters	Parameters values
Rotor Outer Diameter	48.9 mm
Stator Diameter	40.0 mm (1.575 in)
Stator Thickness	35.0 mm (1.024 in)
No. of Stator Arms	12
Magnet Poles	14
Motor Wind	15 Turn Delta
Motor Wire	19-Strand 0.25mm
Motor Kv	250 RPM / Volt
No-Load Current (I_o)	@ 10 v 0.69 Amps
Motor Resistance (R_m)	0.037 Ohms
Max Continuous Current	65 Amps
Max Continuous Power	2700 Watts
Weight	465 Grams (16.40 oz)
Max Lipo Cell	12s
Motor Timing	5deg
Drive Frequency	8kHz

Table 6.3: *Phoenix ICE HV 120 parameters.*

Controller parameters	Parameter values
Dimensions	79×35.5×25.4mm
Weight	107.5g
Max. Amps.	120A
Max. Volts	50V
	12s LiPo
	36 cells NiCad/NiMh

The 6-DOF Silicon Sensing DMU02 inertial measurement unit (IMU) as shown

in Figure 6.7 is used to measure the rotation as well as acceleration in all the three axes. The data from this IMU are collected into the PC via a USB connection.



Figure 6.7: *Silicon Sensing DMU02 IMU sensor.*

The bottom view of the 4 wheeled Maglev vehicle is shown in Figure 6.8. Each EDW is rotated by the corresponding BLDC motor and the speed is measured by the Hall effect sensors. The top view of the Maglev vehicle is shown in Figure 6.9. The vehicle consists of 4 batteries, 4 controllers, laser sensors and one inertial measurement unit sensor on the top.

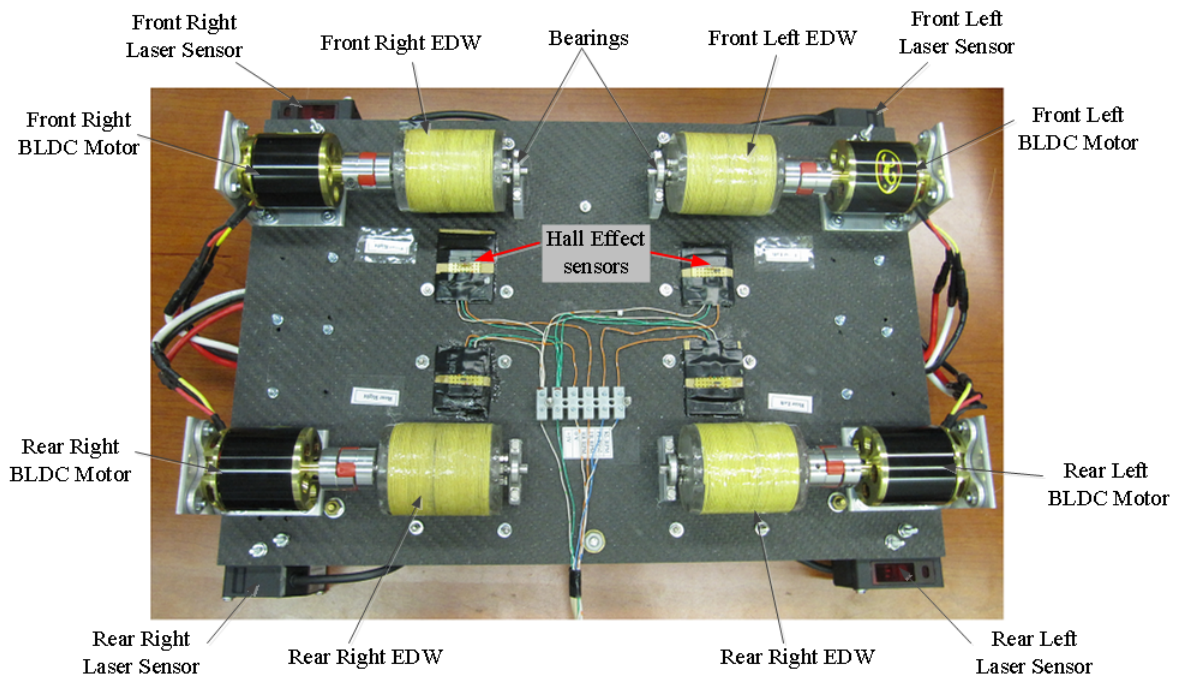


Figure 6.8: *The bottom view of an EDW Maglev vehicle.*

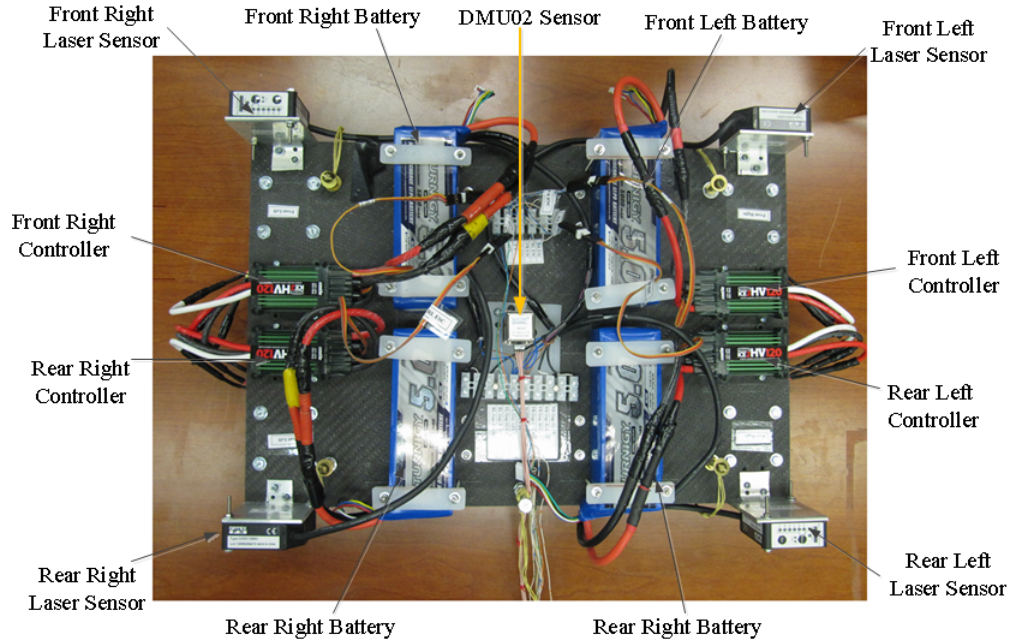


Figure 6.9: *The top view of an EDW Maglev vehicle.*

The magnetic flux density of the each of the constructed rotors are measured and compared with the analytic models developed by S. Paul [204] and D. Bobba [160]. The 3-D analytic source models are based on the Columbian integral [204] and the Bessel solution [160]. The rotors were rotated at a constant RPM and the y -component of the magnetic flux density, B_y was measured using a 5180 Gauss/Tesla meter. The comparison between the measured and the calculated magnetic flux density at a distance of 7.8mm away from the surface of the rotor are shown in the Figure 6.10 to Figure 6.13. The slight distortion in the plots are because the RPM of the rotor was not constant while measuring the field. The rotor RPM values were also measured while measuring the magnetic flux density. The RPM values were used to calculate the magnetic flux density by the analytic models. Therefore, the analytic models are also matching with the experimental even at distored points. The sinusodial magnetic field at 7.8 mm away has the peak values of $\pm 0.4T$ for all of the rotors.

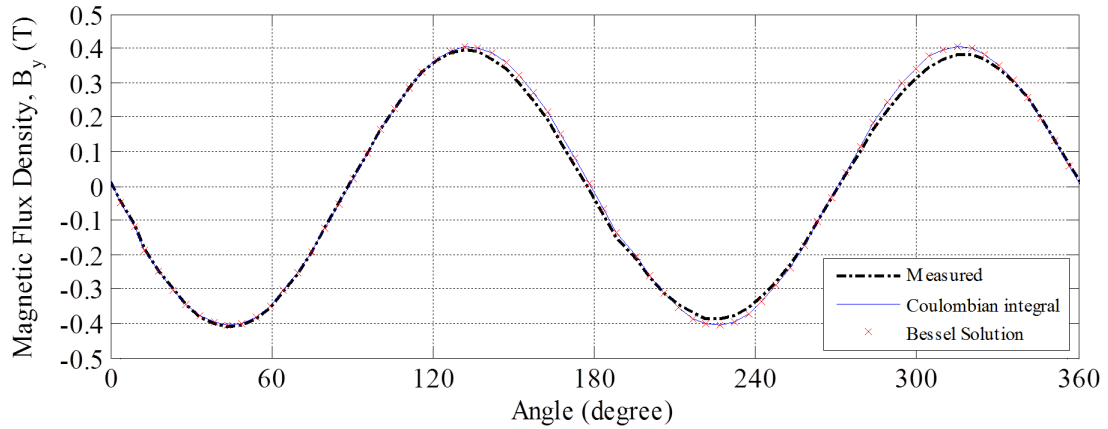


Figure 6.10: *Magnetic flux density, B_y comparison of front left rotor.*

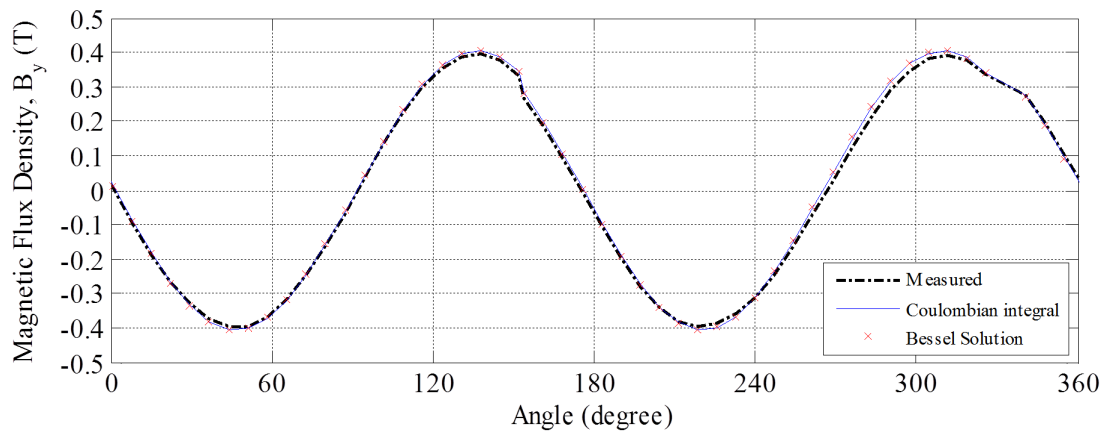


Figure 6.11: *Magnetic flux density, B_y comparison of front right rotor.*

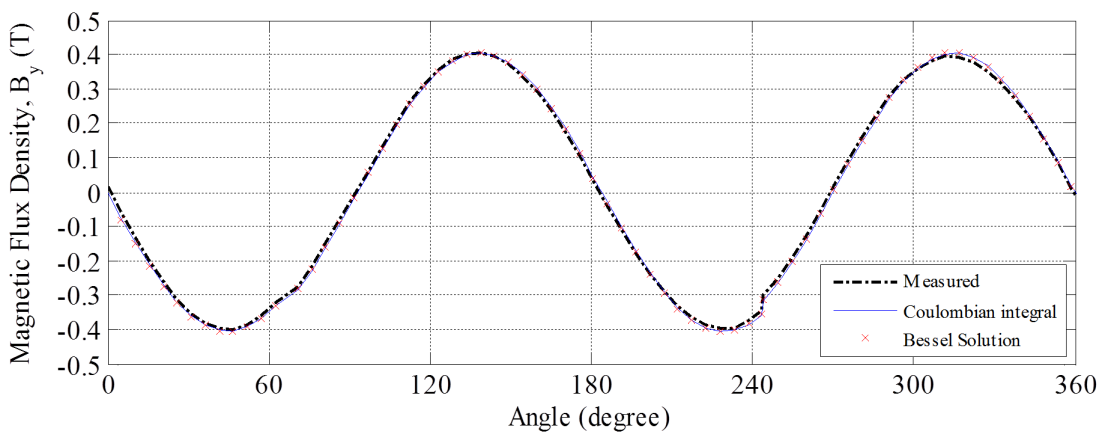


Figure 6.12: *Magnetic flux density, B_y comparison of rear left rotor.*

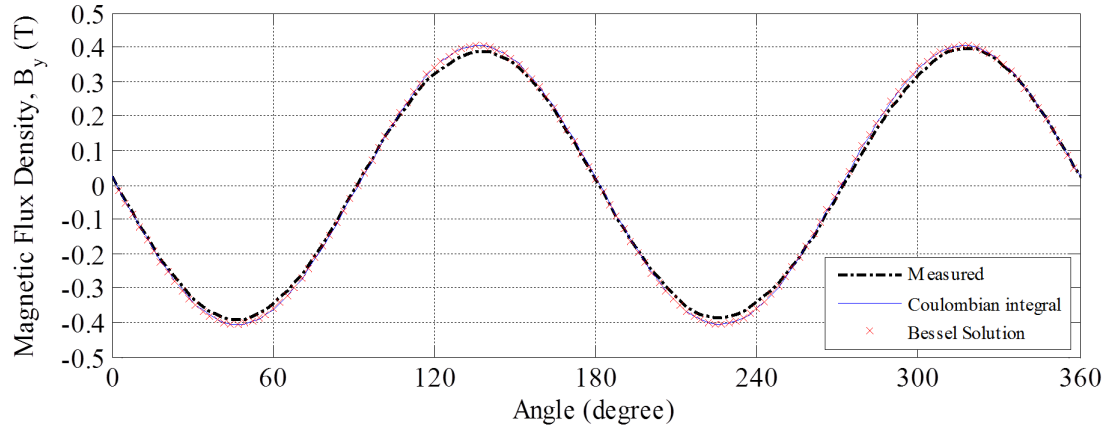


Figure 6.13: *Magnetic flux density, B_y comparison of rear right rotor.*

6.3 A 6-DOF Simulink Maglev Model

The experimental setup was replicated in Simulink SimMechanicsTM software. The mass and dimensions of each part of the experimental Maglev setup were measured. The density of the material of each part was assumed to be uniform throughout the parts. The center of gravity (CG) of each part is identified. The moment of inertia of each part along all the three axes is calculated at their respective CGs. Finally, this information of CG and moment of inertia about the respective CG is used to develop the complete Maglev setup in SimMechanicsTM. The world coordinate system (CS) is selected to be at the midpoint of the vehicle on the ground. The moment of inertia of the complete vehicle in all three axes is calculated. Similarly, the CG of the vehicle is determined. The center of gravity and moment of inertia of each part of the SimMechanicsTM Maglev vehicle is presented in the Table 6.4. The moment of inertia of the vehicle about world CG was calculated to be $[0.0836, 0.1381, 0.0683]$ kg-m².

Using the values of the dimensions, mass, CG and moment of inertia from Table 6.4, the vehicle was modeled using the SimMechanicsTM software. The convex hull picture of this vehicle using the experimental Maglev parameters is shown in Figure 6.14. The detailed simulink block diagrams are included in Appendix C. The magnetic force of the EDW is calculated using the 3-D method developed by S. Paul. The 3-D

Table 6.4: *The parameters of the experimental Maglev vehicle.*

Name of the parts	Moment of inertia (kg-m ²) [I_{xx}, I_{yy}, I_{zz}]	Centre of Gravity (m) [x, y, z]
Main Plate	[0.0332, 0.0479, 0.0147]	[0, 0.0667, 0]
FR* Battery	$[0.3, 1.4, 1.3] \times 10^{-3}$	[0.0799, 0.0923, 0.0800]
FL Battery	$[0.3, 1.4, 1.3] \times 10^{-3}$	[0.0799, 0.0923, -0.0800]
RR Battery	$[0.3, 1.4, 1.3] \times 10^{-3}$	[-0.0799, 0.0923, 0.0800]
RL Battery	$[0.3, 1.4, 1.3] \times 10^{-3}$	[0.0799, 0.0923, -0.0800]
FR Controller	$[0.0852, 0.1093, 0.0369] \times 10^{-3}$	[0.0303, 0.0814, 0.1780]
FL Controller	$[0.0852, 0.1093, 0.0369] \times 10^{-3}$	[0.0303, 0.0814, -0.1780]
RR Controller	$[0.0852, 0.1093, 0.0369] \times 10^{-3}$	[-0.0303, 0.0814, 0.1780]
RL Controller	$[0.0852, 0.1093, 0.0369] \times 10^{-3}$	[-0.0303, 0.0814, -0.1780]
FR Laser Sensor Holder	$[0.1580, 0.0628, 0.0957] \times 10^{-4}$	[0.1508, 0.1007, 0.2036]
FL Laser Sensor Holder	$[0.1580, 0.0628, 0.0957] \times 10^{-4}$	[0.1508, 0.1007, -0.2036]
RR Laser Sensor Holder	$[0.1580, 0.0628, 0.0957] \times 10^{-4}$	[-0.1508, 0.1007, 0.2036]
RR Laser Sensor Holder	$[0.1580, 0.0628, 0.0957] \times 10^{-4}$	[-0.1508, 0.1007, -0.2036]
FR Laser Sensor	$[0.4321, 0.2054, 0.2833] \times 10^{-4}$	[0.1624, 0.0998, 0.2036]
FL Laser Sensor	$[0.4321, 0.2054, 0.2833] \times 10^{-4}$	[0.1624, 0.0998, -0.2036]
RR Laser Sensor	$[0.4321, 0.2054, 0.2833] \times 10^{-4}$	[-0.1624, 0.0998, 0.2036]
RR Laser Sensor	$[0.4321, 0.2054, 0.2833] \times 10^{-4}$	[-0.1624, 0.0998, -0.2036]
FR Motor Holder	$[0.3563, 0.4121, 0.4121] \times 10^{-4}$	[0.0959, 0.0464, 0.2115]
FL Motor Holder	$[0.3563, 0.4121, 0.4121] \times 10^{-4}$	[0.0959, 0.0464, -0.2115]
RR Motor Holder	$[0.3563, 0.4121, 0.4121] \times 10^{-4}$	[-0.0959, 0.0464, 0.2115]
RR Motor Holder	$[0.3563, 0.4121, 0.4121] \times 10^{-4}$	[-0.0959, 0.0464, -0.2115]
FR BLDC Motor	$[0.1936, 0.1936, 0.1390] \times 10^{-3}$	[0.0959, 0.0303, 0.1931]
FL BLDC Motor	$[0.1936, 0.1936, 0.1390] \times 10^{-3}$	[0.0959, 0.0303, -0.1931]
RR BLDC Motor	$[0.1936, 0.1936, 0.1390] \times 10^{-3}$	[-0.0959, 0.0303, 0.1931]
RR BLDC Motor	$[0.1936, 0.1936, 0.1390] \times 10^{-3}$	[-0.0959, 0.0303, -0.1931]
FR Shaft Coupling	$[0.3422, 0.3422, 0.2344] \times 10^{-5}$	[0.0959, 0.0303, 0.1422]
FL Shaft Coupling	$[0.3422, 0.3422, 0.2344] \times 10^{-5}$	[0.0959, 0.0303, -0.1422]
RR Shaft Coupling	$[0.3422, 0.3422, 0.2344] \times 10^{-5}$	[-0.0959, 0.0303, 0.1422]
RR Shaft Coupling	$[0.3422, 0.3422, 0.2344] \times 10^{-5}$	[-0.0959, 0.0303, -0.1422]
FR EDW Rotor	$[0.4609, 0.4609, 0.2839] \times 10^{-3}$	[0.0959, 0.0303, 0.0873]
FL EDW Rotor	$[0.4609, 0.4609, 0.2839] \times 10^{-3}$	[0.0959, 0.0303, -0.0873]
RR EDW Rotor	$[0.4609, 0.4609, 0.2839] \times 10^{-3}$	[-0.0959, 0.0303, 0.0873]
RR EDW Rotor	$[0.4609, 0.4609, 0.2839] \times 10^{-3}$	[-0.0959, 0.0303, -0.0873]
Total Maglev Vehicle	[0.0462, 0.1381, 0.0309]	[0, 0.0575, 0]
Weight of vehicle	11.315 kg	

*FR = Front Right, FL = Front Left, RR = Rear Right and RL = Rear Left.

forces of the EDWs are stored as a lookup table subsystem as shown in Figure C.9. The input to this subsystem are the z -axis offset, air-gap, v_x , v_y and ω_m and the outputs are the forces F_x , F_y and F_z . The Maglev vehicle (convex hull) developed in Simulink is illustrated in Figure 6.14.

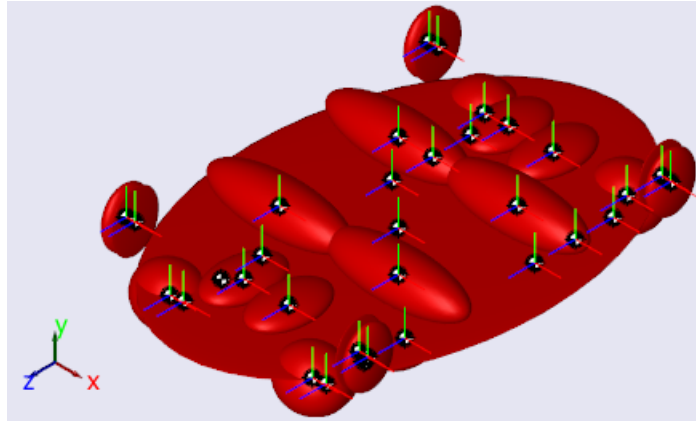


Figure 6.14: *The SimMechanicsTM Maglev vehicle (Convex hull).*

The co-ordinate system used for this simulation is shown in Figure 6.15. The direction of the 3-D forces as well as the directional convention of roll, yaw and pitch in three axes: x , y and z respectively are shown in this figure. The lift and thrust forces produced by each experimental EDWs at an air-gap of 5mm, z -offset of 0mm and $v_y = 0\text{ms}^{-1}$ are shown in Figure 6.16 and Figure 6.17. The total weight of the vehicle is 11.315kg (110.89N). In order to lift the vehicle the force produced by four EDWs has to be equal to the total weight of the vehicle. Therefore, the lift force by each EDWs should be 27.72N. If the vehicle is to be lifted at an air-gap, $g = 5\text{mm}$, the velocity $v_x = 0\text{ms}^{-1}$, the RPM of each EDWs should be about 2K (refer Figure 6.16). Significant amount of thrust is produced at this operating conditions as shown in Figure 6.17. The contour plot of the 3-D lift force as a function of RPM and translational velocity, v_x at an air-gap of 4mm and 5mm are shown in Figure 6.18 and Figure 6.19.

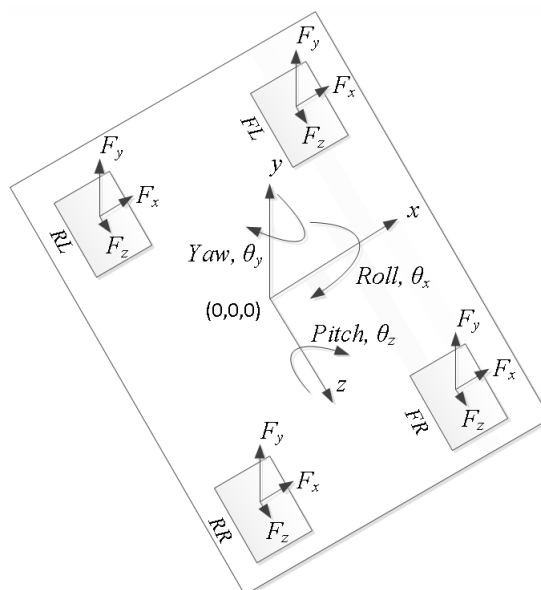


Figure 6.15: *The Maglev co-ordinate system and force directions.*

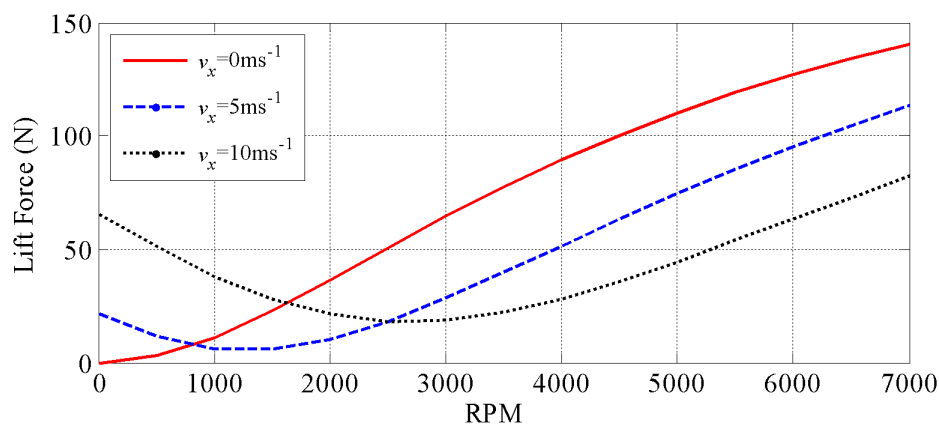


Figure 6.16: *The 3-D lift force for one experimental EDW.*

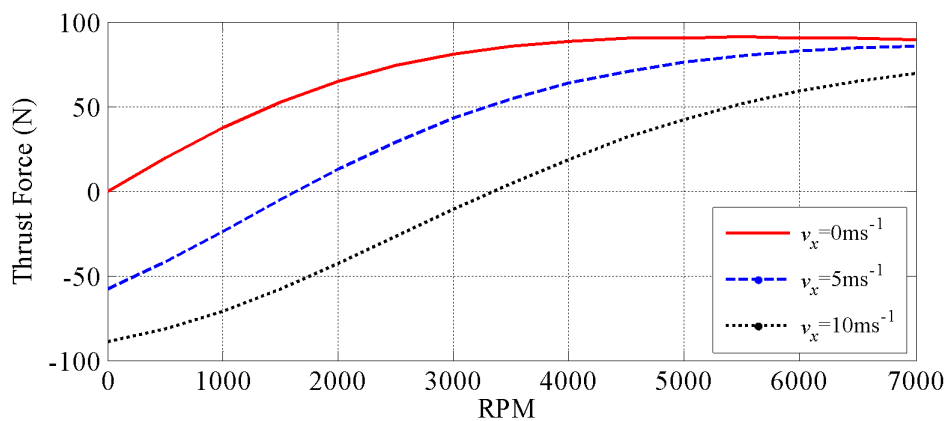


Figure 6.17: *The 3-D thrust force for one experimental EDW.*

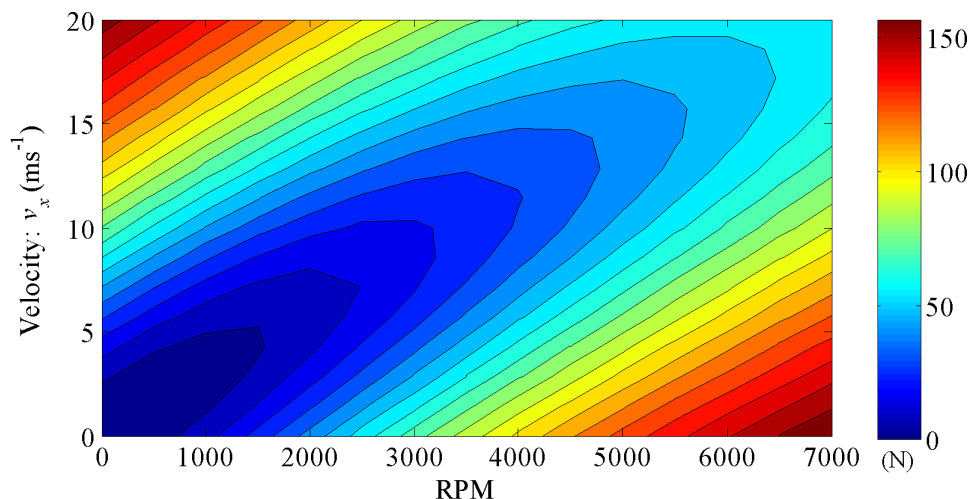


Figure 6.18: *The 3-D lift force contour plot for one experimental EDW at $g = 4\text{mm}$.*

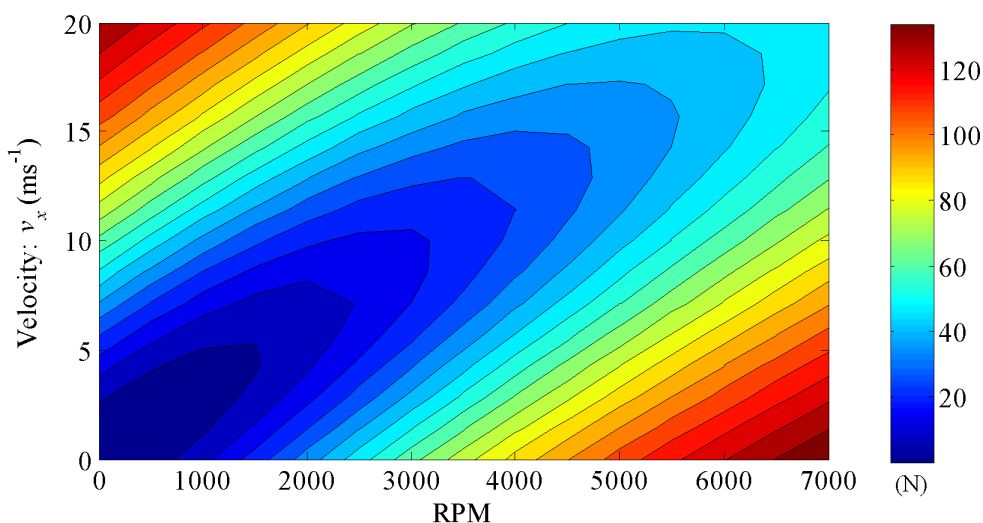


Figure 6.19: *The 3-D lift force contour plot for one experimental EDW at $g = 5\text{mm}$.*

The 3-D lift, thrust and lateral forces for one experimental EDW as a function of z -offset and translational velocity are shown in Figure 6.20 - Figure 6.22. Similarly, the 3-D lift, thrust and lateral forces as a function of z -offset and RPM are shown in Figure 6.23 - Figure 6.25. The lateral force increases with the increase in z -offset and decreases with further increase in z -offset values. This behavior of the lateral force causes the instability in lateral direction. This type of instability is observed during the 6-DOF Maglev simulation and is included in section 6.4.

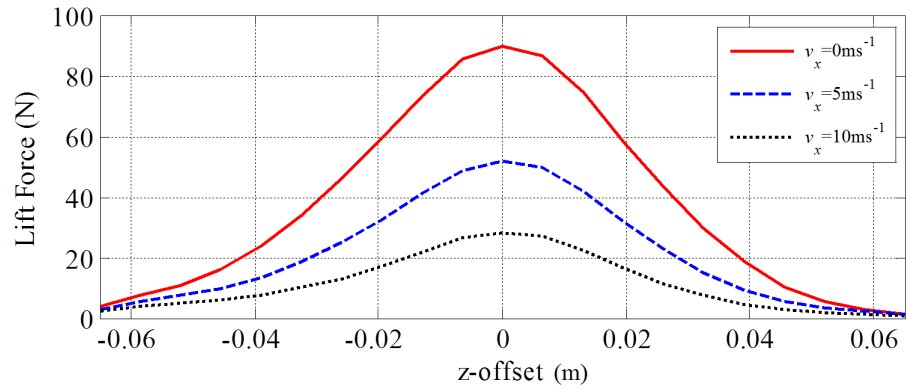


Figure 6.20: *The 3-D lift force as a function of z-offset at 4000RPM and $g = 5\text{mm}$.*

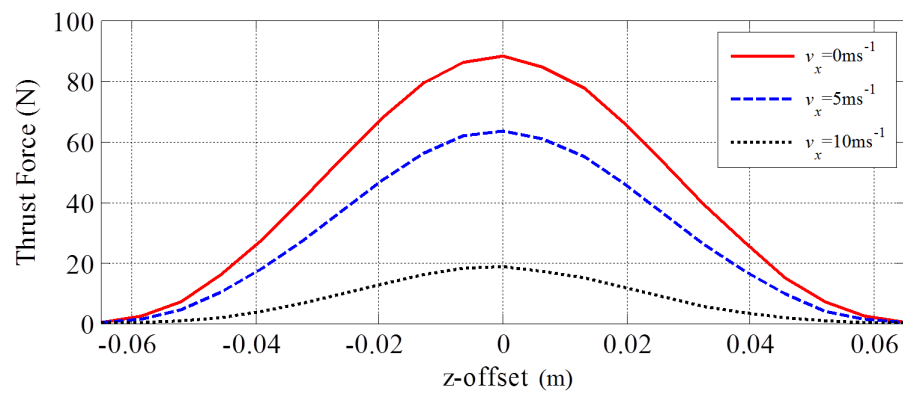


Figure 6.21: *The 3-D thrust force as a function of z-offset at 4000RPM and $g = 5\text{mm}$.*

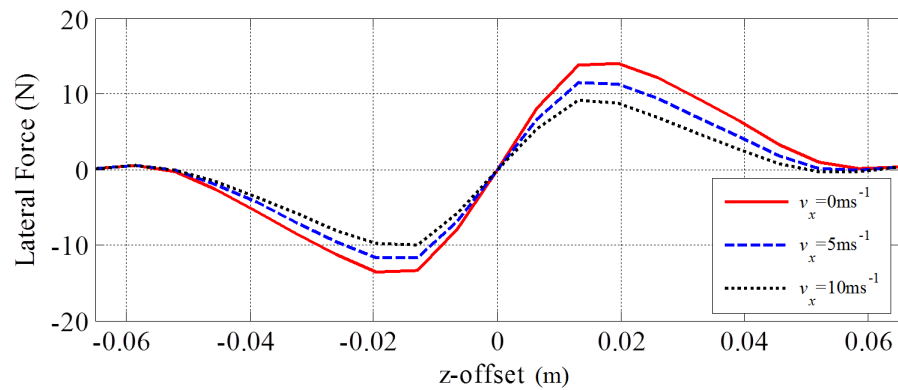


Figure 6.22: *The 3-D lateral force as a function of z-offset at 4000RPM and $g = 5\text{mm}$.*

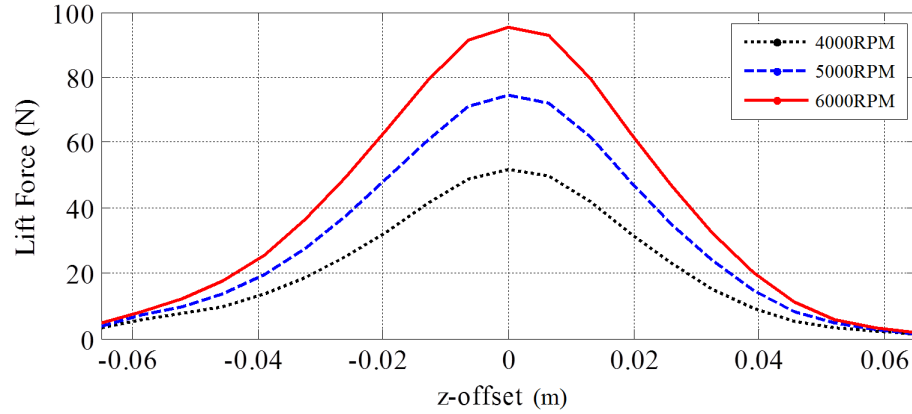


Figure 6.23: *The 3-D lift force as a function of z -offset at $v_x = 5\text{ms}^{-1}$ and $g = 5\text{mm}$.*

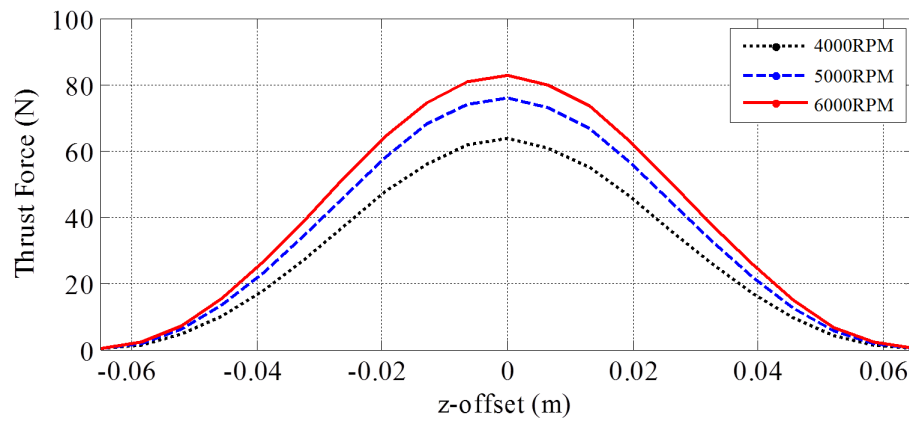


Figure 6.24: *The 3-D thrust force as a function of z -offset at $v_x = 5\text{ms}^{-1}$ and $g = 5\text{mm}$.*

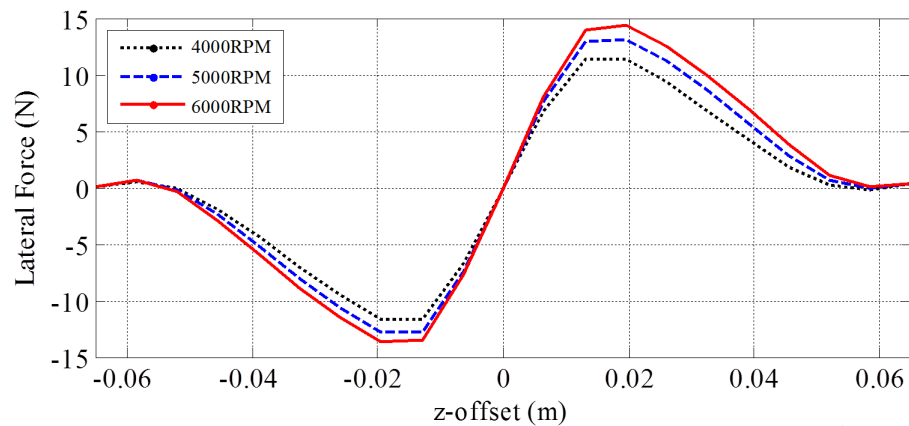


Figure 6.25: *The 3-D lateral force as a function of z -offset at $v_x = 5\text{ms}^{-1}$ and $g = 5\text{mm}$.*

6.4 6-DOF Simulation of the EDW Maglev

The experimental Maglev vehicle has been simulated with 3-D thrust, lift and lateral force. The side view and the front view of the Maglev are shown in Figure

6.26 and Figure 6.27 respectively. The simulation has been performed with the initial conditions: $g_o = 5\text{mm}$, $v_x = 0\text{ms}^{-1}$, $\omega_m = 4000\text{RPM}$. The moment in pitch angle is created about the CG of the Maglev vehicle due to the thrust forces. The vehicle starts to move oscillating in pitch and heave with different air-gap on the front wheels and rear wheels. The moment about the CG created by the thrust forces as shown in Figure 6.26 is responsible for the huge oscillation in the pitch angle. The simulation results are shown in Figure 6.28 - Figure 6.38.

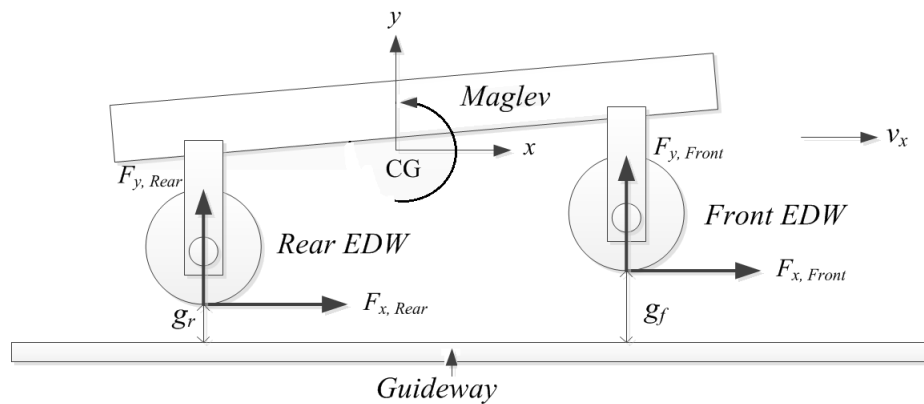


Figure 6.26: *Maglev sketch showing the pitch.*

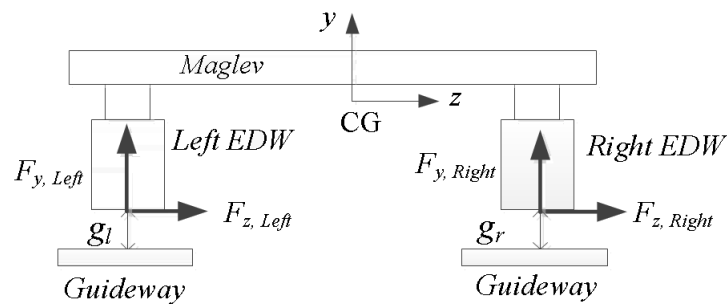


Figure 6.27: *Maglev sketch front view with $z\text{-offset} = 0\text{mm}$.*

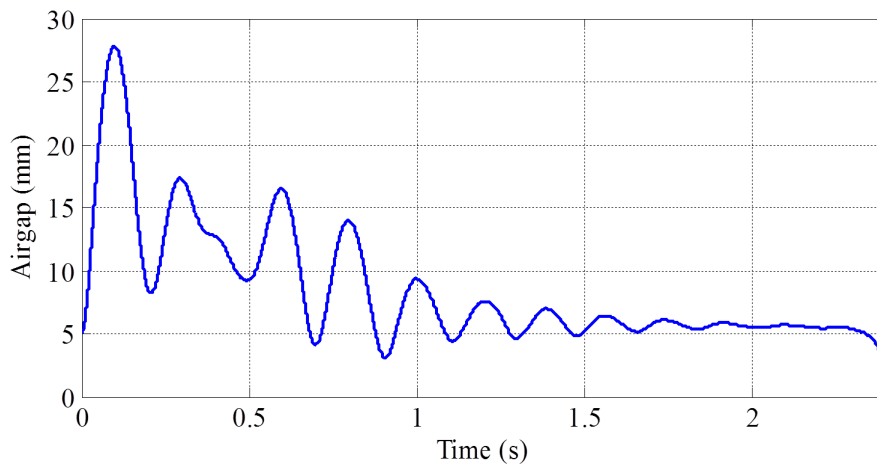


Figure 6.28: *The vehicle air-gap for zero z -offset simulation.*

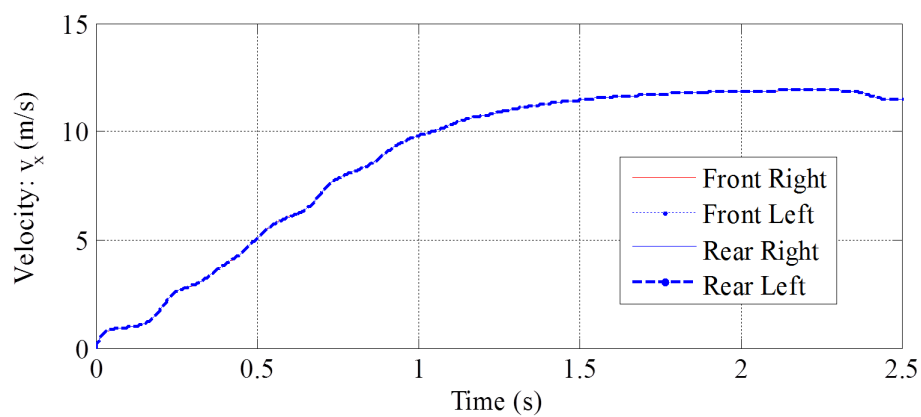


Figure 6.29: *The translational velocity of the front and the rear rotors for zero z -offset simulation.*

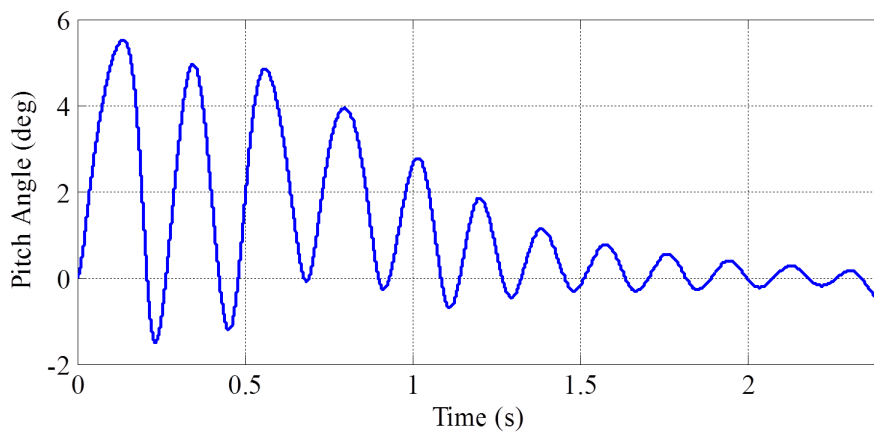


Figure 6.30: *The pitch angle of the Maglev for zero z -offset simulation.*

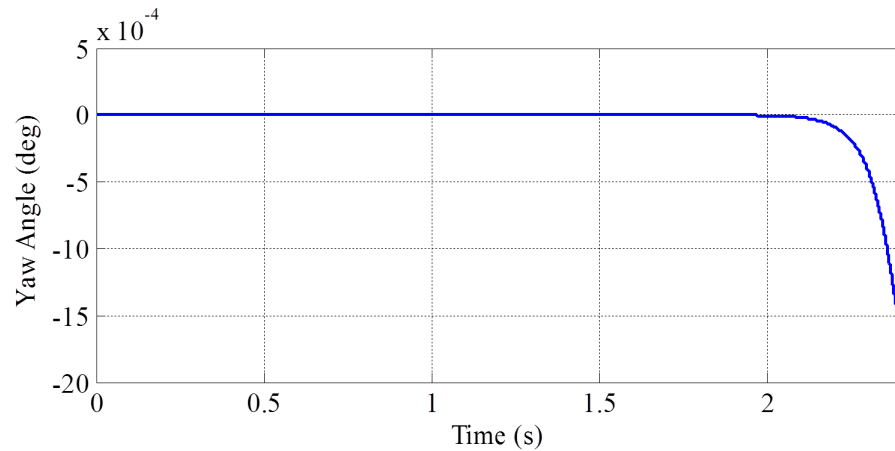


Figure 6.31: *The yaw angle of the Maglev for zero z-offset simulation.*

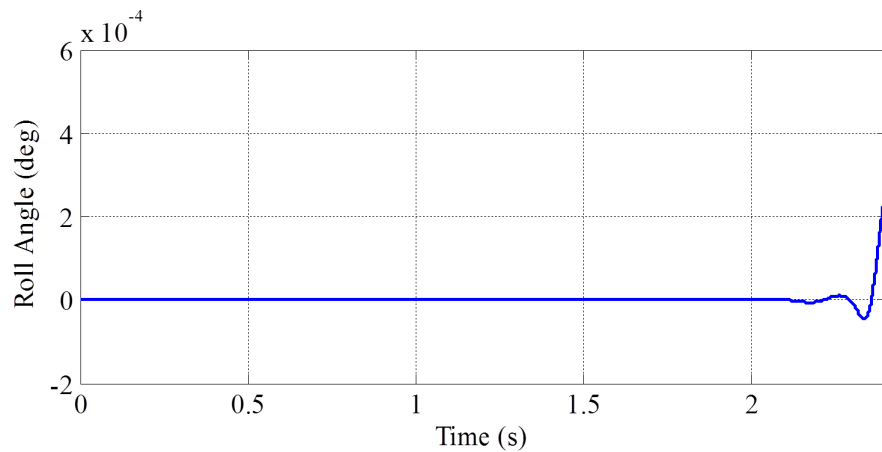


Figure 6.32: *The roll angle of the Maglev for zero z-offset simulation.*

The lift, thrust and lateral forces produced by 4 EDWs are shown in the Figure 6.33 - Figure 6.35. Similarly, the air-gap, the heave velocity and lateral motion of the 4 EDWs from the guideway surface is illustrated in Figure 6.36 - Figure 6.38. The Maglev vehicle is unstable in lateral direction after $t = 2.2$ s. This lateral motion of the vehicle caused the significant decrease in the lift force. Therefore, the vehicle touched the guideway at about $t = 2.4$ s (refer Figure 6.28).

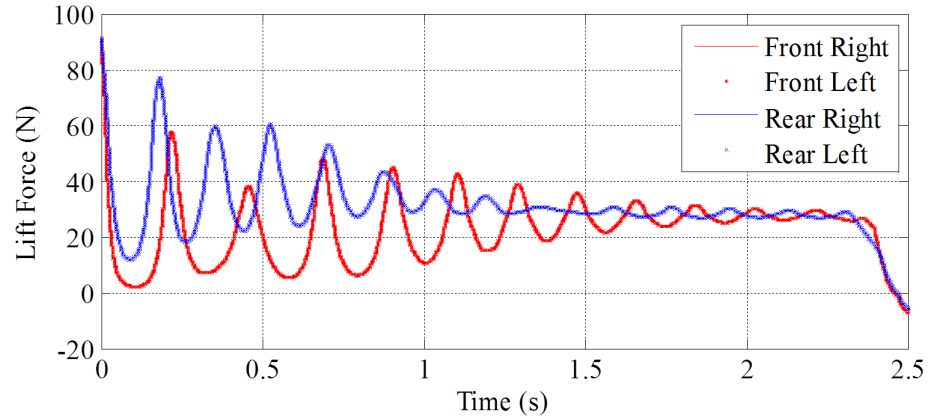


Figure 6.33: *The lift force of the front and rear rotors for zero z -offset simulation.*

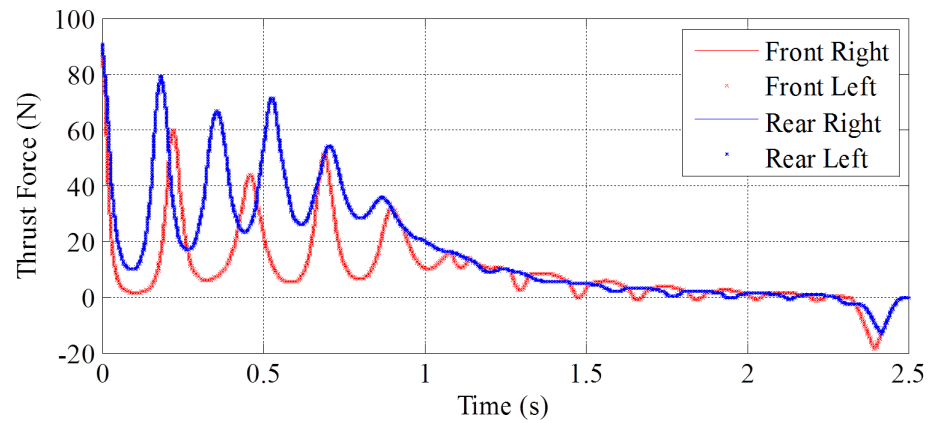


Figure 6.34: *The thrust force of the front and rear rotors for zero z -offset simulation.*

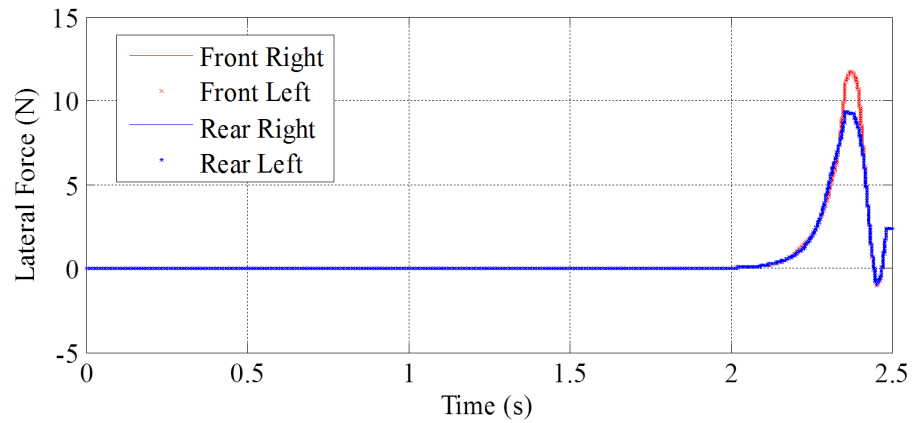


Figure 6.35: *The lateral force of the front and rear rotors for zero z -offset simulation.*

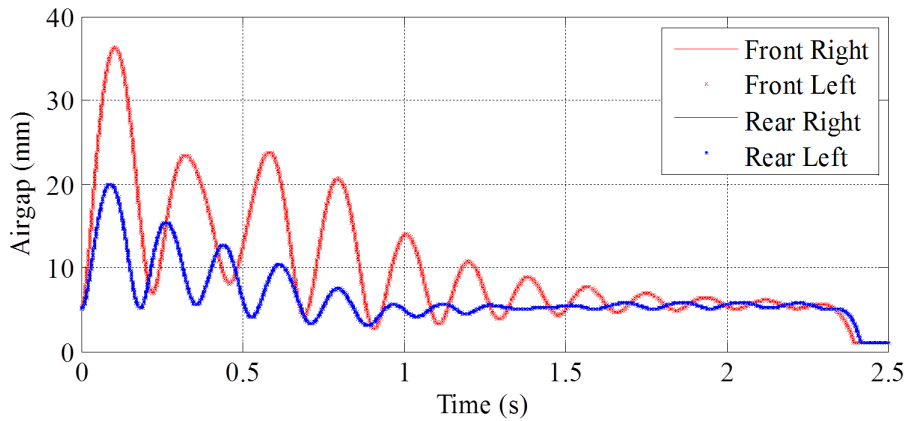


Figure 6.36: *The airgap plot of the front and rear rotors for zero z -offset simulation.*

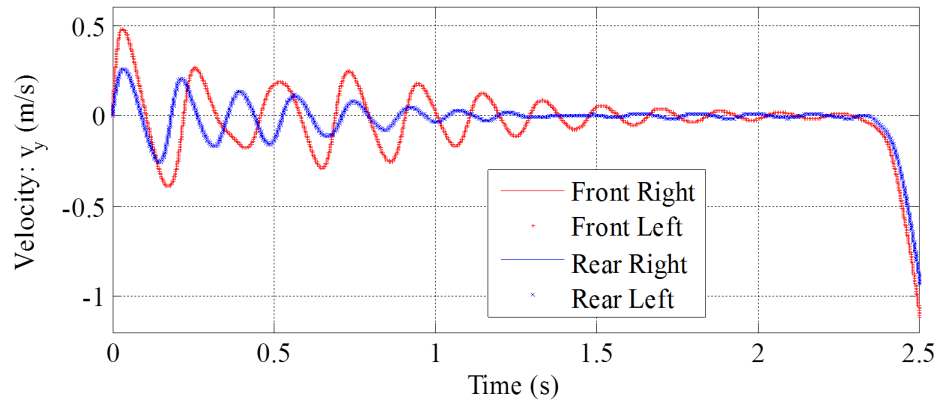


Figure 6.37: *The v_y plot of the front and rear rotors for zero z -offset simulation.*

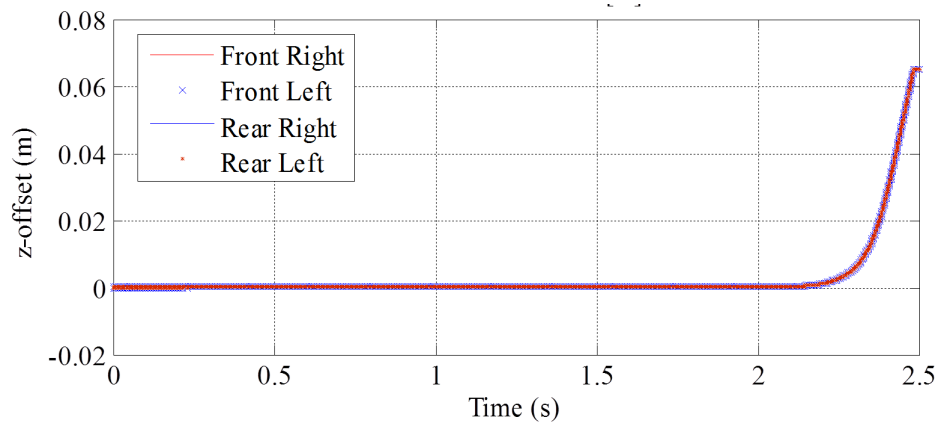


Figure 6.38: *The z -offset of the front and rear rotors for zero z -offset simulation.*

In order to check the influence of the lateral force on the system dynamics, the vehicle as shown in Figure 6.26 was simulated without including the lateral force ($F_z = 0$) in Simulink/SimMechanicsTM. Unlike the simulation result in Figure 6.38,

the vehicle was found stable in lateral direction. The pitch angle oscillation is still presented. However, this oscillation in pitch is not causing the lateral instability. From this simulation, it was found that the lateral instability was purely due to the unstable lateral forces.

The lift, thrust and lateral forces are highly coupled for the EDW Maglev setup. In the experimental setup the forward motion of the Maglev vehicle is kept fixed allowing the guideway to move. The vehicle is fixed in x -direction by holding the rear part of the vehicle with a tether. The pitch angle oscillation can be minimized for the experimental setup by placing the tether at an appropriate position. It was found that the best position of the tether to hold the experimental Maglev vehicle is along the line of F_x force as shown in Figure 6.39. The thrust force is being balanced by the opposite force on the tether. Therefore, there will be a no moment on the pitch.

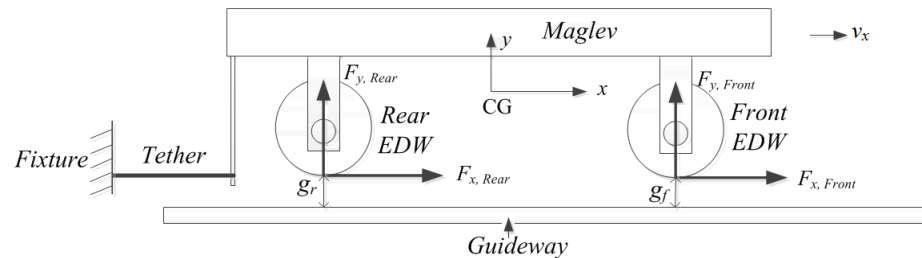


Figure 6.39: *The Maglev sketch with the tether along the thrust axis.*

The 4-wheeled EDW Maglev setup was hung above the guideway using four flexible string of Kevlar thread at the four corners as shown in Figure 6.40. The vehicle was positioned such that all the EDWs were at center of guideway. The air-gap between each EDWs was adjusted manually. The vehicle was fixed in the x -direction by the Kevlar thread as shown in Figure 6.40. However, the guideway was freely rotating. The air-gap sensors were used to measure the distance of each corner from the guideway. The cooling fans were used to cool the BLDC motor controllers. As soon as the EDWs started rotating, the lift, lateral and thrust force was produced. Since, the vehicle was fixed in the x -direction, the thrust force tried to rotate the

guideway in opposite direction.

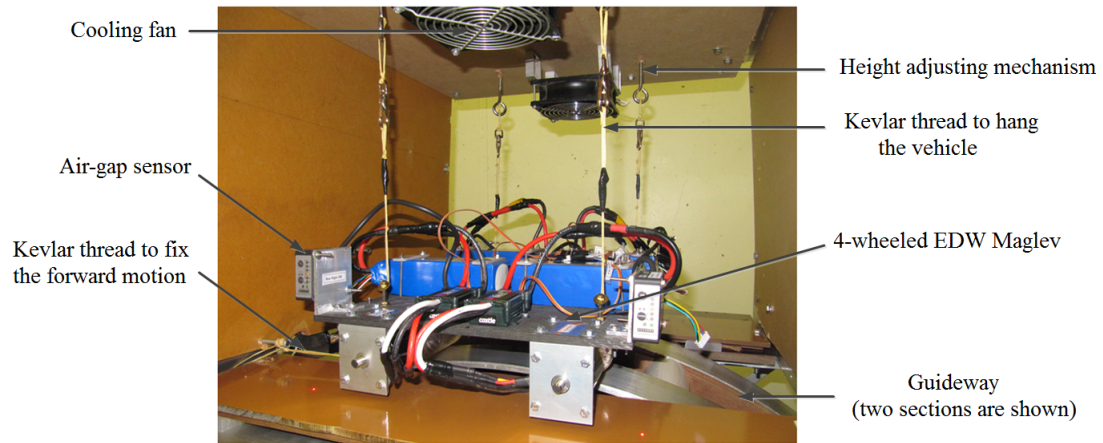


Figure 6.40: A 4-wheeled EDW Maglev hanging setup with adjustable height mechanism.

Several tests were performed to operate the experimental Maglev. The first test was with the single tether that fixed the forward motion of the vehicle. The tether was fixed at the mid-point of the rear part of the vehicle. The x -axis of tether was aligned with the direction of the thrust force (refer Figure 6.39). The vehicle was pushed to the sides depending on the position of z -offset. In addition, it was not possible to lift the vehicle at center. The vehicle was moving completely off the guideway. Secondly, the vehicle forward motion was fixed by two tether on either side of the rear part of the vehicle. During this test, the vehicle was again pushed completely off the guideway. It was not possible to lift the vehicle at the center. The centering force was not enough to bring the vehicle back to the guideway.

The following reasons could be the source of instability that have been encountered during the operation of the setup as shown in Figure 6.40.

- The guideway is not perfectly circular. The guideway section on the left side is more irregular compared with the one on the right side. The guideway irregularities could be the reason for the instability of the vehicle.
- Since the guideway is a curve, it is very difficult to adjust the position of each rotors at the same air-gap. The slight mismatch between the air-gap will cause

the mismatch in force production, therefore, cause the instability problem.

- The speed of each wheels were not perfectly matched. This mismatch results in the production of different forces. Which was the another cause of the instability.
- The vehicle was not optimally designed interms of stability. The position of the motors are outside to the EDW rotors. This selection was done because of the space limitation of the guideway. However, the vehicle stability could be improved by placing the EDW outside and motor inside.

6.5 An EDW Maglev Experiment with z -offset

The lateral stability of the EDW Maglev can be achieved by placing the EDWs above the guideway with z -offset. The experimental Maglev vehicle has been modified to achieve the lateral stability. The bottom view of this experimental Maglev vehicle is shown in Figure 6.41. The lateral configuration of the EDWs and the guideway is shown in Figure 6.42. The center of the EDW was off from the center of the guideway by 31.5mm (z -offset = 31.5mm). Therefore, only 33.5mm axial length of the rotor was overlapping with the guideway. The lift and thrust forces produced by the rotor was overlapping with the guideway. The lift and thrust forces produced by the experimental EDWs at z -offset = 31.5mm are shown in Figure 6.43 and Figure 6.44 respectively. The lateral force as a function of z -offset for 4000RPM and $g = 5$ mm is shown in Figure 6.45. The operation region is also highlighted in this figure. With the z -offset of 31.5mm, the vehicle has been stablized in lateral direction. However, the lift and thrust forces were decreased. Since, the centering force is increasing with the increase in z -offset and the value of centering force is higher compared with the off-centering force on the opposite side, the vehicle is always stable in this configuration.

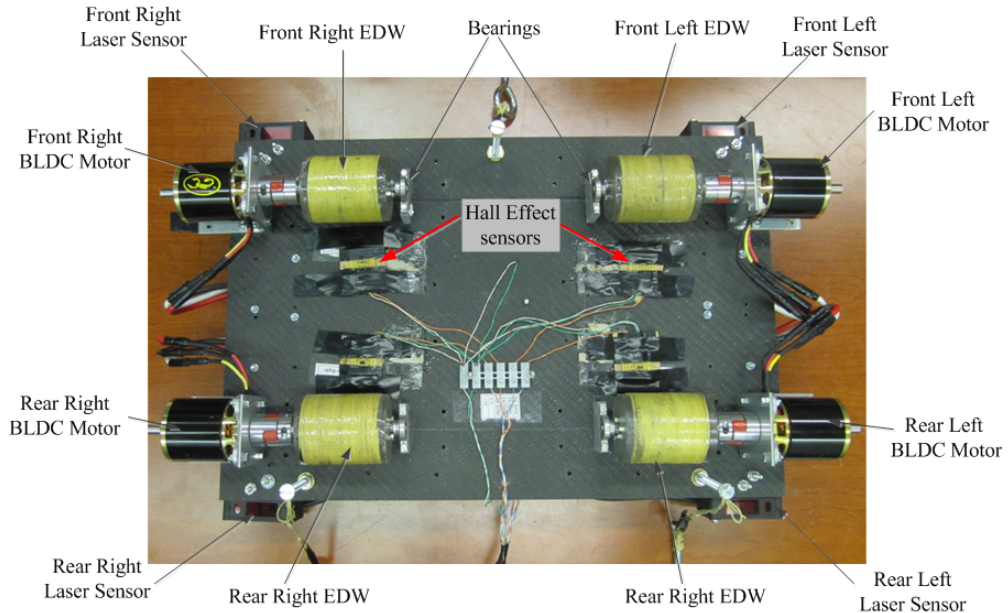


Figure 6.41: The bottom view of the experimental Maglev vehicle with lateral stability.

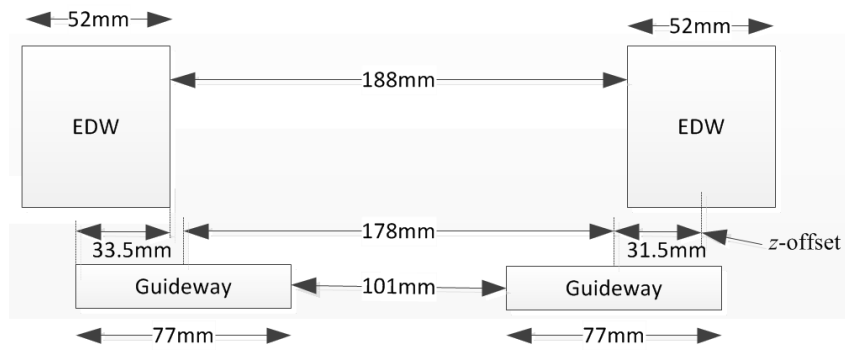


Figure 6.42: The EDW and guideway lateral configuration for lateral stability.

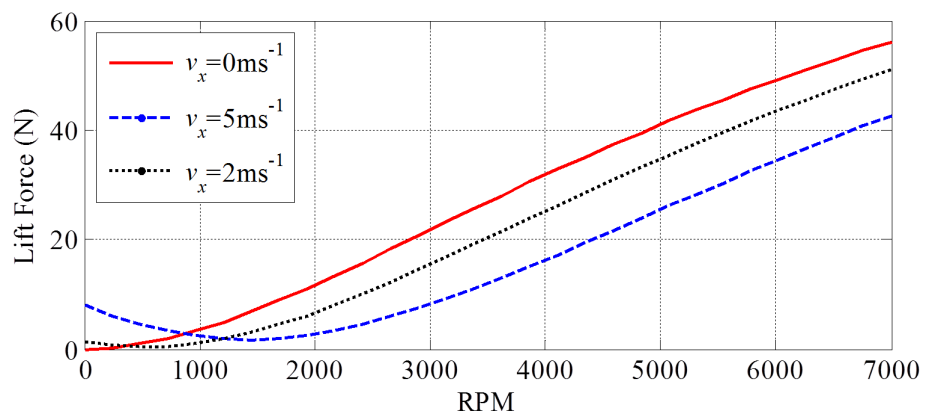


Figure 6.43: The lift force of an experimental EDWs at $g = 5\text{mm}$ and $z\text{-offset} = 31.5\text{mm}$.

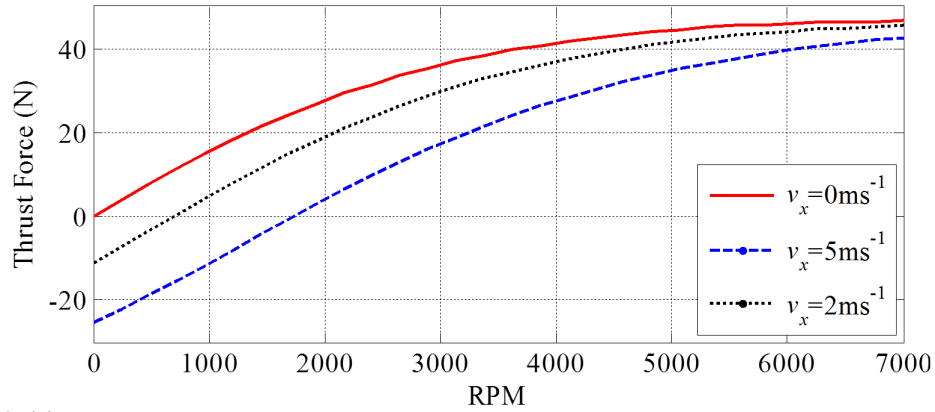


Figure 6.44: The thrust force of an experimental EDWs at $g = 5\text{mm}$ and $z\text{-offset} = 31.5\text{mm}$.

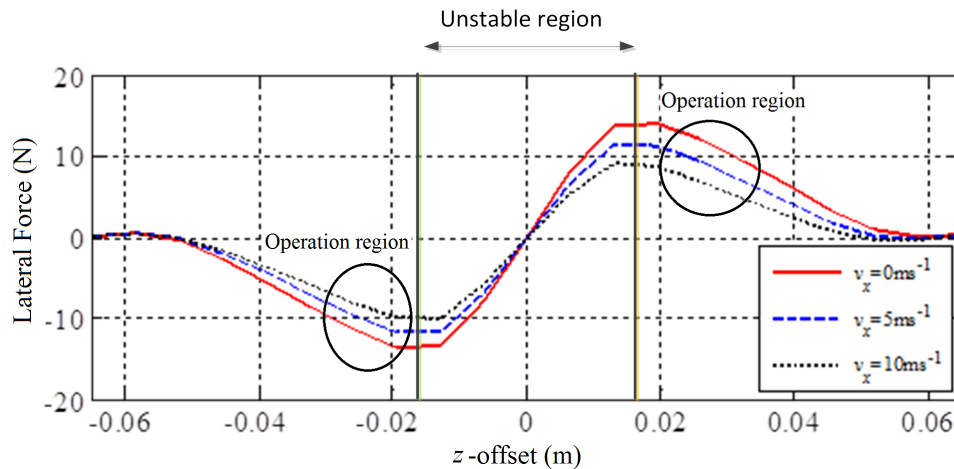


Figure 6.45: The lateral force as a function of $z\text{-offset}$ at 4000RPM and $g = 5\text{mm}$.

The vehicle was initially hung at $g = 4\text{mm}$. The angular speed of the EDWs was increased upto 5000RPM and the vehicle was lifted. The lifted air-gap of each of the EDWs were measured. The air-gap measurements are shown in Figure 6.46 - Figure 6.49. The rear right side of the vehicle was lifted by only about 1mm . Whereas other sides were lifted upto 6mm . The uneven lift could be due to the vehicle not being properly aligned above the guideway and due to the misalignment on the position of the kevlar thread holding the vehicle. These results could be improved by placing the vehicle properly above the guideway. This setup could be used to study the dynamics in 5-DOF.

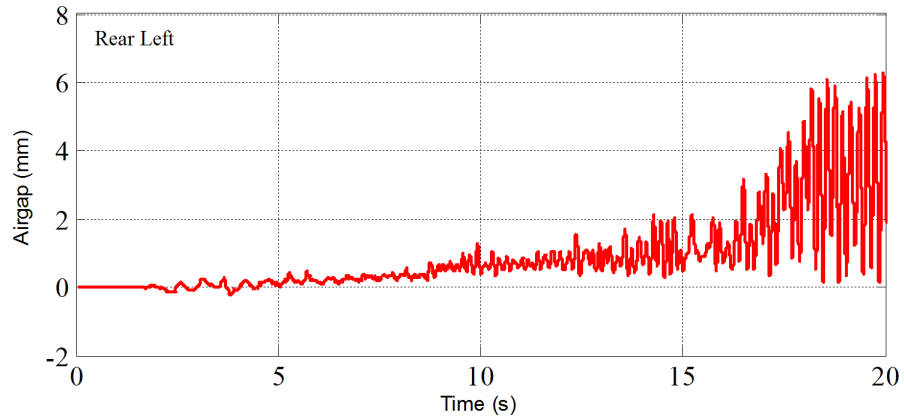


Figure 6.46: *The rear left EDW air-gap measurement from initial $g = 4\text{mm}$.*

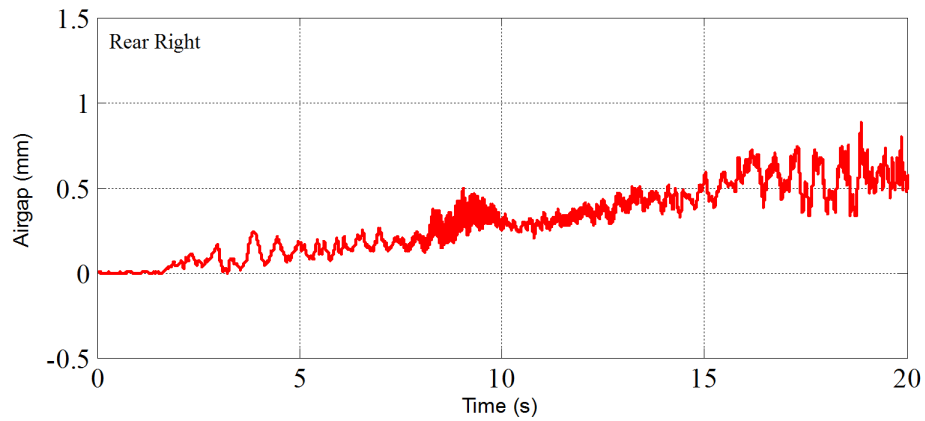


Figure 6.47: *The rear right EDW air-gap measurement from initial $g = 4\text{mm}$.*

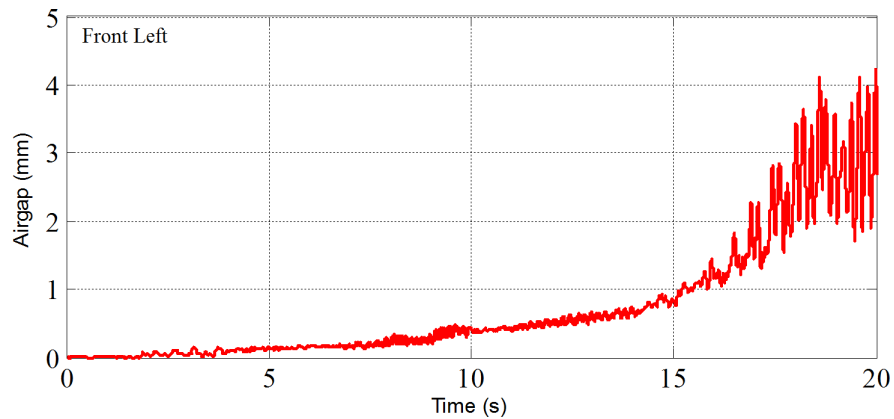


Figure 6.48: *The front left EDW air-gap measurement from initial $g = 4\text{mm}$.*

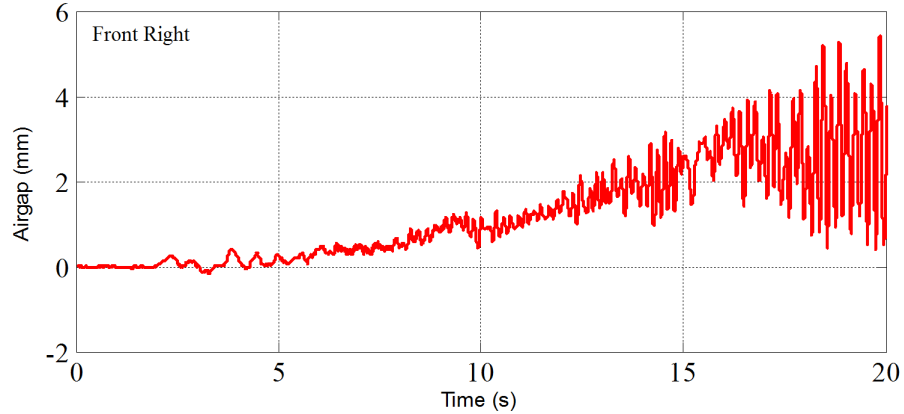


Figure 6.49: *The front right EDW air-gap measurement from initial $g = 4\text{mm}$.*

6.6 Summary

The multi-DOF EDW Maglev setup has been constructed. The SimMechanicsTM model of this experimental setup has been developed in Matlab/Simulink. The dynamic simulation of the vehicle has been performed for 6-DOF. The vehicle was found unstable in all degree of freedom when placed at zero z -offset and simulated for 6-DOF. The experimental setup was also found unstable. The vehicle was moved completely off the guideway during the experimental tests. Several sources of instability of this Maglev setup were identified. The setup was modified to achieve the lateral stability by placing the EDW above the guideway with z -offset. The vehicle was successfully lifted with lateral stability. This setup could be used for the study of the dynamics in multi-degree of freedom.

CHAPTER 7: CONCLUSION AND FUTURE WORKS

7.1 Introduction

The focus of this research was to develop an analytic model of an eddy-current device such as an electrodynamic wheel for Maglev application and investigate its dynamic behavior. The main conclusion of the research is summarized in section 7.2. The key contributions of this thesis is discussed in section 7.3. The suggestions and the recommendations for the future direction of this research is given in section 7.4.

7.2 Conclusion

The electromagnetic model of an eddy-current device such as an EDW Halbach rotor above a conductive guideway has been developed analytically and the dynamic behavior of EDW Halbach rotor has been validated experimentally.

The 2D analytic steady-state model of an eddy-current device which is simultaneously rotating as well as translationally and normally moving above a linear conductive passive guideway was developed. The force and power loss equations were derived for the case when an arbitrary magnetic source is rotated and moved in two directions above a conductive guideway using a spatial Fourier transform technique. The problem was formulated using both the magnetic vector potential, \mathbf{A} , and scalar potential, ϕ . Using this novel \mathbf{A} - ϕ approach the rotor field needs to be incorporated only in the boundary conditions of the guideway and only the magnitude of the source field along the guideway surface is required in order to compute the forces and power loss. This analytic based eddy-current model was validated by comparing it with a 2-D FEA model using a single Halbach rotor as well as multiple Halbach rotors in series. The computational time was significantly reduced compared to the FEA

model. This model could be used for optimization of the parameters of the EDW for future high-speed ground transportation.

2-D analytic transient eddy-current force and power loss equations were derived for the case when an arbitrary magnetic source is moving and oscillating above a conductive guideway. These general equations for force and power loss are derived using a spatial Fourier transform and temporal Laplace transform approach. The derived equations are capable of accounting for a step change in the input parameters or continuous changes in input conditions. The equations are validated for both step change as well as continuous changes in input conditions using the 2-D transient finite-element model.

The analytic equations for the self as well as mutual damping and stiffness coefficients of an EDW Maglev are derived using 2-D analytic steady-state eddy-current force equations. The dynamics of an EDW Maglev was investigated by using both steady-state and transient eddy-current models. The steady-state eddy-current model when including a heave velocity was determined to accurately predict the dynamic behavior of the 2-degree of freedom EDW Maglev vehicle built in SimMechanics™.

The 1-DOF pendulum setup of an EDW Maglev was built using a single Halbach rotor of 50mm diameter and 50mm axial length. This pendulum setup was hung next to a rotating aluminum guideway in order to investigate the dynamics of the EDW Maglev. The dynamic model of an EDW Maglev was validated using this pendulum setup when calculating the forces using the 2-D and 3-D electromagnetic EDW force models. Several dynamic tests were performed to validate the dynamics of the developed model.

The multi-DOF Maglev vehicle prototype setup was constructed using four 2 pole-pair EDWs placed over a split aluminum guideway. The setup can be used to investigate the dynamic behavior of EDW Maglev in the future.

7.3 Research Contributions

The main technical achievements and contributions of this research are:

- A 2-D analytic based steady-state eddy-current model has been developed. The general force and power equations are derived for a arbitrary magnetic source rotating and/or moving above a conductive guideway. These equations have been validated using a steady-state FEA model with a Halbach rotor as a source.
- A 2-D analytic based transient eddy-current model has been developed to calculate the force and power loss for arbitrary magnetic source rotating and moving above a linear conductive guideway. This model has been validated using a Halbach rotor as a source using the transient FEA model.
- The analytic equations for the magnetic stiffness and damping of an EDW Maglev have been derived using the steady-state force equations and investigated for a wide range of velocities, air-gaps and RPMs.
- The dynamic behavior of an EDW Maglev has been investigated using a 2-DOF vehicle model with the 2-D steady-state as well as transient force equations. The heave velocity has been included into the steady-state force equations. It was determined that the transient electromechanical simulation of EDW Maglev vehicle closely matched the steady-state.
- A 1-DOF pendulum experimental setup has been constructed in order to experimentally investigate the dynamic behavior of the EDW Maglev and validate the analytic model.
- A multi-DOF EDW Maglev experimental setup has been constructed in order to experimentally investigate the dynamic behavior of the EDW Maglev vehicle. This setup could be used for future research in the area of dynamics and control of multi-DOF EDW Maglev.

7.4 Future Research Works

During the course of this dissertation, it was found that this research could be extended further in several different aspects.

- The 2-D model developed in this research could be used to quickly optimize the parameters of the EDWs for the initial design phase.
- The fast analytic 3-D model of an EDW could be developed so that the force could be calculated in real time which is essential to develop an appropriate control system. The 3-D force model could be extended to include the roll, yaw and pitch.
- The multi-DOF EDW Maglev setup could be further improved to study the dynamics of this Maglev system for wide range of operating conditions such as step changes in the RPM of an EDWs, guideway irregularities, and for other disturbances such as sudden change in the weight at different locations, wind and gusts conditions etc.
- The control system could be developed based on the steady-state force equations. It is highly likely that the traditional control system will not work for this complicated problem because the only control parameter in this system is an angular velocity of the EDWs. Therefore, multi-input multi-output (MIMO) adaptive control algorithms could be developed for the successful control of this Maglev system.
- Similar study could be done on a flat guideway structure using multiple EDWs in series and develop an appropriate control system for it.

BIBLIOGRAPHY

- [1] “High-tech for flying on the ground,” tech. rep., Transrapid International, 2003.
- [2] L. Hyung-Woo, K. Ki-Chan, and L. Ju, “Review of maglev train technologies,” *IEEE Transactions on Magnetics*, vol. 42, no. 7, pp. 1917–1925, 2006.
- [3] S. Yamamura, *Theory of Linear Induction Motors*. University of Tokyo Press, 1979.
- [4] K. Glatzel, G. Khurdok, and D. Rogg, “The development of the magnetically suspended transportation system in the federal republic of germany,” *IEEE Transactions on Vehicular Technology*, vol. 29, no. 1, pp. 3–17, 1980.
- [5] D. Atherton, “Passive secondary magnetic damping for superconducting maglev vehicles,” *Journal of Applied Physics*, vol. 47, no. 10, p. 4643, 1976.
- [6] D. L. Atherton and A. R. Eastham, “Superconducting magnetic levitation and linear synchronous motor propulsion for high-speed guided ground transportation, phase ii contract report,” tech. rep., Canadian Maglev Group, mar 1975.
- [7] I. Boldea, “Magnibus - the romanian linear inductor (synchronous) motor (passive guideway) maglev,” vol. 1, pp. 149–154, IMech, 1984.
- [8] I. Boldea, A. Trica, G. Papusoiu, and S. Nasar, “Field tests on a maglev with passive guideway linear inductor motor transportation system,” *IEEE Transactions on Vehicular Technology*, vol. 37, no. 4, pp. 213–219, 1988.
- [9] H. Coffey, J. Solinsky, J. Colton, and J. Woodbury, “Dynamic performance of the sri maglev vehicle,” *IEEE Transactions on Magnetics*, vol. 10, no. 3, pp. 451–457, 1974.
- [10] M. N. Cummings, B. Baldi, L. Blow, J. Caviola, H. Chin, W. W. Hirschfeld, R. Johnson, and G. Shearin, “California-nevada interstate maglev project,” vol. 1, pp. 177–185, 2004.
- [11] W. W. Dickhart, “Status of transrapid maglev,” *Electro International*, pp. 613–617, April 16-18 1991.
- [12] P. Doh Young, S. Byung Chun, and H. Hyungsuk, “Korea’s urban maglev program,” *Proceedings of the IEEE*, vol. 97, no. 11, pp. 1886–1891, 2009.
- [13] H. Gurol, R. Baldi, P. Jeter, I. K. Kim, and D. Bever, “Low speed maglev technology development program, final report,” tech. rep., General Atomics, San Diego, CA, 2002.
- [14] J. L. He, D. M. Rote, and H. T. Coffey, “Study of japanese electrodynamic-suspension maglev systems,” Tech. Rep. ANL/ESD-20, 1994.

- [15] R. Thronton, T. Clark, B. Perreault, J. Wieler, and S. Levine, “An m³ maglev system for old dominion university,” *The 20th International Conference on Magnetically Levitated Systems and Linear Drives*, 15-18 Dec. 2008.
- [16] V. Anisimow, J. Wilson, W. C. Womack, R. J. Kaye, A. A. Akhil, O. H. Paananen, J. M. Covan, D. Munoz, M. Takahashi, J. Kato, and M. Ashley, “Urban maglev technology development program, colorado maglev project, final report,” tech. rep., Colorado, 2004.
- [17] D. W. Doll, R. Kratz, M. J. Newman, A. B. Plunkett, and R. D. Blevins, “Linear synchronous motor control for an urban maglev,” vol. 1, pp. 275–285, 2004.
- [18] S. Gurol, B. Baldi, and R. Post, “General atomics urban maglev program status,” 15-18 Dec. 2008.
- [19] S. Gurol, R. Baldi, and D. Bever, “Status of the general atomics low speed urban maglev technology development program,” vol. 1, pp. 269–274, 2004.
- [20] J. He, Z. Wang, D. M. Rote, H. Coffey, J. Hull, T. Mulcahy, and Y. Cai, “Dual-keel electrodynamic maglev system,” *Argonne National Laboratory*, 1996.
- [21] A. Heller, “Maglev on the development track for urban transportation,” *Science & Technology Review*, pp. 14–17, Nov. 2003.
- [22] C. Lang and W. Jones, “Virginia maglev system off to shaky start,” *IEEE Spectrum*, vol. 40, no. 11, pp. 14–15, 2003.
- [23] H. J. Lever, “Technical assessment of maglev system concepts, final report by the government maglev system assessment team,” tech. rep., CRREL-SR-98-12, US Army, CRREL, Oct. 1998.
- [24] K. Matsui, T. Saijo, and T. Umemori, *A Japanese MAGLEV project using a D.C. linear motor*, pp. 89–121. Elek Books Ltd, 1977.
- [25] T. M. Mulcahy, J. R. Hull, J. D. Almer, and T. D. Rossing, “Edge effects on forces and magnetic fields produced by a conductor moving past a magnet,” *IEEE Transactions on Magnetism*, vol. 28, no. 5, pp. 3318–3320, 1992.
- [26] T. Murai and T. Sasakawa, “Characteristics of sc coil configuration for eds maglev to reduce leakage flux with strengthened magnetomotive force,” *18th International Conference on Magnetically Levitated Systems and Linear Drives*, vol. 2, pp. 966–972, 2004.
- [27] H. Ohsaki, R. W. Early, and E. Suzuki, “Numerical simulation of the vehicle dynamics of the superconducting maglev system,” *The 16th International Conference on Magnetically Levitated Systems and Linear Drives, Rio de Janeiro*, pp. 230–235, 2000.

- [28] T. Ohtsuka and y. Kyotani, "Superconducting maglev tests," *IEEE Transactions on Magnetics*, vol. 15, no. 6, pp. 1416–1421, 1979.
- [29] R. Rhodes, B. Mulhall, J. Howell, and E. Abel, "The wolfson maglev project," *IEEE Transactions on Magnetics*, vol. 10, pp. 398–401, Sept. 1975.
- [30] D. Rogg, "The research and development program 'magnetically suspended high speed transport systems' in the federal republic of germany," vol. 1, IEE, 1986.
- [31] Y. Seda-Sanabria and J. Ray, "Dynamic analysis of the american maglev system," tech. rep., US Army Corps of Engineers Waterways Experiment Station, 1996.
- [32] R. Thome and A. Radovinsky, "Eds levitation and guidance using sheet guide ways," *Maglev 2000 Conference*, pp. 236–241, 2000.
- [33] L. Yan, "Progress of the maglev transportation in china," *IEEE Transactions on Applied Superconductivity*, vol. 16, no. 2, pp. 1138–1141, 2006.
- [34] M. Ono, S. Koga, and H. Ohtsuki, "Japan's superconducting maglev train," *IEEE Instrumentation & Measurement Magazine*, vol. 5, no. 1, pp. 9–15, 2002.
- [35] Y. Luguang, "Development and application of the maglev transportation system," *IEEE Transactions on Applied Superconductivity*, vol. 18, no. 2, pp. 92–99, 2008.
- [36] G. Atomics:, "<http://www.ga.com/groups.php>."
- [37] "The m³ urban transportation system," tech. rep., MagneMotion Inc., 2003.
- [38] B. Jayawant, *Electromagnetic Levitation and Suspension Techniques*. Edward Arnold, 1981.
- [39] N. Fujii, M. Chida, and K. Ogawa, "Three dimensional force of magnet wheel with revolving permanent magnets," *IEEE Transactions on Magnetics*, vol. 33, no. 5, pp. 4221–4223, 1997.
- [40] N. Fujii, G. Hayashi, and Y. Sakamoto, "Characteristics of magnetic lift, propulsion and guidance by using magnet wheels with rotating permanent magnets," *Ind. Appl. Conf.*, pp. 257–262, 2000.
- [41] J. Bird, *An investigation into the use of electrodynamic wheels for high-speed ground transportation*. PhD thesis, University of Wisconsin-Madison, 2007.
- [42] J. Hogan and H. Fink, "Comparison and optimization of lift and drag forces on vehicles levitated by eddy current repulsion for various null and normal flux magnets with one or two tracks," *IEEE Transactions on Magnetics*, vol. 11, no. 2, pp. 604–607, 1975.

- [43] J. Wang, S. Wang, Z. Ren, X. Dong, G. Lin, J. Lian, C. Zhang, H. Huang, C. Deng, and D. Zhu, "A scheme of maglev vehicle using high T_c bulk superconductors," *IEEE Transactions on Applied Superconductivity*, vol. 9, no. 2, pp. 904–907, 1999.
- [44] R. Rhodes and B. E. Mulhall, *Magnetic Levitation for Rail Transport*. Oxford University Press, 1981.
- [45] E. Riches, "Will maglev lift off?," *IEE Review*, vol. 34, no. 11, pp. 427–430, 1988.
- [46] M. Murai and M. Tanaka, "Normal conducting hsst maglev," *Japan Railway & Transport Review*, vol. 25, October 2000.
- [47] S. Kusagawa, J. Baba, K. Shutoh, and E. Masada, "Multipurpose design optimization of ems-type magnetically levitated vehicle based on genetic algorithm," *IEEE Transactions on Applied Superconductivity*, vol. 14, no. 2, pp. 1922–1925, 2004.
- [48] R. Thornton, T. Clark, and K. Stevens, "Magnemotion maglev system," *Journal of the Transportation Research Board*, vol. 1838, pp. 50–57, 2003.
- [49] J. R. Hull, "Attractive levitation for high-speed ground transport with large guideway clearance and alternating-gradient stabilization," *IEEE Transactions on Magnetics*, vol. 25, no. 5, pp. 3272–3274, 1989.
- [50] Z. Guoqiang, F. Youtong, S. Fuchuan, Z. Guiping, and W. Zanji, "Optimal design and fem analysis of the superconducting magnets of ems-maglev models using bi-2223 tapes," *IEEE Transactions on Applied Superconductivity*, vol. 14, no. 2, pp. 1850–1853, 2004.
- [51] J. R. Powell and G. Danby, "A 300-mph magnetically suspended train," *Mechanical Engineering*, no. Nov, pp. 30–35, 1967.
- [52] J. Powell and G. Danby, "Electromagnetic inductive suspension and stabilization system for a ground vehicle," Nov. 1969.
- [53] L. Davis and J. Reitz, "Eddy currents in finite conducting sheets," *Journal of Applied Physics*, vol. 42, pp. 4119–4127, Oct. 1971.
- [54] J. R. Reitz, "Forces on moving magnets due to eddy currents," *Journal of Applied Physics*, vol. 41, pp. 2067–2070, apr 1970.
- [55] J. R. Reitz and L. Davis, "Force on a rectangular coil moving above a conducting slab," *Journal of Applied Physics*, vol. 43, pp. 1547–1553, apr 1972.
- [56] L. Davis and D. Wilkie, "Analysis of motion of magnetic levitation systems: implications for high-speed vehicles," *Journal of Applied Physics*, vol. 42, pp. 4779–4793, Nov. 1971.

- [57] L. Davis, "Drag force on a magnet moving near a thin conductor," *Journal of Applied Physics*, vol. 43, no. 10, pp. 4256–4257, 1972.
- [58] R. Borcherts and L. Davis, "Force on a coil moving over a conducting surface including edge and channel effects," *Journal of Applied Physics*, vol. 43, pp. 2418–2427, may 1972.
- [59] M. Iwamoto, T. Yamada, and E. Ohno, "Magnetic damping force in electro-dynamically suspended trains," *IEEE Transactions on Magnetics*, vol. 10, pp. 458–461, Sep. 1974.
- [60] M. T., Iwamoto and T. Y. Ito, "Magnetic damping force in inductive magnetic levitation system for high-speed trains," *Electrical Engineering Japan*, vol. 94, no. 1, pp. 49–54, 1974.
- [61] R. Borcherts, L. Davis, J. Reitz, and D. Wilkie, "Baseline specifications for a magnetically suspended high-speed vehicle," *Proceedings of the IEEE*, vol. 61, pp. 569–578, may 1973.
- [62] E. Ohno, M. Iwamoto, and T. Yamada, "Characteristics of superconductive magnetic suspension and propulsion for high-speed trains," *Proceedings of the IEEE*, vol. 61, no. 5, pp. 579–586, 1973.
- [63] D. Rote and Y. Cai, "Review of dynamic stability of repulsive-force maglev suspension systems," *IEEE Transactions on Magnetics*, vol. 38, pp. 1383–1390, mar 2002.
- [64] K. Sawada, "Development of magnetically levitated high speed transport system in japan," *IEEE Transactions on Magnetics*, vol. 32, pp. 2230–2235, jul 1996.
- [65] Wikipedia, "<http://en.wikipedia.org/wiki/jr>
- [66] E. Freeman and C. Papageorgiou, "Spatial fourier transforms: a new view of end effects in linear induction motors," *Proceedings of the IEE*, vol. 125, pp. 747–753, aug 1978.
- [67] M. Iwamoto, E. Ohno, T. Itoh, and Y. Shinryo, "End-effect of high-speed linear induction motor," *IEEE Transactions on Industry Applications*, vol. 9, no. 6, pp. 632–638, 1973.
- [68] A. Z. Bazghaleh, M. R. Naghashan, and M. R. Meshkatoddini, "Optimum design of single-sided linear induction motors for improved motor performance," *IEEE Transactions on Magnetics*, vol. 46, no. 11, pp. 3939–3947, 2010.
- [69] E. Laithwaite, "Application of linear induction motors to high-speed transport system," *Proceedings of the IEE*, vol. 116, no. 5, pp. 713–724, 1969.
- [70] Y. Luguang, "The linear motor powered transportation development and application in china," *Proceedings of the IEEE*, vol. 97, no. 11, pp. 1872–1880, 2009.

- [71] J. F. Gieras and Z. J. Piech, *Linear synchronous motors : transportation and automation systems*. CRC Press, 1999.
- [72] Transrapid International, "Transrapid international, superspeed maglev system," NaN.
- [73] F. Daldaban and N. Ustkoyuncu, "A new linear switched reluctance motor with maglev effect," pp. 420–422, Nov. 5-8 2009.
- [74] I. Boldea and S. Nasar, *Linear Motion Electrical Machines*. Wiley, 1976.
- [75] A. M. El-Antably, J. Edwards, G. Willians, and P. Lindon, "Steady-state performance characteristics of linear reluctance motors," *IEEE Transactions on Magnetics*, vol. 15, pp. 1440–1442, Nov. 1979.
- [76] J. S. Chahal, "The hybrid flux linear reluctance machine in urban transport," *Electric Machines and Electromechanics*, vol. 4, pp. 341–348, 1979.
- [77] R. Krishnan, "Propulsion with and without wheels," pp. P11–P19, 14-17 Dec. 2005.
- [78] T. Umemori, Y. Hosoda, M. Iwasaki, and M. Toyoshima, "Development of a dc linear motor - fundamental construction and feasibility," *IEEE Transactions on Power Apparatus and Systems*, vol. 98, no. 5, pp. 1456–1465, 1979.
- [79] T. Umemori, M. Kawashima, M. Oda, and S. Ohsawa, "Development of a dc linear motor (ii) - research for a ground coil and a field-magnet," *IEEE Transactions on Power Apparatus and Systems*, vol. 98, no. 5, pp. 1786–1795, 1979.
- [80] S. A. Nasar and I. Boldea, *Linear Electric Motors: Theory, Design, and Practical Applications*. Prentice-Hall, 1987.
- [81] A. Basak, *Permanent-Magnet DC Linear Motors*. Oxford University Press, 1996.
- [82] R. J. Kaye, W. R. Chambers, J. Dempsey, R. Dykhuizen, J. Keller, G. Mann, B. Marder, and B. Turman, "Seraphim urban maglev propulsion design," tech. rep., Sandia National Laboratories, Albuquerque, NM, 2002.
- [83] B. N. Turman, B. M. Marder, G. J. Rohwein, D. P. Aeschliman, J. B. Kelley, M. Cowan, and R. Zimmerman, "The pulsed linear induction motor concept for high-speed trains," tech. rep., Sandia National Laboratories, Albuquerque, NM, jun 1995.
- [84] B. Marder, "The physics of seraphim," tech. rep., Sandia National Laboratories, Albuquerque, NM, Oct. 2001.

- [85] R. Hellinger and P. Mnich, "Linear motor-powered transportation: History, present status, and future outlook," *Proceedings of the IEEE*, vol. 97, no. 11, pp. 1892–1900, 2009.
- [86] E. R. Laithwaite, *A History of Linear Electric Motors*. Macmillan, 1987.
- [87] "A wound rotor motor 1400ft long," *Westinghouse Engineering*, vol. 6, pp. 160–162, 1946.
- [88] E. Laithwaite, *Propulsion Without Wheels*. English Universities Press, 1970.
- [89] G. Stumberger, D. Zarko, M. Timur Aydemir, and T. A. Lipo, "Design and comparison of linear synchronous motor and linear induction motor for electromagnetic aircraft launch system," *IEEE International Electric Machines and Drives Conference*, vol. 1, pp. 494–500 vol.1, 1-4 June 2003.
- [90] D. C. Meeker and M. J. Newman, "Indirect vector control of a redundant linear induction motor for aircraft launch," *Proceedings of the IEEE*, vol. 97, no. 11, pp. 1768–1776, 2009.
- [91] D. Hall, J. Kapinski, M. Krefta, and O. Christianson, "Transient electromechanical modeling for short secondary linear induction machines," *IEEE Transactions on Energy Conversion*, vol. 23, no. 3, pp. 789–795, 2008.
- [92] C. Han-Wook, S. Ho-Kyoung, S. So-Young, Y. Dae-Joon, and J. Seok-Myeong, "Design and characteristic analysis on the short-stator linear synchronous motor for high-speed maglev propulsion," *IEEE Transactions on Magnetics*, vol. 44, no. 11, pp. 4369–4372, 2008.
- [93] J. A. Ross, "Romag transportation system," *Proceedings of the IEEE*, vol. 61, pp. 617–620, may 1973.
- [94] S. Nasar and L. Cid, "Propulsion and levitation forces in a single-sided linear induction motor for high-speed ground transportation," *Proceedings of the IEEE*, vol. 61, pp. 638–644, may 1973.
- [95] E. Levi, "Linear synchronous motors for high-speed ground transportation," *IEEE Transactions on Magnetics*, vol. 9, pp. 242–248, Sept. 1973.
- [96] E. Levi, "Preliminary design studies on iron cored synchronously operated linear motors," tech. rep., Department of Transport,, 1976.
- [97] A. R. Eastham, G. E. Dawson, R. Ong, and L. W. Coathup, "The design and operation of the homopolar linear synchronous motor for linear drive and for integrated suspension/propulsion applications," *Proceedings of International Conference on Maglev Transport Now and the Future, IMechE*, vol. 1, pp. 95–104, 1984.

- [98] J. F. Eastham, M. J. Balchin, and D. Rodger, "A comparison of some propulsion methods for magnetically-levitated vehicles," *ibid*, vol. 1, pp. 111–118, 1984.
- [99] G. W. McLean and A. N. West, "Combined lift and thrust for maglev vehicles using the zig-zag synchronous motor," *ibid*, vol. 1, pp. 87–93, 1984.
- [100] G. W. McLean, "Review of recent progress in linear motors," *IEE Proceedings Part B*, vol. 135, pp. 380–416, Nov. 1988.
- [101] A. Casset, M. Rosenmayr, N. Macabrey, and M. Jufer, "Swissmetro and transrapid comparison of the electromechanical components and the power supply in a specified vacuum tunnel environment," *Maglev 2000, Rio de Janeiro*, pp. 119–129, June, 2000.
- [102] "Swissmetro homepage: <http://www.swissmetro.ch/>," 2009.
- [103] J. F. Eastham and E. Laithwaite, "Linear induction motors as 'electromagnetic rivers'," *Proceedings of the IEE*, vol. 121, pp. 1099–1108, Oct. 1974.
- [104] J. F. Eastham and S. Williamson, "Experiments on the lateral stabilisation and levitation of linear induction motors," *IEEE Transactions on Magnetics*, vol. 10, pp. 470–473, Sept. 1974.
- [105] J. F. Eastham and D. Rodger, "The performance of induction levitators," *IEEE Transactions on Magnetics*, vol. 20, pp. 1684–1686, Sept. 1984.
- [106] R. M. Katz, A. Eastham, G. E. Dawson, D. A. Atherson, and C. L. Schwalm, "Integrated magnetic suspension and propulsion of guided ground transportation vehicles with a slim," *IEEE transactions on Magnetics*, vol. 15, no. 6, pp. 1437–1439, 1979.
- [107] B. V. Jayawant, J. D. Edwards, L. S. Wickramaratne, W. R. C. Dawson, and T. C. Yang, "Electromagnetic launch assistance for space vehicles," *Science, Measurement & Technology, IET*, vol. 2, no. 1, pp. 42–52, 2008.
- [108] National Aeronautics & Space Administration, "<http://www.nasa.gov/topics/technology/features/horizontallaunch.html>," 2011.
- [109] J. Bird and T. Lipo, "An electrodynamic wheel: an integrated propulsion and levitation machine," *IEEE IEMDC 2003*, vol. 3, pp. 1410–1416, jun 2003.
- [110] R. H. Borcherts and L. C. Davis, "The superconducting paddlewheel as an integrated propulsion levitation machine for high speed ground transportation," *Electric Machines and Electromechanics*, vol. 3, pp. 341–355, Apr-June 1979.
- [111] N. Fujii, G. Hayashi, and Y. Sakamoto, "Characteristics of a moving magnet rotator over a conducting plate," *IEEE Transactions on Magnetics*, vol. 41, pp. 3811–3813, Oct. 2005.

- [112] L. C. Davis and R. H. Borcherts, "Superconducting paddle wheels, screws, and other propulsion units for high-speed ground transportation," *Journal of Applied Physics*, vol. 44, pp. 3294–3299, jul 1973.
- [113] N. Fujii, K. Naotsuka, K. Ogawa, and T. Matsumoto, "Basic characteristics of magnet wheels with rotating permanent magnets," *IEEE IAS*, vol. 1, pp. 203–209, 1994.
- [114] J. Bird and T. Lipo, "Calculating the forces created by an electrodynamic wheel using a 2d steady-state finite element model," *IEEE Transactions on Magnetics*, vol. 44, pp. 365–372, mar 2008.
- [115] J. Bird and T. Lipo, "Characteristics of an electrodynamic wheel using a 2-d steady-state model," *IEEE Transactions on Magnetics*, vol. 43, pp. 3395–3405, Aug. 2007.
- [116] "Comsol, femlab," 2011.
- [117] J. Duncan, "Linear induction motor - equivalent-circuit model," *IEE Proceedings Part B*, vol. 130, pp. 51–57, Jan. 1983.
- [118] T. Lipo and T. Nondahl, "Pole-by-pole d-q model of a linear induction machine," *IEEE Transactions on Power Apparatus and Systems*, vol. 98, pp. 629–639, March/April 1979.
- [119] T. Nondahl and D. Novotny, "Three-phase pole-by-pole model of a linear induction machine," *IEE Proceedings Part B*, vol. 127, pp. 68–82, mar 1980.
- [120] A. S. Gercek and V. M. Karsh, "Performance prediction of the single-sided linear induction motors for transportation considers longitudinal end effect by using analytic method," *Contemporary Engineering Sciences*, vol. 2, no. 2, pp. 95–104, 2009.
- [121] R. Pai, I. Boldea, and S. A. Nasar, "A complete equivalent circuit of a linear induction motor with sheet secondary," *IEEE Transactions on Magnetics*, vol. 24, no. 1, pp. 639–653, 1988.
- [122] J. Faiz and H. Jafari, "Accurate modeling of single-sided linear induction motor considers end effect and equivalent thickness," *IEEE Transactions on Magnetics*, vol. 36, pp. 3785–3790, Sept 2000.
- [123] L. Junyong and M. Weiming, "Research on end effect of linear induction machine for high-speed industrial transportation," *IEEE Transactions on Plasma Science*, vol. 39, no. 1, pp. 116–120, 2011.
- [124] X. Wei, Z. Jian Guo, Z. Yongchang, L. Yaohua, W. Yi, and G. Youguang, "An improved equivalent circuit model of a single-sided linear induction motor," *IEEE Transactions on Vehicular Technology*, vol. 59, no. 5, pp. 2277–2289, 2010.

- [125] X. Wei, Z. Jian Guo, Z. Yongchang, L. Zixin, L. Yaohua, W. Yi, G. Youguang, and L. Yongjian, "Equivalent circuits for single-sided linear induction motors," *IEEE Transactions on Industry Applications*, vol. 46, no. 6, pp. 2410–2423, 2010.
- [126] P. Richards and M. Tinkham, "Magnetic suspension and propulsion systems for high-speed transportation," *Journal of Applied Physics*, vol. 43, pp. 2680–2691, jun 1972.
- [127] R. L. Byer, R. F. Begley, and G. R. Stewart, "Superconducting, magnetically levitated merry-go-round," *American Journal of Physics*, vol. 42, pp. 111–125, 1974.
- [128] S. Lee and R. Menendez, "Forces at low-and high-speed limits in magnetic levitation systems," *Journal of Applied Physics*, vol. 46, no. 1, pp. 422–425, 1975.
- [129] J. Maxwell, "On the induction of electric currents in an infinite plane sheet of uniform conductivity," *Proceedings of the Royal Society of London*, vol. A20, no. 160, 1872.
- [130] J. Maxwell, *A Treatise on Electricity & Magnetism*, vol. 2. Dover Publications Inc, 1954.
- [131] T. Rossing and J. Hull, "Magnetic levitation," *The Physics Teacher*, pp. 552–562, Dec 1991.
- [132] W. R. Smythe, "On eddy currents in a rotating disk," *Transactions of the American Institute of Electrical Engineers*, vol. 61, no. 9, pp. 681–684, 1942.
- [133] R. J. Hill, "Teaching electrodynamic levitation theory," *IEEE Transaction on Education*, vol. 33, pp. 346–354, Nov. 1990.
- [134] B. Ooi and D. White, "Traction and normal forces in the linear induction motor," *IEEE Transactions on Power Apparatus and Systems*, vol. 89, pp. 638–645, apr 1970.
- [135] M. Chari and S. Salon, *Numerical Methods in Electromagnetism*. Academic Press, 2000.
- [136] A. Foggia, J. C. Sabonnadiere, and P. Silvester, "Finite element solution of saturated travelling magnetic field problems," *IEEE Transactions on Power Apparatus and Systems*, vol. 94, pp. pp 866–871, May/June 1975.
- [137] D. Rodger, T. Karaguler, and P. J. Leonard, "A formulation for 3d moving conductor eddy current problems," *IEEE Transactions on Magnetics*, vol. Vol. 25, pp. pp 4147–4149,, Sep 1989.

- [138] D. Rodger, P. J. Leonard, and T. Karaguler, "An optimal formulation for 3d moving conductor eddy current problems with smooth rotors," *IEEE Transactions on Magnetism*, vol. 26, pp. 2359–2363, Sep. 1990.
- [139] L. Gaul, M. Kögl, and M. Wagner, *Boundary element methods for engineers and scientists : an introductory course with advanced topics*. Springer, 2003.
- [140] L. T. Klauder, "A magnetic field diffusion problem," *American Journal of Physics*, vol. 37, pp. 323–325, Mar. 1969.
- [141] K. Oberretl, *Three-dimensional analysis of the linear motor*, pp. 217–248. Elek Books Ltd, 1977.
- [142] J. Bird and T. Lipo, "Modeling the 3-d rotational and translational motion of a halbach rotor above a split-sheet guideway," *IEEE Transactions on Magnetism*, vol. 45, pp. 3233–3242, Sept. 2009.
- [143] S. Lee and R. Menendez, "Force on current coils moving over a conducting sheet with application to magnetic levitation," *Proceedings of the IEEE*, vol. 62, pp. 567–577, may 1974.
- [144] D. Rodger and J. F. Eastham, "A formulation for low frequency eddy current solutions," *IEEE Transactions on Magnetism*, vol. 19, pp. 2450–2452, Nov 1983.
- [145] C. J. Carpenter, "Comparison of alternative formulations of 3-dimensional magnetic-field and eddy-current problems at power frequencies," *Proceedings of the Institution of Electrical Engineers*, vol. 124, no. 11, pp. 1026–1034, 1977.
- [146] H. Knoepfel, *Magnetic fields: A Comprehensive Theoretical Treatise for Practical Use*. John Wiley & Sons, 2000.
- [147] O. Zienkiewicz, J. Lyness, and D. R. J. Owen, "Three-dimensional magnetic field determination using a scalar potential - a finite element solution," *IEEE Transactions on Magnetism*, vol. 13, pp. 1649–1656, Sept. 1977.
- [148] M. Ziolkowski and H. Brauer, "Fast computation technique of forces acting on moving permanent magnet," *IEEE Transactions on Magnetism*, vol. 46, no. 8, pp. 2927–2930, 2010.
- [149] A. Polyanin and A. Manzhirov, *Handbook of Mathematics for Engineers and Scientists*. Chapman & Hall, 2007.
- [150] R. Churchill, *Operational Mathematics*. McGraw-Hill, Inc., third ed., 1972.
- [151] T. Theodoulidis, "Developments in calculating the transient eddy-current response from a conductive plate," *IEEE Transactions on Magnetism*, vol. 44, no. 7, pp. 1894–1896, 2008.

- [152] F. Fu and J. Bowler, "Transient eddy-current driver pickup probe response due to a conductive plate," *IEEE Transactions on Magnetics*, vol. 42, no. 8, pp. 2029–2037, 2006.
- [153] D. J. Griffiths, *Introduction to Electrodynamics*. Prentice Hall, 3rd ed., 1999.
- [154] S. Paul, D. Bobba, N. Paudel, and J. Z. Bird, "Source field modeling in air using magnetic charge sheets," *IEEE INTMAG*, vol. in press, 2012.
- [155] E. P. Furlani, *Permanent Magnet and Electromechanical Devices*. Academic Press, 2001.
- [156] H. Toda, Z. Xia, J. Wang, K. Atallah, and D. Howe, "Rotor eddy-current loss in permanent magnet brushless machines," *IEEE Transactions on Magnetics*, vol. 40, pp. 2104–2106, jul 2004.
- [157] K. Atallah, D. Howe, P. Mellor, and D. Stone, "Rotor loss in permanent-magnet brushless ac machines," *IEEE Transactions on Industry Applications*, vol. 36, pp. 1612–1618, Nov/Dec 2000.
- [158] Z. P. Xia, Z. Q. Zhu, and D. Howe, "Analytical magnetic field analysis of halbach magnetized permanent-magnet machines," *IEEE Transactions on Magnetics*, vol. 40, no. 4, pp. 1864–1872, 2004.
- [159] P. K. . Kythe and M. R. . Schäferkötter, *Handbook of Computational Methods for Integration*. Chapman and Hall/CRC, 2004.
- [160] D. Bobba, "3-d analytic based modeling of an electrodynamic wheel and the performance of electrodynamic wheels in series for urban transportation," Master's thesis, University of North Carolina at Charlotte, 2011.
- [161] S. K. Burke and M. E. Ibrahim, "Mutual impedance of air-cored coils above a conducting plate," *Journal of Applied Physics*, vol. 37, no. 13, pp. 1857–1868, 2004.
- [162] B. A. Auld and J. C. Moulder, "Review of advances in quantitative eddy current nondestructive evaluation," *Journal of Nondestructive Evaluation*, vol. 18, no. 1, pp. 3–36, 1999.
- [163] V. O. de Haan and P. A. de Jong, "Analytical expressions for transient induction voltage in a receiving coil due to a coaxial transmitting coil over a conducting plate," *IEEE Transactions on Magnetics*, vol. 40, no. 2, pp. 371–378, 2004.
- [164] K. Connor and J. Tichy, "Analysis of an eddy current journal bearing," *ASME Journal of Tribology*, vol. 110, pp. 320–326, apr 1988.
- [165] T. Yoshimoto, "Eddy current effect in a magnetic bearing model," *IEEE Transactions on Magnetics*, vol. 19, no. 5, pp. 2097–2099, 1983.

- [166] W. Renhart, C. A. Magele, K. R. Richter, P. Wach, and R. Stollberger, "Application of eddy current formulations to magnetic resonance imaging," *IEEE Transactions on Magnetics*, vol. 28, no. 2, pp. 1517–1520, 1992.
- [167] L. Feng and S. Crozier, "An fdtd model for calculation of gradient-induced eddy currents in mri system," *IEEE Transactions on Applied Superconductivity*, vol. 14, no. 3, pp. 1983–1989, 2004.
- [168] H. A. Sodano and J. Bae, "Eddy current damping in structures," *The Shock and Vibration Digest*, vol. 36, no. 6, pp. 469–478, 2004.
- [169] M. T. Thompson, "Eddy current magnetic levitation. models and experiments," *IEEE Potentials*, vol. 19, no. 1, pp. 40–44, 2000.
- [170] F. C. Moon, *Superconducting Levitation*. John Wiley & Sons, 1994.
- [171] K. Davey, "Calculation of motion induced eddy current forces in null flux coils," *IEEE Transactions on Magnetics*, vol. 31, pp. 4214–4217, Nov 1995.
- [172] V. M. Sapunov, "Eddy-current inspection of sheet of nonmagnetic material by superposed transducer excited by pulsed current with nonideal shape," *Russian Journal of Nondestructive Testing*, vol. 27, no. 10, pp. 743–750, 1991.
- [173] D. L. Waidelech, "Pulsed eddy-current testing of steel sheets," *Eddy Current Characterization of Materials and Structures*, vol. STP-722, pp. 367–373, 1981.
- [174] S. M. Panas and E. E. Kriezis, "Determination of the field and the forces on a current filament moving above a conducting plate," *Electrical Engineering (Archiv fur Elektrotechnik)*, vol. 68, no. 4, pp. 293–298, 1985.
- [175] L. Hannakam, "Transienter skinneffekt in einer platte endlicher dicke bei beliebiger form der erregenden leiterschleife," *Electrical Engineering (Archiv fur Elektrotechnik)*, vol. 60, no. 6, pp. 361–371, 1978.
- [176] H. Fink and C. Hobrecht, "Instability of vehicles levitated by eddy current repulsion-case of an infinitely long current loop," *Journal of Applied Physics*, vol. 42, pp. 3446–3450, Aug. 1971.
- [177] M. Clemens, T. Weiland, and M. Wilke, "Transient eddy current formulation including moving conductors using the fi method," *IEEE Transactions on Magnetics*, vol. 36, no. 4, pp. 804–808, 2000.
- [178] T. V. Yioultsis, K. S. Charitou, C. S. Antonopoulos, and T. D. Tsiboukis, "A finite difference time domain scheme for transient eddy current problems," *IEEE Transactions on Magnetics*, vol. 37, no. 5, pp. 3145–3149, 2001.
- [179] K. Muramatsu, T. Nakata, N. Takahashi, and K. Fujiwara, "Linear ac steady-state eddy current analysis of high speed conductor using moving coordinate system," *IEEE Transactions on Magnetics*, vol. 32, no. 3, pp. 749–752, 1996.

- [180] K. Muramatsu, T. Nakata, N. Takahashi, and K. Fujiwara, "Comparison of coordinate systems for eddy current analysis in moving conductors," *IEEE Transactions on Magnetics*, vol. 28, pp. 1186–1189, 1992.
- [181] T. Iwahana, T. Iketani, and T. Fujimoto, "Characteristics of a maglev running on aluminum sheet guideways," tech. rep., Japanese National Railways, 1980.
- [182] Y. Sato, A. Matsuura, S. Miura, and Y. Satoh, "Development of guideway for maglev," *Proceedings International Conference on Maglev Transport '85*, pp. 243–250, 1985.
- [183] H. Yoshioka, E. Suzuki, H. Seino, M. Azakami, H. Oshima, and T. Nakanishi, "Results of running tests and characteristics of the mlx01 yamanashi test vehicles," *Proceedings of Maglev Conference '98*, pp. 225–230, Apr 1998.
- [184] E. R. Laithwaite, *Transport without wheels*. Westview Press, 1977.
- [185] F. Moon, "Laboratory studies of magnetic levitation in the thin track limit," *IEEE Transactions on Magnetics*, vol. 10, no. 3, pp. 439–442, 1974.
- [186] D. Chu and F. Moon, "Dynamic instabilities in magnetically levitated models," *Journal of Applied Physics*, vol. 54, pp. 1619–1625, mar 1983.
- [187] Y. Cai, D. M. Rote, T. M. Mulcahy, Z. Wang, S. S. Chen, and S. Zhu, "Dynamic stability of repulsive-force maglev suspension systems," tech. rep., Argonne National Laboratory, Argonne, IL, 1996.
- [188] Y. Cai and S. Chen, "A review of dynamic characteristics of magnetically levitated vehicle systems," tech. rep., Argonne National Laboratory, Argonne, IL, Nov. 1995.
- [189] Y. Cai and S. Chen, "Numerical analysis for dynamic instability of electrodynamic maglev systems," *Shock and Vibration*, vol. 2, no. 4, pp. 339–349, 1995.
- [190] Y. Cai, S. S. Chen, T. M. Mulcahy, and D. M. Rote, "Dynamic stability of maglev systems," Tech. Rep. ANL-92/21, Argonne National Laboratory, Argonne, Illinois, 1993.
- [191] Q. Han, *Analysis and modeling of the EDS maglev system based on the Halbach permanent magnet array*. PhD thesis, University of Central Florida, 2004.
- [192] W. Ko, *Modeling and analysis of the EDS maglev system with the Halbach magnet array*. PhD thesis, University of Central Florida, 2007.
- [193] S. Chen, S. Zhu, and Y. Cai, "On the unsteady-motion theory of magnetic forces for maglev," Tech. Rep. ANL-93/39, Argonne National Laboratory, 1993.

- [194] T. Saitoh, N. Maki, T. Kobayashi, M. Shibata, and T. Takizawa, “Electromagnetic force and eddy-current loss in dynamic behavior of superconducting magnetically levitated vehicle,” *Applied Superconductivity Conference*, Aug. 26 1992.
- [195] S. Chen, S. Zhu, Y. Cai, and D. Rote, “Magnetic damping for maglev,” tech. rep., Argonne National Laboratory, 1995.
- [196] J. L. He, D. M. Rote, and S. S. Chen, “Characteristics and computer model simulation of magnetic damping forces in maglev system,” tech. rep., Argonne National Laboratory, Argonne, IL, 1994.
- [197] J. L. He and H. Coffey, “Magnetic damping forces in figure-eight-shaped null-flux coil suspension systems,” *IEEE Transactions on Magnetism*, vol. 33, pp. 4230–4232, Sept. 1997.
- [198] T. Gillespie, *Fundamentals of Vehicle Dynamics*. Society of Automotive Engineers, Inc., 1992.
- [199] N. Paudel, J. Bird, S. Paul, and D. Bobba, “Modeling the dynamic suspension behavior of an eddy current device,” *IEEE Energy Conversion Congress & Expo*, 2011.
- [200] B. Ooi, “Electromechanical stiffness and damping coefficients in the repulsive magnetic levitation system,” *IEEE Transactions on Power Apparatus and Systems*, vol. 95, pp. 936–943, May/June 1976.
- [201] S. G. Kelly, *Fundamentals of mechanical vibrations*. New York: McGraw-Hill, 1993.
- [202] W. J. Bottega, *Engineering vibrations*. CRC/Taylor & Francis, 2006.
- [203] S. Paul, N. Paudel, J. Z. Bird, and B. Walter, “Analytic based 3-d eddy current modeling in a finite width conducting plate,” ECCE-2012, Raleigh, Submitted., 2012.
- [204] S. Paul, D. Bobba, and J. Z. Bird, “Source field modeling in air using magnetic charge sheets,” in *IEEE INTMAG, Vancouver, Canada*, May 7-11 2012.
- [205] J. Bird and T. Lipo, “A 3d steady-state magnetic charge finite element model of an electrodynamic wheel,” *IEEE Transactions on Magnetism*, vol. 44, pp. 253–265, Feb. 2008.

APPENDIX A: A 2-D TRANSIENT FINITE-ELEMENT MODEL

A 2-D transient FEA model has been developed by S. Paul. This is capable of simultaneously modeling both translational and rotational motion. For completeness this derived model is presented here. If the source in the non-conducting region is analytically modeled then the problem region will simplify down to a conducting region, Ω_2 , and non-conducting regions, Ω_n ($n = 1, 3$) as shown in Figure 3.1.

A.1 Non-Conducting Regions

The governing equation (2.12) is used for the non-conducting regions in this model. The weighted residual formulation of (2.12) will be [41]

$$\int_{\Omega_n} w_n \nabla^2 \phi_n d\Omega_n = 0 \quad \text{for } n = 1 \text{ and } 3 \quad (\text{A.1})$$

where w_n ($n = 1, 3$) is the weighting function. The necessary boundary conditions in (A.1) can be explicitly introduced by using the Green's first identity

$$w_n \nabla^2 \phi_n = \nabla \cdot (w_n \nabla \phi_n) - \nabla w_n \cdot \nabla \phi_n \quad (\text{A.2})$$

Hence, the weak form of (A.1) will be

$$-\int_{\Omega_n} \nabla \phi_n \cdot \nabla w_n d\Omega_n + \int_{\Gamma_c} w_n (\nabla \phi_n \cdot \mathbf{n}_{nc}) d\Gamma_c = 0 \quad \text{for } n = 1 \text{ and } 3 \quad (\text{A.3})$$

where \mathbf{n}_{nc} is the unit outward normal vector on Γ_c for conducting region

A.2 Conducting Guideway Region

The governing equation for the conducting guideway region (2.27) is modified by setting $v_y = 0$ for this FEA model. Unlike the 2-D transient analytical model, the

translational speed, v_x is included in the guideway equation as given by

$$\frac{\partial^2 A_z}{\partial x^2} + \frac{\partial^2 A_z}{\partial y^2} = \mu_0 \sigma \left(\frac{\partial A_z}{\partial t} + v_x \frac{\partial A_z}{\partial x} \right) \quad \text{on } \Omega_2 \quad (\text{A.4})$$

Using the Galerkin weighted residual method, (A.4) can be written in the weak form, using Green's first identity (A.2) to yield [205]

$$\begin{aligned} 0 = & - \int_{\Omega_2} \nabla N_z \cdot \nabla A_z d\Omega_2 - \mu_0 \sigma \int_{\Omega_2} N_z \left(v_x \frac{\partial A_z}{\partial x} + \frac{\partial A_z}{\partial t} \right) d\Omega_2 \\ & + \int_{\Gamma_c} N_z (\nabla A_z \cdot \mathbf{n}_c) d\Gamma_c \end{aligned} \quad (\text{A.5})$$

where $\Gamma_c = \Gamma_{12}, \Gamma_{23}$ and N_z is the shape function and \mathbf{n}_c is the unit outward normal vector on Γ_c for conducting region.

A.3 Boundary Conditions

The effect of the source field on the conductive region is accounted for by incorporated it into the interface between the conductive and non-conductive regions. The normal and tangential field components on the conductive boundary, Γ_c are given by

$$- \mu_0 \nabla \phi_1 \cdot \mathbf{n}_{nc} + \mathbf{B}^s \cdot \mathbf{n}_{nc} = \nabla \times \mathbf{A} \cdot \mathbf{n}_{nc} \quad \text{on } \Gamma_c \quad (\text{A.6})$$

$$- \mathbf{n}_c \times \mu_0 \nabla \phi + \mathbf{n}_c \times \mathbf{B}^s = \mathbf{n}_c \times \nabla \times \mathbf{A} \quad \text{on } \Gamma_c \quad (\text{A.7})$$

In order to couple the conducting and non-conducting regions, the scalar boundary condition in (A.3) needs to be expressed in terms of vector potential terms. Using (A.6), the boundary term in (A.3) can be written as

$$\int_{\Gamma_{12}} w_1 \nabla \phi_1 \cdot \mathbf{n}_{nc} d\Gamma_{12} = \int_{\Gamma_{12}} \frac{w_1}{\mu_0} (B^s - \nabla \times \mathbf{A}) \cdot \mathbf{n}_{nc} d\Gamma_{12} \quad (\text{A.8})$$

$$\int_{\Gamma_{23}} w_3 \nabla \phi_3 \cdot \mathbf{n}_{nc} d\Gamma_{23} = \int_{\Gamma_{23}} \frac{w_3}{\mu_0} (-\nabla \times \mathbf{A}) \cdot \mathbf{n}_{nc} d\Gamma_{23} \quad (\text{A.9})$$

Similarly the vector potential boundary conditions in (A.5) must be replaced with scalar potential terms. The boundary condition in (A.5) is

$$\int_{\Gamma_c} N_z \left[\frac{\partial A_z}{\partial x} \mathbf{n}_{cx} + \frac{\partial A_z}{\partial y} \mathbf{n}_{cy} \right] d\Gamma_c = 0 \quad (\text{A.10})$$

Expanding (A.6) enables (A.10) to be expressed in terms of scalar potential terms and source field as

$$\int_{\Gamma_{12}} N_z \left[\left(\mu_0 \frac{\partial \phi_1}{\partial y} - B_y^s \right) \mathbf{n}_{cx} + \left(-\mu_0 \frac{\partial \phi_1}{\partial x} + B_x^s \right) \mathbf{n}_{cy} \right] d\Gamma_{12} = 0 \quad (\text{A.11})$$

$$\int_{\Gamma_{23}} N_z \left[\left(\mu_0 \frac{\partial \phi_1}{\partial y} \right) \mathbf{n}_{cx} + \left(-\mu_0 \frac{\partial \phi_1}{\partial x} \right) \mathbf{n}_{cy} \right] d\Gamma_{23} = 0 \quad (\text{A.12})$$

The Dirichlet boundary condition has been applied on all of the remaining non-conducting and conducting boundaries

$$\phi = 0 \quad \text{on } \Gamma_1 \text{ and } \Gamma_3 \quad (\text{A.13})$$

$$A_z = 0 \quad \text{on } \Gamma_2 \quad (\text{A.14})$$

Using (A.5) and (A.3) within conducting and non-conducting regions as well as boundary conditions (A.8) and (A.13), enables the convective finite element $A_z - \phi$ model to be developed.

A.4 Rotor Magnetic Field

In the FEA transient model, the vector potential source rotor field (2.163) only has a real component. Thus one obtains

$$A_z^s(r, \theta, t) = \frac{C}{P r^P} \cos(P\theta - \omega_e t) \quad (\text{A.15})$$

The radial and azimuthal magnetic flux densities are then

$$B_r^s(r, \theta, t) = \frac{1}{r} \frac{\partial A_z^s}{\partial \theta} = -\frac{C \sin(P\theta - \omega_e t)}{2r^{P+1}} \quad (\text{A.16})$$

$$B_\theta^s(r, \theta, t) = -\frac{\partial A_z^s}{\partial r} = \frac{C \cos(P\theta - \omega_e t)}{2r^{P+1}} \quad (\text{A.17})$$

Converting (A.16) and (A.17) into Cartesian coordinates gives

$$B_x^s(x, y, t) = -\frac{C \sin(P\theta - \omega_e t)}{(x^2 + (y - y_o)^2)^{\frac{(P+1)}{2}}} \cos(\theta) - \frac{C \cos(P\theta - \omega_e t)}{(x^2 + (y - y_o)^2)^{\frac{(P+1)}{2}}} \sin(\theta) \quad (\text{A.18})$$

$$B_y^s(x, y, t) = -\frac{C \sin(P\theta - \omega_e t)}{(x^2 + (y - y_o)^2)^{\frac{(P+1)}{2}}} \sin(\theta) + \frac{C \cos(P\theta - \omega_e t)}{(x^2 + (y - y_o)^2)^{\frac{(P+1)}{2}}} \cos(\theta) \quad (\text{A.19})$$

where

$$\theta = \tan^{-1} \left(\frac{y - y_o}{x} \right) \quad (\text{A.20})$$

The equations (A.18) and (A.19) have been used in the boundary condition equations (A.11).

APPENDIX B: ADDITIONAL EXPERIMENTAL RESULTS

The additional experimental test cases performed in order to investigate the dynamics of the EDW pendulum setup are included in this Appendix.

- **Test-C :**

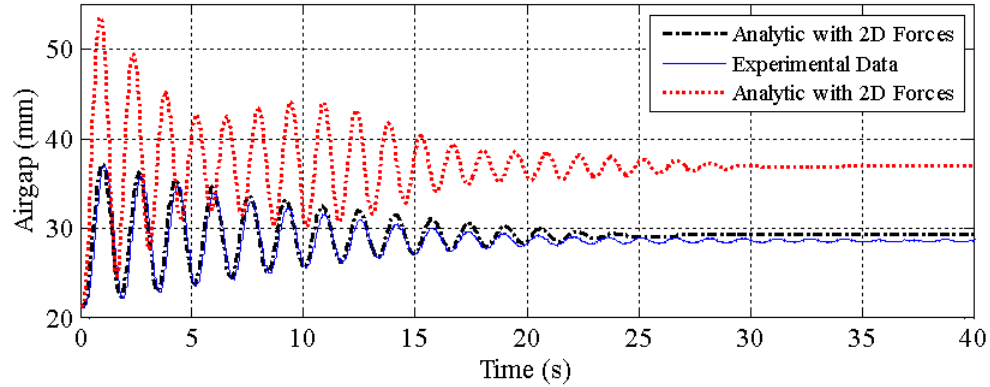


Figure B.1: *An air-gap profile using 2-D and 3-D forces and experimental results for Test-C.*

- **Test-D :**

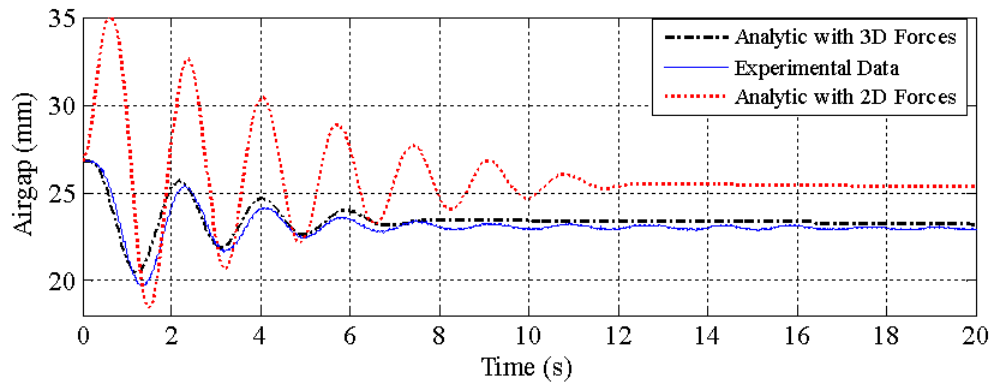


Figure B.2: *An air-gap profile using 2-D and 3-D forces and experimental results for Test-D.*

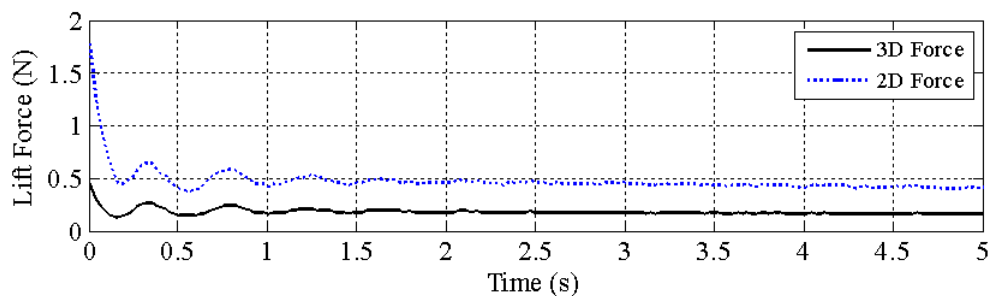


Figure B.3: *2-D and 3-D lift forces at the operating points of Test-D.*

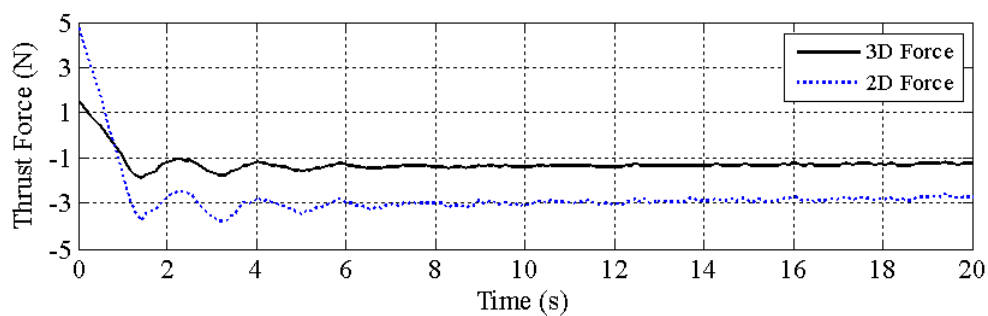


Figure B.4: *2-D and 3-D thrust forces at the operating points of Test-D.*

• **Test-E :**

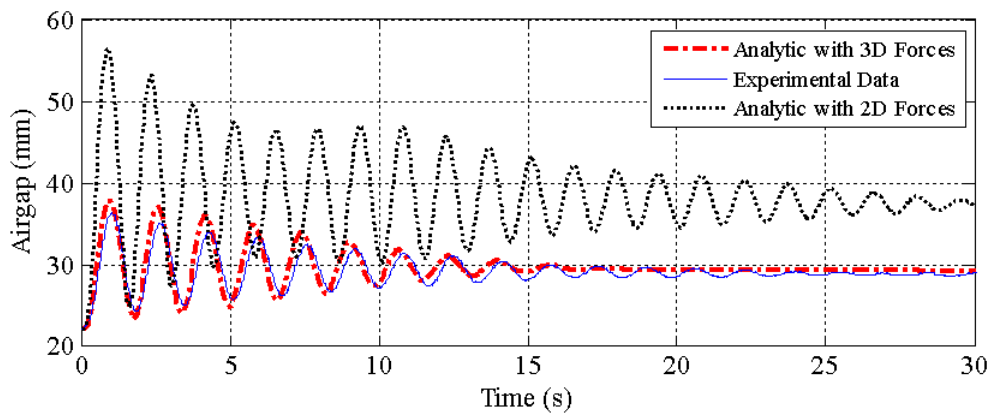


Figure B.5: *An air-gap profile using 2-D and 3-D forces and experimental results for Test-E.*

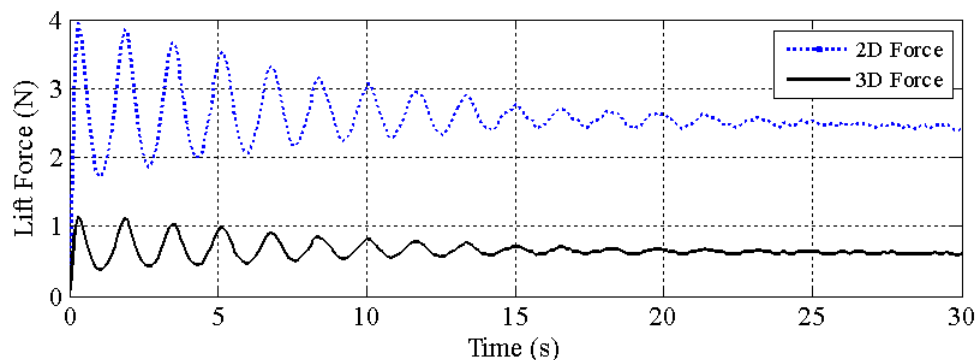


Figure B.6: 2-D and 3-D lift forces at the operating points of Test-E.

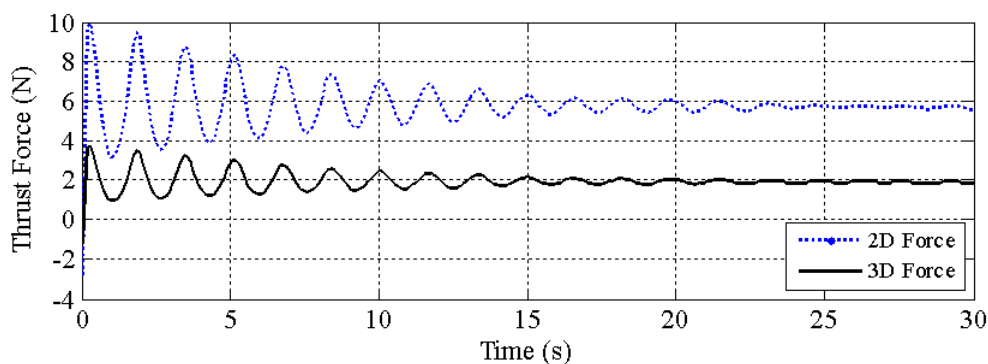


Figure B.7: 2-D and 3-D thrust forces at the operating points of Test-E.

- Test-F** : This test is very similar to the Test-A in Chapter 5. The translational velocity of the guideway is zero. The air-gap value at equilibrium state is 11.95mm. The step change in ω_m is applied at $t = 0$ s and the dynamics between the measured and the analytic (both using 2-D and 3-D forces) has been compared.

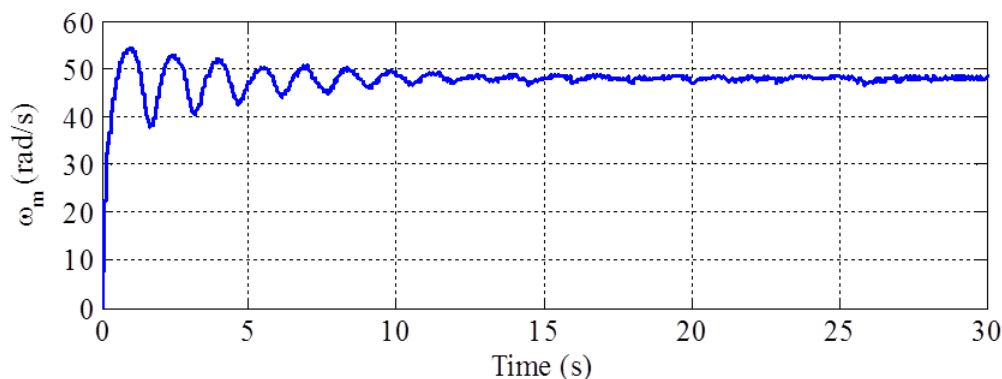


Figure B.8: The measured ω_m of the EDW for Test-F.

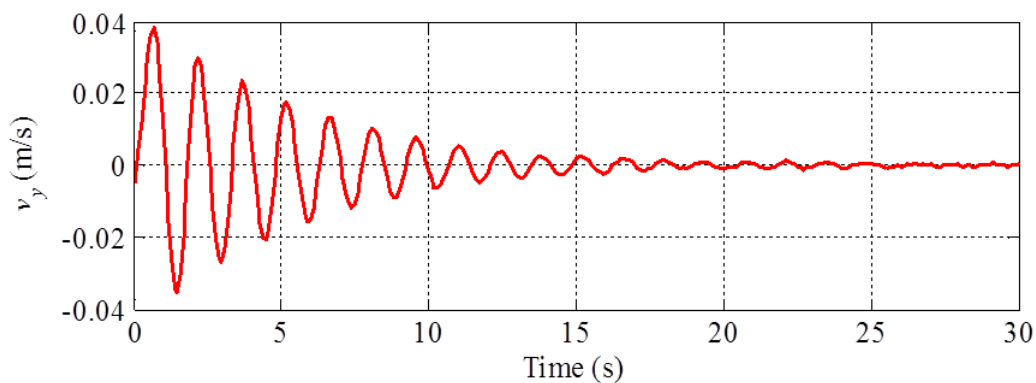


Figure B.9: *The measured v_y of the EDW for Test-F.*

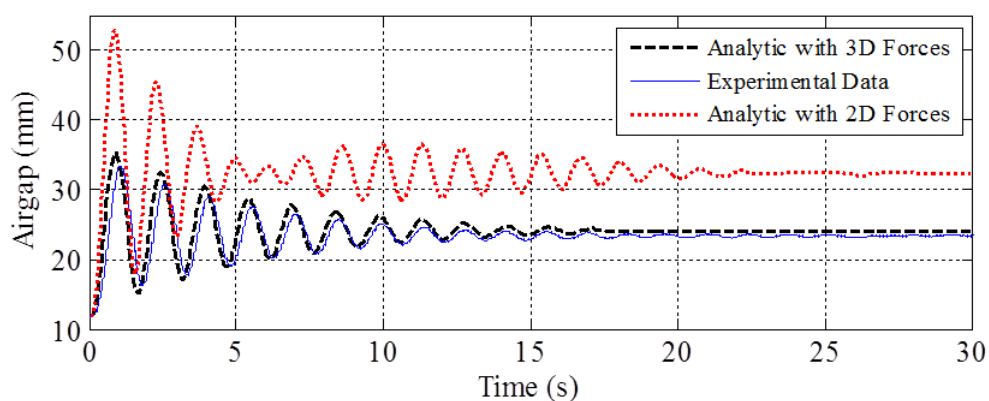


Figure B.10: *An air-gap profile using 2-D-forces, 3-D forces and experimental results for Test-F.*

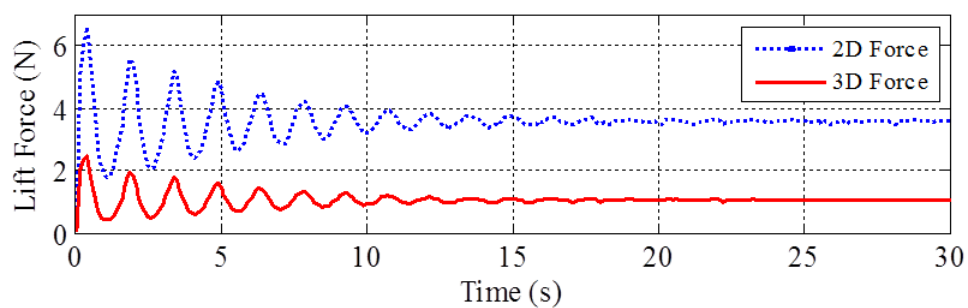


Figure B.11: *2-D and 3-D lift forces at the operating points of Test-F.*

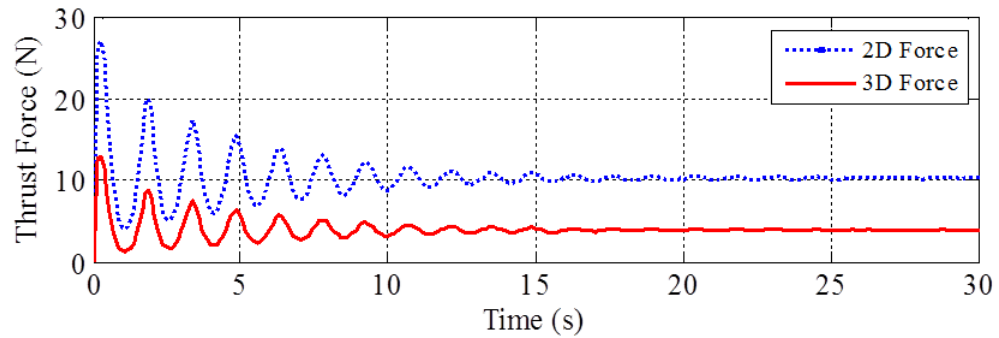


Figure B.12: 2-D and 3-D thrust forces at the operating points of Test-F.

- Test-G** : The translational velocity of the guideway is zero in this test. The air-gap value at equilibrium state is 21.5mm. Before time $t = 0$ s the pendulum is in steady-state at $g = 34$ mm and $\omega_m = 103.8$ rad/s. The step down to 50.29 rad/s in ω_m applied at $t = 0$ s and the dynamics between the measured and the analytic (both using 2-D and 3-D forces) has been compared. The air-gap using 3-D forces reached the steady-state at 28.82mm whilst the experimental one at 28.51mm.

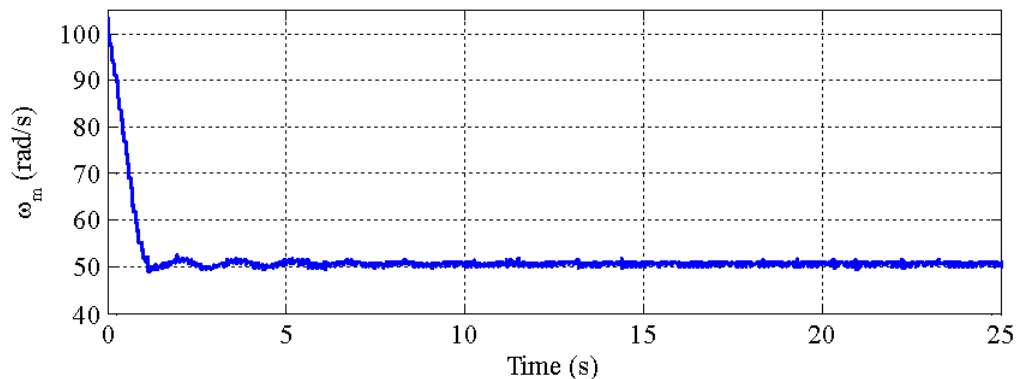


Figure B.13: The measured ω_m of the EDW for Test-G.

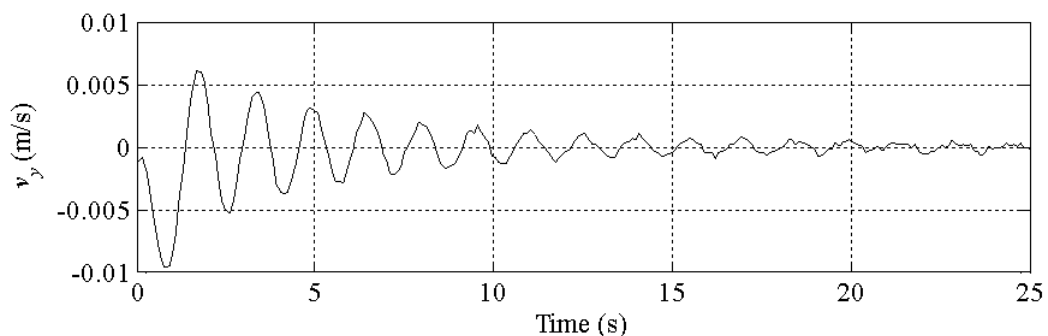


Figure B.14: The measured v_y of the EDW for Test-G.

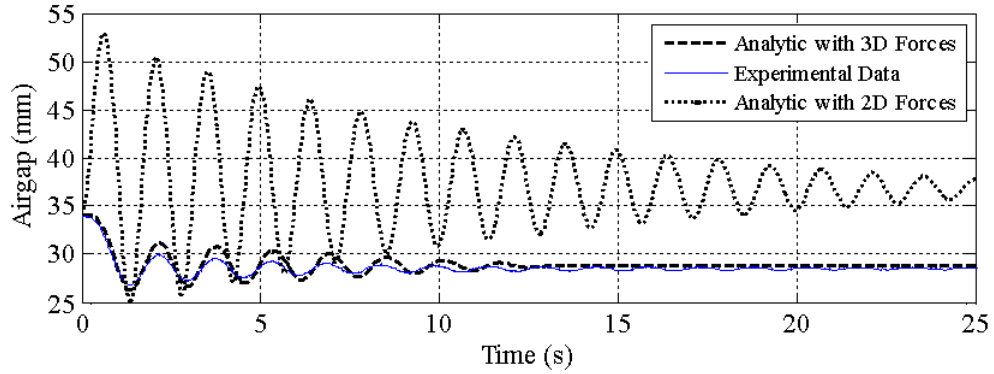


Figure B.15: An air-gap profile using 2-D forces, 3-D forces and experimental results for Test-G.

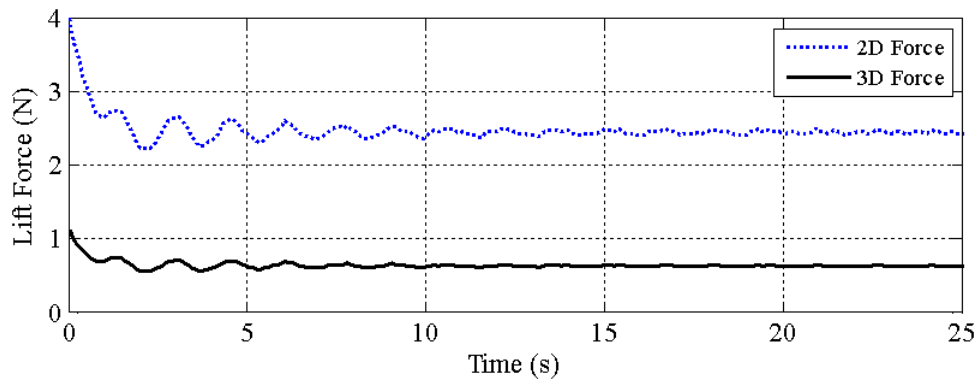


Figure B.16: 2-D and 3-D lift forces at the operating points of Test-G.

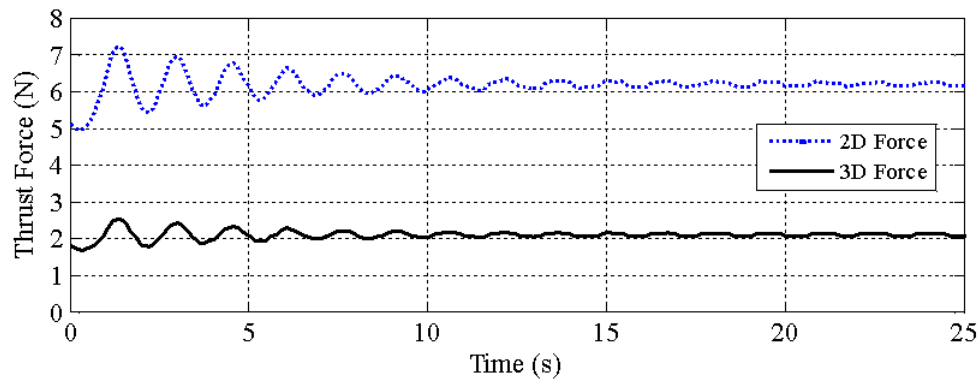


Figure B.17: 2-D and 3-D thrust forces at the operating points of Test-G.

- Test-H :** The translational velocity of the guideway is varying in this test. The air-gap value at equilibrium state is 21.5mm. Before time, $t = 0$ s the pendulum is in steady-state at $g = 22.13$ mm, $v_x = 1.977$ ms⁻¹ and $\omega_m = 15.27$ rads⁻¹. The step change in ω_m is applied at $t = 0$ s from 15.27rads⁻¹ to 77.72rads⁻¹ and the

dynamics between the measured and the analytic (both using 2-D and 3-D forces) has been compared. The air-gap using 3-D forces reached the steady-state at 29.31mm whereas the experimental measured value is 28.75mm.

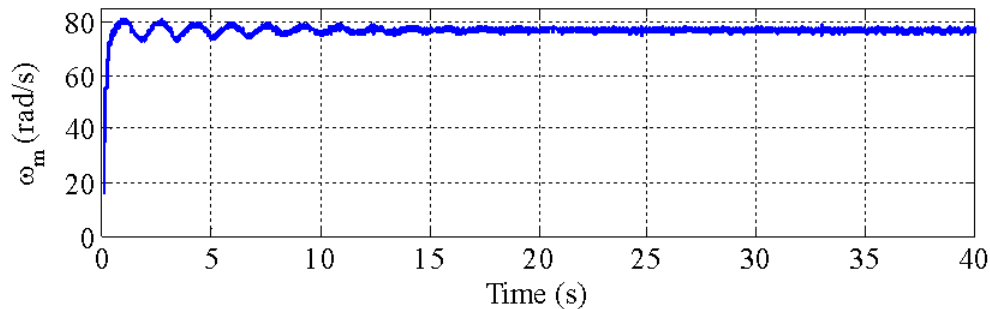


Figure B.18: *The measured ω_m of the EDW for Test-H.*

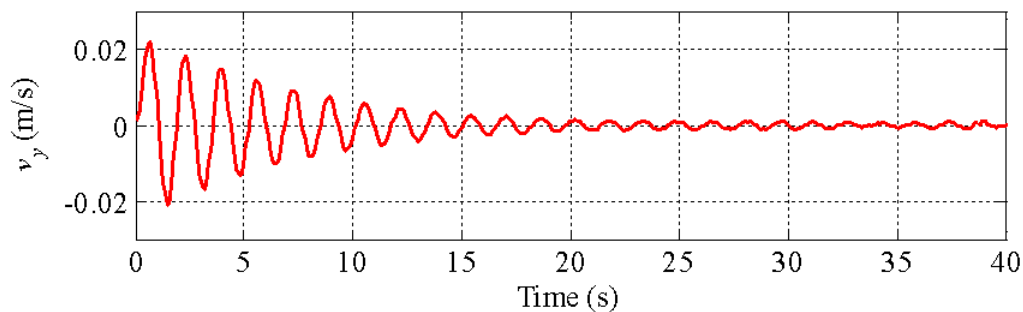


Figure B.19: *The measured v_y of the EDW for Test-H.*

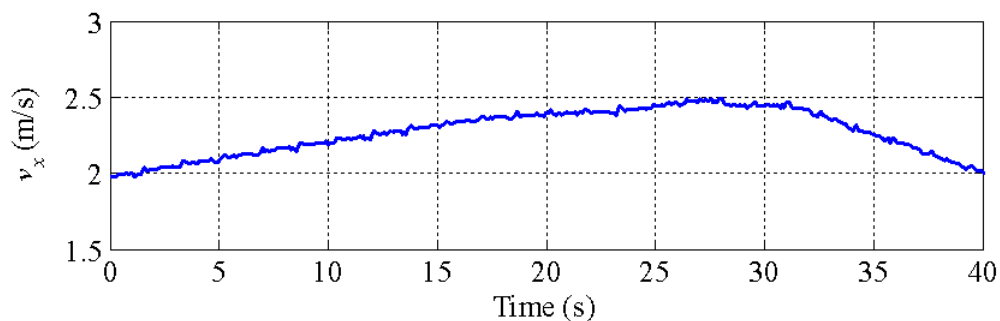


Figure B.20: *The measured v_x of the guideway for Test-H.*

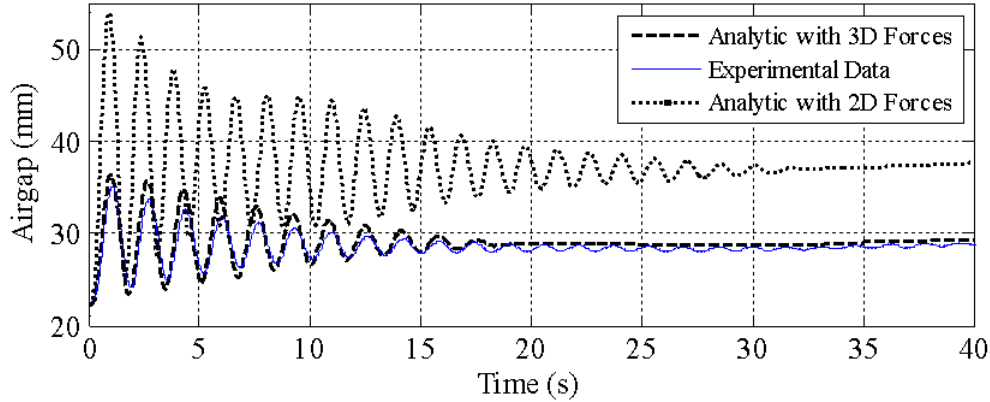


Figure B.21: An air-gap profile using 2-D forces, 3-D forces and experimental results for Test-H.

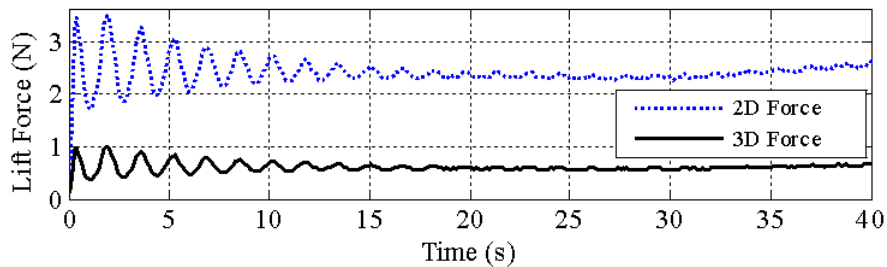


Figure B.22: 2-D and 3-D lift forces at the operating points of Test-H.

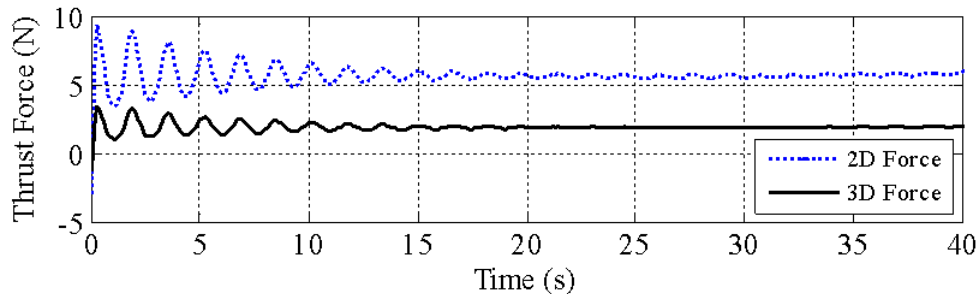


Figure B.23: 2-D and 3-D thrust forces at the operating points of Test-H.

- Test-I** : This test is very similar to Test-H. The air-gap value at equilibrium state is 21.5mm. Before time, $t = 0$ s the pendulum is in steady-state at $g = 22.41$ mm, $v_x = 1.983$ ms⁻¹ and $\omega_m = 28.52$ rads⁻¹. The step change in ω_m is applied at $t = 0$ s from 28.52rads⁻¹ to 76.41rads⁻¹ and the dynamics between the measured and the analytic (both using 2-D and 3-D forces) has been compared. The air-gap using 3-D forces reached the steady-state at 29.85mm whereas the experimental one at 29.35mm.

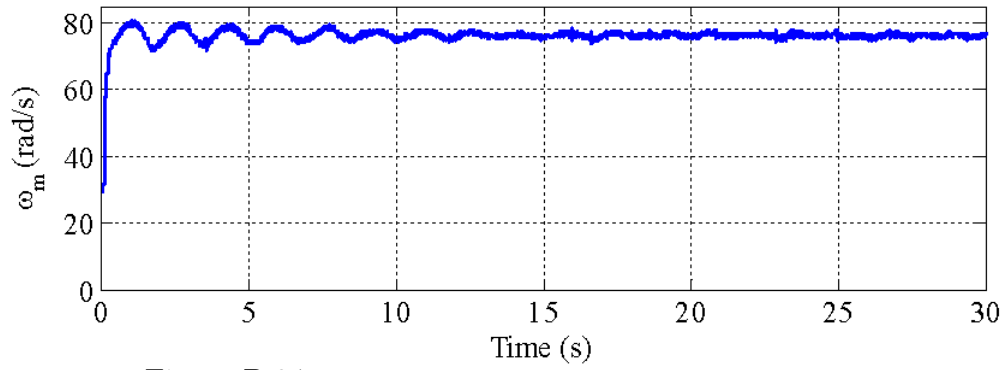


Figure B.24: *The measured ω_m of the EDW for Test-I.*

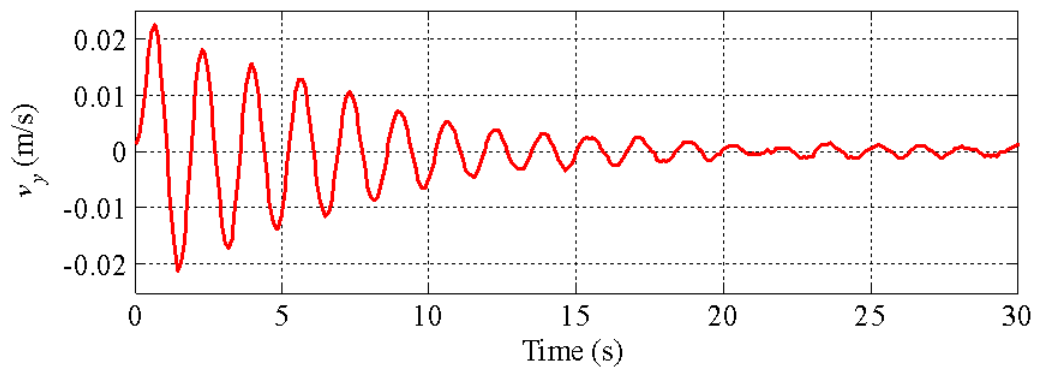


Figure B.25: *The measured v_y of the EDW for Test-I.*

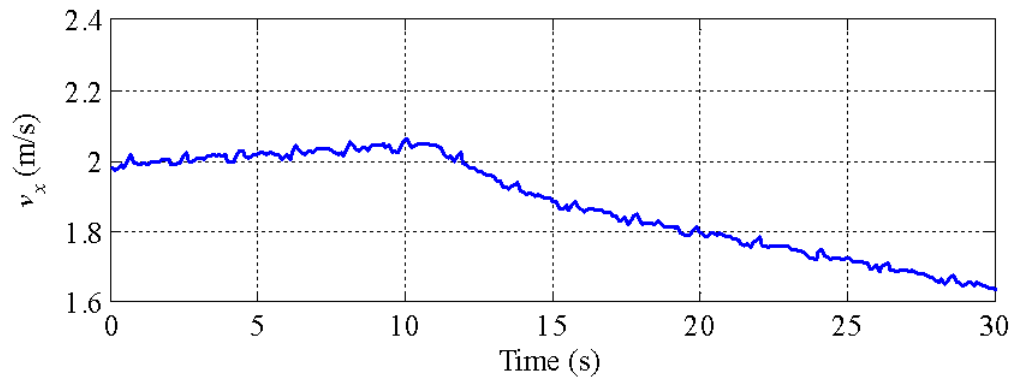


Figure B.26: *The measured v_x of the guideway for Test-I.*

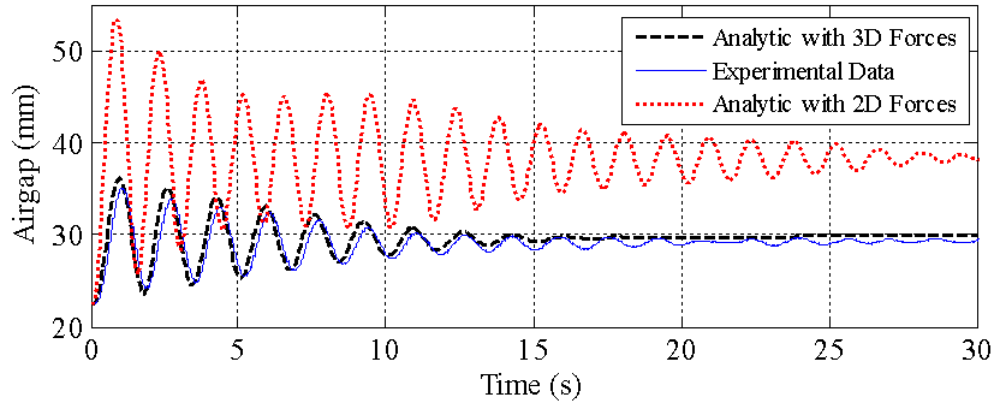


Figure B.27: An air-gap profile using 2-D forces, 3-D forces and experimental results for Test-I.

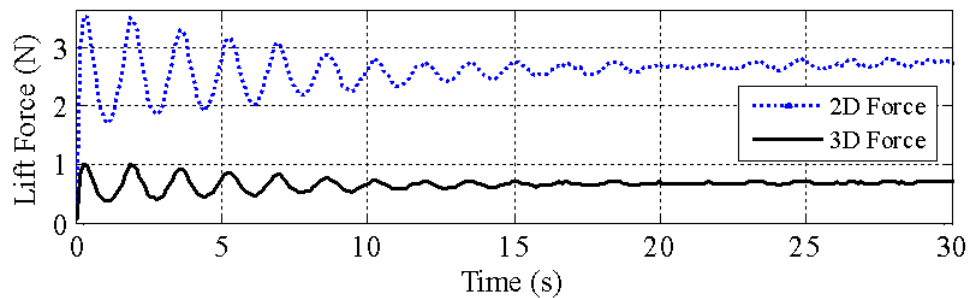


Figure B.28: 2-D and 3-D lift forces at the operating points of Test-I.

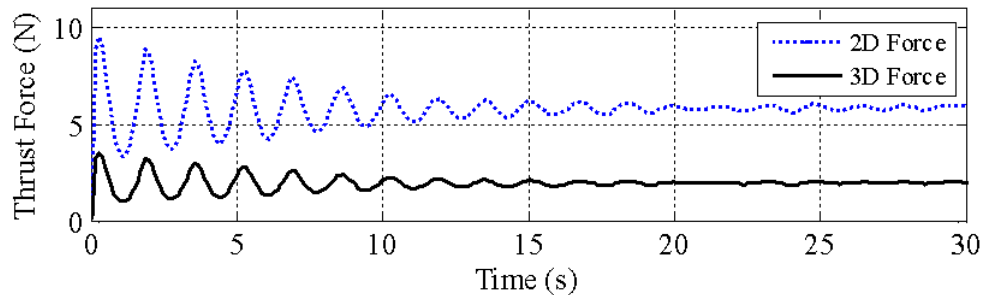


Figure B.29: 2-D and 3-D thrust forces at the operating points of Test-I.

- **Test-J** : The translational very similar to Test-D. The air-gap value at equilibrium state is 21.5mm. Before time, $t = 0$ s the pendulum is in steady-state at $g = 31.2$ mm, $v_x = 2.31$ ms⁻¹ and $\omega_m = 102.3$ rad⁻¹. The step change in ω_m is applied at $t = 0$ s from 102.3rad⁻¹ to 52.65rad⁻¹ and the dynamics between the measured and the analytic (both using 2-D and 3-D forces) has been compared.

The air-gap using 3-D forces reached the steady-state at 24.8mm whereas the experimental one at 24.7mm.

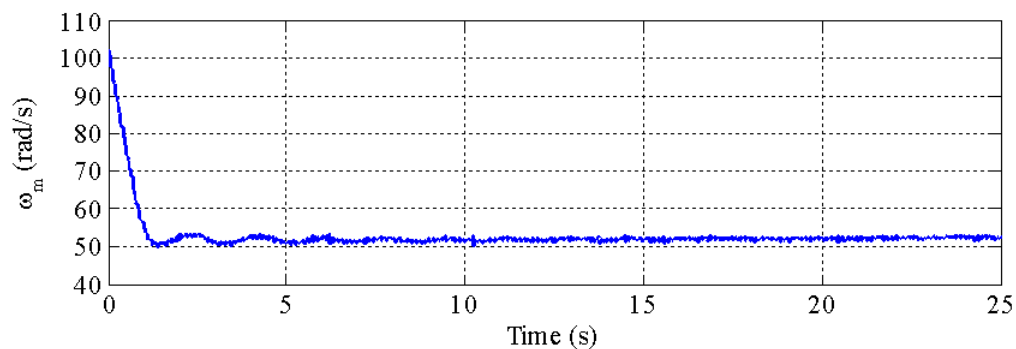


Figure B.30: *The measured ω_m of the EDW for Test-J.*

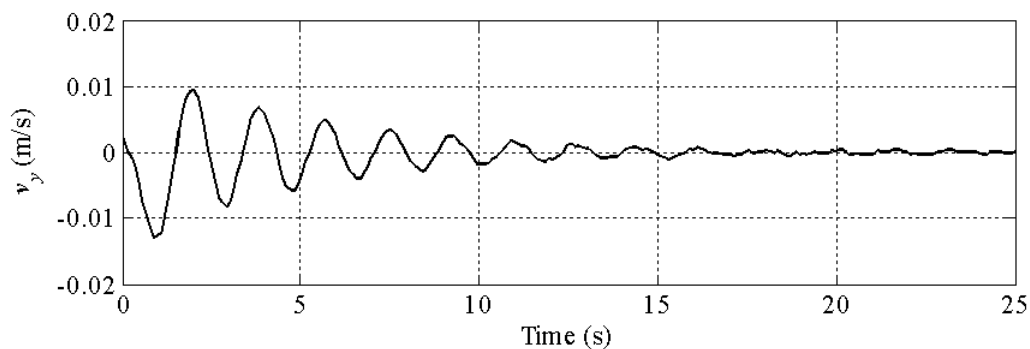


Figure B.31: *The measured v_y of the EDW for Test-J.*

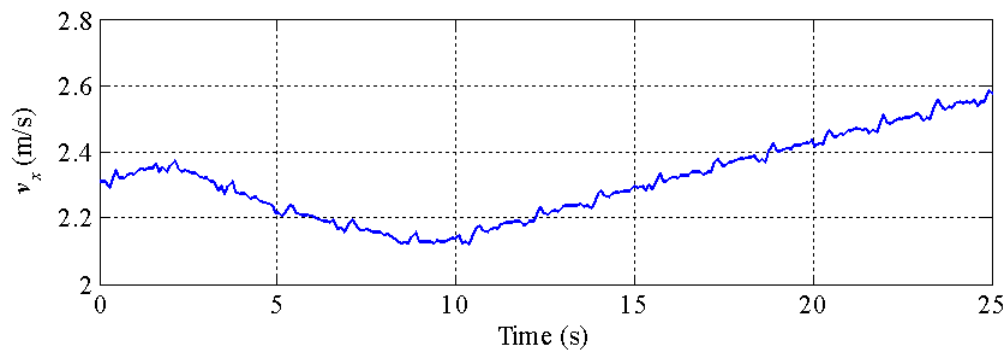


Figure B.32: *The measured v_x of the guideway for Test-J.*

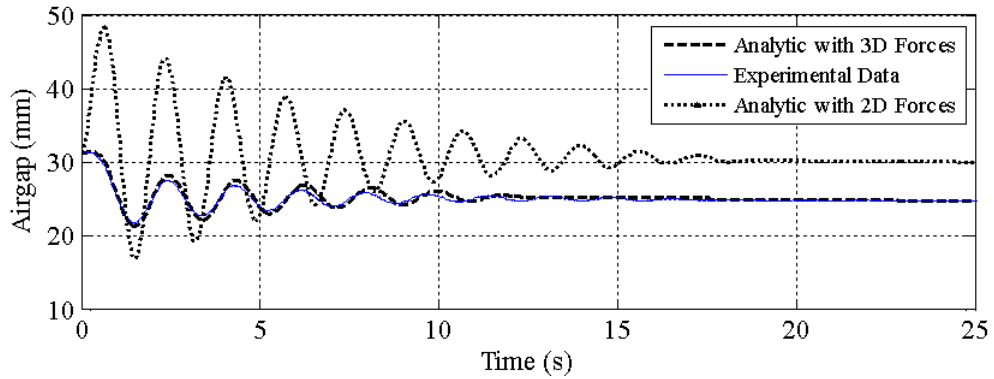


Figure B.33: *An air-gap profile using 2-D forces, 3-D forces and experimental results for Test-J.*

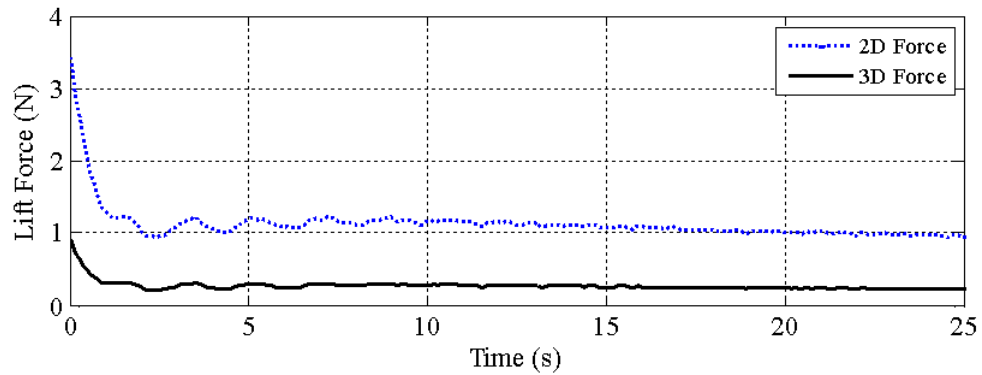


Figure B.34: *2-D and 3-D lift forces at the operating points of Test-J.*

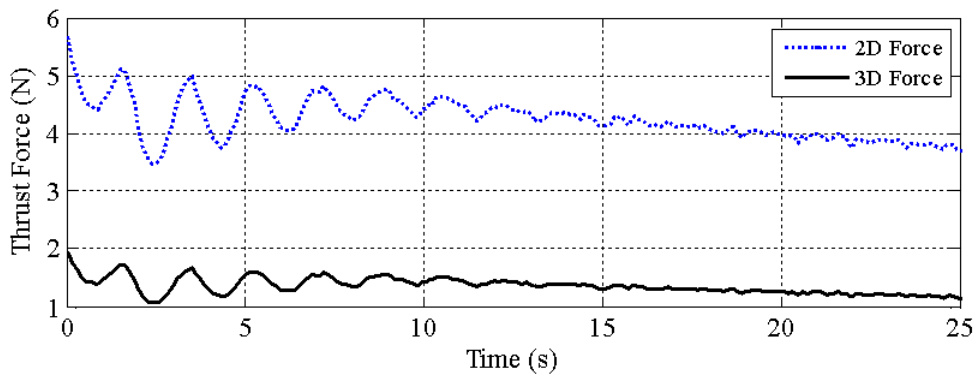


Figure B.35: *2-D and 3-D thrust forces at the operating points of Test-J.*

- Test-K** : This test is very similar to Test-J. The air-gap value at equilibrium state is 21.5mm. Before time, $t = 0$ s the pendulum is in steady-state at $g = 30$ mm, $v_x = 3.492\text{ms}^{-1}$ and $\omega_m = 102.3\text{rads}^{-1}$. The step change in ω_m is applied at $t = 0$ s from 102.3rads^{-1} to 27.96rads^{-1} and the dynamics between the

measured and the analytic (both using 2-D and 3-D forces) has been compared. The air-gap using 3-D forces reached the steady-state at 24.08mm whereas the experimental one at 23.54mm.

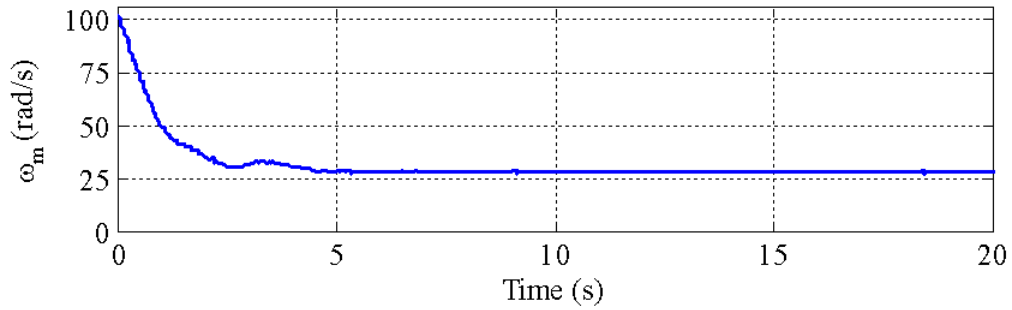


Figure B.36: *The measured ω_m of the EDW for Test-K.*

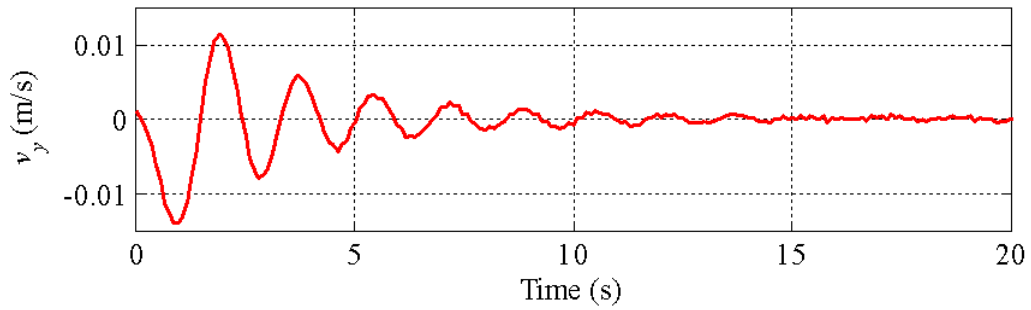


Figure B.37: *The measured v_y of the EDW for Test-K.*

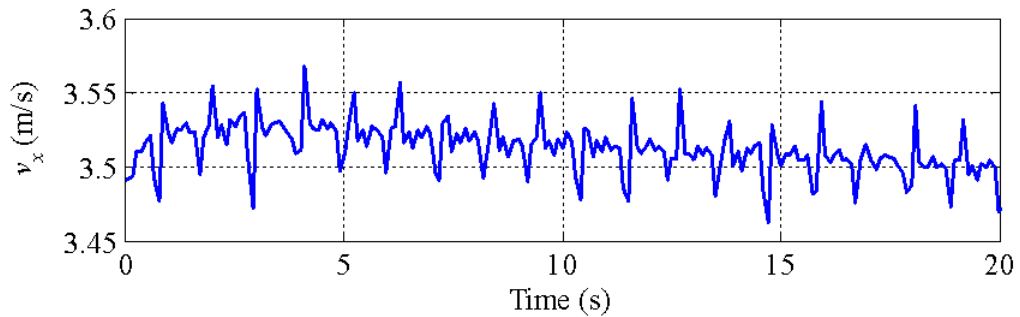


Figure B.38: *The measured v_x of the guideway for Test-K.*

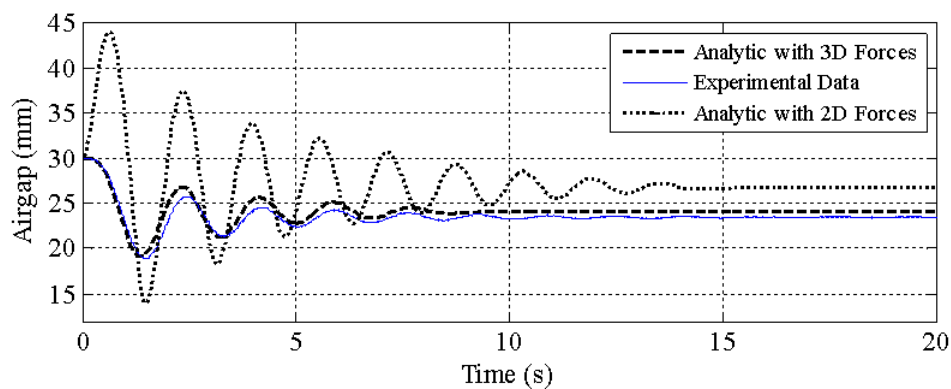


Figure B.39: An air-gap profile using 2-D forces, 3-D forces and experimental results for Test-K.

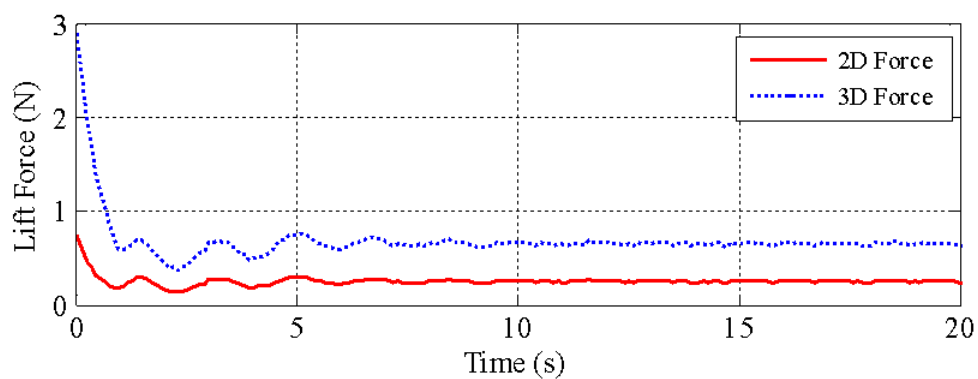


Figure B.40: 2-D and 3-D lift forces at the operating points of Test-K.

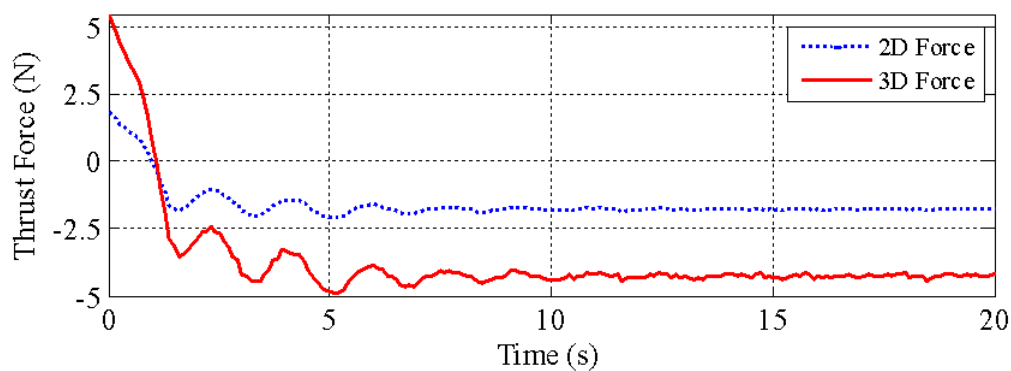


Figure B.41: 2-D and 3-D thrust forces at the operating points of Test-K.

APPENDIX C: SIMULINK MAGLEV VEHICLE

The detailed simulink block diagrams of EDW Maglev are included in this Appendix. Figure C.1 is the main block diagram consisting of several subsystems. The torque subsystem includes the torque applied to all of the four BLDC motors during the operation. The maglev vehicle subsystem is given in detail in Figure C.2. The several subsystems of the maglev vehicle subsystems are included in Figure C.3 to Figure C.7. The only the force calculation subsystem for front right EDW is shown in Figure C.8. However, the similar subsystems were adapted for other EDWs.

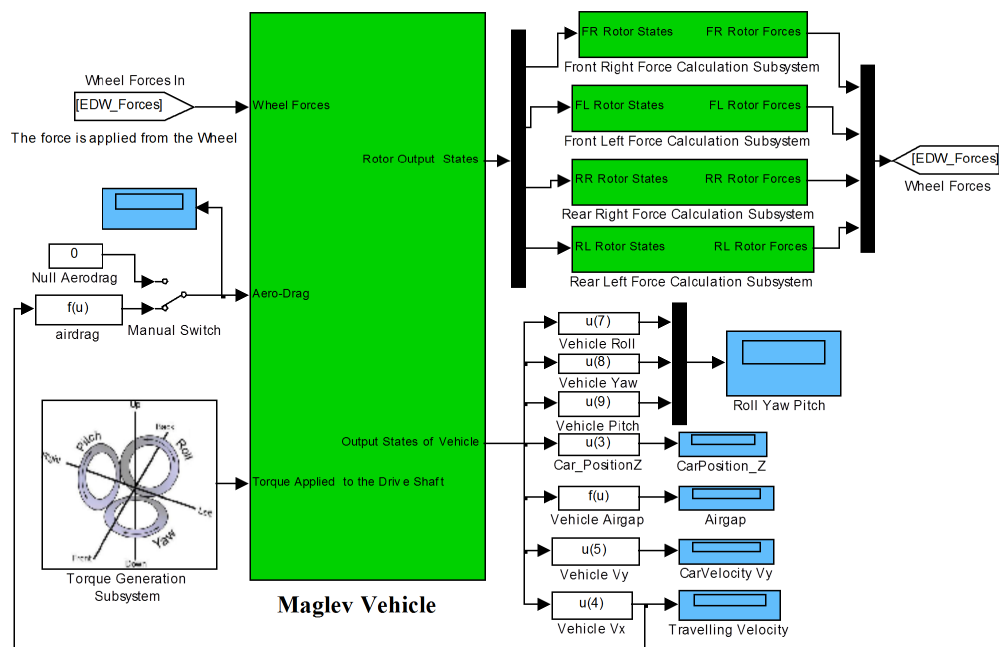


Figure C.1: *Simulink block diagram of the Maglev vehicle with experimental setup parameters.*

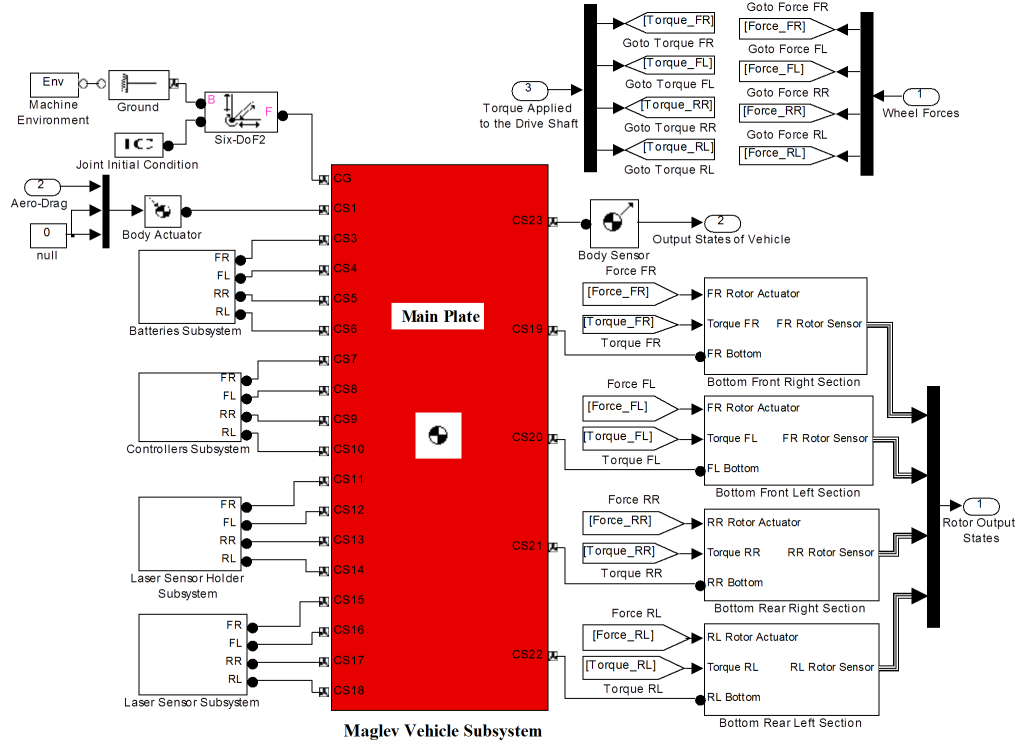


Figure C.2: Simulink diagram of the Maglev Vehicle Subsystem.

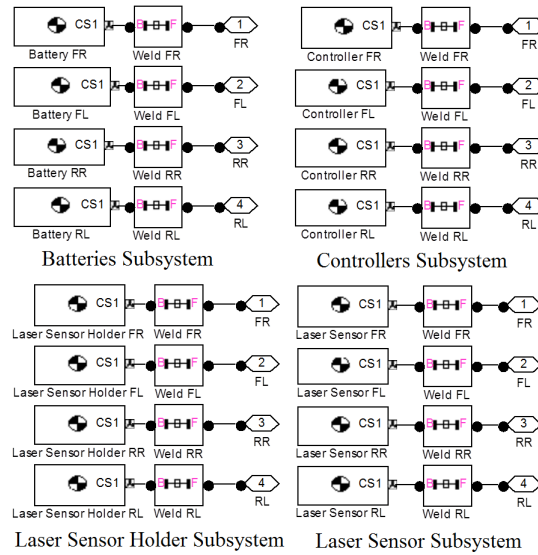


Figure C.3: Simulink block diagram of the batteries, controllers, laser sensor holders and sensors subsystems.

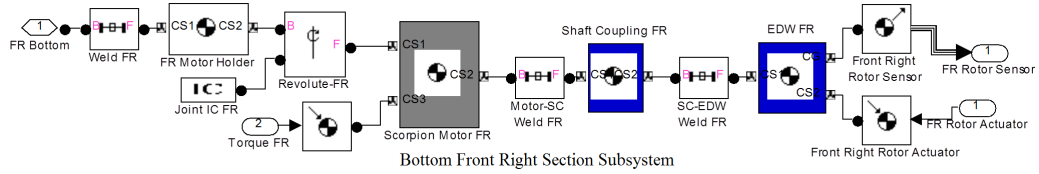


Figure C.4: Simulink block diagram of the bottom front right section subsystem.

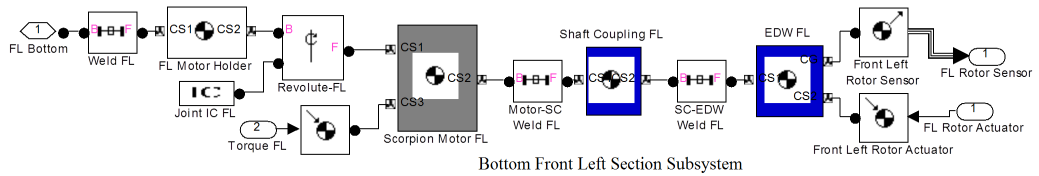


Figure C.5: Simulink block diagram of the bottom front left section subsystem.

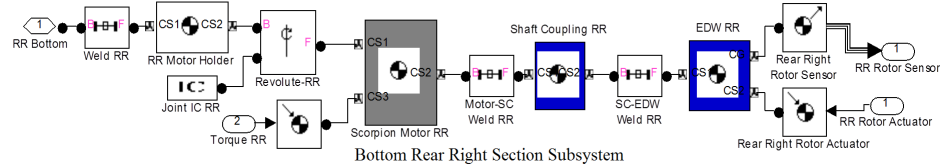


Figure C.6: Simulink block diagram of the bottom rear right section subsystem.

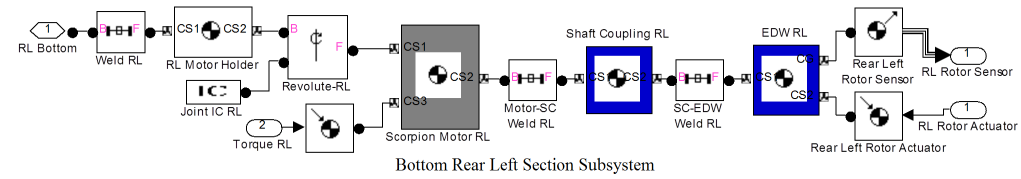


Figure C.7: Simulink block diagram of the bottom rear left section subsystem.

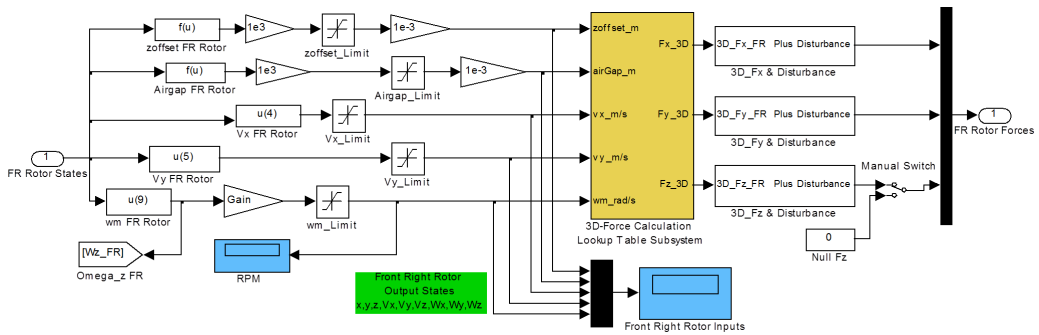


Figure C.8: Simulink block diagram of the front right force calculation subsystem.

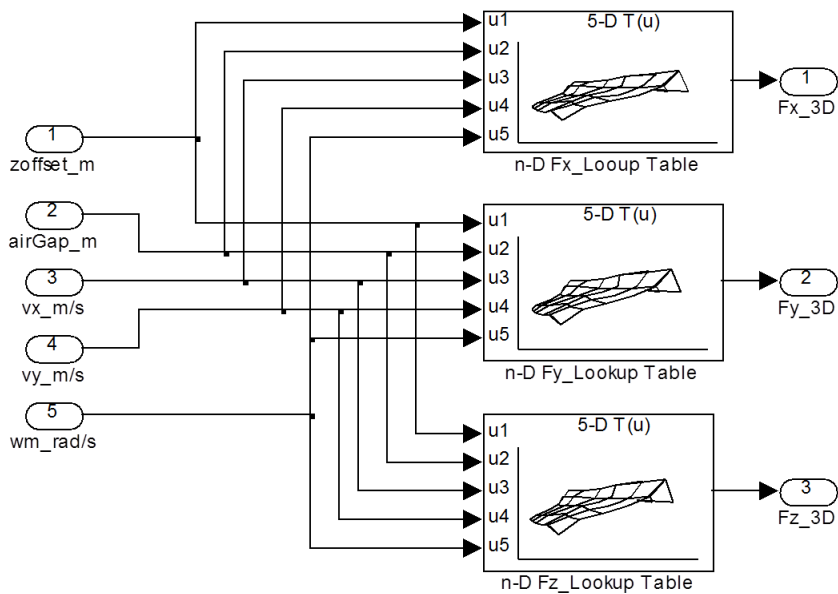


Figure C.9: *Simulink block diagram of the 3-D forces calculation lookup table subsystem.*